



Swansea University
Prifysgol Abertawe



Swansea University E-Theses

Novel anti-corrosion coatings on steel.

Bennett, Andrew Richard

How to cite:

Bennett, Andrew Richard (2009) *Novel anti-corrosion coatings on steel.*. thesis, Swansea University.
<http://cronfa.swan.ac.uk/Record/cronfa42310>

Use policy:

This item is brought to you by Swansea University. Any person downloading material is agreeing to abide by the terms of the repository licence: copies of full text items may be used or reproduced in any format or medium, without prior permission for personal research or study, educational or non-commercial purposes only. The copyright for any work remains with the original author unless otherwise specified. The full-text must not be sold in any format or medium without the formal permission of the copyright holder. Permission for multiple reproductions should be obtained from the original author.

Authors are personally responsible for adhering to copyright and publisher restrictions when uploading content to the repository.

Please link to the metadata record in the Swansea University repository, Cronfa (link given in the citation reference above.)

<http://www.swansea.ac.uk/library/researchsupport/ris-support/>

Novel Anti-Corrosion Coatings on Steel

Andrew Richard Bennett
Doctor of Engineering Thesis
2009

Supervisor: Prof. H. N. McMurray
Materials Research Centre
School of Engineering
Swansea University

ProQuest Number: 10798018

All rights reserved

INFORMATION TO ALL USERS

The quality of this reproduction is dependent upon the quality of the copy submitted.

In the unlikely event that the author did not send a complete manuscript and there are missing pages, these will be noted. Also, if material had to be removed, a note will indicate the deletion.



ProQuest 10798018

Published by ProQuest LLC (2018). Copyright of the Dissertation is held by the Author.

All rights reserved.

This work is protected against unauthorized copying under Title 17, United States Code
Microform Edition © ProQuest LLC.

ProQuest LLC.
789 East Eisenhower Parkway
P.O. Box 1346
Ann Arbor, MI 48106 – 1346



Summary

The primary objective of the work detailed in this thesis was to further explore the inhibitory performance of polyaniline for the prevention of corrosion-driven cathodic disbondment on steels and zinc-alloy coated steels. Polyaniline was investigated under atmospheric conditions so as to make possible further elucidation of the mechanisms by which it would provide this inhibition. Accordingly it is suggested that the positive performance of polyaniline indicated within this report, in addition to further mechanistic understanding, paves the way for industrial use of polyaniline as an inhibitor. To provide further mechanistic support to the inhibitory performance of polyaniline, polyaniline micro-films were applied to the metal substrate surfaces, allowing the visualisation of electrochemical and acid-base state changes resulting from substrate contact and corrosion.

Due to industrial concerns over the current cost associated with polyaniline inhibitor pigments, the inhibitory properties of novel organic acid etch primers were explored on both iron and zinc substrates. The findings of this study led to the proposition that the presence of polyaniline may not be required within the model organic coating system in order to provide a similar level of inhibition.

Alongside the investigations of inhibitory organic coating systems, attention was directed towards novel Mg-Al-Zn metallic coatings. These are shown to provide inhibition of cathodic disbondment of organic coatings where no form of in-coating inhibition is present. These alloy-coated steels were found to suffer from a novel form of corrosion and full mechanistic proposition is provided, as well as important initiation factors.

Finally, the photovoltaic possibilities of polyaniline were explored in order to find novel, high value coating systems for the pre-painted steel industry. Accordingly the photovoltaic properties of polyaniline are compared to established photovoltaic polymers.

Declaration

This work has not previously been accepted in substance for any degree and is not being concurrently submitted in candidature for any degree.

Signed..... (candidate)

Date..... 28/08/2009.....

Statement 1

This thesis is the result of my own investigation, except where otherwise stated. Other sources are acknowledged by footnotes giving explicit references.

Signed..... . (candidate)

Date..... 24/08/2009.....

Statement 2

I hereby give consent for my thesis, if accepted, to be available for photocopying and for inter-library loans after expiry of a bar on access approved by the University of Wales on the special recommendation of the Constituent Institution concerned. I also give my consent for the title and summary to be made available to outside organisations.

Signed.... (candidate)

Date..... 28/08/2009.....

Acknowledgments

I would like to take this opportunity to gratefully acknowledge the Engineering and Physical Sciences Research Council and Corus Group Plc for their full financial support from the beginning to end of this research project.

Throughout this work a great deal of time and effort was put towards its successful completion by Prof Neil McMurray. Prof McMurray provided strong support throughout by the constant input of various ideas, hypotheses and suggestions that allowed the research to develop in a positive and rewarding manner. I will always remember the regular long talks and wealth of information scribbled on pieces of paper during this time.

Another invaluable source of guidance and support came from Dr Geraint Williams both before and after his promotion to Lecturer. Without Geraint it may have been impossible to operate the scanning Kelvin probe and other equipment required to complete my studies. Not only was Geraint an invaluable source of technical support, he spent much time mentoring me through the intricacies of experimental science providing an important source of motivation.

I would also like to acknowledge the input of Paul Jones of Corus Group Plc. Paul provided the opportunity to open my eyes to the world of developing novel industrially relevant technology. This provided motivation to understand and research thin film organic photovoltaics, which I found to be a very rewarding and enjoyable subject.

I would like to thank the corrosion group within the School of Engineering at Swansea University, staff and students both past and present. Many people over the course of my research provided ideas and support, which undoubtedly shaped the way in which my work progressed. Thanks must also go to my mum, dad, friends and family for understanding and support throughout, both inside university and outside.

Table of Contents

	Page
Chapter 1: Introduction	1
1.1 Research Aims and Objectives	2
1.2 Pre-painted Steels	3
1.2.1 Substrate Cleaning and Preparation	4
1.2.2 Multilayer Coating Systems for Pre-Painted Steels	5
1.3 Corrosion Failure Mechanisms	8
1.3.1 The Theory of Aqueous Corrosion	8
1.3.2 Pourbaix Diagrams	9
1.3.3 Atmospheric Corrosion of Coated Metal Surfaces	10
1.3.3.1 Corrosion-Driven Cathodic Disbondment	10
1.3.3.2 Conventional Filiform Corrosion	16
1.4 Metallic Coatings	20
1.4.1 Anodic and Cathodic Metallic Coatings	21
1.4.2 Hot-Dip Galvanised Steel (HDG)	22
1.4.3 Galfan® Metallic Coatings	23
1.4.4 Magizinc®	24
1.5 Corrosion Inhibitors	28
1.6 Chromates for Corrosion Control	31
1.7 Conducting Polymers for Corrosion Control	33
1.7.1 Polyaniline (PAni)	35
1.7.1.1 Polyaniline Protection of Ferrous Metals	38
1.7.1.2 Polyaniline Protection of Zinc	41
1.8 The Scanning Kelvin Probe	43
1.8.1 SKP Theory	44
1.9 Secondary Ion Mass Spectrometry	47
1.10 Photovoltaics	49
1.10.1 Electromagnetic Radiation and Photons	50
1.10.2 Semiconductor Photovoltaic Theory	51
1.10.3 Measurement of Photovoltaic Cell Parameters	54
1.10.4 Electrical Properties of Polymers	57
1.10.5 Organic Photovoltaics	58
1.10.5.1 Schottky Photovoltaic Cells	58
1.10.5.2 Organic Bilayer Heterojunction Solar Cells	61

1.10.5.3	Organic Bulk Heterojunction Solar Cells	62
1.10.6	Polythiophene for Photovoltaic Applications	64
1.10.7	Polyaniline for Photovoltaic Applications	66
1.11	References	67
Chapter 2: Experimental Design		75
2.1	Materials	76
2.1.1	Metals	76
2.1.2	Chemicals	77
2.2	Preparation of Model Coatings	79
2.2.1	The Model Matrix	79
2.2.2	Preparation of Model Composite Coatings	80
2.2.3	Preparation of Model Polyaniline Casting Solutions	81
2.2.4	Preparation of Coated Substrates	82
2.2.4.1	Casting of Composite Dispersions	82
2.2.4.2	Application of Homogeneous Polymer Micro-films	84
2.3	The Scanning Kelvin Probe (SKP) Technique	85
2.3.1	The Scanning Kelvin Probe Apparatus	85
2.3.2	Calibration of the SKP	89
2.3.3	SKP Studies of Cathodic Disbondment	92
2.3.4	SKP Studies of Filiform Corrosion (FFC)	93
2.4	Time Lapse Digital Photography of Cathodic Delamination	94
2.5	Secondary Ion Mass Spectrometry (SIMS)	94
2.6	Atomic Force Microscope (AFM)	95
2.7	UV-VIS Absorption Measurement	96
2.8	Four Point Conductivity Measurements	97
2.9	Metallographic Preparation of Magnesium Substrates	98
2.10	Electrochemical Reduction of Polyaniline Micro-films	99
2.11	Scanning Electron Microscope	99
2.12	Fabrication and Performance Testing of Hybrid Solar Cells	100
2.13	References	103

Chapter 3: Polyaniline Micro-films Adherent to Iron	104
3.1 Introduction	105
3.2 Experimental	107
3.3 Results and Discussion	109
3.3.1 Measurement of Micro-film Thickness	109
3.3.2 Under-film Potentiometry	112
3.3.3 Delamination of PVB Control Coatings	116
3.3.4 Delamination of PANi-EB – PVB Bilayer Coatings	118
3.3.5 Delamination of PANi-ES – PVB Bilayer Coatings	119
3.3.6 Optical Cathodic Disbondment Studies	125
3.3.7 Comparing Polyaniline Micro-films with Composite Coatings	133
3.4 Conclusions	138
3.5 References	140
Chapter 4: Polyaniline as an Inhibitor on Zinc	141
4.1 Introduction	142
4.2 Experimental	144
4.3 Results and Discussion	146
4.3.1 PANi-EB in PVB on Zinc	146
4.3.2 Visualisation of Interfacial Electrochemistry	150
4.3.3 PANi-ES – PVB Composite Coatings	152
4.3.3.1 SKP Potentiometry	152
4.3.3.2 Oxide Growth Studies	157
4.3.3.3 Delamination of PANi-ES – PVB Composite Coatings	164
4.3.4 Strontium Chromate Pigmented PVB on Zinc	172
4.4 Conclusions	178
4.5 References	180

Chapter 5: Organic Acid Etch Primers	182
5.1 Introduction	183
5.2 Experimental	184
5.3 Results and Discussion	185
5.3.1 Inhibition of Cathodic Disbondment on Iron	185
5.3.2 Inhibition of Cathodic Disbondment on Zinc	194
5.4 Conclusions	201
5.5 References	203
Chapter 6: Corrosion Studies of Mg-Al-Zn Galvanised Steels	204
6.1 Introduction	205
6.2 Experimental	208
6.3 Results and Discussion	209
6.3.1 The Microstructure of Hot Dip Mg 1.5/Al 1.5/Zn Coatings	209
6.3.2 Cathodic Delamination Testing	212
6.3.3 Exposing the Steel at the Defect Edge	214
6.3.4 Mechanism of Conventional FFC	218
6.3.5 SKP Analysis of FFC Attack on Magizinc	220
6.3.6 Exploring the Significance of Exposed Steel	222
6.3.7 Indications of Unconventional FFC	226
6.3.8 Further Investigations into the Active FFC Mechanism	228
6.3.9 Proposition of the Active FFC Mechanism	230
6.3.10 Exploring the Factors of FFC Initiation	233
6.3.11 Acetate Release from the Organic Layer	238
6.4 Conclusions	241
6.5 References	243

Chapter 7: Photovoltaic Applications of Polyaniline	244
7.1 Introduction	245
7.2 Experimental Details	246
7.3 Results and Discussion	249
7.3.1 Single Organic Layer Hybrid Photocells	249
7.3.2 Cell Performance at Varying Light Intensity	259
7.3.3 PA _n i-ES Cell Performance after Light Soaking	262
7.3.4 Addition of a PEDOT:PSS Surface Electrode	266
7.4 Conclusions	270
7.5 References	272
Chapter 8: Conclusions and Future Work	273
8.1 Conclusions	274
8.2 Future Work	276

Chapter 1

Introduction

1.1 Research Aims and Objectives

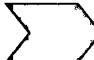
The mechanism by which polyaniline acts to provide inhibition of corrosion-driven cathodic disbondment on iron has been the subject of much debate over the previous years. Further mechanistic understanding is provided here through the visualisation of polyaniline state changes through the use of optically transparent micro-films.

 **Chapter 3**

Polyaniline emeraldine salt has been proven to effectively inhibit corrosion-driven cathodic disbondment of organic coatings on zinc. A mechanistic appraisal of the polyaniline dopant choice is conducted through systematic variations in polyaniline pigment loadings.

 **Chapter 4**

Model acid etch primers based upon organic acids are investigated as possible environmentally friendly alternatives to strontium chromate. The extent by which these inhibit cathodic delamination on both iron and zinc substrates is highlighted and discussed.

 **Chapter 5**

A novel form of filiform corrosion (FFC) is discovered to occur, undermining organic coatings adherent to a novel Zn/Mg/Al alloy metallic coating. The active propagation mechanisms and important initiation factors of this FFC are presented.

 **Chapter 6**

Polyaniline has been shown to be an effective corrosion inhibitor, and alternative applications are presented here. The viability of utilising the semiconductor properties of polyaniline for photovoltaic applications is investigated. The possibility creating thin-film hybrid photovoltaic cells as part of an organic coating system for pre-painted steels is proposed.

 **Chapter 7**

1.2 Pre-painted steels

Coatings of many different types are applied to metal surfaces, mostly to separate the environment from the metal, but often to control the micro environment on the metal surface. It is usual for the first coat applied to bare metal to be a primer coating and the final coat is generally known as a top coat, with all other in between coats termed intermediate coats [1]. A coating system is the name given to the complete coating, where the coating system is made up of one or more layers. Each coat in a coating system is carefully selected for the task, whether that task be corrosion protection or to create an aesthetically pleasing finish.

Paint consists of a vehicle, a pigment and additives or fillers. The vehicle is the liquid that gives the paint its fluidity and is commonly made up of an amorphous polymer and a solvent. Amongst others the types of polymers generally used in commercially produced paint are alkyd resins, phenolic resins, epoxy resins, polyurethanes. It is the character of the polymer that determines the physical properties of the paint coating. There is a large range of solvents suitable for use within organic coatings such as acetone, benzene, methyl acetone, toluol, butanol, amyle acetate and others. The solvent enhances the fluidity of the coating and almost completely evaporates as the films are formed [2]. The reason why additives are included in paint is to lower the brittleness of the final solidified paint film, and hence decrease the susceptibility of the coating to mechanical damage defects such as crazing whilst in service.

Pigments are added to paint either to provide corrosion protection of the underlying metal and/or to give pleasing aesthetic characteristics to the finished product. Generally a paint film will always have certain permeability to moisture and water, which is especially the case at defects and pores in the coating. Protective action required from the paint is generally given by various corrosion inhibiting pigments [3]. The common corrosion inhibiting pigments in practical use today are almost always chromates [2], although other corrosion inhibitors exist and these are discussed later. Some of the coating defects that may be found in the finished paint film can include [4]:

1. Irregularity of vehicle molecules (e.g. localised distribution of bridging groups).
2. Solvent Residue.
3. Difference in expansion coefficients in multilayer coatings.
4. Residual Stress.
5. Poor adhesion of polymer to pigment.

1.2.1 Substrate Cleaning and Preparation

The oily/greasy substances that will most probably be present on the surface of a metal substrate prior to coating are likely to originate from the various handling and storage processes the substrate has been subjected to. It is important to remove these contaminants before coil coating application of an organic layer in order to maximise the adhesive and corrosion protective properties of the coating. The oily substances fall into two categories, the first is biological fats (animal or vegetable) and the second is mineral oils. Biological fats can be removed from the substrate by using strong alkalis, while the mineral oils can be effectively removed with soaps or synthetic detergents [5].

In order to provide long term protection of the metal, it is important that mill scale and rust is removed prior to coating in order to give lasting protection. This is especially true in the case of coil coating, where the surface of strip steel is allowed to marginally decay whilst in storage awaiting further processing. There are a number of different processes that can be successfully utilised to remove mill scale and rust such as pickling or blast cleaning [6].

1.2.2 Multi-layer Coating Systems for Pre-painted Steels

The corrosion protective ability of a paint coating generally increases with the coating thickness. Thick paint films can be problematic in that they tend to crack due to internal stresses, hence leading to coating failure. Therefore there is an upper limit to the thickness of an effective coating. One way of overcoming this problem is to apply a coating comprising of multiple individual coating films, building one on top of the other to create a multilayer organic coating system [2]. A good example of the application of multilayer coating systems is for pre-finished steels for construction applications, where prerequisites are high flexibility, long service life and high aesthetic quality.

Organically coated steels (OCS) are increasingly popular for cladding usage in the construction industry due to the mass production of functional buildings. At the root of this popularity is the fact that these steels allow the rapid construction of cost effective buildings with a long expected life-time. The Corus commercial multilayer coating system used in the production of pre-painted OSC for construction applications is called Colorcoat® HPS200. Colorcoat® materials are guaranteed against corrosion and coating failure for a period of up to 30 years during their final location dependent upon local environmental conditions. Production of HPS200 takes place via continuous coil coating, as illustrated schematically in figure 1.1, onto 0.5 – 0.7mm gauge strip steel coated with a Galfan galvanised layer (described fully in section 1.3.3). The organic coating system applied to the front side of the galvanised strip steel is 200µm of PVC, and the underside (back-coat) is a 15µm dry film thickness polyester. Additionally a range of pre-treatments and primers are also used within the systems to provide further corrosion protection.

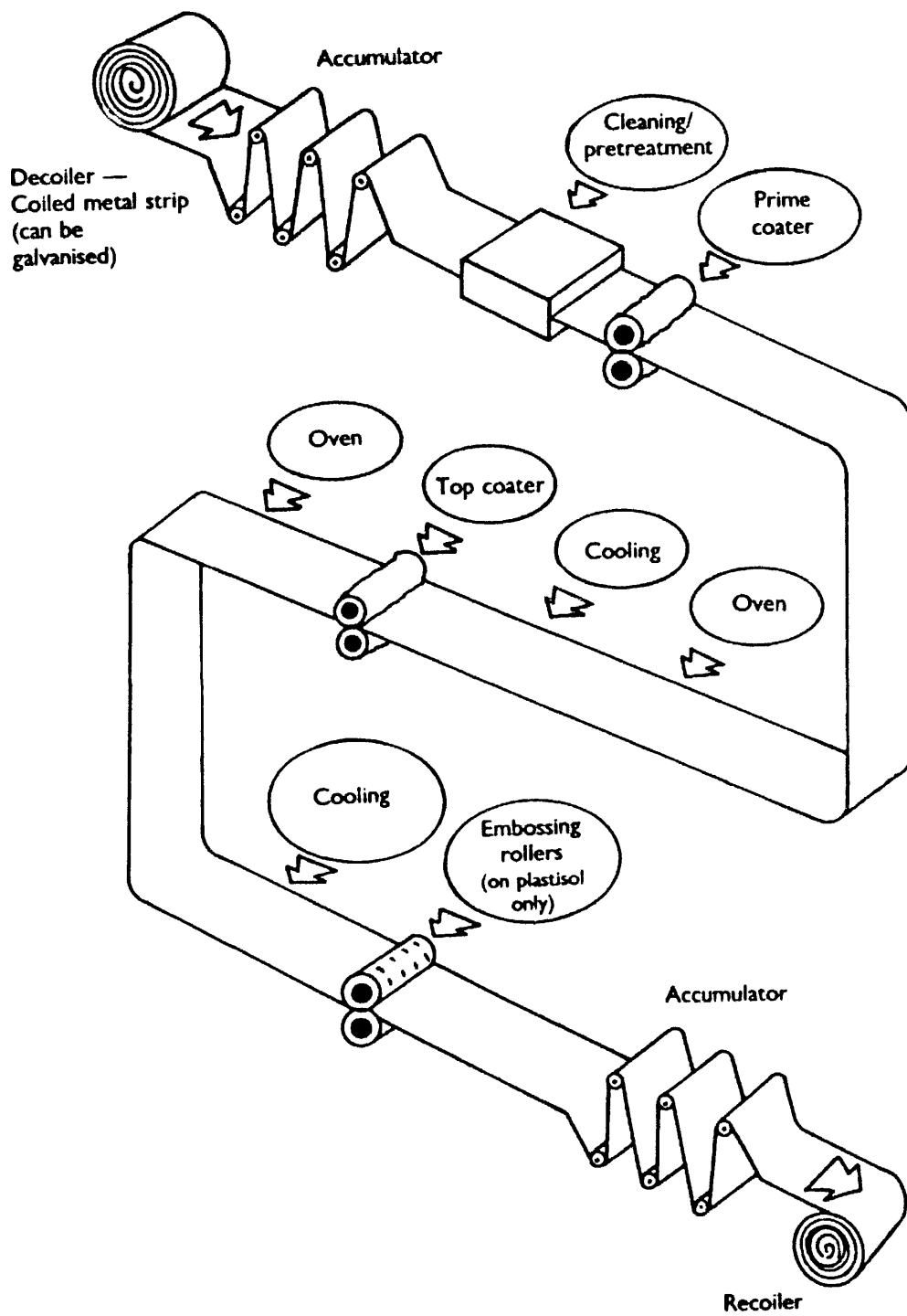


Figure 1.1 Schematic diagram of the production process for continuously coated organically coated galvanised steels [7].

The first stage in producing the finished HPS200 OCS strip is to apply a pre-treatment by initially cleaning the Galfan surface using a caustic spray, followed by application of an inorganic conversion coating (10 – 60nm) with a final chromic acid rinse. The purpose of this pre-treatment stage is to prepare the substrate surface (Galfan) chemically and physically for subsequent organic coating application. Two organic coatings are then applied to each side of the substrate via roller coating, beginning with a primer coat followed by subsequent curing. The primer is generally epoxy, acrylic or polyester based and has a dry film thickness of approximately 5µm. Corrosion inhibitors based on sparingly soluble strontium chromate are typically contained within this primer coating to provide corrosion inhibition. Upon curing of the primer layers the top-coat and back-coat layers of 200µm PVC and 15µm Polyester respectively are applied simultaneously on the coating line. Typical curing conditions involve the metal reaching a peak temperature of approximately 220°C for up to 50 seconds. The finished HPS200 coating system looks as shown schematically within figure 1.2, where each part of the coating system is shown.

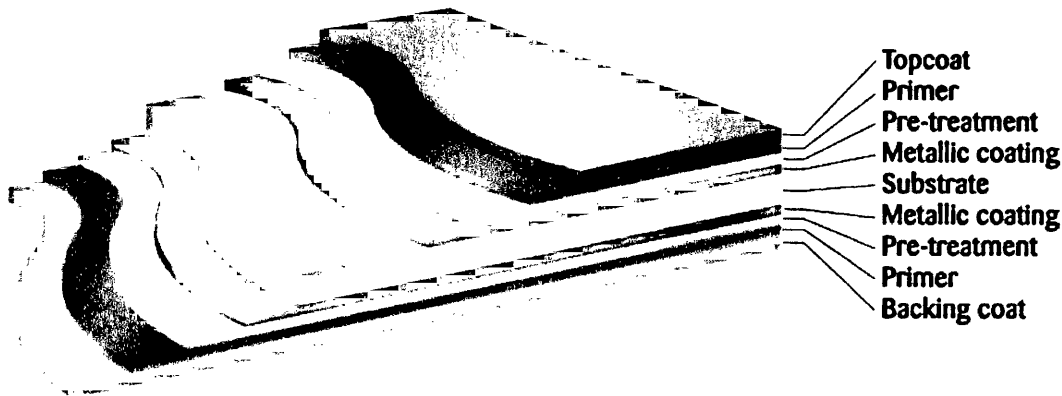


Figure 1.2 Representation of pre-finished steel from Corus Colorcoat®

The organic topcoat is an excellent barrier to the ingress of corrosive species, and accordingly the most common failure area where corrosion inhibition is needed most is located at cut edges. Cut edges are unavoidable when the steel is used for construction applications and a small quantity of steel and Zn are exposed to the environment, leading to 54% of all warranty failures [7] and highlighting the requirement of in-coating corrosion inhibitors.

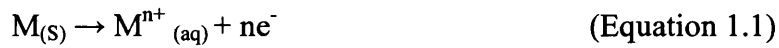
1.3 Corrosion failure mechanisms

1.3.1 The Theory of Aqueous Corrosion

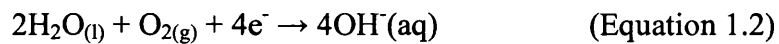
Corrosion combines theories and techniques from numerous disciplines including chemistry, physics, electronics and engineering. Corrosion also has huge financial implications for the majority of industries around the world, which has led to a great deal of time and effort being expended to gain a fundamental understanding of corrosion in order to develop cost effective corrosion engineering solutions. Corrosion can be described as the degradation of a metal by an electrochemical reaction with its environment, and the type of degradation a metal will encounter is highly dependant upon the nature of that environment in which it is located.

Steel is one of the most widely used metallic materials throughout the world due primarily to its combination of low cost and physical properties. The popularity of steel as an engineering material has meant that it is widely considered a commodity product, and accordingly is used to provide a diverse range of engineering solutions from heavy duty construction such as ships to lightweight packaging. The susceptibility of steel to corrosion means that a number of corrosion preventative treatments have been developed that allow steel products to last longer under corrosive conditions. The most common method of preventing steel corroding under damp and marine atmospheric conditions is to apply a paint coating (barrier coating), which isolates the metal from the corrosive conditions. If breakdown of this barrier coating occurs, there is a high probability that the steel will undergo corrosion, which in the simplest terms can be described as the thermodynamically unstable (high energy) steel changing to a more thermodynamically favourable state (low energy) through the onset of corrosion.

Aqueous corrosion refers to the presence of a conductive electrolyte, which can be described as water containing ionic salts. When a metal is in contact with an electrolyte, anodes and cathodes become active where dissolution of the metal (oxidation of the metal) occurs at the anode and O_2 reduction occurs at the cathode at an equivalent rate. The half reaction equation for the anodic dissolution of a metal is shown in equation (1.1).



The anodic reaction of metal dissolution is always coupled to a cathodic reaction, which is the balancing reaction to equation 1.1. The cathodic reaction occurs at the cathodic site and is the area where reduction occurs as in equation 1.2. The electrical current that occurs as a result of this reaction is known as the corrosion current, which involves electrons flowing from a lower potential to a higher potential.



Under conditions of lower pH the product of the cathodic reaction will not be OH⁻ evolution as in equation 1.2, but H₂ evolution as shown in equation 1.3. The two half reactions (anodic and cathodic) make up the corrosion cell, and if electrical connection between these two components is broken for some reason, the electrochemical cell will be broken, leading to the termination of corrosion.



1.3.2 Pourbaix Diagrams

Pourbaix diagrams can most accurately be described as a graphical means of identifying the likely corrosion that will occur on a metal depending upon the conditions of pH and potential to which it is subjected. The Pourbaix diagram was developed by Marcel Pourbaix during the mid part of the 20th century to graphically illustrate how the stability of a metal is affected by its environment. It was decided that a metal is only in a corroding condition if the concentration of its ions in solution is $\geq 10^{-6}$ M. It was also decided that when the concentration is less than this, the metal is deemed to be immune to corrosion. A different Pourbaix diagram is required for each metal.

In the Pourbaix diagram the metal can be assumed to be in a number of conditions, either; corroding, immune or passive. An example of when a metal becomes passive is when, through corrosion (oxidation) an insoluble corrosion product forms on the

metal surface (oxide formation). Generally this insoluble oxide prevents electrolyte coming into contact with the metal, and so greatly reduces the corrosion rate.

1.3.3 Atmospheric Corrosion of Coated Metal Surfaces

The corrosion control of engineering metals under non-immersion conditions is usually achieved by the use of protective organic coatings. The primary form of corrosion prevention offered by organic coatings is barrier protection, whereby electrolyte is physically stopped from reaching the metal. Unfortunately nearly all organic coatings inherently contain flaws that will at some point allow the ingress of electrolyte through to the metal. Over time moisture and O₂ will penetrate even the most resilient organic coating whether coating defects exist or not due to through coating diffusion. If no corrosion inhibitors are present within the organic coating system there is a strong chance that failure of the organic coating will occur through corrosion driven coating disbondment (cathodic delamination), corrosion driven anodic disbondment (filiform corrosion), or general anodic undercutting depending upon the particular metal and environmental conditions.

1.3.3.1 Corrosion-Driven Cathodic Disbondment

Corrosion driven coating delamination (cathodic disbondment) affects organic coatings adherent to a number of different metal substrates including ferrous metals and Zn. For this reason, cathodic disbondment is a fundamental coating failure mechanism of uninhibited coatings applied to pre-painted steels for construction and domestic applications. An electrochemical cathodic delamination cell is created upon the presence of a corrosive electrolyte such as rain water at a defect within an organic coating. Defects within the organic coating that are capable of creating a cathodic disbondment cell include general areas of cut edges or exposed substrate metal. The species that are involved in corrosion-driven cathodic disbondment are water, oxygen, free electrons and some form of counter ion to balance and maintain electroneutrality [8]. According to Skar et al [9], on a damaged coating with cut edges or defects there are three possible routes to be taken by the counter ions towards the delamination front. These routes are (a) along the coating-substrate

interface, (b) through the detached coating or (c) through the intact coating ahead of the delamination front.

The basic failure mechanism is where the bonds between coating and the substrate are destroyed through the creation of the cathodic delamination cell. Considering a cathodic delamination cell on a Zn substrate, the predominant reaction is anodic Zn dissolution of the exposed metal within the defect or at the cut edge following equation 1.4.



Coupled to the anodic zinc dissolution at the defect is a cathodic O₂ reduction reaction (equation 1.2). It is the increased alkalinity created by O₂ reduction reaction that causes disbondment of the organic coating through degradation of the polymer-substrate bond. Upon cathodic disbondment of the organic coating, the intact substrate-polymer interface will be replaced by two new interfaces; substrate-electrolyte and electrolyte polymer. It is not possible by conventional electrochemical techniques to follow the electrochemical activity within this system because the reactions are occurring under a relatively insulating organic coating. Standard electrochemical techniques will only be able to measure corrosion occurring at the defect under immersion conditions. One technique recognised as an ideal tool to measure under-film corrosion activity is the scanning Kelvin probe (SKP) [10].

The SKP is non-contact electrochemical scanning technique ideally suited to measuring spatially resolved under-film potentials at regions of both intact and delaminated coatings. Figure 1.3 shows a schematic diagram of a cathodic disbondment cell, and the graph shown above the schematic is an example of a spatially resolved SKP potential plot (E_{corr}) (under-film corrosion potential profile). This also shows how the E_{corr} profile coincides with the main features of the delamination cell.

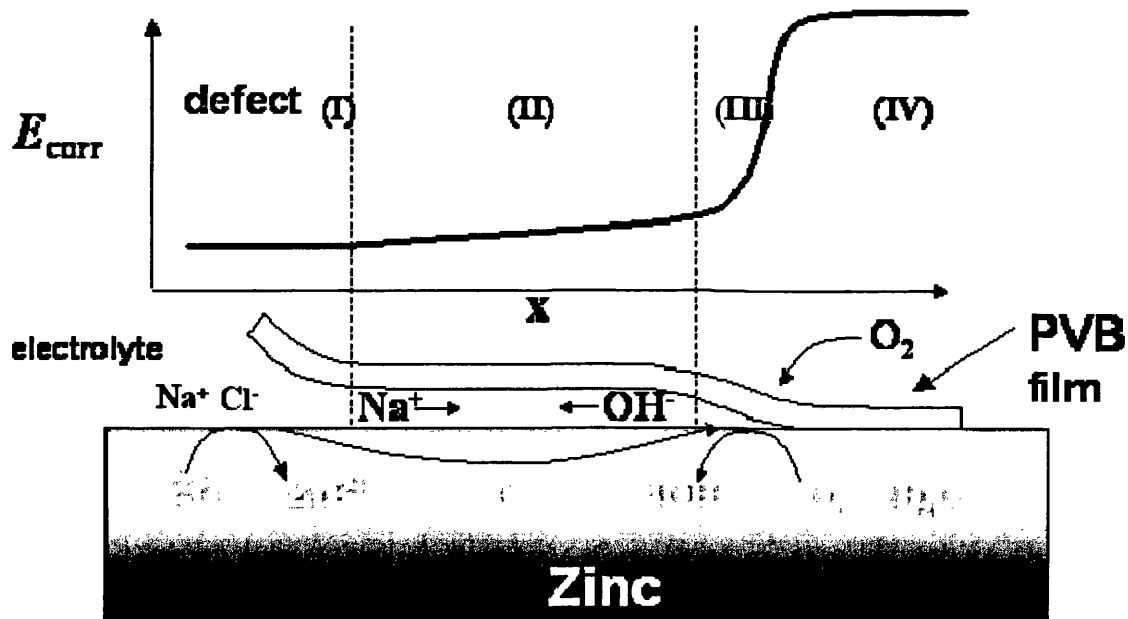


Figure 1.3 Proposed cathodic disbondment mechanism on Zn substrates.

On this profile there are four discrete sections, with each section corresponding to an important stage of the delamination process [11]:

- (I) This part of the delamination cell is immediately next to the defect, and as such the E_{corr} values for this region are similar to a freely corroding zinc-electrolyte interface.
- (II) The second region of the E_{corr} profile shows an almost linear increase from left to right, where the E_{corr} profile becomes more positive as it approaches the third region. It is this region that links region (I) and (III).
- (III) As can be seen on the profile, region (III) has a very sharp transition from low to high E_{corr} values., which may be seen to shift from left to right as delamination proceeds away from the defect.
- (IV) Region (IV) is the remaining un-delaminated coating (E_{intact}). This is the intact region of the coating and has considerably more positive E_{corr} values compared to the freely corroding Zn region (I).

As can be seen from the schematic of cathodic disbondment shown in figure 1.3, the corrosion that takes place under the delaminated region of an organic coating is driven by an electrochemical process where a cathodic region is in ionic contact to an anodic region. The delamination is caused by the activity of a galvanic element

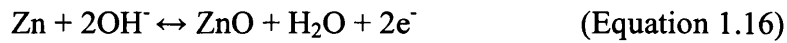
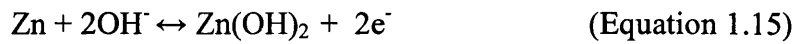
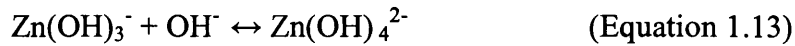
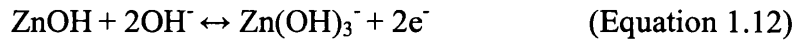
between the defect (local anode) and the delaminated part of the surface (local cathode), where O_2 reduction occurs at the tip of the delamination front [12, 13]. The cathodic O_2 reduction reaction that occurs at the tip of the delamination front is described through equation 1.2.

As can be seen from equation 1.2 that the product of this reaction is OH^- , although during cathodic O_2 reduction it is possible that many short lived intermediaries may form at the interface that could be more destructive than OH^- [14] such as:



At a defect on an organic coated Zn substrate, upon exposure to an aqueous sodium chloride electrolyte, anodic Zn dissolution is prevalent, which in turn provides electrons that fuel the cathodic O_2 reduction reaction [14].

It has been suggested by Stratmann that as a result of the cathodic reaction generating OH^- the delaminated area that now contains an electrolyte film becomes alkaline. This alkaline medium is believed to lead to significant growth of an oxide/hydroxide layer on the zinc coated substrate. The growth of the oxide/hydroxide layer can be interpreted in terms of the following anodic reactions which follow after cathodic delamination [15]:



The claim that oxygen reduction should result in a highly alkaline pH within the thin electrolyte layer at the Zn-polymer interface has been demonstrated using phenolphthalein pigments in the coating [16]. Indeed, it is proposed by Leidheiser that as a result of the cathodic reaction in the area beneath the coating, a pH of approximately 14 may be reached in the case of cathodic disbondment on steel [17].

The thickness of the oxide layer by which the above anodic reactions (equations 1.11 to 1.17) allow its growth have been estimated by Scholl et al to be roughly 50 nm. It is also proposed that the formation mechanism of the ZnO layer is by dissolution/precipitation [18]. By carrying out depth profiles on the oxide growth after the delamination of an amine-modified epoxy ester film on electro-galvanised steel, Furbeth and Stratmann have also supported these findings [15].

It can be seen from the schematic of a delamination cell in figure 1.3 that cations such as Na^+ are transported from the anode towards the cathode at the delamination front. Opposing this flow of cations is a flow of OH^- anions heading towards the anode located within the artificial defect.

It has been proposed by Leng et al that in order to form such a delamination cell there are four requirements that have to be met [10]:

- (1) A potential difference must exist between the isolated sites (defect and intact coating) to act as a driving force for ionic conductivity to begin.
- (2) The potential of the defect should be shifted in the anodic direction and the potential below the coating should shift in the cathodic direction. The potential below the coating is in fact shifted several hundred mV after the formation of the delamination cell. It is the sudden cathodic potential shift

that marks the delamination front of an SKP profile and can be viewed schematically as part (III) of the Ecorr profile plotted above the proposed mechanism in figure 1.3.

- (3) In order for the proposed model to be functional, the migration of cations from the defect along the substrate-polymer interface is required. For this reason cation size could have an effect on the rate of delamination, with small cations allowing delamination to occur faster than larger ones. This theory has been proven by Leidheiser et al [19].
- (4) An ohmic potential drop should be observed between the defect (anode) and the front of the delaminated zone (cathode).

Cohesive failure within the oxide layer could be the cause of cathodic disbondment due to the high under-film pH causing thick oxide growth resulting in mechanically weakening the oxide structure. Conversely to this, a study by Castle and Watts [20] has concluded that dissolution of the oxide layer is not a significant factor in the cathodic delamination process. There are theories to support these findings by Castle and Watts whereby the responsibility of failure is with the polymer coating rather than the oxide film. The alternative explanation is that the alkaline solution generated beneath the coating film attacks the coating itself. The investigation by Koehler [21] regarding oleoresinous and polybutadiene coatings on steel concluded that delamination was due to saponification of the polymers. During this testing it was found that disbondment may occur at pH 11.7, i.e. well below the pH required for dissolution of the oxide layer. This theory of polymer degradation being the main failure mechanism has been reported by Hammond et al [22] who by testing epoxy coatings on steel found by analysing interfacial compositions of delaminated surfaces by XPS, that failure of the coating was due to polymer degradation.

1.3.3.2 Conventional Filiform Corrosion

The phenomenon of filiform corrosion (FFC) was first reported in the scientific literature by Sharman in 1944 [23], who noticed the occurrence of the thread-like corrosion occurring on lacquer coated steel. FFC is a form of atmospheric corrosion that is known to occur principally on organic coated aluminium or iron, and sometimes magnesium surfaces, originating from organic coating defects. An example of the typical appearance of FFC is shown photographically within figure 1.4, which highlights the under-film corrosive attack as can occur on organic coated aerospace aluminium. A key observation of this form of corrosion is that the detrimental affects are considered to be superficial in nature, rather than structurally damaging.

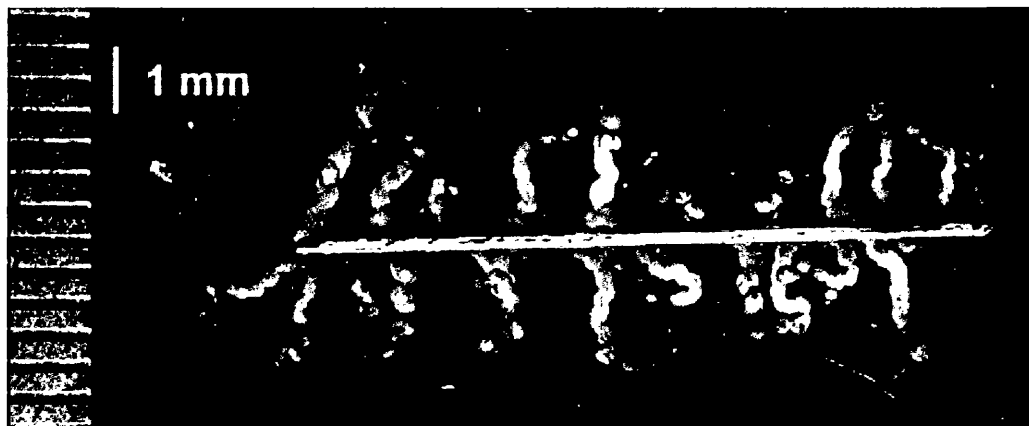


Figure 1.4. Filiform corrosion occurring between the coating-substrate interface of aluminium alloy AA2024-T3 coated with a clear film of poly-vinyl butyral (PVB).

FFC is a process that occurs under oxygen rich, moist and humid environments in the presence of soluble ionic species such as Cl^- , where access to the metal substrate is possible through a penetrative organic coating defect. Generally the FFC filaments that occur are $\sim 200\mu\text{m}$ wide when occurring on the surface of steel and $\sim 500\mu\text{m}$ - $1000\mu\text{m}$ wide when occurring on the surface of aluminium [24]. A comprehensive review of previous literature has been carried out by Bautista, who thoroughly describes the nature of the phenomenon alongside much of the previous literature investigating such corrosion [25]. It is generally accepted that FFC propagation is directionally stable, and it has been reported that on aluminium surfaces filament

propagation occurs along the rolling axis [25]. The observed preferential movement of filaments in specific directions has been attributed to the corrosion movement following a path of least resistance.

The simplest description of an FFC filament requires a breakdown of the corrosion phenomenon into two separate parts; the filament head and the filament tail. The filament head is filled with electrolyte and contains the soluble aggressive anions such as Cl^- . The filament tail is the track left behind as the mobile filament head progressively moves across the metal surface, and is filled with dry porous corrosion product. The filament head is the region where both the anodic and cathodic corrosion reactions take place, the cathode lies at the rear of the head and the anode is situated at the leading edge of the head. Accordingly, due to cation hydrolysis from the anodic metal dissolution in this region at the leading edge of the head, a very low pH exists (pH 1).

The likely mechanism by which FFC becomes initiated, particularly in the case of organic coated aluminium alloy, is illustrated within figure 1.5 and this demonstrates the generation of active heads. It is assumed that a thin layer of adsorbed electrolyte exists within a penetrative coating defect, which contains aggressive Cl^- anions and an abundant supply of atmospheric O_2 . The active filament head is created through a process of differential aeration, whereby oxygen transport to the metal surface through the thin adsorbed electrolyte layer is significantly more facile than through the relatively thick organic coating layer. This creates a situation whereby cathodic O_2 reduction is favoured on the exposed metallic substrate, while anodic metal dissolution will become prevalent at the O_2 deficient region underneath the organic coating.

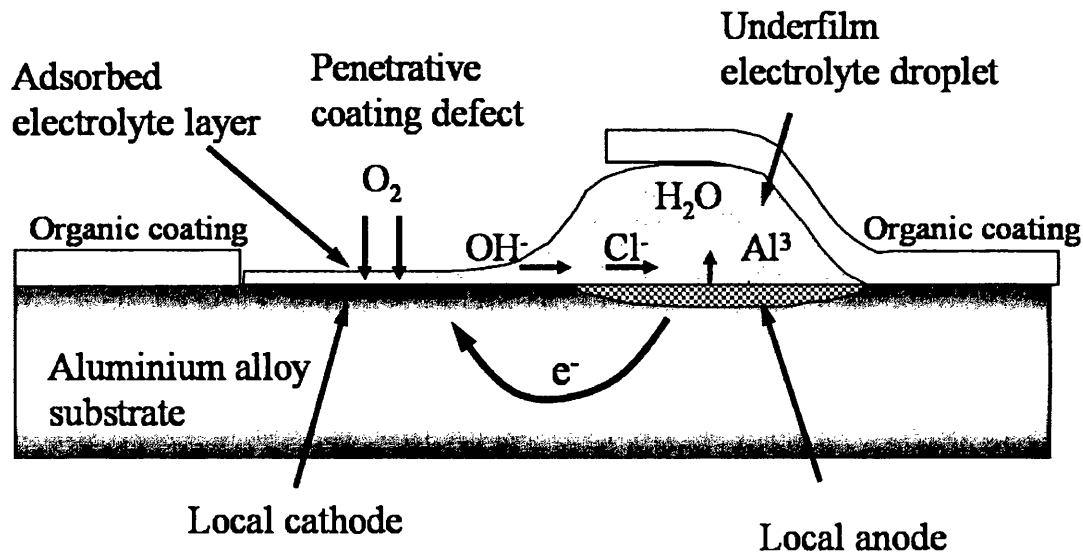


Figure 1.5. Schematic illustrating the initiation of FFC, in this case on organic coated aluminium substrates, in the presence of an organic coating defect.

Once the FFC anodic delamination cell has initiated from the penetrative organic coating defect, filament head movement follows a mechanism as outlined schematically within figure 1.6. This illustrates how all the electrolyte previously located within the coating defect has become located solely within the filament head, leaving the filament tail region totally dry, providing a pathway for O_2 to reach the rear of the filament head. Anodic metal dissolution occurs at the filament head leading edge, creating metal cations that migrate towards the cathodic region located at the rear. These metal cations subsequently combine with the OH^- anions generated as a result of the cathodic O_2 reduction. Stepwise hydrolysis of the metal cations leads to the precipitation of water insoluble corrosion product, which precipitates out of solution as a solid corrosion product. The constant migration of Cl^- anions towards the anodic leading edge of the filament head results in the presence of all water-soluble ions in this region. Due to the resulting ionic concentration gradient within the filament head, all liquid water is drawn forwards by osmosis. This osmotic process leaves the filament tail full of porous corrosion product and completely free of moisture, and explains why electrolyte exists solely within the filament head.

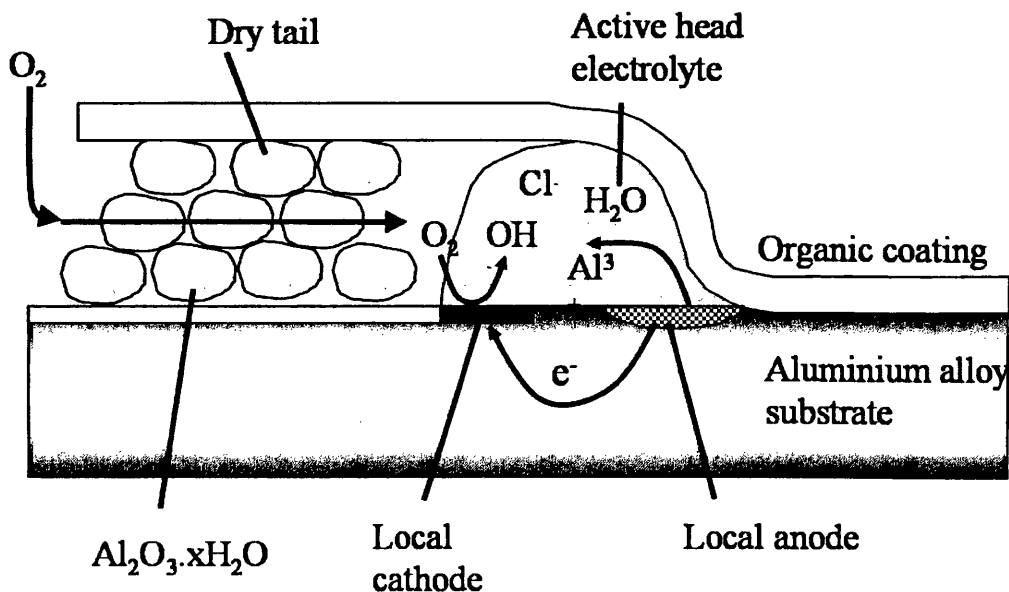


Figure 1.6. Mechanistic illustration of FFC propagation undermining an intact organic coated adherent to an aluminium substrate.

A key notation regarding the mechanism of FFC as outlined here is that due to the corrosion cell relying upon a system of differential aeration in order to be maintained, the filament heads are unable to traverse filament tails. This is caused by the filament tails being rich in atmospheric O_2 as previously explained. Upon contact with a filament tail, the filament head will be forced to change direction so as to move away from the O_2 previously contained within the tail. For this reason FFC filaments can not cross each others path if they follow the mechanism described here.

Traditional electrochemical techniques are unable to monitor FFC attack because of the lack of bulk electrolyte, i.e. because the phenomenon is atmospheric in nature. An ideal way of studying FFC and its propagation through previously intact organic coatings is via the use of the scanning Kelvin probe (SKP). The SKP is capable of visualising the free corrosion potential (E_{corr}) distributions associated with individual corrosion filaments. In-situ SKP scanning has also been used to generate a series of time-dependent E_{corr} distribution patterns which provide information on filament initiation, propagation and termination [26, 27]. The same in-situ techniques have also been used to investigate inhibition of FFC based upon conventional Cr(VI) chemistry [28] and novel anion-exchange hydrotalcite minerals [29, 30].

1.4 Metallic coatings

Historically steel is an established low cost commodity material that has been utilised for many different applications. The corrosion susceptibility of steel has led to the required development of methods to prevent corrosion failure whilst increasing the portfolio of applications. One such method developed to meet these criteria is through the application of metallic coatings to the steel surface. The main reasons why the application of metallic coatings to the steel surface may be required are; to attempt to prevent the corrosion of the substrate metal, to modify the physical or mechanical properties of the substrate metal, or purely for aesthetical purposes.

A classical example of using metallic coatings for aesthetical purposes is the application of a thin chromium layer to coat strip steel for decoration, and such applications as steel for car bumpers and bright work. Chromium is a metal that has an extremely high resistance to atmospheric corrosion, allowing it to remain untarnished for long periods of time. Chromium is also a very hard metal that shows a high level of wear resistance allowing it to be used successfully as a coating material for engineering tools.

Depending upon the requirements of the particular application, the appearance of other metallic coatings may be deemed acceptable, although their main role is the corrosion protection of the underlying steel substrate. A good example of this is the use of galvanised steels for the production of low cost items such as steel waste bins and crash barriers, where functionality is more important than over-all appearance. Modern metallic coating technology is gradually increasing, with higher performing alloy combinations being developed over time that optimise long term corrosion protection whilst remaining within economic limitations of today's industrial climate. The traditional metallic coating materials are zinc, tin, aluminium, nickel, copper and chromium.

1.4.1 Anodic and Cathodic Metallic Coatings

Metallic coatings that are anodic or cathodic to the substrate are both used in practice, where the coatings that are anodic to the substrate will provide sacrificial protection at areas of metallic coating – substrate defects such as at regions of cut edges as in the case of galvanised strip steels for cladding applications. In cases where the metallic coating is anodic to the substrate, the coating does not have to be defect free in order to provide protection because protection is provided both by simple barrier protection, and by galvanic action [31].

When used as coating materials on steel substrates, both cadmium and zinc will act to provide sacrificial protection to the steel at cut edges, and depending upon the environment, aluminium and tin can also act in a sacrificial manner. In industrial environments zinc will protect steel for a longer period than cadmium, although in marine or rural environments the opposite is true, where cadmium generally protects steel for longer than zinc [32]. It is theorised that this phenomenon is caused by the nature of the corrosion products, and the way they interact with the environment. In industrial atmospheres it is expected that the atmosphere contains high levels of sulphur, which has the effect of creating sulphates of the zinc or cadmium metallic coatings. These sulphates are subsequently washed away with rain water, leaving corrosion of the metallic coating to continue freely. The reason why the zinc lasts longer than the cadmium in these environments is because the zinc generally has a much lower potential than cadmium meaning that it is a more efficient anode. In marine environments, cadmium coatings last longer than the zinc coatings because the cadmium carbonates and basic chlorides that are formed are insoluble, which has the effect of stifling corrosion to a greater extent than the more soluble zinc carbonates and basic chlorides [33].

Metallic coatings that are cathodic to the underlying substrate have the effect of reversing the sacrificial protection, where the steel substrate will sacrificially corrode to provide corrosion protection to the coating. The corrosive attack on the substrate can in some cases be localised and accelerated, leading to corrosion penetration through the substrate.

1.4.2 Hot dip Galvanised Steel (HDG)

One of the oldest methods of applying a protective zinc coating to the surface of steel is via the process of hot-dip galvanising. Steel to be coated via this process is immersed in a bath of molten zinc and subsequently removed to leave a solidified metallic coating. The solidified zinc coating on the steel surface is highly adherent due to the formation of a zinc-steel intermetallic layer created by the diffusion of the molten zinc into the steel. The large-scale production of HDG is commercially possible at speeds of up to 200m/min, and is current common practice throughout the strip steel industry.

The hot dipping process involves the immersion of the strip steel into a bath of the molten zinc that is held between 450 – 480°C. The rate of reaction between the steel and zinc is parabolic with time, where the majority of the coating thickness is achieved upon initial immersion into the molten zinc. It is well known within the steel industry that the higher the zinc bath temperature, the faster the achieved coating growth. Under typical conditions immersion time of the steel within the molten zinc is approximately 5 seconds. In order to fully and accurately control the thickness of the galvanised layer, a process of gas wiping is used to blow excess molten zinc back into the metal bath. Gas wiping can be described as a process of blowing air in a fully controlled manner onto the strip surface through air knives to remove the excess zinc. In the case of architectural steels the remaining zinc coating thickness is approximately 20µm.

Application of zinc coating layer via the method of HDG is beneficial in that compared to techniques such as electroplating, it allows the application of much higher coating weights. The higher coating weight has the advantage of providing significant levels of barrier protection and long-term sacrificial protection. One drawback with HDG for practical applications is that the finish tends to be aesthetically displeasing.

1.4.3 Galfan® Metallic Coatings

Galfan® metallic coatings (also known as Galvalloy®) have similar applications to those already described for HDG steels, particularly for higher value applications. Galfan has a number of benefits over HDG in that it is more formable due to being intermetallic free, and also offers superior corrosion resistance [34]. The Galfan coating is an alloy of zinc with 4.6 – 5% Al, near the minimum melting point (eutectic point) in the Zn-Al system. Galfan also contains approximately 0.1% misch metal, which is comprised of rare earth metals such as Cerium and Yttrium, and is added to improve the wettability and fluidity of the molten bath and thus prevent uncoated spots on the final product whilst not affecting the corrosion resistance. In addition, sometimes a small percentage of Mg (0.05%) is often added to the system in order to improve the surface corrosion resistance of the coating [35].

The Galfan coating comprises primary zinc dendrites in a Zn/Al eutectic matrix. In terms of microstructural changes, the addition of magnesium to the melt has the effect of increasing the number and size of the primary zinc dendritic phase. This may reduce the resistance to cut edge corrosion in organically coated steels, whereas in the case of bare steel products may give superior surface corrosion properties [36]. In non-marine environments the corrosion of Galfan takes place via a two-step process, the first of which is the formation of an aluminium oxide passive layer due to the presence of Al additions in the coating. This is followed by a zinc galvanic step in which zinc sulphate forms on top of this oxide layer [35]. The corrosion of the zinc contained within the Galfan coating is initially focussed at the primary zinc dendrites. The formation of zinc corrosion products is slowed due to diffusion through the aluminium oxide layer and so Galfan offers improved corrosion resistance over conventional zinc HDG coated steels [35].

1.4.4 Magizinc®

The recent upward trend in zinc metal prices has proven to be the catalyst for the development of novel alloy coating systems with superior corrosion resistance with the aim of reducing the metallic coating thickness without sacrificing product performance. Magizinc® is a novel hot dip zinc based coating system with small additions of both aluminium and magnesium, and the subsequent increase in corrosion resistance compared to conventional HDG steels allows zinc usage to be significantly reduced.

It is of general consensus that the small addition of approximately 2% magnesium to the zinc decreases the susceptibility of the metallic coating towards corrosion, particularly the corrosion driven delamination (cathodic disbondment) of an adherent organic layer. To illustrate the reason why this is the case, the zinc – magnesium phase diagram is shown in figure 1.7. The portion of the phase diagram concerned with these alloy coatings lies to the right hand side, and is demarked by the vertical line through the hypereutectic region. At this low level of magnesium content the microstructure of the binary alloy coating is as illustrated photographically within figure 1.8, where primary zinc dendrites are surrounded by an $MgZn_2$ eutectic phase.

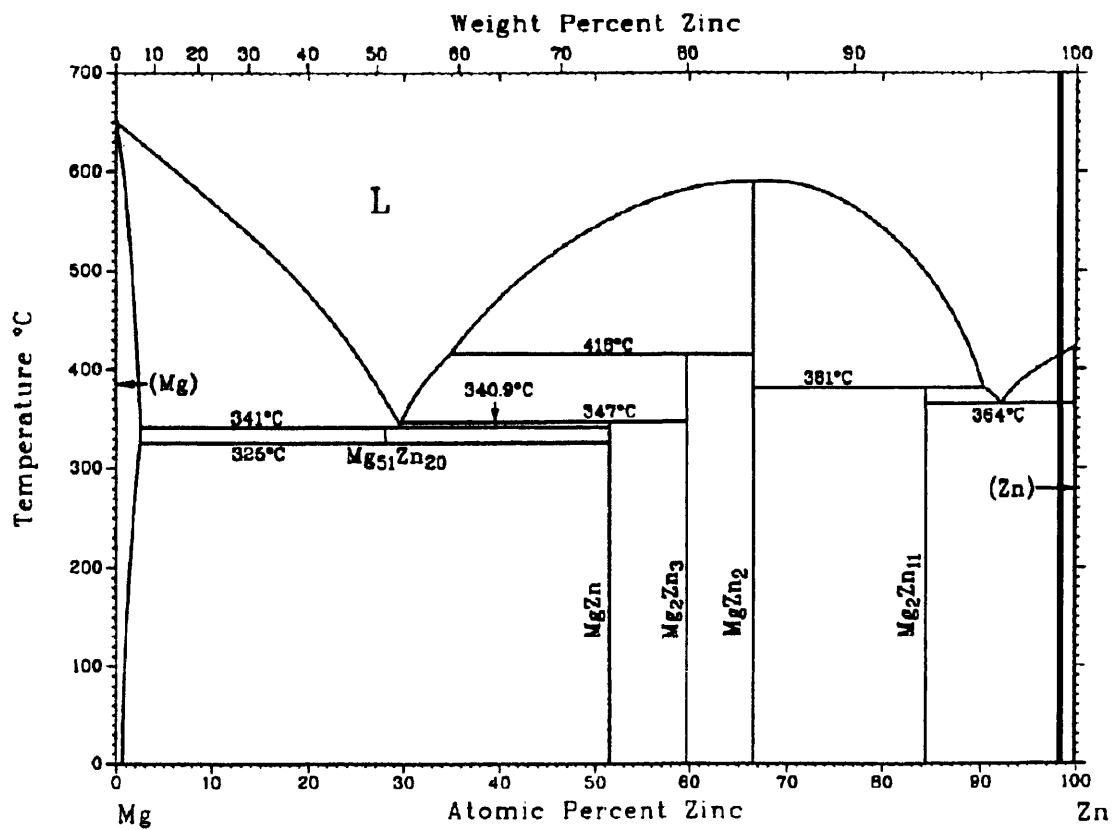


Figure 1.7. Zinc – magnesium phase diagram

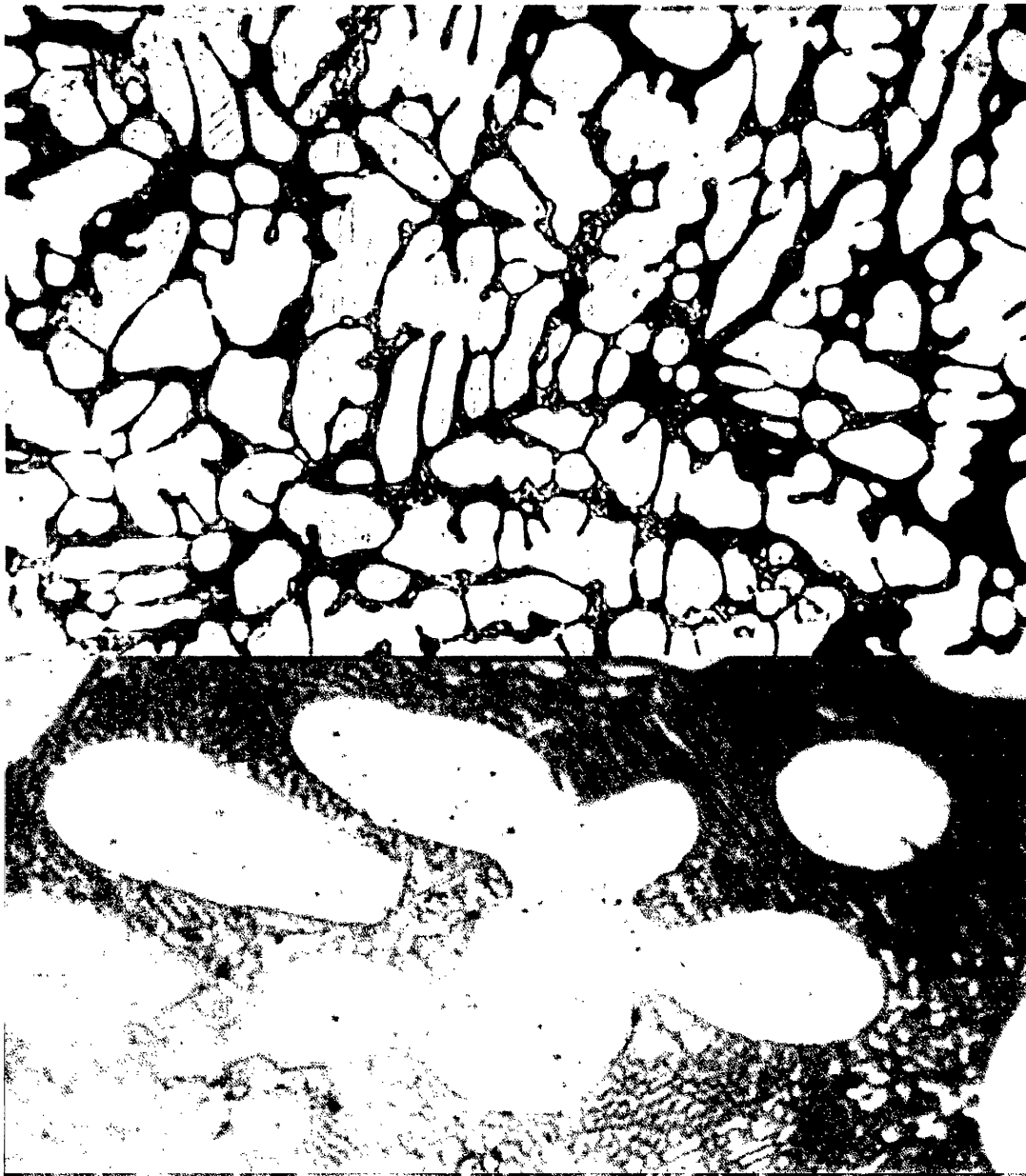


Figure 1.8. Microstructure of a zinc – 2% magnesium galvanised coating, showing primary zinc dendrites surrounded by an $MgZn_2$ eutectic phase [37].

The findings of Hausbrand et al have led to the proposition of significant cause of the inhibition organic coating disbondment from magnesium containing zinc alloy substrates [38]. It was found that the effect of the magnesium was significant at areas of intact organic coating, where the potential of the intact interface as recorded by SKP potentiometry (E_{intact}) is more negative than the anodic region. This reverses the

normal polarity of the cathodic delamination cell and causes there to be no driving force for cathodic delamination. Conversely, if the substrate was non-alloyed zinc, then the driving force for cathodic delamination would exist because anodic defect area would be of a lower potential than the region of intact coating [15]. The more negative under-film potential exhibited by the magnesium containing alloys is attributed to the surface oxide layer that forms over the $MgZn_2$ at the coating-substrate interface. The potential is low because this oxide layer has a large band gap, i.e. the electronic properties at the surface are more like MgO than ZnO. Thus the increased resistance to cathodic disbondment on $MgZn_2$ derives from the electronic properties of MgO.

In the case of Magizinc, the microstructure is very similar to the photomicrograph shown in figure 1.8, where the eutectic is $MgZn_2$, with aluminium in solid solution. The dendritic phase is predominantly Zn, although it will have some aluminium and magnesium in solid solution. Due to the similarities between Magizinc and the more conventional zinc – magnesium alloy coatings, it is expected that the corrosion performance in terms of the inhibition of cathodic disbondment will be similar.

1.5 Corrosion Inhibitors

The definition of a corrosion inhibitor is a substance that when added to an environment in small quantities is able to reduce the corrosion rate of a metal in that environment [39]. Corrosion inhibitors can fall into one of two categories, anodic or cathodic, depending upon whether they affect the anodic or cathodic process.

Anodic inhibitors work by increasing the polarisation of the metal surface via the formation of a passive film or the creation of a salt layer of limited solubility. This is achieved by reaction of the anodic inhibitor with ions of the corroding metal. Adding an anodic inhibitor as part of a coating system has the effect of reducing the corrosion current whilst correspondingly increasing the free corrosion potential of the metal (E_{corr}), this is illustrated graphically with the Evans diagram shown in figure 1.9. If for some reason an insufficient amount of anodic inhibitor is contained within the coating system, the corrosion rate at the remaining sites is actually higher than it would have been and for this reason anodic inhibitors are often referred to as dangerous inhibitors [39].

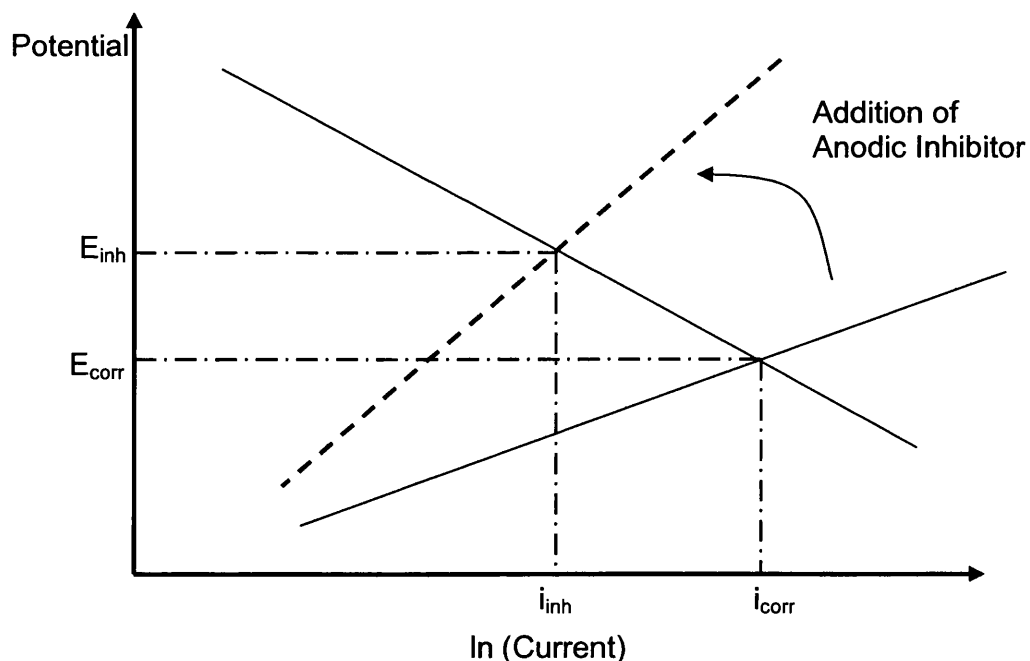


Figure 1.9. Evans diagram illustrating how anodic inhibitors increase the free corrosion potential.

Anodic inhibitors can be placed into one of two sub-categories; precipitation inhibitors and oxidising agents (cathodic depolarisers). Anodic precipitation inhibitors are anions that react with the metal cations generated at the point of corrosion from anodic metal dissolution, forming insoluble salts. This leads to the generation of an insoluble salt film that is deposited over the anodic area, breaking the electrochemical corrosion cell by denying the access of electrolyte to the metal surface and passivating the system. Phosphates are the most effective and commonly industrially used anodic precipitation inhibitors.

Oxidising agents (cathodic depolarisers) function by increasing the efficiency of the oxygen reduction reaction, this shifts the free corrosion potential of the metal to cause passivation. Further corrosion is prevented upon passivation by the formation of insoluble oxides and hydroxides on the metal surface. In neutral environments the inhibitors that provide protection by this mechanism are chromates and nitrates [40].

Cathodic inhibitors can be split into two different groups in the same manner as anodic inhibitors. The two groups are precipitation inhibitors and cathodic poisons, and as illustrated in the Evans diagram of figure 1.10, the main principal of cathodic inhibitors is that they increase the cathodic polarisation of the metal surface. The result is a simultaneous decrease in both the free potential and the corrosion current. Whereas anodic inhibitors are known as dangerous inhibitors if they are not applied in sufficient quantities, cathodic inhibitors are known as safe inhibitors [1] because even if the amount of inhibitor added is not enough to stop all cathodic activity the rate of corrosion is still reduced. The reduction in corrosion is still reduced for two reasons, firstly the thermodynamic driving force for corrosion is decreased, and secondly the cathodic area is decreased.

The cathodic process generates hydroxyl ions at cathodic sites, and the cathodic precipitation inhibitors work whereby the inhibitor cation reacts electrochemically with these hydroxyl ions to form an insoluble layer that is deposited at the cathodic site. The insoluble layer is impervious to electrolyte and so breaks the electrochemical cell, causing inhibition of corrosion.

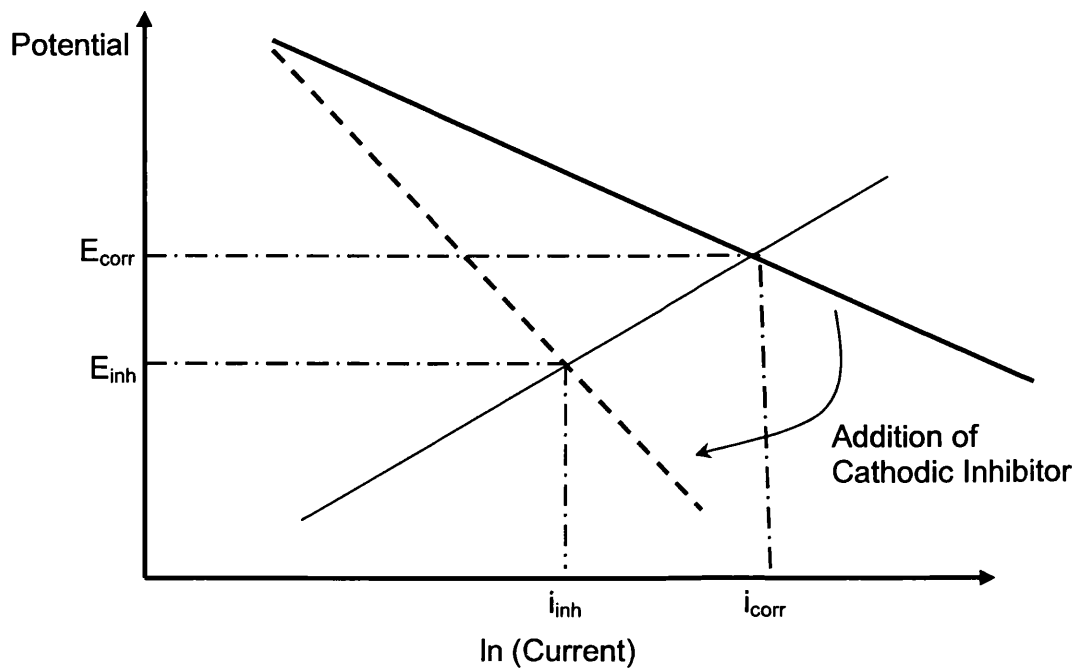


Figure 1.10. Evans diagram illustrating cathodic inhibitors decrease the free corrosion potential and the corrosion current.

Inhibitors that fall under the category of cathodic poisons are generally not used in organic coating systems. The main use of this type of inhibitor is to prevent corrosion of industrial pipelines etc, where the cathodic process causes hydrogen evolution. Examples of inhibitors that prevent corrosion by cathodic poisoning are salts of metals such as bismuth, arsenic and antimony. When added to the system these salts react to produce a layer of adsorbed hydrogen on the cathode surface hence ceasing the cathodic reaction [1].

1.6 Chromates for Corrosion Control

Chromates salts, although highly effective corrosion inhibitors are notoriously toxic [41] and have been proven to be highly carcinogenic [42]. These known dangers are the driving force for the development of replacement inhibitors, although chromates are currently the most effective [11]. The strong reputation of chromates is especially proven concerning the inhibition of cathodic disbondment of organic coatings under atmospheric conditions.

Pre-painted strip steels for outdoor applications usually comprise a HDG coating that acts to provide sacrificial protection to the underlying strip steel substrate (section 1.3). It is also important that the sacrificial metallic coating is itself protected from corrosion for as long as possible, which will have the effect of lengthening the lifespan of the product as a whole. This is especially critical considering that the typical thickness of the sacrificial metallic coating is limited to approximately 25 μ m, implying that anodic zinc dissolution of unprotected coatings would occur rapidly under humid atmospheric conditions. The lifespan of zinc or cadmium metallic coatings adherent to steel substrates is typically increased by chromate passivation. The most commonly used passivation process is the Cronak process, which was developed in 1936 by the New Jersey Zinc Co [32]. The Cronak process involves the immersion of the zinc in a solution containing 182g/l of sodium dichromate and 6ml/l of sulphuric acid. The immersion time of 5 – 10 seconds forms a golden glistening film on the zinc surface. Other commercial variants of the leading Cronak process exist, all of which are also based upon the use of dichromate (or chromic acid). There are a number of draw-backs with the chromate film deposited on zinc in this way. The deposited film contains a substantial quantity of hexavalent chromium, part of which is soluble in water. A degree of care needs to be taken of the chromated substrate in order to maintain the protective nature of the coating. For example, the coating should not be subject to excessive amounts of hot water for fear of washing out the soluble protective hexavalent chromate. Similar care should be taken not to over heat the passivation layer, which can lead to dehydration of the hexavalent chromate rendering it insoluble upon further moisture contact. For aesthetic purposes the yellow colour of the passivation layer may not be desirable for some applications,

a solution to this is subject the coating to an aqueous extraction (bleaching) treatment with detrimental effects to the protective properties [32].

A substantial world market currently exists for organic coated galvanised steels and the primer coatings used in their manufacture typically incorporate dispersions of corrosion inhibitor pigments. Many possible inhibitor chemistries are available, but to date, sparingly soluble chromate salts have been proved by far to be the most effective and widely used. A number of studies have been undertaken in order to investigate the possibilities of replacing chromate inhibitor technology with safer alternatives [11, 43, 44]. Similarly many studies have been undertaken to fully understand the ways in which inhibition of cathodic disbondment in particular is provided by strontium chromate [11, 45, 46]. It was found by Williams et al [11] that a particulate dispersion of strontium chromate (SrCrO_4) within a polyvinyl butyral (PVB) organic binder produces a high level of inhibition of coating delamination of organic coatings adherent to zinc substrates without significantly inhibiting the anodic dissolution of the zinc in the defect area. It was found in this study that the rate of coating delamination decreased with increasing in-coating pigment volume fraction of strontium chromate (Φ_{sc}). Cathodic delamination of the organic coating was found to be totally inhibited for the higher pigment volume fractions tested. In the study it was proposed that inhibition of the cathodic delamination is marginally helped by pigment-derived CrO_4^{2-} inhibiting the anodic reaction at the coating defect margin. It is thought that the primary method of inhibition by strontium chromate on zinc substrates occurs as a result the O_2 reduction reaction being replaced by a self-limiting under-film CrO_4^{2-} reduction reaction.

1.7 Conducting Polymers for Corrosion Control

The Nobel prize winning discovery of intrinsically conducting polymers was made by Heeger, MacDiarmid and Shirakawa in the late 1970's by the discovery of iodine doped polyacetylene [47-49]. This discovery opened up a new field of science known as synthetic metals, which is the classification of materials to which inherently conducting polymers are assigned. The most promising feature of ICP's is that they mix the electronic properties of semi-conductors and the processing advantages of more conventional polymers.

Following on from the initial discovery of ICP's in the 1970's, many other conducting polymers have subsequently been discovered and recognised as useful materials. Polymers such as polyaniline, polypyrrole, polythiophene, polyfuran, polyindole and polyazulene are all examples of ICP's that have been discovered since the initial discovery of conducting polyacetylene [50]. ICP's are widely referred to in the literature as conjugated polymers. The term conjugated refers to the fact that ICP's are molecularly composed of conjugated chains containing π -electrons delocalised along the polymer backbone with alternating single and double bonds, these provide a pathway for free electron charge carriers. An ICP can be conducting or non-conducting depending upon its protonation state and it is the doping process (protonation) that makes an ICP physically conduct.

The conducting states of ICP's are the oxidised and reduced states. In the case of the oxidised state electrons are removed from the polymer backbone (p-doped), and the least common reduced state where electrons are added to the polymer backbone (n-doped) [51]. The nature of conductivity of an ICP is electronic as opposed to ionic [51], and conduction of ICP's in general can range from values equivalent to insulators ($<10^{-10}$ S/cm) to values equivalent to metals (10^5 S/cm) [52]. According to Tallman et al partially oxidised (P-Doped) polymers can be classified into three general types based upon the nature of the oxidation process [53]:

- Type 1:* Applies to PANi, where the process involves the protonic/electronic doping of the polymer, incorporating both protons and anions into the polymer.
- Type 2:* This applies to PPy and involves the electronic doping with anion incorporation.
- Type 3:* Applies to sulfonated polyaniline, where electronic doping with cation expulsion either from a covalently attached acid group or from a sufficiently large, physically entrapped immobile acid.

The vast majority of applications that ICP's have been employed are due to the need to combine the physical properties of a polymer with the conductivity levels of a strong semiconductor or even metal. There is a vast diversity of applications for conducting polymers including use for actuators [54], batteries [55], electrochromic windows/displays [56], bio/chemical sensors [57] and photovoltaics [58]. Possibly the most important application ICP's from the perspective of the pre-painted steel industry is for the corrosion protection of metallic substrates. ICP's have the possibility to act as an environmentally friendly alternative to conventional chromate corrosion inhibitors. A large amount of research has been undertaken with regards to applying ICP's as corrosion inhibitors beginning as far back as the early eighties [59].

For the corrosion control of ferrous metals and zinc alloy substrates, the two conducting polymers that have received the most research are polyaniline (PANi) and polypyrrole (PPy), the former being the most researched. These two polymers are conjugated and they both display levels of conductivity or semi-conductivity. The reason why ICP's were considered as corrosion inhibitors is that they are redox active materials and are similar to chromate in that they have equilibrium potentials that are more positive than metals such as iron and aluminium [53].

There have been a number of mechanisms proposed with respect to how conducting polymers such as PANi or PPy provide corrosion protection to metallic substrates. One such mechanism is the ennobling mechanism, where it is thought that

conductive redox polymers like PANi or PPy act as oxidisers to the metal surface when applied in their oxidised state [60], and possibly provide a degree of ennoblement of the underlying substrate at areas of small defects, maintaining the metal in the passive domain at these points, i.e. providing anodic protection to the underlying metal [61, 62]. Another mechanism that it is thought conducting polymers such as PANi and PPy act is to shift the primary factor of cathodic disbondment, the cathodic O₂ reduction reaction away from the metal – polymer coating interface, into the polymer itself. The reason why the O₂ reduction reaction in cathodic disbondment causes the final corrosion driven failure of the organic coating is that products and side products of this reaction such as the OH⁻ radical are responsible for the degradation of the interfacial polymer-metal substrate bonds [63].

Organic coatings containing inherently conducting polymers have been found to fail under immersion conditions when a large penetrating coating defect is present within the coating system. If the coating defect is small, the coating has been found to provide a degree of protection to the metal at that defect [64, 65]. It is thought by Rohwerder et al [66] that the reason why coatings containing ICP's fail under immersion conditions when a larger penetrative coating defect is present is that the reduction current of the in-coating ICP will be lower than the current required to overcome the critical passivation current density in the defects. Conversely, if the coating defect size is small, it will be much more likely that this reduction current of the conducting polymer will be sufficient to overcome this critical passivation current density level, and subsequently protect the defect through passivation.

1.7.1 Polyaniline (PANi)

Polyaniline (PANi) coatings and coatings that contain PANi as a pigment dispersion have recently been the subject of much publicised research [53, 67]. The first reported synthesis of PANi was in 1862 by Letheby [68]. One of the more easily recognisable conducting polymers, PANi can be prepared by polymerisation of the aniline monomer in hydrogen chloride solution using ammonium persulfate ((NH₄)₂S₂O₈) as the oxidising agent [69]. The synthesis occurs by dissolving the two components separately in hydrogen chloride solution, followed by mixing together in small quantities to bring about the exothermic reaction. The reaction product is the PANi

and this precipitates out as fine particulates. PANi has gained a reputation as being a useful engineering material due to its relatively easy polymerisation, high sensitivity to acid-base conditions, resistance to physical degradation resulting from environmental exposure and varying levels of conductivity [70].

PAni can exist in one of five oxidation or acid-base states as either; pernigraniline base, leucoemeraldine base, emeraldine base (PAni-EB), leucoemeraldine salt and emeraldine salt (PAni-ES), of which it is only the PAni-ES form that is conductive. Each of the five versions are differentiated by their oxidation levels as well as their protonation levels, and the passage from one form to another involves complex reactions [71].

The structures of PAni as illustrated within figure 1.11 have been established by means of solid state NMR spectroscopy [72], titration by $TiCl_3$ [70, 73], IR spectroscopy [74, 75] and XPS measurement.

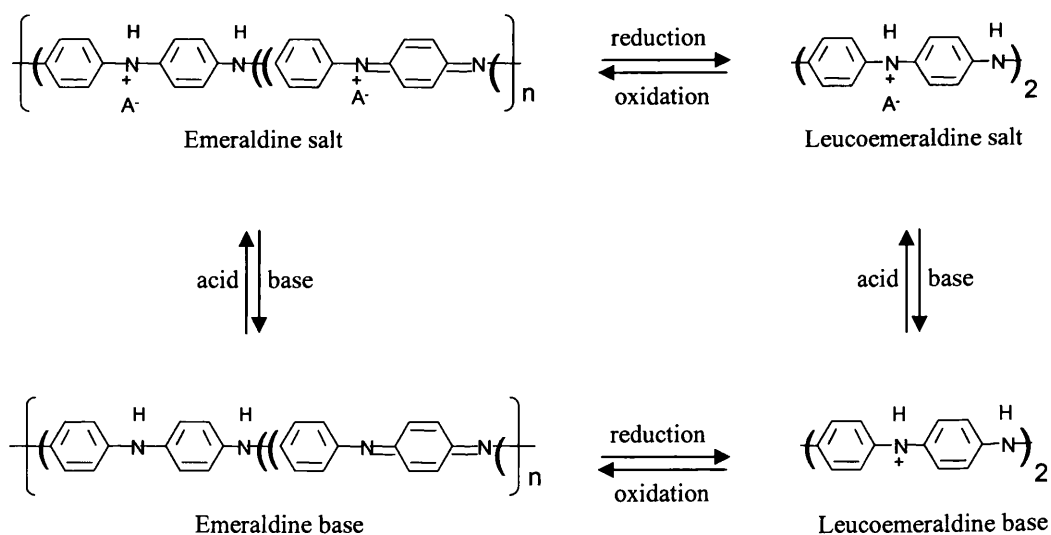


Figure 1.11. The structures of polyaniline.

An advance in the characterisation of the polymer back-bone structure was also achieved by the observation that PAni is moderately soluble in polar organic solvents such as N, N-dimethylformamide (DMF), dimethylsulfoxide (DMSO) and N-methylpyrrolidone (NMP) [76-79].

The protonation of PANi-EB occurs using a Bronsted acid such as phosphoric [71], hydrochloric [80] and para-toluenesulphonic acid [81] to name but a few. The protonation process is sometimes known as doping, and occurs when the Bronsted acid is mixed intimately with the PANi-EB. The PANi-EB is a proton acceptor (H^+ ion donor), and the Bronsted acid is a proton donor. This procedure results in protonation of the polymers imine nitrogen's along with the incorporation of the Bronsted acid into the polymer back-bone as a counter-anion. This incorporation of the counter anion into the polymer back-bone occurs at a ratio of one dopant acid anion per two aniline residues. Under normal environmental conditions, the PANi exists in its oxidised emeraldine state. Whether the emeraldine is salt or base depends upon the local pH conditions the polymer is subjected to. The pKa of PANi is 5.5, meaning that the polymer can only be protonated by acids with a pKa is less than this. Under more alkaline (basic) conditions of $pH \geq 5.5$ PANi-ES will become de-protonated and change state to the non-conducting PANi-EB.

The most useful form of PANi for the corrosion protection of metals is PANi-ES. This may be applied to a substrate as a homogeneous coating (micro-film) by a number of techniques; One method involves the application of the PANi-ES micro-film via electro-deposition, whereby aniline is dissolved in a strong acid and then electro-deposited onto the metal substrate. In order to gain a good film by electro-deposition, it has been found that the formation of a highly passive layer is very important [71]. Another method to produce PANi-ES micro-films is the application of the PANi-ES via solvent casting of PANi-EB followed by in-situ doping of the PANi-EB to produce PANi-ES [81]. The solvent casting of PANi, although possible is not popular due to the insoluble nature of the polymer in the majority of solvents. PANi-ES has been found to dissolved satisfactorily in M-Cresol [82] and to some extent in chloroform [83], allowing reproducible solvent cast micro-films of PANi-ES to be created. An alternative way of applying PANi-ES to a substrate is to add it as powder dispersion (pigment) to an organic binder material to create a pigmented composite coating system. This is the currently the most viable method of utilising PANi-ES as a commercial corrosion inhibiting pigment due to the ease of processing when compared to solvent-cast micro-films. Organic binders suitable to carry dispersions of PANi-ES are organic polymers such as epoxy resins [84] or polyvinyl butyral [85]

(PVB). It is this application method that is utilised in the production of CORRPASSIV®, which is a commercial PANi containing primer [86].

It has been thought that the simplest method by which PANi provides corrosion protection is by barrier protection. Electronic impedance spectroscopy (EIS) has been used to show that the pore resistance of pure PANi-EB coatings provided twice the pore resistance of PANi-ES coatings doped with paratoluenesulfonate [87]. The proposed reason for this is because of the polyelectrolyte nature of the ICP (PANi-ES) that allows easy ingress of electrolyte into and through the coating.

1.7.1.1 Polyaniline Protection of Ferrous Metals

The possibility of using of PANi coating systems for the corrosion protection of ferrous metals to create a more environmentally friendly alternative to chromate has led to a considerable amount of past interest. This has not led to any agreement regarding the mechanisms by which inhibition is provided, although it is agreed the effects are positive.

Investigations into the possibility of using PANi as a corrosion preventative coating material has been carried out by investigating how the polymer acts under immersion conditions. Much of this immersion testing has concluded that PANi does not provide inhibition these specific conditions, and inhibition is predominantly provided by the PANi acting as a barrier coating. In this regard it is the emeraldine base that is the most successful at providing barrier protection due to its low levels of ionic conductivity compared to the conductive PANi-ES. However, one piece of work providing clues to the fact PANi coatings act to provide inhibition other than simple barrier protection was completed by Lu et al [88] and Pud et al [89], where homogeneous films of emeraldine salt were coated onto ferrous substrates followed by covering this layer with an epoxy. This system was to create a bilayer coating system whereby the highly efficient barrier properties of the epoxy top coat allowed the PANi-ES to be cut off electrochemically from the external conditions, i.e. immersion in chloride solutions. The drilled holes through the emeraldine salt-epoxy coated steel led to the exposure of ferrous substrate would lead to the formation of a cathodic delamination cell prior to the onset of cathodic disbondment of the coating

system. The results of this testing showed that cathodic coating delamination was inhibited by the presence of the isolated PANi-ES layer adherent to the ferrous substrate beneath the epoxy top coat, hence proving that PANi does act to provide inhibition in ways other than as a barrier coating alone. As a result it is a general consensus that the corrosion inhibiting capacity of PANi-ES is highly dependant upon the conditions to which it is subjected.

In the case of pre-painted steels intended for architectural cladding usage, corrosion is most likely to occur under atmospheric conditions rather than immersion conditions, which opens up the possibility of using PANi as a replacement for strontium chromate. This has led to later studies that have brought to light the cathodic disbondment inhibiting properties of PANi-ES under the conditions these products will most likely be expected to reside. Scanning Kelvin probe (SKP) studies have shown PANi-ES to be an extremely effective corrosion inhibitor when applied as a composite coating, i.e. a pigmented dispersion within an organic polymer matrix such as polyvinyl butyral (PVB) when adherent to iron or plain carbon steel. The possible mechanisms responsible for this inhibition of cathodic disbondment have been proposed extensively [90, 91]. It is thought that upon initiation of a cathodic delamination cell, interfacial PANi-ES at the iron-coating interface is reduced to leucoemeraldine base by the interaction with iron and cyclically re-oxidised back to PANi-ES. This mechanism was proposed because potentiometric measurements of the intact coating (E_{intact}) made using the SKP showed E_{intact} to be considerably higher at ca. 0.50V vs. SHE when the organic coating contains PANi-ES. This is in comparison to the lower value of ca. 0.20V vs. SHE when uninhibited coatings are applied. This ennoblement is attributed to the PANi-ES – leuco base redox couple resulting from contact with the underlying iron under atmospheric conditions.

The work of Williams et al [90] has also highlighted the dopant dependency of the PANi-ES with regards to the mechanism by which PANi-ES acts to inhibit cathodic disbondment. In the case of the non-conductive PANi-EB, when this was utilised as a pigment dispersion it was found that no substrate ennoblement is observed, instead E_{intact} remains similar to non-inhibited PVB coatings (0.20V vs. SHE). Upon secondary mass spectrometry (SIMS) analysis of the iron surface, the PANi-EB was found to have produced no oxide growth. This would suggest that the PANi-EB does

not undergo any electrochemical interactions with the iron surface, requiring protonation to PANi-ES to become active. The PANi-ES of different dopants were all found to provide ennoblement over areas of intact coating albeit to different extents. SIMS analysis of the dopant dependant interactions of PANi-ES adherent to the iron substrates found that PANi-ES of sulphonate dopants causes the growth of an iron (III) oxide film at the coating-substrate interface, growing at a linear rate as a function of time. The linear nature of the oxide growth as a function of time suggests that the in-coating PANi-ES is always in electrical contact with the iron substrate, which allows the assumption that this iron (III) oxide layer is electrically conducting. It is this oxide film that is believed to give PANi-ES increased adhesion strength to the underlying substrate [92], and the oxide film occurs because PANi is acting as a redox catalyst and as a noble metal with respect to iron. In the case of phosphonate dopants, this interaction was found to produce a self limiting interfacial salt film of the dopant anion, which due to its self limiting properties indicates that the nature of this interfacial salt layer is non-conducting. In terms of the inhibition of cathodic delamination it was proven that these interfacial films in isolation do not inhibit disbondment to any great extent. It was also found that the addition of the dopant to the defect electrolyte on its own also has limited effect.

For coatings of PANi-ES dispersed as a particulate within a PVB matrix, higher pigment volume fractions of in-coating PANi-ES were found to alter the delamination kinetics from parabolic (cation migration controlled) to linear (interfacial electron transfer controlled). The proposition was that the PANi-ES reduction to leucoemeraldine wholly or partially replaces the cathodic O₂ reduction reaction at the coating disbondment zone. The leucoemeraldine becomes re-oxidised by atmospheric O₂, but as coating alkalisation proceeds, the product of this re-oxidisation is no longer PANi-ES, but non-protecting PANi-EB. Greater inhibition of cathodic delamination was observed when investigating the PANi-ES produced by protonation with phosphonate dopants. This increased inhibition was attributed to the subsequent interfacial salt film hindering electron transfer between the PANi-ES and the substrate.

The work of Williams et al [90] is the latest investigation of the inhibitory properties of PANi on ferrous metals when the PANi is applied as a pigmented dispersion.

Following on from this investigation, Gabriel et al [93] investigated the proposals made by Williams with a study of homogeneous micro-films of PANi-ES coated directly onto steel substrates. The methodology behind this research was to use visual redox changes resulting from cathodic disbondment to prove the previously proposed mechanisms. This took into account that the different PANi redox states and acid-base states exhibit different optical absorbance characteristics (colours) [93, 94] – where PANi-ES is green, PANi-EB is blue and the two leuco forms are colourless. Even after this work, a full understanding regarding the role of de-doping along with the precise mechanism that PANi acts to inhibit cathodic disbondment remains elusive. Most importantly, the findings of these studies show that PANi is not capable of stopping cathodic disbondment of organic coatings adherent to ferrous substrates, only significantly slowing it.

1.7.1.2 Polyaniline Protection of Zinc

There is interest in using ICP's such as PANi as environmentally friendly chromate replacements to provide atmospheric corrosion protection of galvanised steels at organic coating defects. The published literature reporting the atmospheric corrosion protection of organic coated zinc by PANi has been reviewed. The conclusion of this review is that very little work regarding this subject is reported [53] and very little work on this subject has been published since. The application of PANi micro-films directly onto the zinc substrate has been proven unsuccessful due to the formation of an insulating passive layer preventing its electro-polymerisation [95].

The most practical method of applying PANi as a protective coating to the zinc surface is as a pigmented dispersion within a binder material as is the case in work published by Williams et al [96]. The PANi-ES of paratoluenesulfonate was investigated as a means of protecting organic coated zinc from cathodic disbondment. It was found that by increasing the pigment volume fraction of PANi-ES contained within the coating caused a decrease in delamination rates. It was also noted that under these conditions of high relative humidity, a ZnO layer was found to develop on the zinc surface as a result of the in-coating PANi. SIMS was employed to fully investigate this oxide, and it was found that oxide growth is complete within 6 hours of coating application and the thickness of the coating is directly proportional

to the pigment volume fraction of PANi-ES dispersed within the PVB binder material. Finally, it was noted that over the time taken for the oxide layer growth to complete (ca. 6hrs) E_{intact} dropped from ca. 0.40V vs. SHE (E° PANi-ES) to ca. -0.25V vs. SHE, which is the value usually attributed to non-inhibited PVB coated zinc.

Propositions based upon the aforementioned findings were that inhibition of cathodic delamination of organic coatings by PANi occurs principally as a result of the ZnO layer blocking cathodic O_2 reduction at the zinc-coating interface. It was also proposed that this effect is lengthened by the pH buffering action of residual in-coating emeraldine salt of paratoluenesulfonate. This means that the PANi acts to absorb the OH^- ions produced by cathodic O_2 reduction, and so prevent or delay alkaline dissolution of the ZnO barrier layer.

1.8 The Scanning Kelvin Probe

The scanning Kelvin probe (SKP) is a non-contact, non-destructive vibrating capacitor device used to measure the work function difference between a conducting material and the probe itself. The work function of a material is the least amount of energy required to move an electron from the surface of a conducting material to a position just outside, with zero kinetic energy. The scientific principles behind the measuring the work function of a material was first developed and introduced by William Thomson (later Lord Kelvin) in 1898 [97]. The principles discovered by Lord Kelvin were further developed by William Zismann of Harvard University in 1932. In his work Zismann mounted a vibrating reference above a conductive sample, and it was shown that the output voltage varies periodically as the tip vibrates, and the peak-to-peak voltage depends upon the difference between the contact potential and the external voltage [98]. The measurement of the work function inhomogeneity using Kelvin's principle was presented in more recent times by Bonnet [99], and the achievable lateral resolution of the technique was confined to an area of a few millimetres.

The development of the modern SKP as used today for the measurement of under-film corrosion potentials as used widely throughout this study has been described by Stratmann [13]. In this work he suggested that the Volta potential of a polymer coated metal surface can be determined by the corrosion potential of the substrate and that information on the corrosion kinetics can be deduced. This then led to ability to map changes in localised potential distributions caused by various surface or interfacial electrochemical phenomena under intact organic coatings. Unlike other electrochemical techniques for the measurement of potentials, the SKP does not require electrolyte contact between the reference electrode and working electrode, allowing it to be used for the measurement of corrosion under true atmospheric conditions.

In the case of SKP apparatus used to monitor the cathodic disbondment of organic coatings from metallic substrates, an oscillating flat ended gold wire tip is positioned vertically approximately 100 μ m from the sample surface as illustrated in figure 1.12. The experimental arrangement is that the tip of the reference probe (125 μ m diameter

gold wire) is held at earth potential and positioned inside a stainless steel environment chamber. This environment chamber fulfils two different functions; firstly it allows a high relative humidity to be maintained, and secondly acts as a faraday cage to reduce electrical noise. In order to be a scanning Kelvin probe as opposed to a Kelvin probe, the apparatus has the ability to move/scan the gold wire tip over the sample in a stepwise fashion recording potentials at different regions over the surface. The SKP used throughout his study for the monitoring of under-film corrosion phenomena is described in more detail within section 2.3.

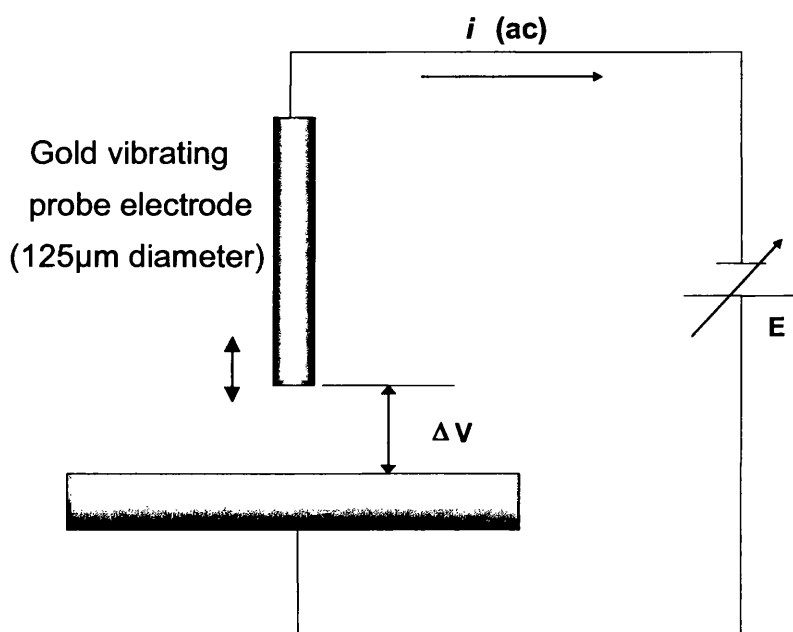


Figure 1.12. Schematic diagram illustrating the principal of surface Volta potential difference measurement using the SKP.

1.8.1 SKP Theory

Within this work the SKP has been used to monitor under-film corrosion phenomena occurring on a variety of different metallic substrates. If a Volta potential difference (ΔV) exists between the probe tip and sample surface, the periodic fluctuation in capacitance caused by the probe vibration generates an alternating current in the external circuit [100]. The Volta potential of a polymer coated substrate is directly linked to the electrode potential of the substrate – polymer interface [101]. As the working electrode and reference electrode are connected by an external circuit the

Fermi levels of both materials are identical and the sum of the energies (necessary to transfer an electron from the working electrode through the several interfaces into the reference surface are zero [101]. It has been shown that for a bare metal surface covered with a layer of electrolyte solution, the half cell potential ($E_{1/2}$) of the metal/solution interface is given by [10, 101]:

$$E_{1/2} = \frac{\alpha_e^{ref}}{F} - \chi_{gas}^{sol} + \Delta\psi_{sol}^{ref} \quad (\text{Equation 1.17})$$

Where α_e^{ref} is the electronic work function of the reference probe material, F is the faraday constant, χ_{gas}^{sol} is the dipole potential of the solution – gas interface, and $\Delta\psi_{ref}^{sol}$ is the measured Volta potential difference between the reference probe and the solution surface.

Similarly for a polymer coated metal substrate:

$$E_{1/2} = \frac{\alpha_e^{ref}}{F} - \chi_{gas}^{pol} + \Delta\psi_{pol}^{ref} \quad (\text{Equation 1.18})$$

Where χ_{gas}^{pol} is the dipole potential of the polymer – gas interface and $\Delta\psi_{pol}^{ref}$ is the Volta potential difference measured between the reference probe and the polymer surface. When delamination has occurred, a layer of electrolyte exists between the substrate metal and the polymer layer. Equation 1.18 then becomes [10]:

$$E_{1/2} = \Delta\psi_D + \frac{\alpha_e^{ref}}{F} - \chi_{gas}^{pol} + \Delta\psi_{pol}^{ref} \quad (\text{Equation 1.19})$$

Where $\Delta\psi_D$ is the Donnan potential equivalent to the Galvani potential difference established between the polymer layer and the electrolyte solution ($\psi^{sol} - \psi^{pol}$). If

the gas-phase composition does not change, the quantities of α_e^{ref} , χ_{gas}^{pol} and χ_{gas}^{sol} in equations 1.17 to 1.19 are all expected to remain constant over time.

The free corrosion potential (E_{corr}) of the metal substrate surface is usually expressed vs. a reference electrode such that:

$$E_{corr} = E_{1/2} + E_{1/2}^{ref} \quad (\text{Equation 1.20})$$

Where $E_{1/2}$ is the half-cell potential defined in equations 1.17 to 1.19 and $E_{1/2}^{ref}$ is the half-cell potential of the reference electrode. Given what has been said regarding the value of α_e^{ref} , χ_{gas}^{pol} and χ_{gas}^{sol} , equation 1.2 may be used to re-write equations 1.17 and 1.18 as follows:

$$E_{corr} = A + \Delta\psi_{sol}^{ref} \quad (\text{Bare substrate – solution interface}) \quad (\text{Equation 1.21})$$

$$E_{corr} = B + \Delta\psi_{pol}^{ref} \quad (\text{Substrate – intact polymer interface}) \quad (\text{Equation 1.22})$$

or (Substrate – delaminated polymer interface)

Where A and B are constants for the substrate – solution and substrate – polymer systems respectively.

The value of A in equation 1.21 may be determined by simultaneous measurements of E_{corr} (vs. a standard reference electrode) and $\Delta\psi_{sol}^{ref}$ using the Kelvin probe. Similarly, the value of B in equation 1.22 may be determined by the simultaneous measurement of E_{corr} and $\Delta\psi_{pol}^{ref}$ of α_e^{ref} , χ_{gas}^{pol} and χ_{gas}^{sol} .

1.9 Secondary Ion Mass Spectrometry

SIMS is a technique that allows the analysis of the surface chemistry of conductive materials, and amongst other things is an especially important tool in the characterisation of surface oxide/salt films. Within this work SIMS has been used to discover the nature of coating induced oxide growth on zinc substrates, and also to identify the chemical composition within corrosion products to help elucidate the corrosion mechanisms taking place. The fundamental concept of SIMS is that a sample surface is bombarded with a primary ion beam, causing the emission of secondary ions from the sample surface. It is these secondary ions that are subsequently analysed via mass spectrometry to provide a localised elemental analysis of the sample surface.

The primary ion beam is produced from a solid Gallium ion source and can be focussed to 1 μ m diameter to allow the exact positioning of the ion beam on the sample surface. Upon ion bombardment, the sample surface is slowly sputtered away as primary ions pass energy to the target atoms. This process releases a mixture of particles of the sample material along with electrons and protons [102], which is illustrated schematically in figure 1.13. The primary ions can penetrate the sample to depths of between 1 and 10nm. The secondary particles released due to the primary ion bombardment carry negative, positive and neutral charges and they have kinetic energies that range from zero to several hundred eV.

There are a number of variants on the SIMS technique that make it useful for a multitude of applications such as static SIMS, dynamic SIMS and imaging SIMS. Static SIMS is generally used for sub-monolayer elemental analysis, whereas dynamic SIMS is useful for obtaining compositional information as a function of depth below the surface and allows the thickness of oxide films to be discovered. Imaging SIMS is useful for creating spatially resolved elemental images of a sample surface, allowing chemical differences over a sample surface to be visualised.

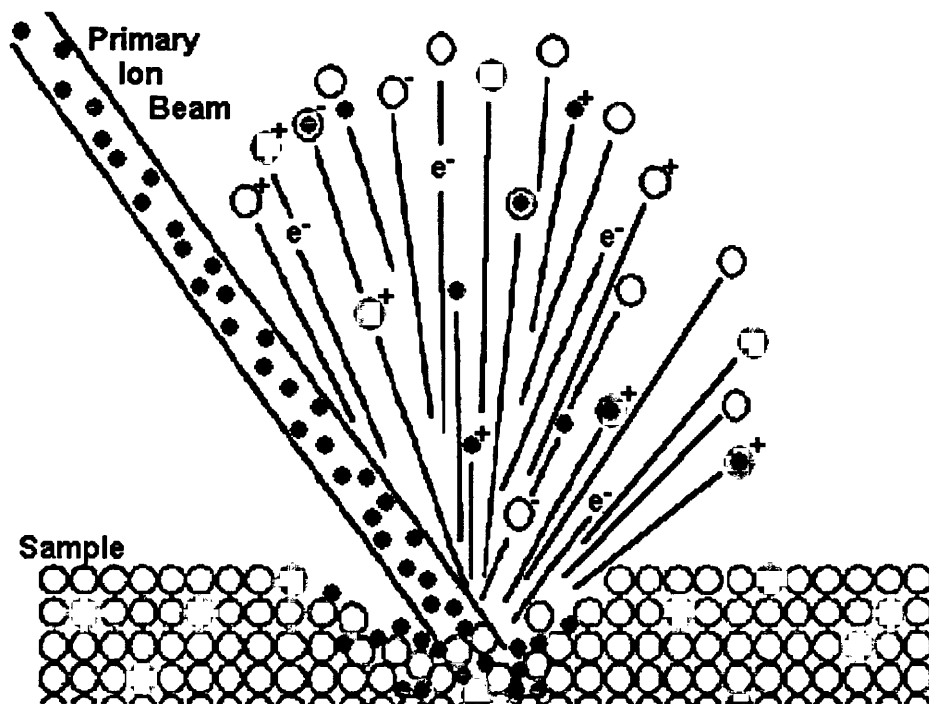


Figure 1.13. Schematic representation of a sample surface being slowly sputtered away during SIMS analysis.

1.10 Photovoltaics

Traditionally the coatings applied to pre-painted steels are designed to provide corrosion protection whilst at the same time providing an acceptable aesthetic appearance. Traditional solar cells (first generation solar cells) based upon single crystal silicon technology are reliant upon relatively bulky and expensive single crystal silicon wafers. It is not feasible to incorporate solar cells made from single crystal silicon directly into the coating systems used for pre-painted steels due to a number of factors. These factors include both material cost and the physical properties of the single crystal silicon making it impossible to form without fracturing.

There is an emerging technology that has the prospect to allow the integration of solar cells directly into coating systems used for the production of pre-painted steels, namely organic photovoltaics. These thin film organic solar cells are reliant upon inherently conducting polymers as a fundamental material to produce electricity from solar radiation. Theoretically, by coating strip steel products with solar electricity generating coatings and using this product to clad buildings in the usual way, buildings will be able to generate their own electricity. This environmentally friendly source of electricity could be engineered so that no external power supply would be required; it is also possible that any excess electricity produced could be sold to the power companies. The idea of cladding buildings with solar cells is not new, and to want to do this is logical in the high state of environmental awareness surrounding the world today. With the ever increasing drive to find sustainable and renewable energy sources for power generation the use of solar energy is not so widely talked about in the media.

One particular building that in the United Kingdom that has utilised solar cells is the CIS tower that was originally built in Manchester during 1962 to house CIS. Currently under renovation that commenced in 2004, the main feature of this building is the solar panel cladding and the expected cost to complete the project is expected to be in the region of £5.5m. Similar photovoltaic systems are available for homeowners to attach to their homes, with the cost of such systems being high at ca. £6000 per 800kW where the average UK home uses 3000kW of electricity per year.

A major factor in the high cost of these solar cells is the process of manufacturing the single crystal silicon that forms the basis of the solar cell design.

It is the relatively high cost of traditional solar cells based upon single crystal technology that is prohibitive to the widespread use of solar cells for widespread renewable electricity generation. It is possible to design innovative power generating systems suitable to be included as a component in pre-painted coating systems through the use of thin film solar cells. These coating systems that could be designed for coating large industrial buildings and retail parks require a number of criteria to be considered, most importantly formability, ease of material processing and cost. A typical building clad from pre-painted steel has a vast surface area and if coated with a low cost photovoltaic coating, emphasis could be taken away from the drive to obtain high efficiencies and put towards low processing costs. By including thin film photovoltaics in coating systems for pre-painted steels, the final cladding product will remain formable so as to allow profiling of the strip steel to take place in the normal way. One possible method of including photovoltaic technology within organic coating systems is through the use of inherently conducting polymers (ICP's). The process of creating solar cells through the use of ICP's is known as organic photovoltaics.

1.10.1 Electromagnetic Radiation and Photons

Sunlight reaches the earth in the form of electromagnetic radiation that consists of a spectrum of photons of different energies (Table 1.1). Provided that a photon of light incident on a solar cell has an energy greater than that of the semiconductor band-gap, an electron will be excited into the conduction band of the semi-conductor. If the photon has energy less than the semiconductor material, it will have no effect other than heating as its energy is dissipated. As a consequence of this phenomenon, photovoltaic devices in direct sunlight may reach temperatures of 20 – 30°C above the ambient temperature.

Radiation Type	Frequency (10^{14} Hz)	Wavelength (nm)	Energy per Photon (10^{-19}J)
Ultraviolet	8.6	350	5.7
Violet	7.1	420	4.7
Blue	6.4	470	4.2
Green	5.7	530	3.8
Yellow	5.2	580	3.4
Orange	4.8	620	3.2
Red	4.3	700	2.8
Infrared	3.0	1000	2.0

Table 1.1. Colour, frequency and wavelength of electromagnetic radiation ($1eV = 1.6022 \times 10^{-19}J$)

1.10.2 Semiconductor Photovoltaic Theory

The photovoltaic effect is the direct conversion of light energy into DC electrical energy without the need for any other intermediate process. This direct process occurs when light falling on a two layer semiconductor material produces a potential difference between these two layers. It is the voltage (potential difference) that provides the driving force for electron flow if the components of an electric circuit were put in place. For this to happen the two semi-conductors must have different properties, where one is an n-type material, with excess free electrons and the other semi-conductor is a p-type, which has excess holes (electron vacancies). If a p-type and an n-type semi-conductor were layered together, the interface where they meet is known as a p-n junction and the properties of the device are dependant upon the quality of this junction. Typically the semiconductors traditionally used in this way are single crystal silicon doped with various impurity elements, of which depends upon whether an n-type or p-type material is required. A schematic of a typical p-n junction photovoltaic cell is shown in figure 1.14.

Semiconductors have two energy bands, where one is known as the valence band and the other the conduction band. These two bands are separated by a band-gap

measured in units of electron volts (eV). When energy of a magnitude greater than the band-gap energy is supplied to a valence electron, the weak bonds holding it there are broken and it is excited to the next level, i.e. the conduction band. The energy to do this can be supplied in the form of photons, and once in the conduction band the electrons are relatively free to flow through the material as electrical current.

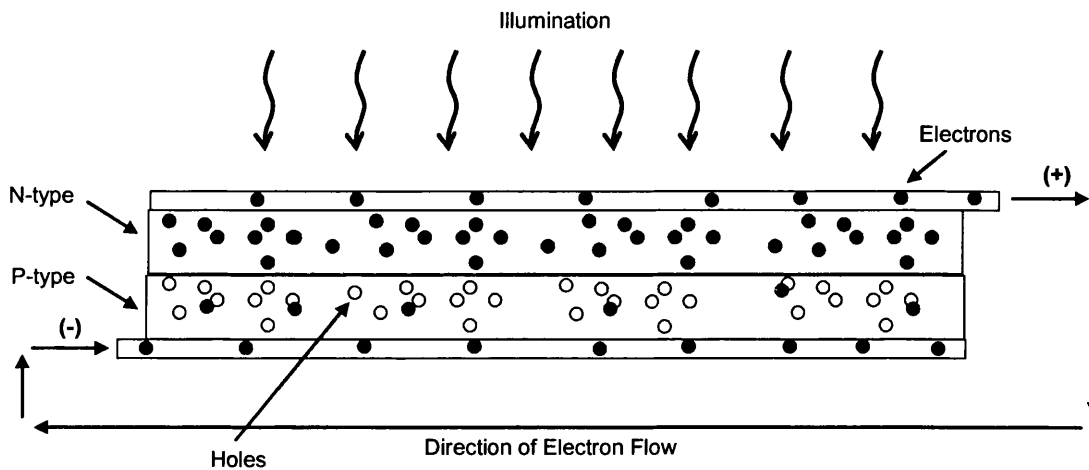


Figure 1.14. Schematic of a typical p-n junction photovoltaic solar cell showing the general principals of photocurrent generation resulting from incident photon energy.

The p-n junction forms a diode and an explanation of the way in which this happens is as follows; both the p-doped silicon and the n-doped silicon are conductive, but the boundary between the two materials, known as the depletion zone is non-conductive. The depletion zone is formed when the electrical charge carriers (both electrons and holes) attract and eliminate each other at the boundary due to a process known as recombination. The p-n junction diode that is formed allows electrical charges to flow in one direction only. Once over the boundary the electrical charges are unable to flow back to where they came from, which creates a situation of single direction charge flow. The negative charges can easily flow from through the junction from n to p, but not from p to n.

When light of an appropriate wavelength strikes a photocell created using a p-n junction and is absorbed, electrons are able to travel randomly through the material. These electrons that are in close proximity to the p-n junction can be swept across the

junction by the fixed field. Because the electrons can easily cross the boundary but are unable to return due to the operational field gradient, a charge imbalance results between the two layers of semi-conductor. These electrons that are swept from the p-type layer to the n-type layer due to the localised effects of the fixed field have a drive to leave the n-type layer and return to the p-type layer in order to correct the charge imbalance. Because these electrons can not cross the diode junction, they are forced to go around an external circuit (if one exists) in order to re-enter the p-type material. Whilst in an external circuit this DC flow is available for use, or conversion into an AC current as required.

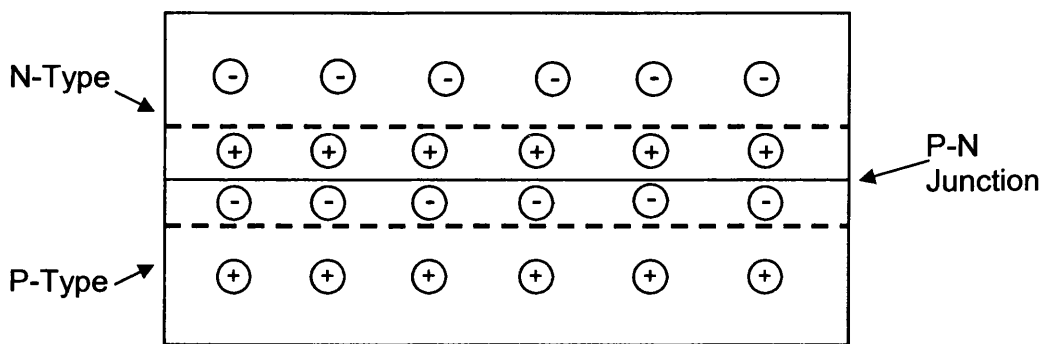


Figure 1.15. Schematic diagram of the depletion zone formed between two differently doped semi-conducting materials, showing the likely position of charges in this region.

The potential that the electrons deliver to an external circuit is determined by the band-gap of the semi-conductor material used rather than the energy of the incident light. As an example consider two photons of light with energies 2eV and 3eV that are incident on a semi-conductor with a band-gap of 1eV. Any external circuit as the result of a p-n junction diode will have a potential difference of slightly less than 1V.

1.10.3 Measurement of Photovoltaic Cell Parameters

Photovoltaic cell efficiency varies depending upon the cell design and material choices, and accordingly there are recognised ways of characterising the performance. The electrical power that a cell produces may be calculated from the number of free electrons flowing in the external circuit (the current) times their potential. This may be written in the form:

$$P = IV \quad (\text{Equation 1.23})$$

Where P is the cell power measured in Watts (W), I is the current in Amps (A) and V is the voltage in Volts (V).

The most widely used method of recording the characteristics of a photovoltaic solar cell is by recording how the cell output current changes with cell voltage to obtain the current-voltage (I-V) characteristic for the cell. A typical I-V characteristic that could be expected from a silicon photovoltaic cell under irradiation is illustrated schematically in figure 1.16.

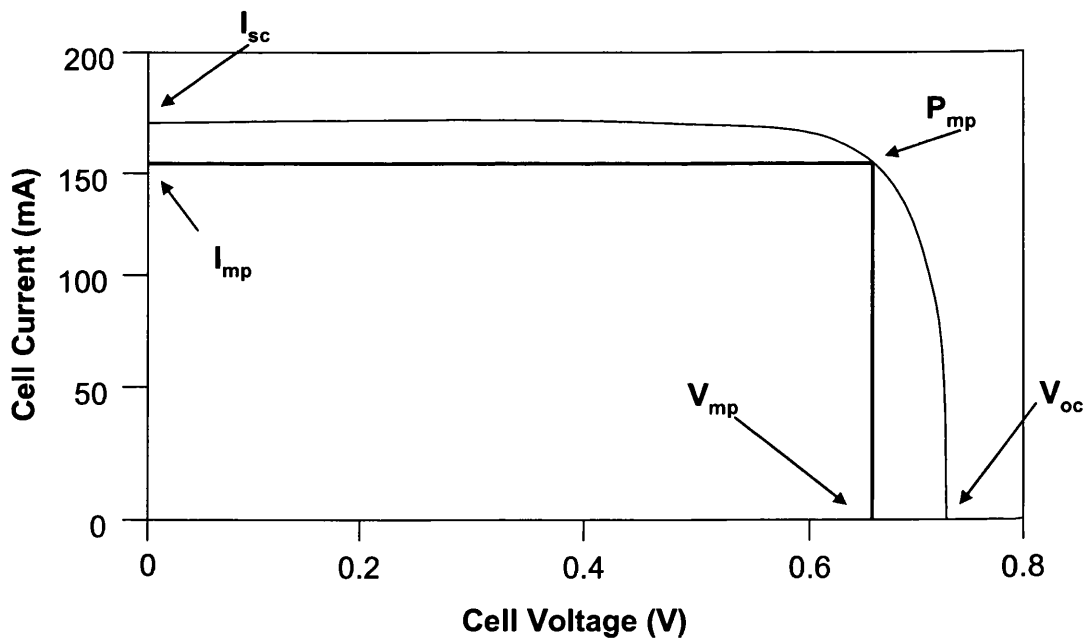


Figure 1.16. Schematic illustration of a forward bias I-V characteristic of a typical Si photovoltaic cell.

The recorded I-V curve has three significant features that are important to allow subsequent analysis of the cell performance.

1. Short-circuit current (I_{sc}), which occurs at the point on the curve where the voltage is zero. At this point the power output of the cell is zero.
2. Open-circuit voltage (V_{oc}), which occurs at the point on the curve where the current is zero. At this point the cell power output is also zero.
3. Maximum power (P_{mp}) is the point on the curve where the product of current (I_{mp}) and voltage (V_{mp}) is a combined maximum following equation 1.23.

The I-V curve is based on the cell being under standard conditions of sunlight, where for the testing and characterisation of photovoltaic cells a value of one sun is generally used. The light intensity required to create conditions of one sun is 1000 Watts of solar energy per square meter (1000 Wm^{-2}), sometimes referred to as peak sun or in some cases AM1.5. When a photovoltaic cell is operating in conditions of less than one sun, the power output of the cell is reduced.

Once the I-V characteristic measurements of the cell have been recorded, analysis of these measurements can be undertaken to determine further cell parameters. One of the most important photovoltaic cell parameters is the cell efficiency, sometimes known as the energy conversion efficiency (η), and can be calculated from equation 1.24:

$$\eta = \frac{P_{mp}}{P_{in}} \quad (\text{Equation 1.24})$$

Where P_{in} is the power input to the cell. The fill factor (FF) determines the shape of the solar cell I-V characteristic and is a useful parameter for quality control tests, with values greater than 0.7 being representative of a good cell and a value of 1 representing an ideal photovoltaic cell. The FF may be calculated according to equation 1.25:

$$FF = \frac{I_{mp} V_{mp}}{I_{sc} V_{oc}} \quad (\text{Equation 1.25})$$

The efficiency by which a silicon solar cell converts solar energy into direct electrical current is highly dependent upon the crystal structure of the silicon. By far the highest quality form of silicon to produce solar cells is single crystal silicon wafer, which produces the highest efficiency cells. The next highest quality is polycrystalline silicon and the poorest quality that creates the least efficient cells is amorphous silicon, which is also the cheapest to produce. The reason why the most efficient single crystal silicon wafer is expensive is because of the difficulties associated with its production. The production of single crystal silicon wafer utilises the Czochralski process, which involves the melting of silicon together with any dopant impurities. This melting process is followed by simultaneously drawing out and solidifying the silicon originating from a seed crystal at carefully controlled speeds under an inert atmosphere to create doped single crystal silicon. The cost is high because the low production speeds results in low production volume. Cylindrical ingots of approximately 25cm diameter and 1m in length are obtained. The ingots are then cut into wafers using a saw, which is a very slow and delicate process with almost half the silicon being lost as sawdust. The wafers are then etched to remove saw marks and create a smoother surface suitable for production of a p-n junction. The p-n junction is then produced by exposing one surface of the wafer to a phosphorous-rich environment at high temperature. The phosphorous atoms penetrate the wafer to a depth of approximately 2µm to form the n-type layer.

Efficiency differences encountered with the variation of the type of silicon is caused primarily by defects within the crystal structure. Single crystal silicon theoretically has the least amount of crystal defects and hence produces the highest efficiencies. Polycrystalline silicon contains grain boundaries and it is these grain boundaries that decrease the energy conversion efficiency. The number of grain boundaries within polycrystalline silicon depends upon the processing parameters used in the production of the material. Amorphous silicon contains the greatest number of internal defects and accordingly causes the lowest efficiency rating of all, although it is by far the cheapest method of producing silicon for photovoltaic applications.

1.10.4 Electrical Properties of Polymers

The mechanism by which inorganic semi-conductors generate electricity from incident photons is well established, and the structure of the crystalline inorganic materials is explained in terms of energy bands. In the case of inorganic semiconductors light of a sufficient energy (eV) is able to excite an electron from the valence band up into the conduction band.

The way in which organic semiconductors such as inherently conducting polymers generate electricity is analogous to the way inorganic semiconductors operate, although there are significant differences in the mechanisms by which they work. The reason why conducting polymers can be thought of as similar to inorganic semiconductors is due primarily to the characteristics of the π bonds within their structure that are present over the entire polymer chain. The quantum mechanical overlap of the p_z orbital results in the creation of two orbital's. One of these orbital's is bonding (π), which is of a lower energy, and the other is anti bonding (π^*) of a higher energy. It is the lower energy (π) orbital that acts as the valence band and the higher energy (π^*) that acts as the conduction band. For this reason inherently conducting polymers can be thought of as having an effective band gap due to the energy differences between the theoretical valence and conduction bands created by these orbital's. It is through the properties of the band gap that the optical properties of the material are determined. The majority of semi-conducting polymers have a band gap in the region of 1.5 to 3.0 eV (i.e. in the optical light range) and accordingly are highly suitable for use within optoelectronic devices [103].

Where the properties of organic semiconductors and inorganic semiconductors differ the most is regarding what happens to the electron when it has been excited from the (π) valence band to the (π^*) conduction band. The mechanisms that occur in organic semiconductors can be thought of as more complex than the mechanisms occurring in inorganic semiconductors. These mechanisms centre around the fact that when an incident photon excites an electron, the resulting electron and hole are bound together as an electron hole pair known as an exciton that moves through the material as one. It is only at interfaces that the generated exciton can be split and the reason this happens is because of the strong electric fields found at interfaces of conductive

materials with different electron affinities and ionisation potentials [104]. This is in contrast to inorganic semiconductors where the electron and hole are simply able to migrate freely to opposite electrodes if present.

The lifetime of an exciton produced within a conducting polymer is very short with the distance over which it is capable of travelling by diffusion is only around 10nm before the electron and hole recombine in a process known as recombination. It is this short range of the exciton that limits the efficiency of organic solar cells because when an electron and a hole recombine the solar energy expended in their creation can not be put to good use.

1.10.5 Organic Photovoltaics

The use of organic semi-conductors are not limited to photovoltaic devices, they can also be used for optoelectronic devices such as organic light emitting diodes (OLED's). Conjugated polymers are sometimes referred to as organic semi-conductors, and some conjugated polymers such as polyaniline have been shown to provide protection to metals against atmospheric corrosion. This presents a great possibility for the development of coatings based upon conjugated polymers that are capable of harvesting solar energy and converting it directly into electricity, whilst at the same time acting as an environmentally friendly corrosion inhibitor.

1.10.5.1 Schottky Photovoltaic Cells

A key factor in photovoltaic cell design is the diode, which is a component that restricts the direction of charge carrier flow. A Schottky diode (a schematic of which is shown in figure 1.17) is a semiconductor diode with a very large voltage drop in the forward direction along with a very fast switching action. A Schottky barrier can be created by a metal-semiconductor junction that has rectifying characteristics. If the metal-semiconductor junction did not have rectifying characteristics it is said to be an ohmic contact rather than a Schottky barrier and whether the junction is ohmic or not depends upon the work function of the metal and the band gap of the semiconductor.

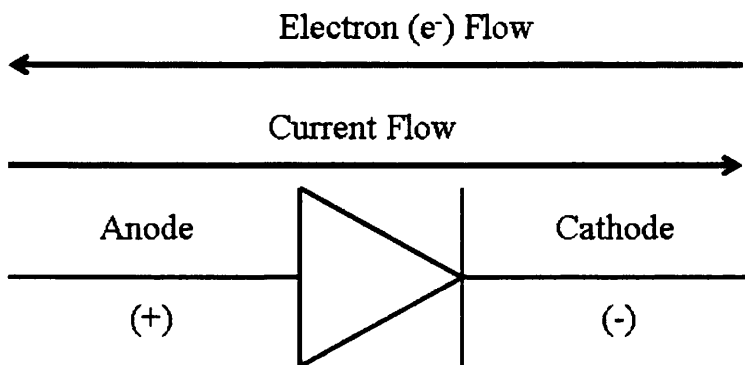


Figure 1.17. Schottky diode schematic showing direction of current flow when as part of a photovoltaic solar cell.

The first generation of organic photocells were based upon Schottky cell design [105]. The design of such cells was simply a single organic layer sandwiched between two conductive electrodes of different work functions [106, 107]. The formation of the Schottky barrier occurs between the p-type (hole conducting) organic layer and the electrode with the lowest work function. This method of organic solar cell production leads to the formation of cells with limited efficiency, which has resulted in them not being considered as viable for commercialisation. One ohmic contact is required as well as the one Schottky barrier contact if the solar cell is to be able to produce its highest possible efficiency [108]. Although intrinsically inefficient, the efficiency of the Schottky barrier solar cell is highly dependant upon the anodic and cathodic electrode choices [109].

Typical efficiencies of Schottky barrier solar cells are ca. $10^{-3}\%$ [110, 111], although efficiencies of up to 0.6% have been achieved [112], which is still far lower than deemed required for effective commercial application. One benefit of Schottky solar cells is they are conceptually very simple, consisting of an organic semi-conductor sandwiched between a cathodic electrode and an anodic electrode of different work functions as illustrated schematically in figure 19.

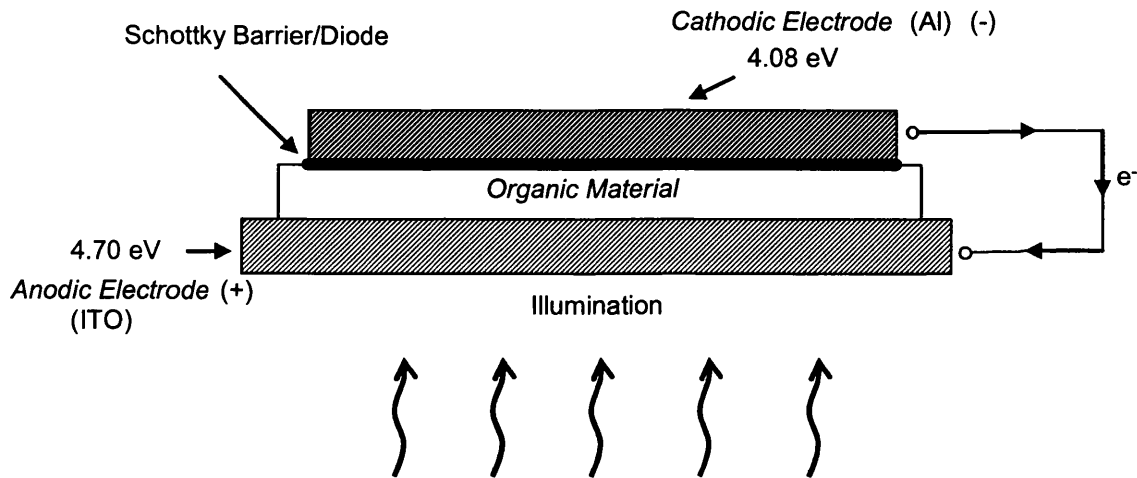


Figure 1.18. Schematic diagram of single organic layer Schottky photovoltaic solar cell. Showing position of the Schottky barrier and the direction of current flow resulting from incident light.

In this schematic the two chosen electrodes are transparent indium tin oxide (ITO) as the anodic electrode and aluminium as the cathodic electrode. ITO has a reported work function of $\sim 4.70\text{eV}$ [113-116] and the work function of aluminium is 4.08eV . For this reason the Schottky barrier formation occurs at the interface between the p-type hole conducting organic layer and the lower work function electrode (the aluminium). Exciton dissociation occurs at this interface, where the holes remain inside the organic layer and the electrons pass over the Schottky barrier into the aluminium. These electrons are unable to return through the Schottky barrier and accordingly are forced to travel around any external circuit to pass into the ITO layer, through the ITO-organic ohmic contact and into the organic layer.

The materials used to create the first Schottky photovoltaic cells were organic pigments such as perylene and phthalocyanine. These devices were found to create small photocurrents under illumination. The inefficiency of Schottky solar cells is attributed to the fact charge photogeneration only takes place in a thin layer near the metal-organic interface. The reason why this process is only effective in close proximity to the interface is because the exciton diffusion length is only ca. 10nm . For this reason only the excitons generated within 10nm of the interface are able to contribute to the photocurrent [117].

1.10.5.2 Organic Bilayer Heterojunction Solar Cells

In contrast to the poor photocurrent created by the single organic layer Schottky cells from sandwiching perylene or phthalocyanine between two electrodes, it was found that larger photocurrents could be produced by creating two layer organic cell [118]. This bilayer heterojunction based upon a two organic layer arrangement of perylene and phthalocyanine was found to generate a large photocurrent of several mA cm^{-2} . Organic bilayer heterojunction photovoltaic cells are most simply described as being two layers of organic semi conducting material sandwiched between two electrodes in an arrangement as shown in the schematic figure 1.19. In the case of Schottky based photovoltaic cells, exciton dissociation occurs due to the strong electric field caused by the interface between the organic layer and the electrode with the lowest work function. This phenomenon of exciton dissociation can also occur due to the strong electric field at the boundary of two materials of different electron affinities and ionisation potentials as is the case at the interface between the two layers in a bilayer organic cell.

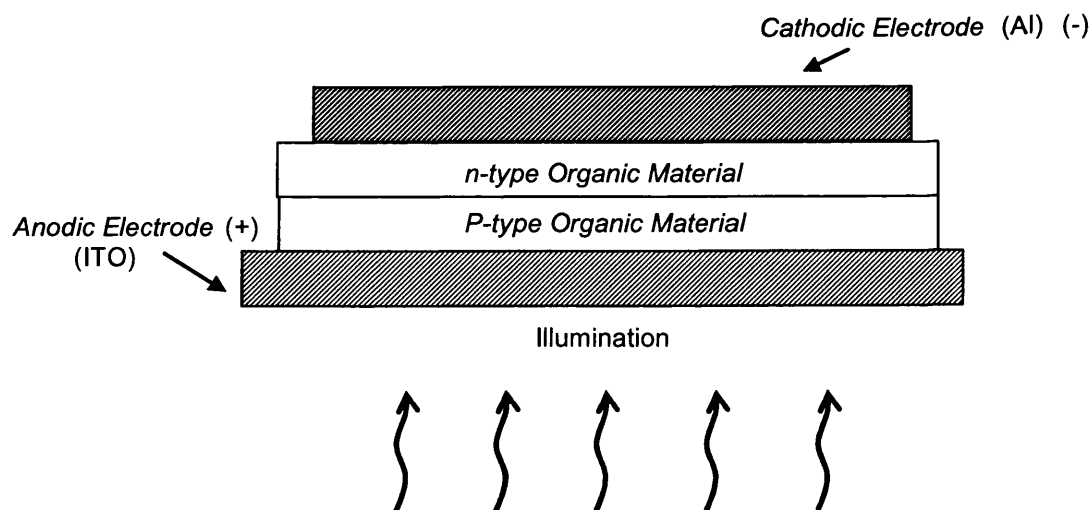


Figure 1.19. Schematic diagram of bilayer Heterojunction organic photovoltaic solar cell.

The sandwich layer of organic semiconductors consists of a thin layer of a p-type material that transports holes, and a laminated n-type material that transports electrons. The bilayer heterojunction photovoltaic cell as illustrated in figure 1.19 is generally more efficient at converting solar radiation into useful electrical current

than the Schottky devices previously considered. The efficiency of bilayer devices following this arrangement is still limited due to the short exciton diffusion length of ca. 10nm for the same reasons as mentioned in the case of Schottky cells. The primary reason why bilayer heterojunction devices are more efficient than the single layer Schottky devices is due to the p-n junction being more efficient at exciton dissociation and electron gathering.

Early organic bilayer heterojunction photovoltaic devices were capable of generating currents (I_{sc}) of up to 10^{-8} A and photo voltages (V_{oc}) of ca. 200mV [119]. These photovoltaic solar cells were created using p-type and n-type dyes made into a sandwich structure between two electrodes. The n-type electron transporting materials used to make these devices were dyes such as rhodamines or triphenylmethane dyes. The p-type hole transporting materials were dyes of phthalocyanines or mecocyanines.

The efficiency of organic bilayer heterojunction devices was reported as much as 2% by Harima et al in 1984 [120]. This level of efficiency was achieved using a two layer device consisting of zinc phthalocyanine (ZnPc) and 5,10,15,20-tetra (3-pyridyl)porphyrin (TPyP). The cell was fabricated using a semi-transparent layer of aluminium as an electrode material, evaporating a 7nm layer of TPyP on top followed by a 50nm layer of Zn Pc to create the organic bilayer heterojunction. The final electrode choice was a thin gold layer, and the success of the device was deemed to be successful in no small part due to the good electrical contacts between the aluminium and gold electrodes to the TPyP and ZnPc respectively [121].

1.10.5.3 Organic Bulk Heterojunction Solar Cells

Due to the efficiency limiting factors experienced with bilayer heterojunction solar cells, namely the short exciton diffusion length of ca. 10nm, the obvious solution to increase the likelihood of exciton dissociation is to increase the junction area within the cell. A schematic diagram illustrating the concept of a bulk heterojunction photovoltaic cell is shown in figure 1.20. In this diagram it can be seen that the overall device configuration is similar to the bilayer heterojunction only differing in the way in which the n-type – p-type interface is created.

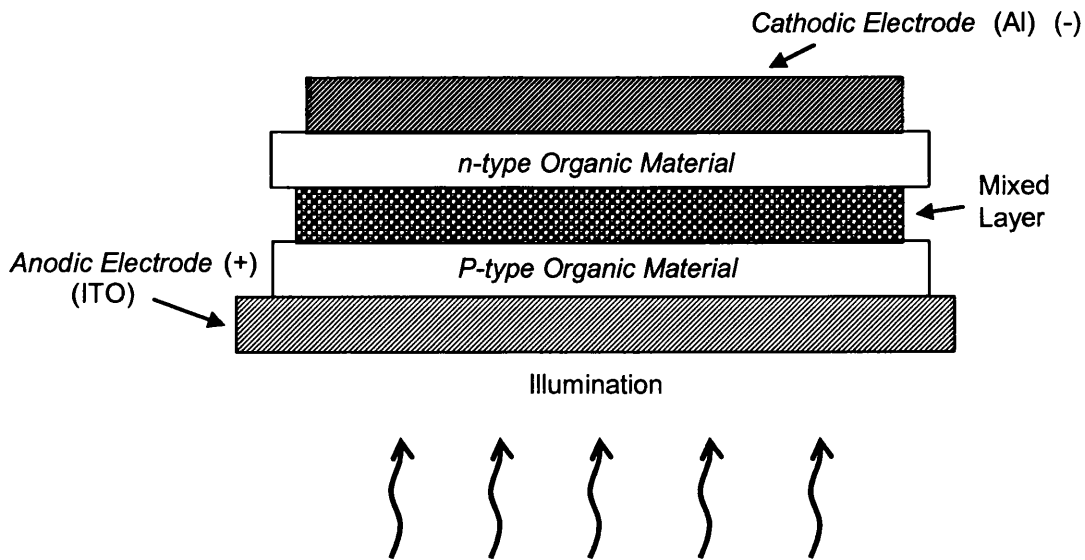


Figure 1.20. Schematic diagram of bulk Heterojunction organic photovoltaic solar cell.

Conceptually a bulk heterojunction photovoltaic cell operates in a similar manner to a bilayer cell in terms of the donor and acceptor mechanisms taking place. A bulk heterojunction solar cell is able to provide higher levels of efficiency compared to bilayer devices because of the higher interfacial area between the hole and electron conducting materials [105]. This higher interfacial area increases the exciton dissociation efficiency within the device wholly because the boundary regions are increased.

Pioneering work on bulk heterojunction photovoltaic cells was undertaken by Hiramoto et al, whereby they developed a three layer cell that comprised of an n-type material and a p-type material laminated around an intermixed layer of the two materials sandwiched in between [122, 123]. Polymer bulk heterojunction solar cells have been shown to exhibit even higher efficiencies of 2.5% [124] and 3.1% [125], which prove that organic solar cells based upon polymeric materials are a viable alternative to inorganic technology for many applications.

1.10.6 Polythiophene for Photovoltaic Applications

One of the most common polymeric materials used in organic photovoltaics is polythiophene. Polythiophene is known to be used as the p-type component within bilayer heterojunction photovoltaic devices in conjunction with an n-type material known as fullerene (C₆₀). The research involving polythiophenes and fullerene has taken place after the evidence of photo-induced electron transfer from the excited state of a conducting polymer onto buckminsterfullerene (C₆₀) [126].

Fullerene (C₆₀) is a carbon molecule and takes the form of a hollow sphere as illustrated in figure 1.21. Fullerenes were discovered in 1985 and have high electron affinity values. They have been the subject of much research within the field of organic photovoltaics with studies of their application within bilayer heterojunction and bulk heterojunction devices. It has been found that the use of fullerenes in conjunction with polythiophenes helps to increase the photovoltaic cell efficiency [127-130]. It is known that the electron transfer between the polymer and the fullerene occurs on a time-scale of ca. 45fsec, and this speed of electron transfer is much faster than any competing process [131].

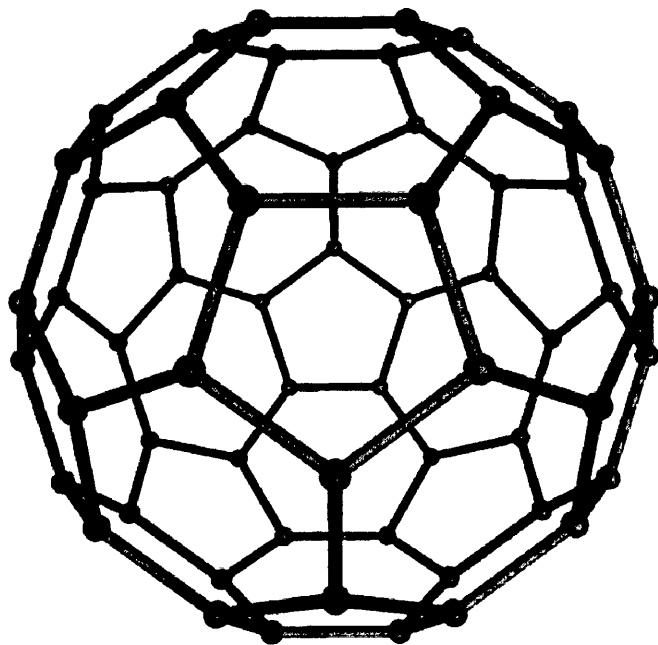


Figure 1.21. Representation of a fullerene (C₆₀) molecule.

The band gaps of polythiophenes can be engineered to be anywhere from 1.7eV to 3eV via simple substitution of the main polymer chain. An additional feature of polythiophenes is that they can be synthesised to be added to aqueous solution for easy processing, or if required they can be deposited chemically [132, 133]. It is also said that polythiophenes can have higher mobility values [134-136], which enables the efficiency of organic solar cells to be increased compared to others.

Typical bilayer devices based upon polythiophene and C60 have been shown to provide fairly efficient photo-conversion. These devices are typically formed by creating a heterojunction between a spin coated layer of a polythiophene and a sublimed layer of C60. Although not entirely suitable for production solar cells, these devices are useful tools to gain a mechanistic understanding of the various interactions taking place between the polymer and the fullerene [104]. An example of a polythiophene derivative studied in this way is 3,4-(1,4)-7-trioxaocetylphenylthiophene (PEOPT), which acts as a donor layer when spin coated and C60 is sublimed on top as an acceptor layer to create a bilayer device [129]. Extensive studies have also been made looking closely at blends of polythiophene and C60 [137], to create a situation where the two materials of differing electron affinity values are mixed to create bulk heterojunction devices.

Another form of polythiophene commonly used as a material within organic photovoltaic devices is PEDOT. This is a commercially available conducting polymer that benefits from being water soluble when doped with polystyrene sulfonic acid (PSS), which is the charge compensating counter anion to the positively charged PEDOT. PEDOT:PSS can be used for such applications as anti-static coatings for photographic films and when cast as a sub-micron film is highly transparent, which makes it ideal for use as an electrode material for other applications such as photovoltaics and light emitting diodes.

Typical aqueous PEDOT solutions contain 1.3wt% of the combined polymers with a PEDOT to PSS of approximately 1:2.5 by weight. The conductivity of PEDOT can be made ranging from 10^{-5} to 10 Scm^{-1} [138]. The high conductivity of PEDOT:PSS leads to the possibility of using it as an ITO replacement material in many thin film electronic applications. Another conducting polymer that could possibly show

promise for similar applications is polyaniline when applied as a thin conducting layer.

1.10.7 Polyaniline for Photovoltaic Applications

Although polyaniline (PAni) has been extensively studied in terms of the corrosion protection of iron and zinc, very little investigation has been conducted into using PAni for organic thin film photovoltaic applications. The small amount of work that has been undertaken involving the application of PAni has mainly concentrated on the junction characteristics and diode behaviours of such devices. Schottky devices made as an Al-PAni-ITO sandwich have been investigated by Chung et al [139]. This work investigated the junction properties of the PAni Schottky diodes made using conductive PAni doped with sulfonic acids, and it was found that dopant choice effects cell performance. A similar investigation into Schottky diodes made using sulphonated PAni was made by Narasimhan et al [140].

PAni has also been investigated as part of dye-sensitised solar cells where it was utilised as the hole transporting layer within cells containing TiO₂ [141], producing an open circuit voltage (V_{oc}) of up to 310 mV and a short circuit current (I_{sc}) of $21\mu Acm^{-2}$. Another study using PAni as part of a dye-sensitised solar cell, also involving TiO₂, was carried out by Liu et al [142] where a V_{oc} of 387mV and an I_{sc} of $120.03\mu mA^{-2}$ was achieved.

A study of the rectifying effect of a heterojunction between porous silicon and a water soluble copolymer of PAni has been undertaken [143]. This shows that diode characteristics are produced by creating a heterojunction between the n-type amorphous silicon layer and the PAni. Knowing that PAni in contact with n-type silicon produces diode characteristics indicates the possibility that the device will be able to act as an organic-inorganic bilayer heterojunction photovoltaic cell.

1.11 References

- [1] K. Tretheway and J. Camberlain, *Corrosion for Science and Engineering*, Longman, 1995.
- [2] I. Suzuki, *Corrosion Resistant Coating Technology*, New York: Marcel Dekker inc, 1989.
- [3] I. A. Von Fraunhofer, *Basic Metal Finishing*, London: Eleck Science, 1976.
- [4] J. Kumanotani, *J. Metal Finishing Soc*: 579 (1981).
- [5] R. M. Burns and W. W. Bradley, *Protective Coatings for Metals*, Rienhold Publishing Corporation, New York, 1967.
- [6] E. Mattson, *Basic Corrosion Technology for Corrosion Scientists and Engineers*, The Institute of Materials, 1996.
- [7] P. A. Ryan, R. P. Wolstenholme, and D. M. Howell, *Durability of Cladding - A state of the art report*, Thomas Telford, 1994.
- [8] H. Leidheiser, W. Wang, and L. Igetoft, *Progress in Organic Coatings* 11:19 (1983).
- [9] J. I. Skar and U. Steinsmo, *Corrosion Science* 35:1385 (1993).
- [10] A. Leng, H. Streckel, and M. Stratmann, *Corrosion Science* 41:547 (1999).
- [11] G. Williams and H. N. McMurray, *Journal of the Electrochemical Society* 148:B377 (2001).
- [12] M. Stratmann, R. Feser, and A. Leng, *Electrochimica Acta* 39:1207 (1994).
- [13] M. Stratmann, M. Wolpers, H. Streckel, and R. Feser, *Berichte Der Bunsen-Gesellschaft-Physical Chemistry Chemical Physics* 95:1365 (1991).
- [14] H. S. Wroblowa, *Journal of Electroanalytical Chemistry* 339:31 (1992).
- [15] W. Furbeth and M. Stratmann, *Corrosion Science* 43:207 (2001).
- [16] W. Furbeth and M. Stratmann, *Fresenius Journal of Analytical Chemistry* 353:337 (1995).
- [17] H. Leidheiser, *Acs Symposium Series* 322:124 (1986).
- [18] P. Scholl, X. Shan, D. Bonham, and G. A. Prentice, *Journal of the Electrochemical Society* 138:895 (1991).
- [19] H. Leidheiser, *Corrosion* 39:189 (1983).
- [20] J. E. Castle and J. F. Watts, *Corrosion Control by Organic Coatings*:78 (1981).

- [21] E. L. Koehler, *Corrosion* **40**:5 (1984).
- [22] J. S. Hammond, J. W. Holubka, J. E. Devries, and R. A. Dickie, *Corrosion Science* **21**:239 (1981).
- [23] C. F. Sharman, *Nature* **153**:621 (1944).
- [24] C. Hanin, *Corrosion*, ASM International, OH, 1987.
- [25] A. Bautista, *Progress in Organic Coatings* **28**:49 (1996).
- [26] G. Williams and H. N. McMurray, *Journal of the Electrochemical Society* **150**:B380 (2003).
- [27] G. Williams, H. N. McMurray, D. Hayman, and P. C. Morgan, *Physchemcomm*:1 (2001).
- [28] H. N. McMurray, G. Williams, and S. O'Driscoll, *Journal of the Electrochemical Society* **151**:B406 (2004).
- [29] H. N. McMurray and G. Williams, *Corrosion* **60**:219 (2004).
- [30] G. Williams and H. N. McMurray, *Electrochemical and Solid State Letters* **7**:B13 (2004).
- [31] J. C. Scully, *The Fundamentals of Corrosion*, Pergamon Press, UK, 1990.
- [32] L. L. Shreir, R. A. Jarman, and G. T. Burstein, *Corrosion; Corrosion Control*, Butterworth Heinemann, Oxford, 1994.
- [33] D. N. Layton, *Trans. I.M.F* **43**:153 (1965).
- [34] R. M. Souto and D. J. Scantlebury, *Progress in Organic Coatings* **53**:63 (2005).
- [35] A. R. Marder, *Progress in Materials Science* **45**:191 (2000).
- [36] S. Bohm, M. Challis, T. Heatley, and D. A. Worsley, *Transactions of the Institute of Metal Finishing* **79**:16 (2001).
- [37] T. Prosek, D. Thierry, and A. Nazarov, *French Corrosion Institute, France, Brest*, 2008.
- [38] R. Hausbrand, M. Stratmann, and M. Rohwerder, *Steel Research International* **74**:453 (2003).
- [39] D. Harrop, *Chemical Inhibitors for Corrosion Control*, Proceedings of the Industrial Division of the RSC and the Institute of Corrosion Science and Technology University of Manchester, 1990.
- [40] S. W. Dean, R. Derby, and G. T. v. d. Bussche, in *NACE International Corrosion Forum*, Toronto, Ontario Canada, 1981.
- [41] S. A. Katz and H. Salem, *Journal of Applied Toxicology* **13**:217 (1993).

- [42] S. Langard and T. Norseth, *British Journal of Industrial Medicine* **32**:62 (1975).
- [43] S. Bohm, R. Greef, H. N. McMurray, S. M. Powell, and D. A. Worsley, *Journal of the Electrochemical Society* **147**:3286 (2000).
- [44] A. Sheffet, I. Thind, A. M. Miller, and D. B. Louria, *Archives of Environmental Health* **37**:44 (1982).
- [45] R. L. Howard, I. M. Zin, J. D. Scantlebury, and S. B. Lyon, *Progress in Organic Coatings* **37**:83 (1999).
- [46] I. M. Zin, R. L. Howard, S. J. Badger, J. D. Scantlebury, and S. B. Lyon, *Progress in Organic Coatings* **33**:203 (1998).
- [47] A. J. Heeger, *Reviews of Modern Physics* **73**:681 (2001).
- [48] A. G. MacDiarmid, *Reviews of Modern Physics* **73**:701 (2001).
- [49] H. Shirakawa, *Reviews of Modern Physics* **73**:713 (2001).
- [50] J. Przulski, *Conducting Polymers - Electrochemistry*, Sci-Tech Publications Ltd, 1991.
- [51] P. Zarras and J. D. Stenger-Smith, *Electroactive Polymers for Corrosion Control*, American Chemical Society, Washington DC, 2003.
- [52] A. J. Epstein, *Mrs Bulletin* **22**:16 (1997).
- [53] D. E. Tallman, G. Spinks, A. Dominis, and G. G. Wallace, *Journal of Solid State Electrochemistry* **6**:73 (2002).
- [54] R. H. Baughman, *Synthetic Metals* **78**:339 (1996).
- [55] T. Osaka and T. Momma, *Electrochimica Acta* **38**:2011 (1993).
- [56] G. Sonmez, P. Schottland, K. K. Zong, and J. R. Reynolds, *Journal of Materials Chemistry* **11**:289 (2001).
- [57] D. T. McQuade, A. E. Pullen, and T. M. Swager, *Chemical Reviews* **100**:2537 (2000).
- [58] M. Gratzel, *Pure and Applied Chemistry* **73**:459 (2001).
- [59] D. W. Deberry, *Journal of the Electrochemical Society* **132**:1022 (1985).
- [60] B. Wessling, *Werkstoffe Und Korrosion-Materials and Corrosion* **47**:439 (1996).
- [61] T. D. Nguyen, M. Keddani, and H. Takenouti, *Electrochemical and Solid State Letters* **6**:B25 (2003).
- [62] J. Reut, A. Opik, and K. Idla, *Synthetic Metals* **102**:1392 (1999).

- [63] M. Rohwerder and M. Stratmann, *Mrs Bulletin* **24**:43 (1999).
- [64] G. Paliwoda-Porebska, M. Rohwerder, M. Stratmann, U. Rammelt, L. M. Duc, and W. Plieth, *Journal of Solid State Electrochemistry* **10**:730 (2006).
- [65] A. Michalik and M. Rohwerder, *Zeitschrift Fur Physikalische Chemie-International Journal of Research in Physical Chemistry & Chemical Physics* **219**:1547 (2005).
- [66] M. Rohwerder and A. Michalik, *Electrochimica Acta* **53**:1300 (2007).
- [67] G. M. Spinks, A. J. Dominis, G. G. Wallace, and D. E. Tallman, *Journal of Solid State Electrochemistry* **6**:85 (2002).
- [68] H. Letheby, *Journal of the Chemical Society* **15**:161.
- [69] Y. Cao, A. Andreatta, A. J. Heeger, and P. Smith, *Polymer* **30**:2305 (1989).
- [70] W. S. Huang, B. D. Humphrey, and A. G. Macdiarmid, *Journal of the Chemical Society-Faraday Transactions I* **82**:2385 (1986).
- [71] M. C. Bernard, S. Joiret, A. Hugot-Le Goff, and P. V. Phong, *Journal of the Electrochemical Society* **148**:B12 (2001).
- [72] C. Menardo, M. Nechtschein, A. Rousseau, J. P. Travers, and P. Hany, *Synthetic Metals* **25**:311 (1988).
- [73] J. C. Chiang and A. G. Macdiarmid, *Synthetic Metals* **13**:193 (1986).
- [74] J. S. Tang, X. B. Jing, B. C. Wang, and F. S. Wang, *Synthetic Metals* **24**:231 (1988).
- [75] W. R. Salaneck, B. Liedberg, O. Inganas, R. Erlandsson, I. Lundstrom, A. G. Macdiarmid, M. Halpern, and N. L. D. Somasiri, *Molecular Crystals and Liquid Crystals* **121**:191 (1985).
- [76] M. Inoue, F. Brown, I. C. Munoz, and F. O. Munoz, *Polymer Bulletin* **26**:403 (1991).
- [77] M. Abe, A. Ohtani, Y. Umemoto, S. Akizuki, M. Ezoe, H. Higuchi, K. Nakamoto, A. Okuno, and Y. Noda, *Journal of the Chemical Society-Chemical Communications*:1736 (1989).
- [78] M. Inoue, R. E. Navarro, and M. B. Inoue, *Synthetic Metals* **30**:199 (1989).
- [79] M. Angelopoulos, G. E. Asturias, S. P. Ermer, A. Ray, E. M. Scherr, A. G. Macdiarmid, M. Akhtar, Z. Kiss, and A. J. Epstein, *Molecular Crystals and Liquid Crystals* **160**:151 (1988).
- [80] T. K. Rout, G. Jha, A. K. Singh, N. Bandyopadhyay, and O. N. Mohanty, *Surface & Coatings Technology* **167**:16 (2003).
- [81] B. Wessling, *Synthetic Metals* **102**:1396 (1999).

- [82] E. R. Holland, S. J. Pomfret, P. N. Adams, and A. P. Monkman, *Journal of Physics-Condensed Matter* **8**:2991 (1996).
- [83] C. D. G. Minto and A. S. Vaughan, *Synthetic Metals* **93**:73 (1998).
- [84] A. Talo, O. Forsen, and S. Ylasaari, *Synthetic Metals* **102**:1394 (1999).
- [85] P. J. Kinlen, Y. Ding, and D. C. Silverman, *Corrosion* **58**:490 (2002).
- [86] B. Wessling and J. Posdorfer, *Electrochimica Acta* **44**:2139 (1999).
- [87] T. P. McAndrew, S. A. Miller, A. G. Gilicinski, and L. M. Robeson, *Abstracts of Papers of the American Chemical Society* **211**:125 (1996).
- [88] W. K. Lu, R. L. Elsenbaumer, and B. Wessling, *Synthetic Metals* **71**:2163 (1995).
- [89] A. A. Pud, G. S. Shapoval, P. Kamarchik, N. A. Ogurtsov, V. F. Gromovaya, I. E. Myronyuk, and Y. V. Kontsur, *Synthetic Metals* **107**:111 (1999).
- [90] G. Williams, A. Gabriel, A. Cook, and H. N. McMurray, *Journal of the Electrochemical Society* **153**:B425 (2006).
- [91] R. J. Holness, G. Williams, D. A. Worsley, and H. N. McMurray, *Journal of the Electrochemical Society* **152**:B73 (2005).
- [92] E. McCafferty, *Journal of the Electrochemical Society* **150**:B342 (2003).
- [93] A. Gabriel, N. J. Laycock, H. N. McMurray, G. Williams, and A. Cook, *Electrochemical and Solid State Letters* **9**:B57 (2006).
- [94] B. Wessling, *Synthetic Metals* **85**:1313 (1997).
- [95] J. L. Camalet, J. C. Lacroix, S. Aeiyaich, K. Chane-Ching, and P. C. Lacaze, *Synthetic Metals* **93**:133 (1998).
- [96] G. Williams, R. J. Holness, D. A. Worsley, and H. N. McMurray, *Electrochemistry Communications* **6**:549 (2004).
- [97] L. Kelvin, *Philos. Mag* **46**:82 (1898).
- [98] W. A. Zismann, *Rev. Sci. Instrum* **3**:367 (1932).
- [99] J. Bonnet, L. Soonckindt, and L. Lassabatere, *Vacuum* **34**:693 (1984).
- [100] H. N. McMurray and D. A. Worsley, *Reviews in Chemical Kinetics*, R. Compton (Ed) **4**:149 (1997).
- [101] K. Doblhofer and M. Cappadonia, *Journal of Electroanalytical Chemistry* **243**:337 (1988).
- [102] J. Clerc, C. Fourre, and P. Fragu, *Cell Biology International* **21**:619 (1997).

- [103] G. G. Wallace, P. C. Dastoor, D. L. Officer, and C. O. Too, *Chemical Innovation*.
- [104] L. S. Roman, *Photovoltaic Devices Based on Polythiophene / C60*, CRC, 2005.
- [105] H. S. Hoppe, N.S, *Bulk Heterojunction Solar Cells*, 2005.
- [106] G. A. Chamberlain, *Solar Cells* **8**:47 (1983).
- [107] D. Wohrle and D. Meissner, *Advanced Materials* **3**:129 (1991).
- [108] P. H. Fang, *Journal of Applied Physics* **45**:4672 (1974).
- [109] B. A. Gregg, *Journal of Physical Chemistry B* **107**:4688 (2003).
- [110] C. Y. Kwong, A. B. Djuricic, P. C. Chui, L. S. M. Lam, and W. K. Chan, *Applied Physics a-Materials Science & Processing* **77**:555 (2003).
- [111] D. K. Wohrle, L. Schlettwein, D., *Phthalocyanines and related macrocycles in organic photovoltaic junctions*, 1996.
- [112] D. L. Morel, A. K. Ghosh, T. Feng, E. L. Stogryn, P. E. Purwin, R. F. Shaw, and C. Fishman, *Applied Physics Letters* **32**:495 (1978).
- [113] L. Fenenko and C. Adachi, *Thin Solid Films* **515**:4812 (2007).
- [114] K. H. Lee, H. W. Jang, K. B. Kim, Y. H. Tak, and J. L. Lee, *Journal of Applied Physics* **95**:586 (2004).
- [115] Y. J. Lin, W. Y. Chou, and S. T. Lin, *Applied Physics Letters* **88** (2006).
- [116] C. W. Tang and S. A. Vanslyke, *Applied Physics Letters* **51**:913 (1987).
- [117] P. A. K. Lane, Z.H., *Solid-State Organic Photovoltaics: A Review of Molecular and Polymeric Devices*, 2005.
- [118] C. W. Tang, *Applied Physics Letters* **48**:183 (1986).
- [119] H. Meier, *Organic Semiconductors*, Weinheim, 1974.
- [120] Y. Harima, K. Yamashita, and H. Suzuki, *Applied Physics Letters* **45**:1144 (1984).
- [121] K. Yamashita, Y. Matsumura, Y. Harima, S. Miura, and H. Suzuki, *Chemistry Letters*:489 (1984).
- [122] M. Hiramoto, H. Fujiwara, and M. Yokoyama, *Applied Physics Letters* **58**:1062 (1991).
- [123] M. Hiramoto, H. Fujiwara, and M. Yokoyama, *Journal of Applied Physics* **72**:3781 (1992).

- [124] S. E. Shaheen, C. J. Brabec, N. S. Sariciftci, F. Padinger, T. Fromherz, and J. C. Hummelen, *Applied Physics Letters* **78**:841 (2001).
- [125] T. Aernouts, W. Geens, J. Poortmans, P. Heremans, S. Borghs, and R. Mertens, *Thin Solid Films* **403**:297 (2002).
- [126] N. S. Sariciftci, L. Smilowitz, A. J. Heeger, and F. Wudl, *Science* **258**:1474 (1992).
- [127] F. Padinger, R. S. Rittberger, and N. S. Sariciftci, *Advanced Functional Materials* **13**:85 (2003).
- [128] L. S. Roman, M. R. Andersson, T. Yohannes, and O. Inganas, *Advanced Materials* **9**:1164 (1997).
- [129] L. S. Roman, W. Mammo, L. A. A. Pettersson, M. R. Andersson, and O. Inganas, *Advanced Materials* **10**:774 (1998).
- [130] G. Yu, J. Gao, J. C. Hummelen, F. Wudl, and A. J. Heeger, *Science* **270**:1789 (1995).
- [131] C. J. Brabec, G. Zerza, G. Cerullo, S. De Silvestri, S. Luzzati, J. C. Hummelen, and S. Sariciftci, *Chemical Physics Letters* **340**:232 (2001).
- [132] M. R. Andersson, M. Berggren, O. Inganas, G. Gustafsson, J. C. Gustafsson-carlberg, D. Selse, T. Hjertberg, and O. Wennerstrom, *Macromolecules* **28**:7525 (1995).
- [133] M. Berggren, G. Gustafsson, O. Inganas, M. R. Andersson, O. Wennerstrom, and T. Hjertberg, *Applied Physics Letters* **65**:1489 (1994).
- [134] Z. Bao, A. Dodabalapur, and A. J. Lovinger, *Applied Physics Letters* **69**:4108 (1996).
- [135] R. J. Kline, M. D. McGehee, E. N. Kadnikova, J. S. Liu, and J. M. J. Frechet, *Advanced Materials* **15**:1519 (2003).
- [136] R. Valaski, E. Silveira, L. Micaroni, and I. A. Hummelgen, *Journal of Solid State Electrochemistry* **5**:261 (2001).
- [137] N. S. Sariciftci, D. Braun, C. Zhang, V. I. Srdanov, A. J. Heeger, G. Stucky, and F. Wudl, *Applied Physics Letters* **62**:585 (1993).
- [138] V. Seshadri and G. Sotzing, *Progress in Optically Transparent Conducting Polymers*, 2005.
- [139] S. F. Chung, T. C. Wen, and A. Gopalan, *Materials Science and Engineering B-Solid State Materials for Advanced Technology* **116**:125 (2005).
- [140] M. Narasimhan, M. Hagler, V. Cammarata, and M. Thakur, *Applied Physics Letters* **72**:1063 (1998).

- [141] S. X. Tan, J. Zhai, M. X. Wan, L. Jiang, and D. B. Zhu, *Synthetic Metals* **137**:1511 (2003).
- [142] Z. R. Liu, J. R. Zhou, H. L. Xue, L. Shen, H. D. Zang, and W. Y. Chen, *Synthetic Metals* **156**:721 (2006).
- [143] J. H. Fan, M. X. Wan, and D. B. Zhu, *Synthetic Metals* **95**:119 (1998).

Chapter 2

Experimental Details

2.1 Materials

2.1.1 Metals

Zinc Foil – 50 x 50mm coupons of 1.5mm thickness and 99.9999% purity, obtained from Goodfellow Metals.

Iron Foil – 50 x 50mm coupons of 1.5mm thickness and 99.9999% purity, obtained from Goodfellow Metals.

Hot Dip Galvanised (HDG) Steel – 300 x 200mm sheets of 1.5mm thickness steel with approximately 20 μ m galvanised zinc layer, obtained from Corus Steel and cut into 50 x 50mm sections using a shear cutter.

Galvalloy – 300 x 200mm sheets of 1.5mm thickness steel with a 20 μ m galvanised layer of Zn – 5% Al alloy, obtained from Corus Steel and cut into 50 x 50mm sections using a shear cutter.

Magizinc – 300 x 200mm sheets of 1.5mm thickness steel with a 10 μ m galvanised layer of Zn – 1.5%Al – 1.5%Mg alloy, obtained from Corus Steel and cut into 50 x 50mm sections using a shear cutter.

Nickel – 0.5mm wire of 99.9999% purity, obtained from Advent Research Materials.

Gold – Gold wire of 99% purity, 0.2mm diameter, obtained from Agar Scientific.

N-Type Single Crystal Silicon – Two layer (substrate and epilayer), substrate thickness 675 μ m and arsenic doped (24-28 Ωcm^{-1}), and the epilayer 40 μ m thick and phosphorous doped (0.001-0.004 Ωcm^{-1}), obtained from Pure Wafer.

2.1.2 Chemicals

Polyaniline Emeraldine Base (PAni-EB) – Average Mw 65,000, granular, obtained from Sigma Aldrich.

Polyaniline Emeraldine Base (PAni-EB) - Average Mw 5,000, granular, obtained from Sigma Aldrich.

Poly(3,4-ethylenedioxythiophene)-poly(styrenesulfonate) (PEDOT:PSS) - 1.3-1.7% in H₂O, (high-conductivity grade), was obtained from Sigma Aldrich.

Poly (vinyl butyral-co-vinyl alcohol-co-vinyl acetate) (PVB) – Mw 70,000 – 100,000 was obtained from Sigma Aldrich in powdered form:

(+)-Camphor-10-sulfonic acid (HCS) - Purum, ≥ 98.0%, Mw 232.3, C₁₀H₁₆O₄S, was obtained from Sigma Aldrich in powdered form.

Phenylphosphonic acid (HPP) – Purum ≥98.0%, Mw 158.09, C₆H₅P(O)(OH)₂, was obtained from Sigma Aldrich in powdered form.

p-Toluenesulfonic acid monohydrate (HpTS) - ACS reagent, ≥98.5%, Mw 190.22, CH₃C₆H₄SO₃H · H₂O, was obtained from Sigma Aldrich in powdered form.

Dodecylbenzenesulfonic acid solution (HDBS) - 70 wt. % in isopropanol, Mw 326.49, C₁₂H₂₅C₆H₄SO₃H, was obtained from Sigma Aldrich.

Phosphoric acid - 85 wt. % in H₂O, 99.999%, Mw 98.00, H₃PO₄ was obtained from Sigma Aldrich.

Glacial acetic acid – Mw 60.05, CH₃CO₂H was obtained from Sigma Aldrich.

Hydrochloric acid (HCl) - ACS reagent, 37%, Mw 36.46, HCl, was obtained from Sigma Aldrich.

Ammonium hydroxide solution - 5.0 N in H₂O, Mw 35.05, NH₄OH, was obtained from Sigma Aldrich.

Copper(II) sulfate pentahydrate - ACS reagent $\geq 98.0\%$, Mw 249.69, CuSO₄ · 5H₂O was obtained from Sigma Aldrich.

m-Cresol - reagent grade, 97%, Mw 108.14, CH₃C₆H₄OH, was obtained from Sigma Aldrich.

Ethanol - 99.8+% (GLC) Analytical Reagent grade was obtained from Fisher Scientific.

1-Methyl-2-pyrrolidinone (NMP) - biotech. grade, $\geq 99.5\%$, Mw 99.13, C₅H₉NO was obtained from Sigma Aldrich.

Iron(II) chloride tetrahydrate - 99.99%, Mw 198.81, FeCl₂ · 4H₂O was obtained from Sigma Aldrich in powdered form.

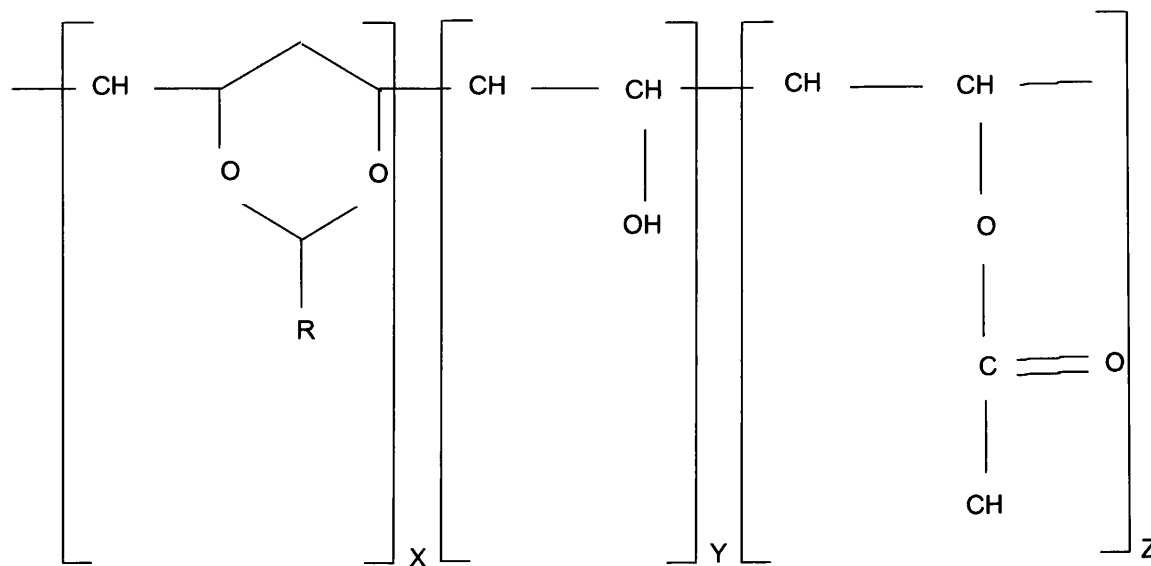
2.2 Preparation of Model Coatings

2.2.1 The Model Matrix

Polyvinyl Butyral (PVB) was chosen as the model matrix material for use within this research for a number of reasons:

1. Allows comparison with previously published results.
2. Can be formulated into a non-toxic liquid of controllable viscosity using ethanol as the solvent material, and is ideal for casting and painting.
3. Consists of hydrophilic and hydrophobic monomers, so has good adhesion to both metallic and non-metallic substrates.
4. Optically transparent (important property for chapter 3).

A full illustration of the molecular structure of PVB is shown within figure 2.1.



R = CH₂ – CH₂ – CH₃

X = No. of vinyl acetal groups

Y = No. of vinyl alcohol groups

Z = No. of vinyl acetate groups

Figure 2.1. Chemical structure of PVB

2.2.2 Preparation of Model Composite Coatings

The inherently conducting polymer polyaniline exists in a number of different redox states and acid base equilibria as shown in chapter 1, section 1.7.1. Powdered PANi-EB was suitable for use as a pigment as purchased. The creation of conductive emeraldine salt pigments (PANi-ES) of phenylphosphonate, camphorsulfonate and phosphate requires protonation of the PANi-EB with at least a stoichiometric quantity of the dopant acid. The method of pigment production is as follows:

- The stoichiometric quantity of dopant required to protonate a specified amount of PANi-EB is calculated, and the amount of dopant required is dependant upon the Mw of the specific dopant acid.
- A ten fold excess of the dopant acid is dissolved in ethanol and the PANi-EB is added to create a particulate dispersion that is stirred via magnetic stirrers for 24hrs to allow full protonation of the PANi causing it to change from the blue non-conductive state to the dark green conductive state.
- The PANi-ES particulates are thoroughly washed by repeated centrifugation through distilled water, which is repeated until a neutral pH is achieved.
- PANi-ES particulates are allowed to dry at room temperature over night before crushing in a pestle and mortar to create PANi-ES of the dopant anion.

Simple two-part model composite coatings consisting of powdered polyaniline (PANi) and a polymer matrix were formulated by dispersing the required quantity of PANi in an ethanolic solution (15.5% by weight) of PVB. The PANi was precisely weighed out into an airtight glass container and a small (~3ml) quantity of ethanol added to form a slurry/paste. To encourage rheological homogeneity within the slurry/paste, an ultrasonic bath was utilised to further breakdown any remaining agglomeration. The ethanolic solution of PVB was then added, and thorough dispersion of the PANi particulates was achieved via shear mixing for approximately fifteen minutes prior to coating application. Model coatings created during this work

vary in pigment loading from 0 to 0.30 pigment volume fraction (Φ), which can be calculated from equation 2.1.

$$M_{pig} = \frac{\phi \cdot M_{pol} \cdot \rho_{pig}}{(1 - \phi) \cdot \rho_{pol}} \quad (\text{Equation 2.1})$$

Where: M_{pig} = mass of pigment
 M_{pol} = mass of polymer (PVB)
 ρ_{pig} = Density of the pigment
 ρ_{pol} = Density of the polymer
 Φ = Volume fraction of pigment

The values used experimentally for the calculations of pigment volume fractions through equation 1 for PVB [1] and PANi-ES [2] are:

$$\rho_{PVB} = 0.8 \text{gcm}^{-3}$$
$$\rho_{ES} = 1.36 \text{gcm}^{-3}$$

Model coatings where the inhibitory component is an organic acid, as in the case of acid etch primers are formulated following the method of Coleman et al [3]. Quantities of organic acid were calculated as a weight percentage, prior to dissolving in a small (<2ml) quantity of ethanol. Ethanolic PVB prepared following the method of section 2.2.1 was added to the ethanolic acid solution and mixed for ten minutes using a high shear mixer.

2.2.3 Preparation of Polyaniline (PANi) Casting Solutions

PANi-EB casting solutions are made by dissolving the Mw 5000 polyaniline powder in n-methylpyrrolidinone, in which it is readily soluble. PANi-ES casting solutions of varying dopants are made by fully dissolving PANi-EB within M-Cresol before adding an exact stoichiometric quantity of the dopant acid to the solution and stirring with magnetic stirrers for 48hrs. Any PANi-ES that precipitates out of solution due to the protonation reaction is removed by centrifugation before solution casting. This is

the case for phenylphosphonate, para-toluenesulfonate, camphorsulfonate and dodecylbenzenesulfonate.

2.2.4 Preparation of Coated Substrates

2.2.4.1 Casting of Composite Dispersions

Substrates coated with composite PANi – PVB coatings were prepared by bar casting the dispersions directly onto the substrate surface, using 120 μ m thick PVC tape as a height guide. This process is illustrated within figure 2.2 (a), where the thin adhesive tape is applied only for the production of cathodic delamination samples. The thickness of the PVC height guide tape allows a dry film composite coating thickness of $30 \pm 5\mu$ m to be achieved.

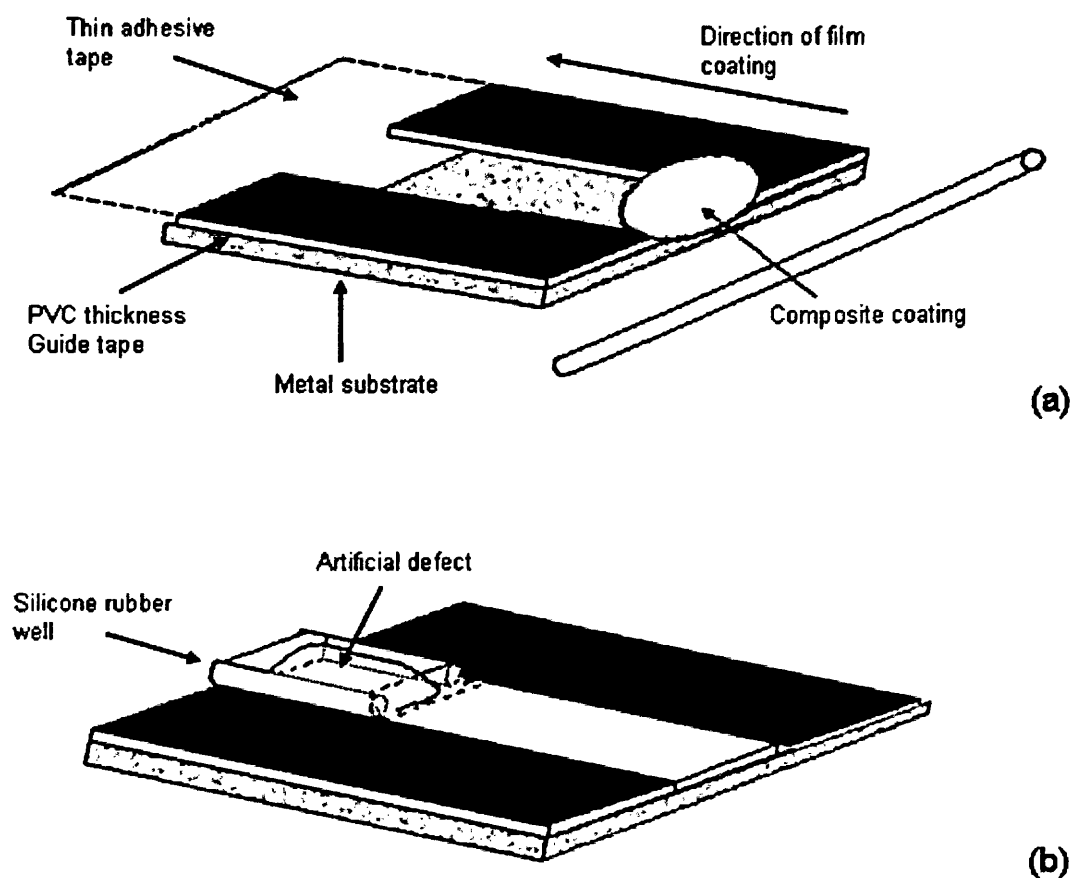


Figure 2.2. Bar coating method, (a) Bar coating to create organic film and (b.) final stage of sample preparation for cathodic delamination test.

To create a cathodic delamination test sample as shown in figure 2.2 (b), firstly a 15mm by 50mm strip of clear adhesive, static-free tape was laid down adjacent to one substrate edge. Following this, two strips of the PVC tape are laid down at right angles to the adhesive tape leaving a strip of *ca.* 2cm of bare metal in the centre of the substrate. The organic coating is subsequently drawn across the substrate surface using the glass bar, over the thin adhesive tape, and the ethanolic component allowed to evaporate. An artificial coating defect is then created following the method of Stratmann et al by cutting a section of the thin static free tape (approximately 20 x 10mm) and lifting the residual lip [4]. The lip is coated with the organic layer,

forming a convenient barrier between the intact polymer-coated metal surface and the defect area to which electrolyte is subsequently applied, as shown in Fig 2.2 (b). To complete the organic defect and fabricate an electrolyte well, non-corrosive silicon sealant obtained from RS Components Ltd is used, as also depicted within figure 2.2 (b).

Substrate preparation used throughout this work varies depending upon material properties and specific experimental requirements. All pure metal substrates used for SKP sample preparation were keyed using 1200 grit metallographic paper in a single direction. Final preparation was achieved by washing with deionised water and final degreasing using ethanol. Thinly metallic coated substrates were prepared by alumina polishing using a 5 μ m aqueous alumina paste to remove surface contaminants, followed by washing with deionised water prior to final degreasing and drying using ethanol. Glass substrates used for conductivity testing of composite coatings within chapter 3 were prepared by degreasing and cleaning using acetone.

2.2.4.2 Application of Homogeneous Polymer Micro-Films

Metal substrate preparation used in conjunction with PANi casting solutions follow exactly the same surface preparation as described previously in the case of composite coatings. Once the 1200 grit surface has been fully degreased using ethanol and dried, the PANi casting solution is applied to the substrate surface using a dropping pipette. Samples are heated using a hotplate to approximately 50°C and the polymer solution is drawn out evenly across the substrate surface using a glass bar.

Non-metallic substrates undergo full cleaning and degreasing using ethanol prior to application of the polymer solution via dropping pipette. The substrates are heated using a hotplate at 50°C to aid solvent removal and the solution is drawn out evenly across the substrate surface using a glass bar.

2.3 The Scanning Kelvin Probe (SKP) Technique

Extensive use has been made of the SKP throughout this research to study electrode potentials underneath organic coatings. The SKP has been utilised primarily to monitor under-coating corrosion phenomena originating from coating defects on organically coated metal substrates. The most common corrosion phenomenon that the SKP is used to investigate within the studies presented here is the cathodic disbondment of organic coatings adherent to 50 x 50mm square metallic substrates. Under-coating anodic disbondment (filiform corrosion) of Zn-Al-Mg alloy coated steel (Magizinc) has also been investigated using the SKP on 50 x 50mm square samples.

2.3.1 The Scanning Kelvin Probe Apparatus

The history and general theory of the SKP is explained in detail within section 1.8. The SKP apparatus used within the studies outlined here is complex, and it is the intention of this section to highlight the key features associated with its design. Figure 2.3 is a schematic diagram showing the major components of the SKP apparatus, and the main feature shown is the vibrating reference probe tip. This consists of a 125µm diameter gold wire (flat ended) that is vibrated normal to the sample surface. The vibrating reference probe assembly is mounted in a fixed position above the test sample. The size of the test samples that can be investigated within the SKP used here are restricted. Sample dimensions of 50 x 50mm are most commonly chosen, and a scanning area within 15mm² across the sample surface is used, determined by the diameter of the gold wire probe used and the achievable scanning rate.

The vibrating reference probe assembly is mounted in a fixed position above where the sample is positioned. The stage that the sample sits on is mobile and allows the position of the sample to change below the probe tip in a step-wise manner, and provides the scanning capability of the machine.

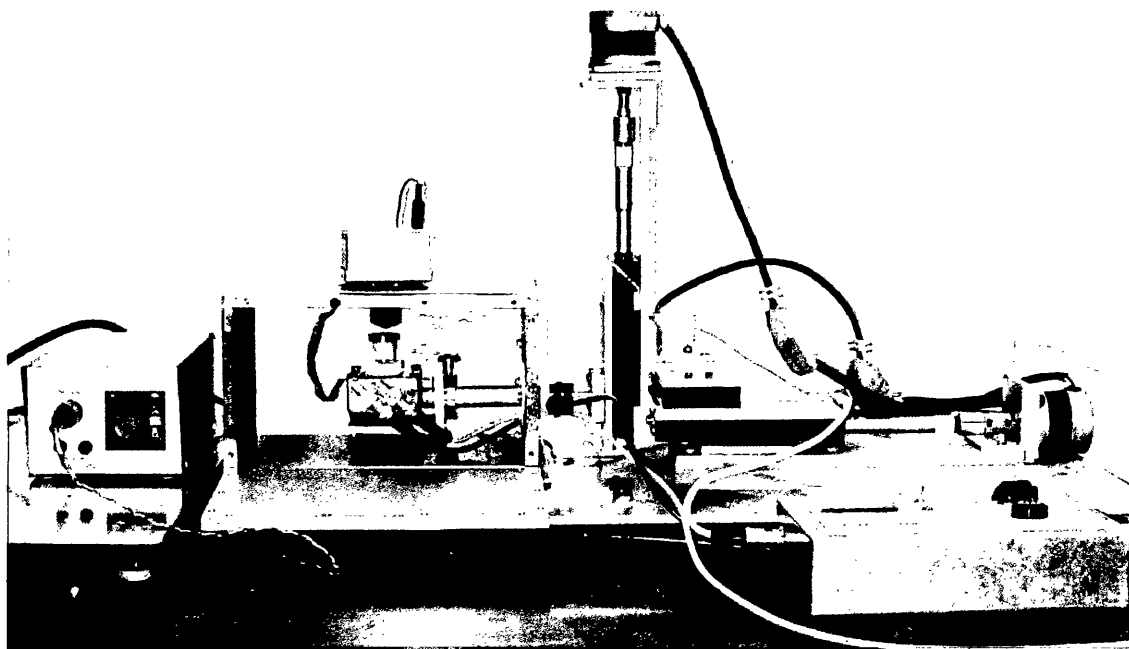
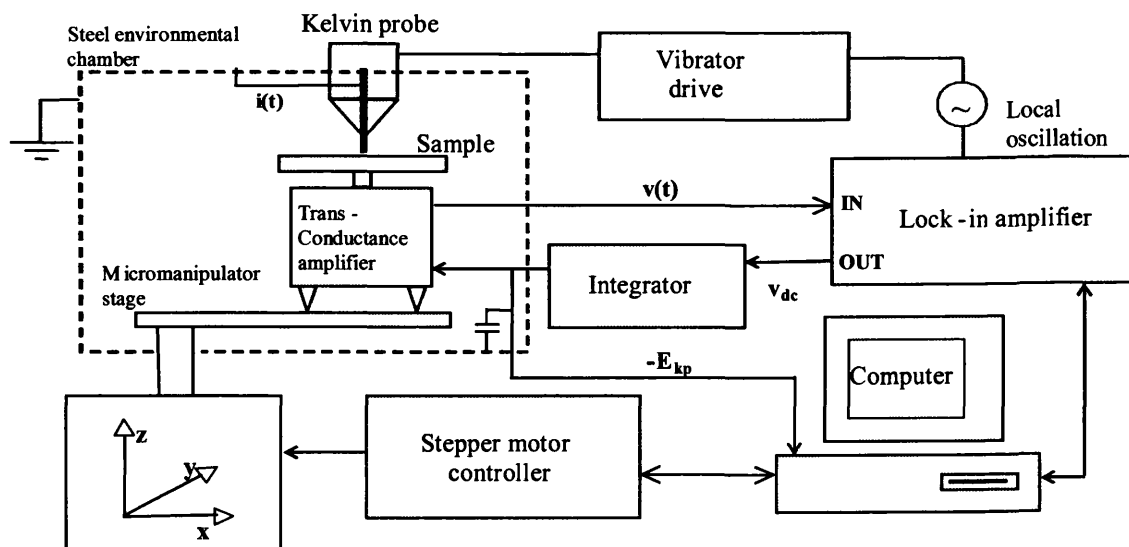


Figure 2.3. Components and photograph of the SKP.

The experimental arrangement is such that the tip of the reference probe is held at earth potential and positioned inside a stainless steel environment chamber (also at earth potential). Positioning and scanning of the test sample is carried out using a micromanipulation stage consisting of three orthogonally arranged x,y,z stepper motor driven linear bearings (Time and Precision Ltd). The optimum height of the probe tip is 100 μ m above the sample surface and measurements are performed by the generation of an ac current in the external circuit connecting the sample and vibrating probe. This then becomes amplified and converted into an ac voltage signal using a

dc-biased transimpedance amplifier circuit. This ac voltage signal is detected using a lock-in amplifier (Perkin Elmer model 7260). The dc output of the lock-in amplifier is transmitted to a feedback system based on an integrator circuit which controls the dc bias (applied to the sample via the transconductance amplifier so as to automatically null the current). Under null current conditions the value of $-E_{KP}$ is equal to the local Volta potential difference existing between the reference probe and the sample surface when the bias voltage is zero. SKP reference probe vibration amplitudes were checked stroboscopically using a microscope and graticule. Probe scanning and data logging are all carried out automatically via computer control.

The SKP reference tip is shown within figure 2.4 where it can be seen that the $125\mu\text{m}$ gold wire is housed within a tapered glass capillary tube and 5mm of the wire protrudes from the tapered end. It is this protruding section of wire that acts as the reference tip, and is sealed in place using epoxy resin (manufactured by Dunlop). The reverse end of the capillary tube is attached to a 50mm actuator (loudspeaker), which in turn is linked to the vibrator drive to provide the required oscillation. The tapered capillary that houses the gold wire reference probe is contained within a copper shroud and connected to an electromechanical actuator. The minimum distance between the probe and sample is typically $100\mu\text{m}$ and the vibration amplitude in the range of $\pm 20\mu\text{m}$.

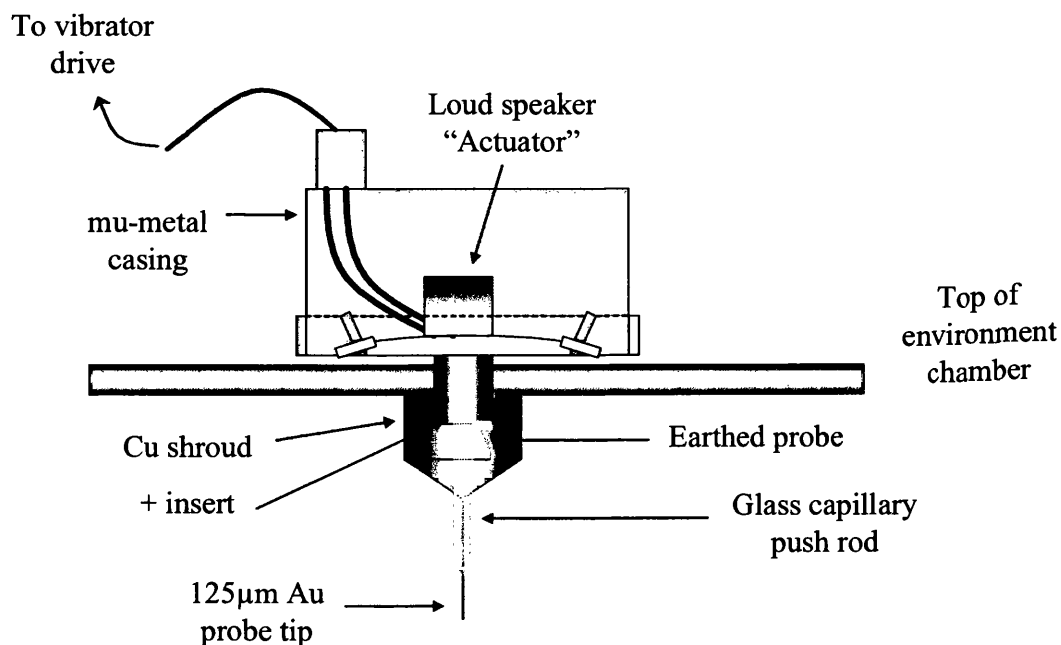


Figure 2.4. Schematic diagram showing the design of the SKP reference tip assembly.

The actuator vibrates the Kelvin probe tip in a plane normal to the sample surface in a purely vertical direction. The amplitude and frequency of vibration depend on the characteristics of the waveform used to drive the mechanical elements [5]. The actuator used throughout these studies is driven at a frequency of 280Hz supplied by the oscillator function of the lock-in amplifier. The actuator is located outside of the environment chamber to ensure effective electrostatic and magnetic shielding.

In addition to the main areas of the SKP already mentioned, the integrator is an important part of the external electronic circuitry. This receives the dc output from the lock-in amplifier and is a feedback system based upon an integrator circuit. It adjusts the dc bias applied to the sample via the transconductance amplifier so as to automatically null the ac current in the external circuit ($i(t)$). The magnitude of the reverse bias (equivalent to $-E_{KP}$) applied via the integrator is measured and converted to a digital signal by the lock-in amplifier and logged by the computer.

2.3.2 Calibration of the SKP

The SKP is calibrated in terms of electrode potential using Ag/Ag^+ , Cu/Cu^{2+} , Fe/Fe^{2+} and Zn/Zn^{2+} redox couples according to a well established calibration procedure [6]. The cells used for calibration were fabricated by machining wells in discs of the relevant metal. These wells were then filled with 0.5 mol dm^{-3} of the respective metal chloride (aq), in the case of Cu, CuSO_4 was put inside the well. Volta potential difference values (E_{KP}) are obtained for each system by positioning the SKP tip to a position of $100\mu\text{m}$ over the metal chloride solution and subsequently obtaining an electrode potential value. Plotting the obtained E_{corr} vs. SHE values for each of the four systems in the order (from left to right) Zn/Zn^{2+} , Fe/Fe^{2+} , Cu/Cu^{2+} and Ag/Ag^+ produces a linear plot as shown in figure 2.5. When considering systems containing polymers, the polymer layer needs to be taken into account. This is achieved by undertaking a further calibration where a layer of the polymer film is placed above, but in contact with the corresponding aqueous salt as illustrated in figure 2.6. To undertake these calibration measurements using the four different metals, the salt solutions are allowed to equilibrate with the metal for a period of 3 hours and the SKP tip is maintained at a distance of $100\mu\text{m}$ from the polymer – air interface. The higher of the two lines in figure 2.5 is $\Delta\psi_{\text{pol}}^{\text{ref}}$ vs. E_{corr} for metal-solution-polymer-air system and the lower line is $\Delta\psi_{\text{sol}}^{\text{ref}}$ vs. E_{corr} for metal-solution-air system. Within experimental error the slope of both sets of data is 1, and the values of A and B obtained from the intercepts are 0.555 and 0.330V respectively. The 0.225 V difference between the observed values is attributed to the difference between the dipole potentials $\chi_{\text{gas}}^{\text{pol}}$ and $\chi_{\text{gas}}^{\text{sol}}$.

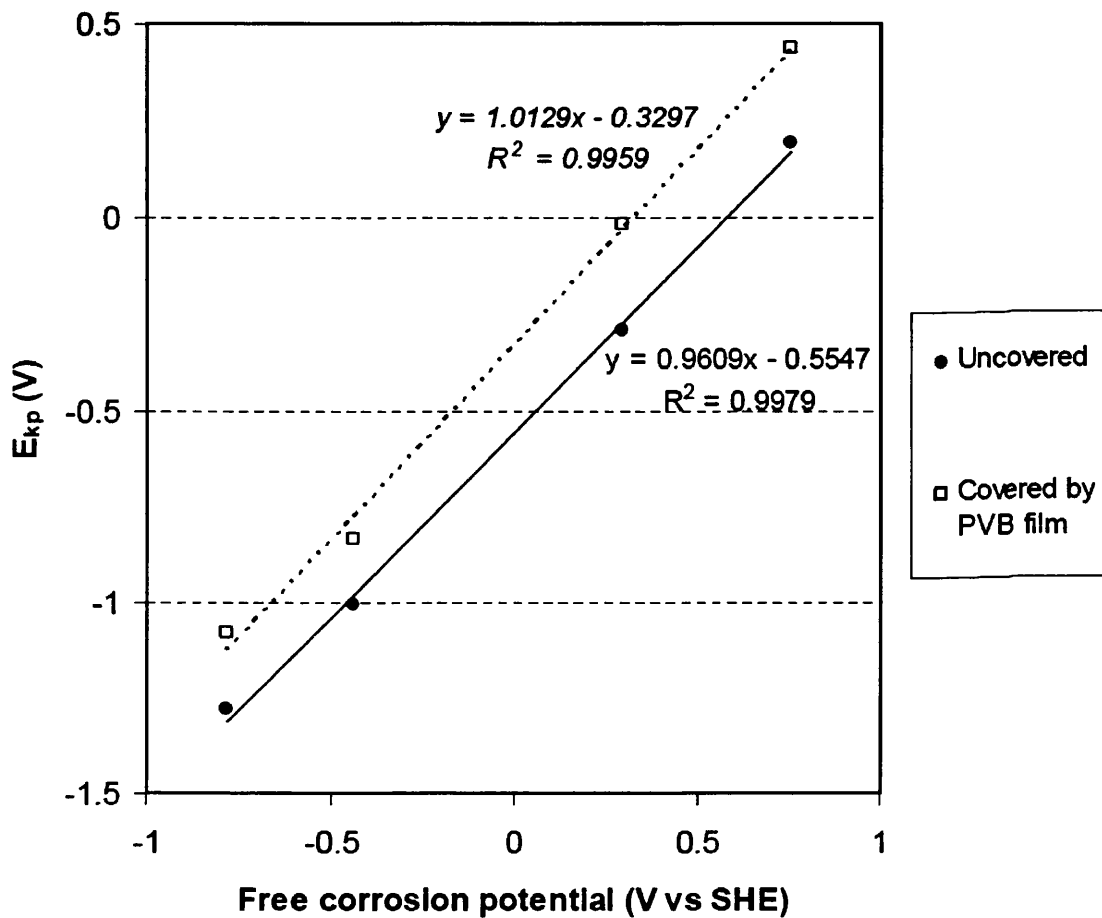


Figure 2.5. Kelvin probe calibration using M/Mn^+ redox couples.

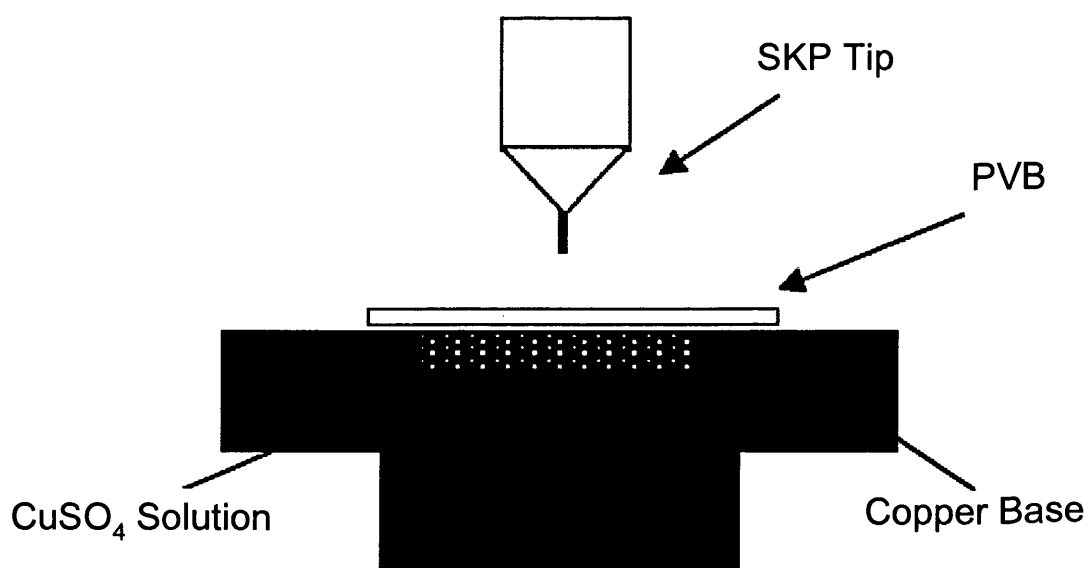


Figure 2.6. Typical setup of SKP calibration cell.

The electrode potentials recorded by the SKP during scanning of the cathodic disbondment and filiform samples studied throughout this research project require calibration before use as meaningful data. Calibration of the SKP on a daily basis was conducted using the Cu/Cu²⁺ redox couple following section 1.8.1. A value for the E_{corr} of Cu is known to be 298mV. It is the value of the Cu/Cu²⁺ couple that is liable to change over time and is used to calculate the calibration value that is subsequently added to each data point recorded by the SKP. Once the value Cu/Cu²⁺ $\Delta\psi_{sol}^{ref}$ is recorded by the SKP it is put into equation (Equ.2.2). As an example to use within the calibration equation (Equ.2.2) it is assumed that a reading of -200mV is recorded by the SKP over the Cu/Cu²⁺, and it follows that:

$$298 = -200 + \text{Constant} \quad (\text{Equation 2.2})$$

$$498 = \text{Constant}$$

A layer of PVB lies between the metal substrate and the SKP tip during the cathodic delamination experiments and filiform experiments and this is to be taken into account to calculate an accurate value of E_{KP}. This is achieved by subtracting the 0.225V (difference between the dipole potentials χ_{gas}^{pol} and χ_{gas}^{sol}) from the calculated value, which in this instance gives 273mV (0.273V vs. SHE). This value is to be added to each individual data point recorded through that individual experiment in order to provide an accurate reading of the under-film potential (E_{KP}).

2.3.3 SKP Studies of Cathodic Disbondment

The preparation of Stratmann-type cathodic delamination test samples as investigated here has been fully described within section 2.2.4. Sample geometries were constantly 50 x 50 mm square for ease of handling within the SKP apparatus. Metal substrate gauges (thicknesses) for cathodic disbondment were uniformly $\geq 1.5\text{mm}$ for ease of sample preparation and testing due to them being less likely to bend under sample preparation. This aids experimental accuracy due to scanning nature of the SKP technique requiring a flat uniform surface. For cathodic delamination testing of organic coatings adherent to metallic substrates the SKP is set up to scan at a height of $100\mu\text{m}$ along a line normal to and contiguous to the defect coating boundary. Under film electrode potentials were scanned at $50\mu\text{m}$ intervals over a 12mm scan length from the intact coating – artificial defect boundary. Throughout all cathodic delamination experiments the experimental humidity was maintained at approximately 96% using a reservoir of 0.86 mol dm^{-3} (5% w/v) aqueous NaCl reference solution. Additionally 0.86 mol dm^{-3} (5% w/v) aqueous NaCl reference solution was applied to the artificial coating defect to initiate cathodic disbondment.

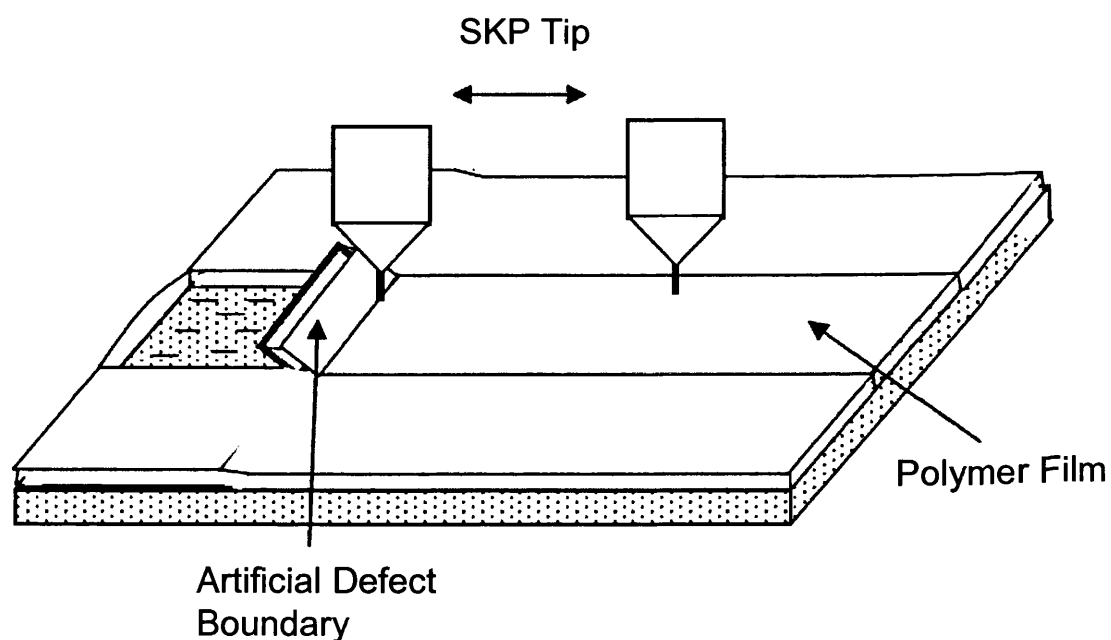


Figure 2.7. Illustration of the SKP scan area during the monitoring of cathodic delamination from an artificial defect.

2.3.4 SKP studies of Filiform Corrosion (FFC)

Within this research project the SKP is used to monitor a form of filiform corrosion (FFC) found to occur on commercial Zn-Al-Mg (Magizinc) alloy galvanised steels. This study of FFC involves the use of two different sample designs, and in common for each technique is the substrate preparation method. As already described in section 2.2.4, the sample preparation of the galvanised Magizinc surface is a process of polishing with 5 μ m alumina to remove surface contaminants prior to degreasing and drying with ethanol. Throughout this study only non-inhibited PVB is used as an organic coating on Magizinc substrates, and is bar coated onto the substrate using PVC tape as a thickness guide to create a $30 \pm 5\mu$ m thick dry coating thickness (described in section 2.2.4).

The initial experimental design leading to the discovery of FFC on Magizinc substrates was through the creation of cathodic disbondment samples following the method described in section 2.2.4. The Magizinc metallic coating in the artificial defect region was stripped away by immersion in concentrated HCl for approximately 5 seconds. Corrosion within the artificial defect was initiated with 0.86 mol dm⁻³ (5% w/v) aqueous NaCl reference solution and high experimental humidity as in section 2.3.3.

The conventional sample design for FFC involves the creation of a 10mm scribe penetrating through the organic layer, which is subsequently inoculated with a corrosive electrolyte. Such samples have been created for use in the study of Magizinc presented here. Additionally, samples of the same design have been investigated with various corrosive electrolytes applied to 10mm scribe defects that are deep enough to penetrate both the organic layer and the metallic layer. Experimental conditions used in the study of FFC on Magizinc are numerous, and accordingly detailed accounts of the exact experimental design and conditions are explained in detail with chapter 6 at the relevant time. The SKP is utilised to produce electrochemical maps of the under-film potentials across the sample surface resulting from the FFC.

2.4 Time Lapse Digital Photography of Cathodic Delamination

The time lapse digital photography of homogenous polyaniline microfilms adherent to iron substrates was undertaken following the method of Gabriel et al [7]. Polyaniline microfilms were cast following the method described in section 2.2.4, and over-coated with a $30\pm 5\mu\text{m}$ transparent PVB coating via bar coating. Experimental apparatus included a Canon Powershot G6 digital camera combined with an external macro-lens. The camera lens was in approximately 20cm above the sample surface. In common with all cathodic delamination experiments the experimental humidity was maintained at approximately 96% using a reservoir of 0.86 mol dm^{-3} (5% w/v) aqueous NaCl reference solution. This high level of relative humidity was maintained by encapsulating the test sample with an optically clear glass covered Petri-dish. The bottom of the Petri-dish had a thin ($\geq 1\text{mm}$) layer of reference solution, over which the test sample was mounted.

2.5 Secondary Ion Mass Spectrometry (SIMS)

SIMS analysis was carried out using a Millbrook Instruments Mc300 (MKII) bench mounted Chemical Microscope fitted with a Gallium (Ga^+) ion source. A lateral resolution of $10\mu\text{m}$ and a mass resolution of ± 0.1 Daltons were used. SIMS is used throughout this research project for a number of different tasks:

- Analysis of surface species.
- Surface oxide/salt film depth measurements.
- Image mapping of corrosion phenomenon.

Analysis of the surface species present on a metallic substrate is important in determining the nature and cause of the surface layers after mechanical removal (peeling) of an organic coating system.

Depth measurements of surface oxide/salt films created by interaction with active coating systems are conducted by bombarding the oxide covered metal surface using the SIMS ion source. The SIMS is programmed to detect the concentration of certain species that are expected to reside as part of the surface layer, such as O^{2-} . The

removal of surface layers that results from ion bombardment, combined with the detection of the O^{2-} ion current allows the accurate determination of surface layer thickness resulting from coating applications when depth measurements are calibrated using an atomic force microscope. Additional uses of SIMS within this work involve applying the technique to provide elemental mapping of substrate surfaces to aid in the elucidation of corrosion mechanisms.

Many of the applications of SIMS throughout this work require the removal of organic coating layers. This is achieved by mechanically peeling away the organic layer from the substrate surface. In cases where under-film corrosion products are to be removed as well, the sample is subject to sonication in distilled water prior to ethanolic solvent drying.

2.6 Atomic Force Microscope (AFM)

AFM work was undertaken using a depth calibrated Topmetrix Explorer atomic force microscope with a standard configuration as shown in figure 2.8. The AFM was used to scan $100 \times 100 \mu\text{m}$ sample surface areas. The primary application of atomic force microscopy throughout this project is the accurate depth measurements of:

- (a) Corrosion features.
- (b) SIMS sputtering craters.
- (c) Micro-layer film thicknesses.

Micro-layer film thickness measurements were undertaken by using the AFM to measure the difference in height between a sample surface and the polymer layer surface. Accordingly scribes were made in the polymer layers using a material softer than the underlying substrate to create a sharp demarcation between the polymer surface and the underlying substrate. The average of five calibrated depth measurements was recorded as the polymer micro-layer thickness in each case.

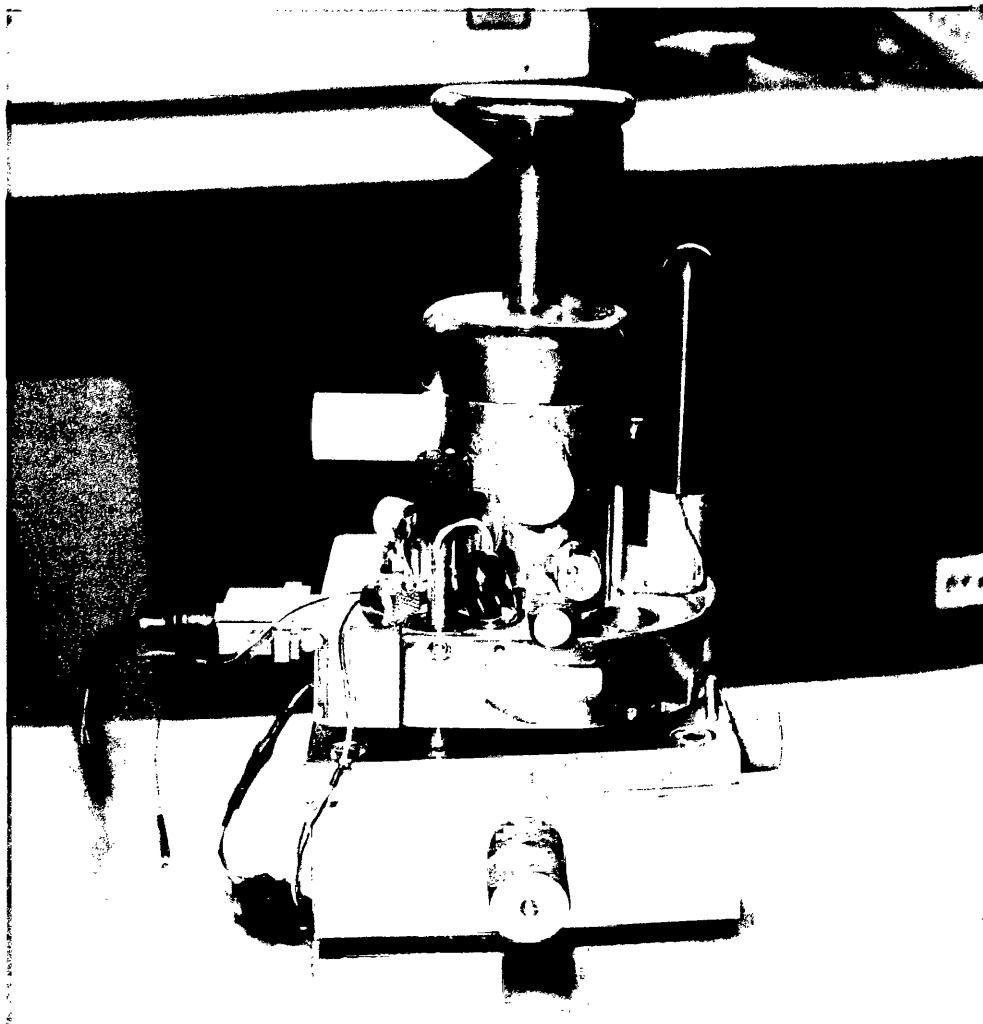


Figure 2.8. Topometrix Explorer Atomic Force Microscope.

2.7 UV-VIS Absorption Measurements

Throughout the duration of this project a Perkin Elmer Lambda 1 UV-VIS Spectrophotometer was used for all UV-VIS absorption measurements. A photo of the machine used is shown in figure 2.9, and this technique was for a number of applications:

- (a) Determination of homogeneous polyaniline layer thicknesses.
- (b) Measurement of polyaniline re-oxidation kinetics in atmosphere.

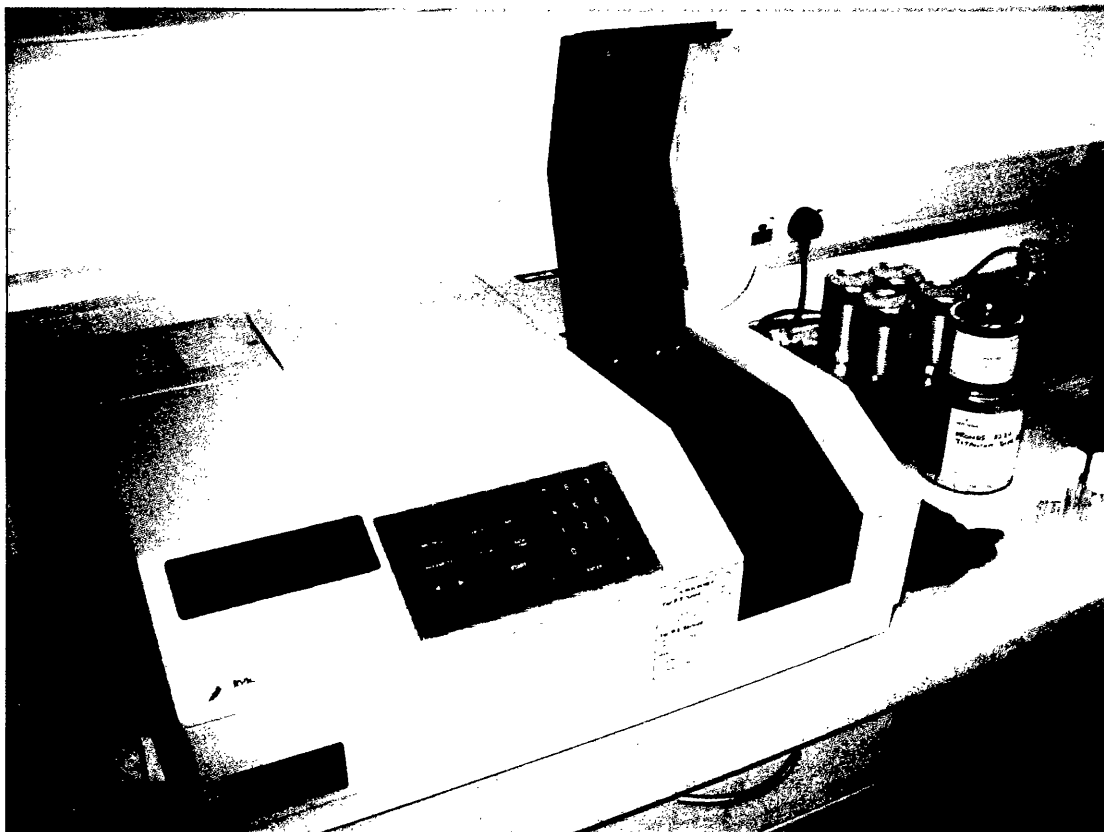


Figure 2.9. Perkin Elmer Lambda 1 UV-VIS Spectrophotometer.

2.8 Four Point Conductivity Measurements

Polyaniline composite coatings were applied to glass microscope slides following the method described in section 2.2.4 (a) to produce a coating thickness of approximately $30 \pm 5 \mu\text{m}$. Gold electrode contacts were applied to the coating surface via vapour deposition using an Edwards vapour deposition machine under vacuum conditions. The electrode positions on the sample surface are shown schematically in figure 2.10. Controlled potentiodynamic measurements of through-coating current were made using an EG&G 263A Potentiostat/Galvanostat. The applied voltage was applied potentiodynamically from -1 to 1V, and the resulting I-V plot was linear indicating an Ohmic relationship. The calculated resistance value was converted to conductivity via equations 3 – 5.

$$V = IR \quad (\text{Equation 2.3})$$

$$\text{Resistivity} = \frac{R \times \text{Area}}{\text{Length}} \quad (\text{Equation 2.4})$$

$$\text{Conductivity} = \frac{1}{\text{Resistivity}} \quad (\text{Equation 2.5})$$

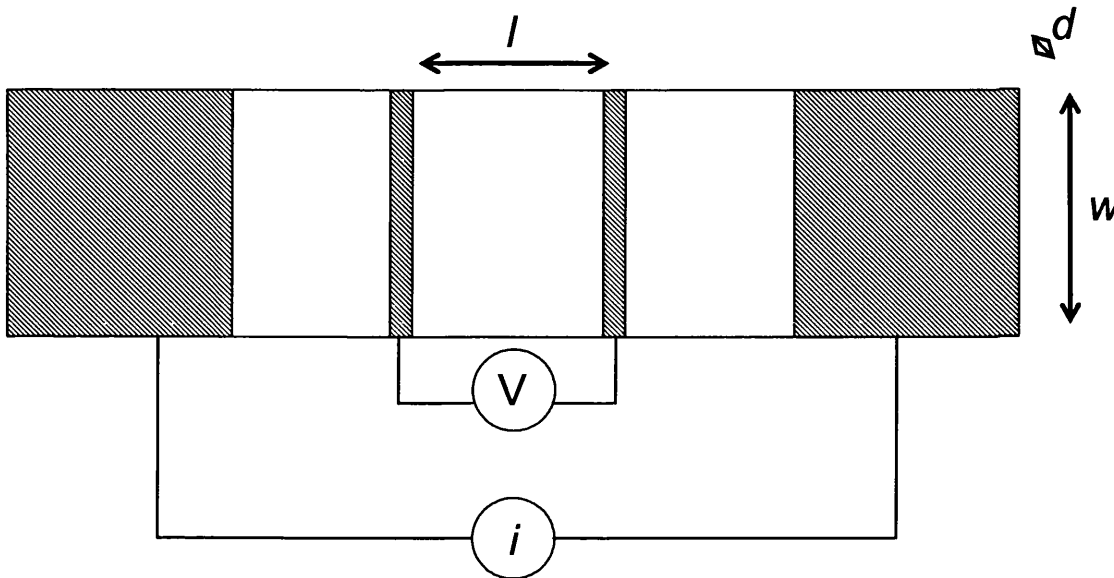


Figure 2.10. Schematic diagram of 4-point conductivity test sample design.

2.9 Metallographic Preparation of Magizinc Substrates

Hot dip Zn-1.5%Al-1.5%Mg coated steel panels obtained from Corusgroup were prepared for microscopic evaluation by metallographic polishing with 1 μ m diamond paste. Images through the height cross-section of the metallic coating were obtained by removing the coating layer by varying amounts. A gradual change in amount of metallic coating removed from the bare steel surface through to the metallic coating surface was achieved by polishing the substrate at an angle as illustrated in figure 2.11.

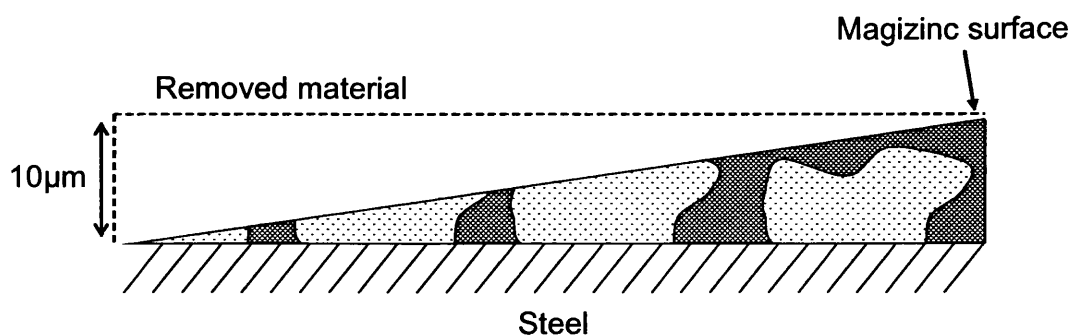


Figure 2.11. Illustration of metallographic preparation to reveal Magizinc microstructure as a function of distance from the steel surface.

Following metallographic polishing the Magizinc microstructure was revealed by etching for a short period of time with dilute Nital. Optical microscopy was undertaken using a Meiji light microscope and image recording using an adapted Nikon Coolpix Digital Camera.

2.10 Electrochemical Reduction of Polyaniline Micro-films

Optically transparent glass slides with a high conductivity ITO surface layer were purchased from Dyesol, and coated with polyaniline emeraldine salt (PAni-ES) by the method outlined in section 2.2.4 (b). Coated slides were connected to an EG&G 263A Potentiostat/Galvanostat and immersed in 0.86 mol dm^{-3} (5% w/v) aqueous NaCl electrolyte. To reduce the PAni-ES to leuco base (PAni-LB), a potential of -0.20V vs. SCE was applied. Full reduction of the PAni-ES to PAni-LB was demarked by a visible colour change from green PAni-ES to optically transparent PAni-LB.

2.11 Scanning Electron Microscope

Micrographs were taken using a Phillips XL30CP scanning electron microscope. The SEM was employed here to investigate the microfilm quality and surface topography of cast polyaniline films adherent to highly polished single crystal silicon substrates. Various levels of magnification were required and images were taken using the on-board digital camera.

2.12 Fabrication and Performance Testing of Hybrid Solar Cells

Highly polished phosphorous doped n-type single crystal wafer of 700 μm thickness (pure wafer) was cut into 30 x 30mm square sections and cleaned/degreased using acetone. A 1 μm layer of Ni was Vapour deposited to the rear (unpolished) side of the Si substrate to act as a rear electrode material. Ohmic contact between the Ni and Si was created by high temperature annealing within a Jiplec rapid thermal annealing machine (RTA). The temperature within the RTA was set at 400 $^{\circ}\text{C}$ and Ohmic contact between the Si and Ni was achieved after 2 hours exposure. Ohmic contact between the Si and Ni rear electrode material was tested using a HP4142B Kiethley probe station.

The polished surface (epilayer) of the silicon wafer was solution coated with a thin layer of the required conducting polymer by solution casting at 50 $^{\circ}\text{C}$ following the method described in section 2.2.4. The thickness of the polymer films was measured in each case using depth calibrated atomic force microscopy by the method described in section 2.6. After coating, conducting polymer depth of all cells produced was consistently ca. 1 μm thick as recorded individually.

Gold electrical contacts were applied to the surface of the polymer micro-films through a purpose made shadow mask using an Edwards vapour deposition machine. Shadow mask design is shown photographically in figure 2.12, and this design allows the deposition of gold buss bars to provide electrical contact to the top of the cell. A schematic of the completed single organic layer hybrid photovoltaic cell is shown in figure 2.13, where a p-n junction is formed between the polymer micro-film and the Si respectively.

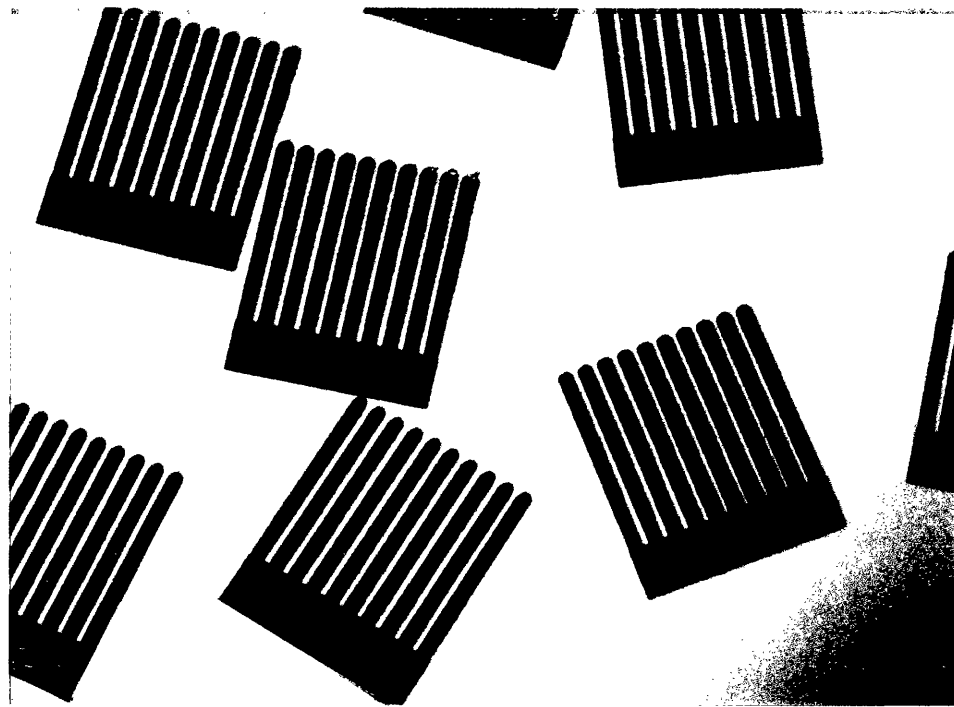


Figure 2.12. Brass shadow masks used to create gold buss bars on photovoltaic cell surface.

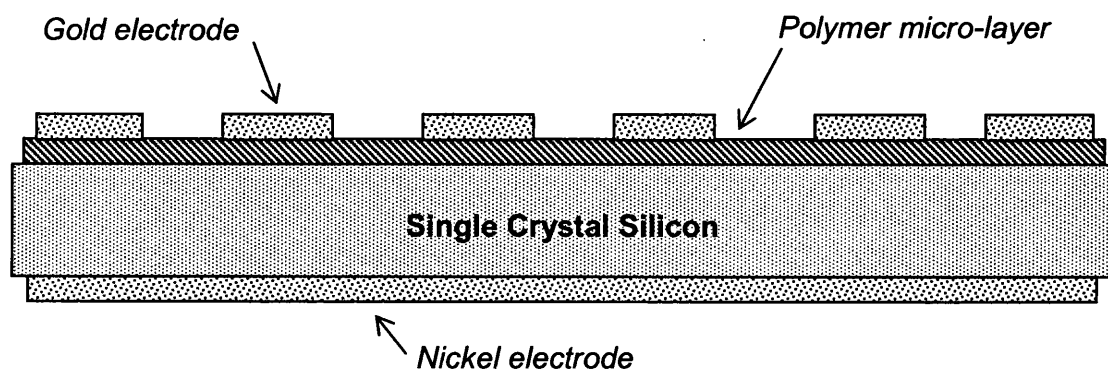


Figure 2.13. Schematic of a single organic layer hybrid photovoltaic cell.

Characterisation of the Photovoltaic cells produced within this study was undertaken using a calibrated Dyesol solar simulator. Cell characterisation involved using the solar simulator to record the I-V curve under calibrated light intensity, allowing calculation of cell parameters.

Crocodile clips were used to achieve electrical contact between the solar simulator and the short electrical wires (PVC equipment wire of 0.22 mm² diameter) used as electrical connection wires that were bonded to the cell electrodes using conducting silver epoxy (RS components Ltd). Light soaking of the hybrid photovoltaic cells was undertaken when required within a calibrated Dyesol light soaker at one sun light intensity.

2.13 References

- [1] H. Dominighaus, *Plastics for Engineers*, Hanser Publications, Munich, 1988.
- [2] J. Stejskal and R. G. Gilbert, *Pure and Applied Chemistry* **74**:857 (2002).
- [3] A. J. Coleman, H. N. McMurray, G. Williams, A. A. Afseth, and G. M. Scamans, *Electrochemical and Solid State Letters* **10**:C35 (2007).
- [4] M. Stratmann, R. Feser, and A. Leng, *Electrochimica Acta* **39**:1207 (1994).
- [5] A. K. Neufield, *American Laboratory* **35**:21 (2003).
- [6] G. Williams and H. N. McMurray, *Journal of the Electrochemical Society* **148**:B377 (2001).
- [7] A. Gabriel, N. J. Laycock, H. N. McMurray, G. Williams, and A. Cook, *Electrochemical and Solid State Letters* **9**:B57 (2006).

Chapter 3

Polyaniline

Micro-films Adherent to Iron

3.1 Introduction

Corrosion-driven coating disbondment[1-4] is a key failure process affecting pre-painted organically coated steel products wherever the metallic substrate becomes exposed at cut edges during manufacturing or through in-service damage. Protection against cathodic disbondment used in commercial pre-painted coating systems is currently provided successfully by strontium chromate. The use of strontium chromate is undesirable due to environmental and health risks associated with its use. This creates an industry wide need to find cost effective, stable and efficient inhibitors of cathodic delamination. This interest in finding alternative technologies to strontium chromate has led to numerous investigations into the possibility of using inherently conducting polymers (ICP's) as replacements. The subject of using ICP's as chromate replacements has been extensively reviewed in the past for non-ferrous metals[5] and ferrous metals[6]. One ICP that has attracted considerable attention in the field of corrosion protection is polyaniline (PAni). PAni has been the focus of many studies with a view of making ICP's commercially viable. In particular it is the emeraldine salt (PAni-ES) prepared by the doping of emeraldine base (PAni-EB) by a Bronsted acid. The choice of dopant has been shown to strongly influence the inhibition efficiency under atmospheric conditions [7].

Some later studies have highlighted the cathodic disbondment inhibiting properties of PAni-ES under atmospheric conditions. Scanning Kelvin probe (SKP) studies have shown PAni-ES to be an extremely effective corrosion inhibitor when applied as a composite coating, i.e. a pigmented dispersion within an organic polymer matrix such as polyvinyl butyral (PVB) on iron and plain carbon steel, and the reasons for this successful inhibition have been proposed extensively [7, 8].

To date a full systematic study into the effects of PAni-ES applied as a homogeneous micro-film as a direct comparison to these dispersion coatings has yet to be reported, although a study into the visual redox changes as a result of cathodic disbondment has been undertaken by Gabriel et al [9]. This takes into account that the different PAni redox states and acid-base states exhibit very different optical absorbance characteristics and hence colours [9, 10] – PAni-ES (green), PAni-EB (blue) and PAni leuco base LB (colourless). Nevertheless, the role of the de-doping and the

precise mechanisms by which PANi acts to inhibit cathodic disbondment remain uncertain.

Inhibition of cathodic disbondment by PANi-ES has only been systematically investigated in the case of composite coatings. Accordingly this study concentrates on looking at homogeneous solid PANi-ES micro-films coated directly onto an iron substrate. An attempt is made to quantify the main differences between solid films and dispersion coatings, i.e. lateral conductivity within the coating and spacing of the polymer. To control the environmental conditions the PANi-ES is subjected to and provide physical integrity to the coating upon delamination, a layer of optically transparent PVB is coated directly on top of the PANi-ES. Under delamination conditions, this transparent top coat allows the various colour changes resulting from PANi state changes to be easily recognised.

Systematic changes in micro-film coating thickness are investigated and the effect towards both intact coating potential (E_{intact}) and the delamination kinetics of cathodic disbondment were recorded using the SKP. Additionally the effect of PANi-ES dopant choice is investigated, where camphorsulfonate (PANi-CSA) doped and phenylphosphonate (PANi-PP) doped PANi-ES are compared directly. Direct comparison between the findings of the micro-films and published data [7] of comparable composite coatings are made. Finally a mechanistic proposal of the PANi-ES dopant dependant inhibition mechanism is made.

3.2 Experimental

A PAni-EB casting solution and PAni-ES casting solutions of camphorsulfonate (PAni-CSA) and phenylphosphonate (PAni-PP) were formulated following the methods outlined in section 2.2.3. PAni-ES solutions were cast directly onto the surface of prepared pure Fe following the method outlined in section 2.2.4.2. To prepare stratmann type delamination cells as described within section 2.2.4.1, PAni-ES micro-films were removed from the region of the artificial defect only. Cathodic delamination samples were completed by the application of a transparent $30 \pm 5 \mu\text{m}$ PVB coating by bar coating over the PAni-ES to create a bilayer coating system following the method of section 2.2.4.1.

The SKP was used to fully monitor the corrosion-driven cathodic disbondment originating from the organic coating defects as described within section 2.3. Time lapse digital photography was also employed to monitor cathodic disbondment following the method described with section 2.4 using a Canon Powershot G6 digital camera. All delamination experiments were carried out in static air at 20°C and approximately 96% relative humidity (RH) in isopiestic equilibrium with a 0.86 mol dm^{-3} (5% w/v) aqueous NaCl reference solution. For corrosion driven coating delamination experiments the sample was first allowed to equilibrate at 96% RH for a period of 6 hours before an aliquot of 0.86 mol dm^{-3} NaCl was applied to create a 1mm thick electrolyte layer at the coating defect (note, not over the coating surface) and initiate corrosion.

PAni micro-film thickness measurements were made using depth calibrated atomic force microscopy (AFM) following the method described within section 2.6. Using the Beer-Lambert law (equation 3.1), the optical absorbance was measured according to PAni-EB film thickness and a value of $2.12 \pm 0.36 \mu\text{m}^{-1}$ was calculated as the PAni-EB absorption coefficient. A UV-VIS Spectrophotometer (section 2.7) was used as an indirect means to measure the micro-film thickness of delaminated PAni-EB coatings at the end of cathodic delamination experiments using the calculated absorption coefficient following equation 3.1. Delaminated PAni-EB films were removed from metal samples and mounted onto glass microscope slides. The optical absorbances of the delaminated films were then recorded using the UV-VIS

spectrophotometer and the peak optical absorbance at 650nm was used to calculate the micro-film thickness.

Lateral conductivity measurements PANi micro-films and PANi-PVB composite coatings were determined using four point conductivity testing as described in section 2.8. Reduction of PANi-ES micro-films in order to determine the rate of atmospheric re-oxidation was achieved following the method described in section 2.10. Green PANi-CSA micro-films were solution cast onto indium tin oxide coated glass and the coating thickness measured directly using the AFM following the method of section 2.6. Coated glass samples were immersed in 100ml of 0.86 mol dm⁻³ (5% w/v) aqueous NaCl electrolyte and reduced to clear leuco base (PANi-LB) by applying a potential of -0.20V vs. SCE. Full deprotonation of the PANi-ES was ensured by adding 1ml of 0.1M aqueous ammonium hydroxide. Upon removal from the electrolyte, the PANi-LB coated sample was immediately mounted in the UV-VIS spectrophotometer (section 2.7). Re-oxidation of the PANi due to atmospheric O₂ was recorded as a function of the increase of optical absorbance at 650nm, indicative of the presence of PANi-EB.

3.3 Results and Discussion

3.3.1 Measurement of Micro-film Thickness

The accurate measurement of homogeneous PANi micro-film thickness is of high importance due to the small differences in coating thicknesses being investigated. PANi micro-film thickness measurements were made directly by atomic force microscope (AFM) or indirectly by measuring the optical absorbance of the delaminated PANi film, and using the Beer-Lambert law (equation 3.1), where d is the PANi coating thickness, A is the optical absorbance and α is the absorption coefficient.

$$d = \frac{A}{\alpha} \quad (\text{Equation 3.1})$$

The UV-VIS spectra of a 0.07 μ m thick homogenous PANi coating is shown in figure 3.1, which shows the UV-VIS spectra of both the emeraldine base (PANi-EB) and emeraldine salt (PANi-ES) states. This data was obtained from the same micro-film, whereby the PANi-ES was deprotonated by immersion in aqueous ammonium hydroxide. Firstly the absorption spectra of the PANi-ES micro-film was recorded, and the same micro-film was then fully de-protonated using aqueous ammonium hydroxide to produce the PANi-EB. Optical absorbance measurements were repeated for the same film in its PANi-EB state. The measured UV-VIS spectra of the PANi-EB is similar those published else where[11-13], as is the UV-VIS spectra of the PANi-ES[10, 14]. The key points on the PANi-EB UV-VIS spectra are the two peak absorbances, one at ca. 325nm (λ_1) and the other at ca. 650nm (λ_{max}) which represent the benzene segments and quinoid segments of the polymer respectively[12]. The value of λ_{max} on the UV-VIS recorded PANi-EB absorption spectra is taken to be the value of absorbance used in calculating the absorption coefficient (α) of the PANi-EB.

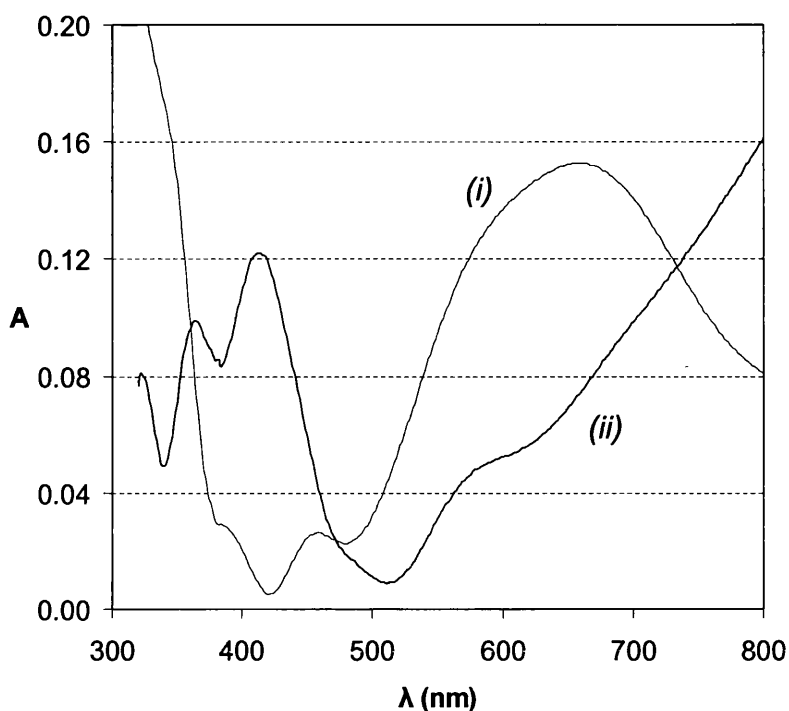


Figure 3.1. UV-VIS absorbance spectrograph of $0.07\mu\text{m}$ thick (i) PANi-EB and (ii) PANi-ES micro-films. λ_{max} PANi-ES = 410nm , λ_{max} PANi-EB = 650nm .

The absorption coefficient of PANi-EB used throughout was calculated directly from calibrated AFM thickness measurements. Optical absorbance spectra of PANi-EB were measured using the UV-VIS spectrophotometer and the peak absorbance at 650nm was used in the absorption coefficient calculation. This was repeated a number of times, figure 3.2, and the calculated absorption coefficient value of $2.12 \pm 0.36 \mu\text{m}^{-1}$ is in the region of those calculated elsewhere[15]. Using this value of the absorption coefficient it has been possible to obtain a value of 1.72 ± 0.23 for the PANi-ES absorption coefficient. Calculation of the PANi-ES micro-film absorption coefficient was undertaken by coating PANi-ES micro-films directly onto glass substrates and recording the PANi-ES absorption spectra. Subsequent deprotonation of the PANi-ES via immersion in 0.1M ammonium hydroxide changed the PANi-ES to PANi-EB of the same coating thickness. This was repeated for each sample to ensure polymer was fully de-protonated by the ammonium hydroxide and to ensure experimental accuracy. To calculate the absorption coefficient of the PANi-ES, the absorption value at $\lambda_{\text{max}} = \text{ca. } 420\text{nm}$ was used in all cases (figure 3.1).

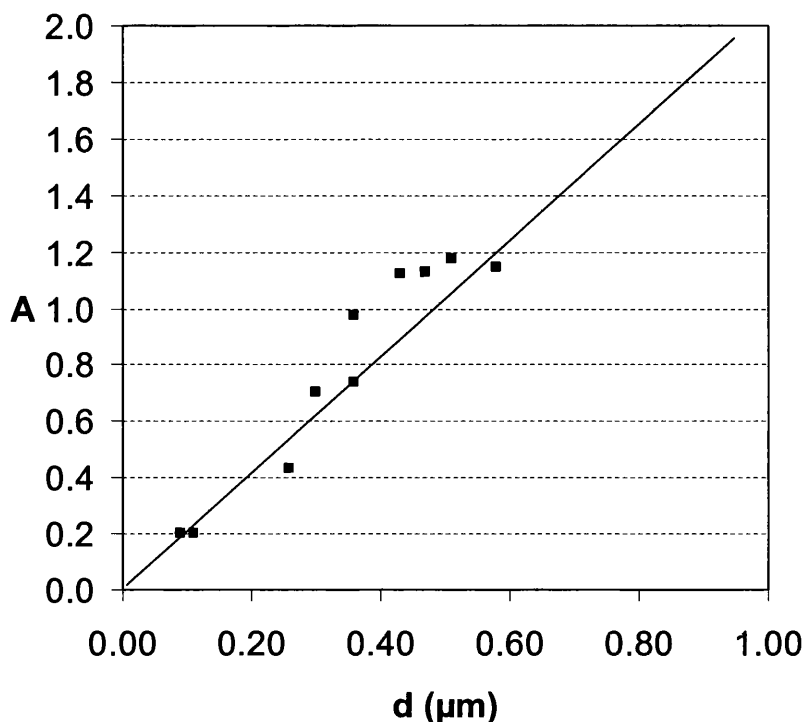


Figure 3.2. Absorption vs. PANi-EB micro-film thickness from coatings of varying thickness on glass microscope slides. Each absorption value is taken from the PANi-EB λ_{max} at 650nm.

Coating thickness measurements of corrosion test samples were undertaken using one of two techniques, either directly by using an AFM, or indirectly by measuring the optical absorbance of the delaminated PANi-EB film. Each of these techniques is of equal accuracy, and so the chosen method of measuring the film thickness is due to convenience depending upon the thickness of the PANi. The AFM is capable of accurately measuring all coating thicknesses, but due to the lengthy measurement process, the technique of recording the absorbance spectra is preferable. Although preferable, recording the absorbance spectra of the delaminated coating was found to be only viable for PANi coating thicknesses of ca. $\leq 1\mu\text{m}$, which is due to the high opacity of the coating. The optical micro-film thickness measurement in each case was undertaken after the corrosion-driven coating delamination has taken place. The delaminated coating (PANi-EB) was mechanically removed in one piece and mounted onto a glass microscope slide from which the UV-VIS absorbance measurement can be readily obtained.

3.3.2 Under-Film Potentiometry

Of particular interest in this study is the effect upon SKP recorded E_{corr} values caused by the PANi micro-films over portions of the sample where the model coating remains adherent to the substrate (E_{intact}). In common with all model coatings tested, the recorded E_{intact} values were substantially uniform over the sample surface, increasing slightly ($<0.1\text{ V vs. SHE}$) as a function of holding time throughout the first few hours within the SKP chamber but remaining constant after this point. This change in E_{intact} with holding time in all cases is an effect of coating humidification under the high relative humidity ($>96\%$) used experimentally within the SKP test chamber. Time dependant E_{intact} values for PANi-CSA and PANi-PP are shown in figures 3.3 (a) and 3.3 (b) respectively. This not only shows the change of E_{intact} potentials due to the initial humidifying of the coating, they clearly show how increasing the PANi-ES coating thickness increases the value of E_{intact} .

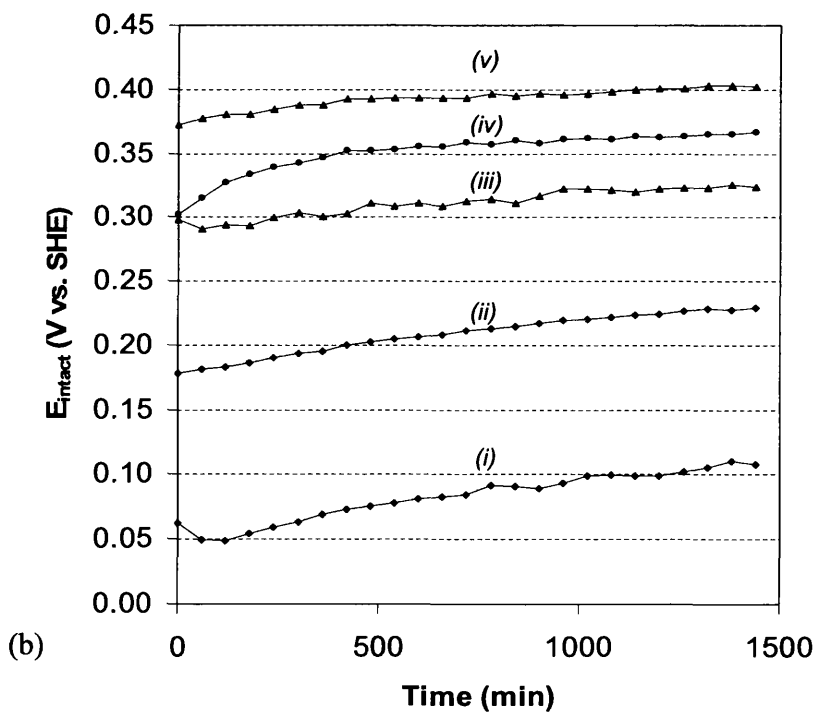
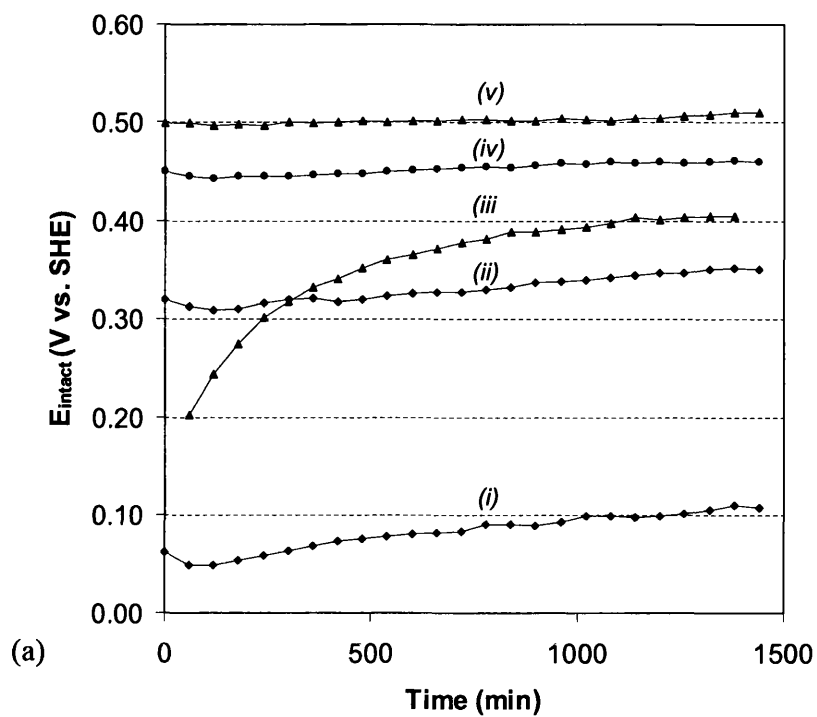


Figure 3.3. E_{intact} vs. time for PANi-CSA micro-films over coated with $30\mu\text{m}$ PVB on Fe, in air at 96% RH and 20°C . (a) PANi-CSA films. Key: d (μm) = (i) 0, (ii) 0.31, (iii) 0.44, (iv) 0.48 and (v) 5.88. (b) PANi-PP films. Key: d (μm) = (i) 0, (ii) 0.16, (iii) 0.33, (iv) 0.49 and (v) 4.49.

As a test of reproducibility, multiple E_{intact} measurements of inert PVB model coatings were undertaken separately. Accordingly an average value of 0.108 +/- 0.018 V vs. SHE is recorded to be the E_{intact} value of model coating systems containing no PANi (control coatings). Studies of the un-protonated, non-conducting PANi-EB solid films of varying thicknesses have shown that E_{intact} neither changes with coating thickness or deviates noticeably from that of PVB coatings (ca.0.108V vs. SHE). Therefore it is proposed that it is the incorporation of dopant anions to the PANi that causes E_{intact} to increase in this manner.

Interactions between PANi-ES micro-films and the Fe substrate surface as a function of PANi-ES micro-film thickness are shown in figure 3.4. Throughout this work it is taken that a PVB coating on Fe has a PANi-ES film thickness of 0 μm . It has been found that PANi-ES additions to the Fe surface and subsequent increases the micro-film thickness has the effect of causing the corresponding value of E_{intact} to rise dramatically upwards. This upward rise is linear until coating thicknesses of ca. 1 μm are reached, which is the case for both PANi-CSA and PANi-PP. The maximum E_{intact} recorded for PANi-CSA micro-films is ca. 0.5V vs. SHE for film thicknesses of ca. 1 μm and above. Similarly, increasing the PANi-PP coating thickness to ca. 1 μm causes the potential to also rise linearly to the maximum potential of ca. 0.4V vs. SHE, which is a significantly lower value than seen with PANi-CSA.

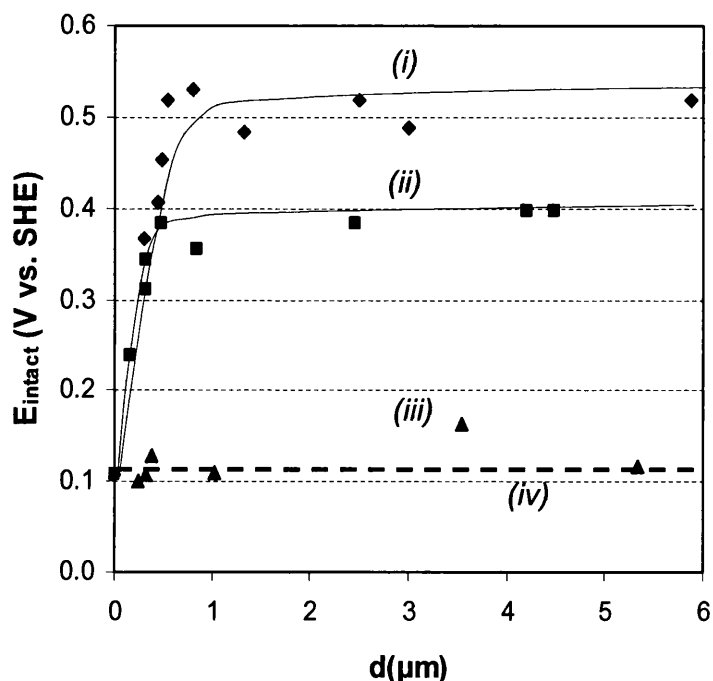


Figure 3.4. E_{intact} vs. thickness comparison for PANi-ES micro-films over coated with $30\mu\text{m}$ PVB on Fe, in air at 96% RH and 20°C . Key: (i) PANi-PP, (ii) PANi-CSA, (iii) PANi-EB and (iv) PVB.

The initial rise of E_{intact} as a function of coating thickness can be explained simply by the conducting PANi entering into interfacial electron transfer with the substrate[7]. The sharp initial linear increase in E_{intact} for the two homogeneous bilayer coating systems as a function of micro-film thickness is caused by a linear relationship between amount of PANi-ES per unit area and the amount of interfacial electron transfer that is able to occur between the substrate and the coating. At coating thickness $\geq 1\mu\text{m}$ the maximum value of redox potential (or Fermi level) of the conducting polymer is reached. Therefore any further coating thickness increase does not increase E_{intact} any further, and from the perspective of substrate ennoblement, can be considered an excess. This is entirely consistent with the findings of Williams et al [7].

3.3.3 Delamination of PVB Control Coatings

Corrosion driven cathodic disbondment mechanisms of uninhibited organic coatings from Fe substrates have been discussed elsewhere [2, 3, 8, 16, 17]. Following electrolyte contact, Fe exposed at the defect became visibly corroded within minutes and delamination began within 3hrs. Thereafter, time-dependent $E_{\text{corr}}(x)$ profiles (where x is the distance from the defect edge) became established as shown in figure. 3.5 (a). It may be seen that E_{intact} remains constant at ca. 0.10V, whereas E_{corr} values in the near defect region fall to that expected of freely corroding Fe, i.e. approximately -0.44V. The $E_{\text{corr}}(x)$ profiles arise from an electrochemical cell in which the principal site of anodic activity ($\text{Fe} \rightarrow \text{Fe}^{2+} + 2e^-$) resides at the coating defect. Ionic current flux passing through a thin, 2-3 μm layer of electrolyte [3] ingressed beneath the delaminated coating produces an ohmic potential gradient linking the defect to the principal site of cathodic O_2 reduction ($\text{O}_2 + 2\text{H}_2\text{O} + 4e^- \rightarrow 4\text{OH}^-$), which occurs at the delamination front. In general, coating disbondment is thought to occur from hydrolysis of polymer functionalities and/or the polymer metal bond by OH^- [17], although oxidation by H_2O_2 , an intermediate of the O_2 reduction reaction, has also been implicated [18].

It is the sharp inflection in figure 3.5(a) travelling from left to right has been identified as a semi empirical means of spatially and temporally identifying the position of the delamination front in $E_{\text{corr}}(x)$ profiles with respect to the defect edge [3]. It is well established that uninhibited delamination rates are controlled by the migration rate of electrolyte cations (Na^+) from the external electrolyte (defect) to the cathodic delamination front [2, 3]. Due to cation migration being rate determining, the further away from the defect the cathodic delamination front becomes over time, the greater the distance that cations must travel, and hence progress of the delamination front is slowed over time, producing parabolic delamination kinetics.

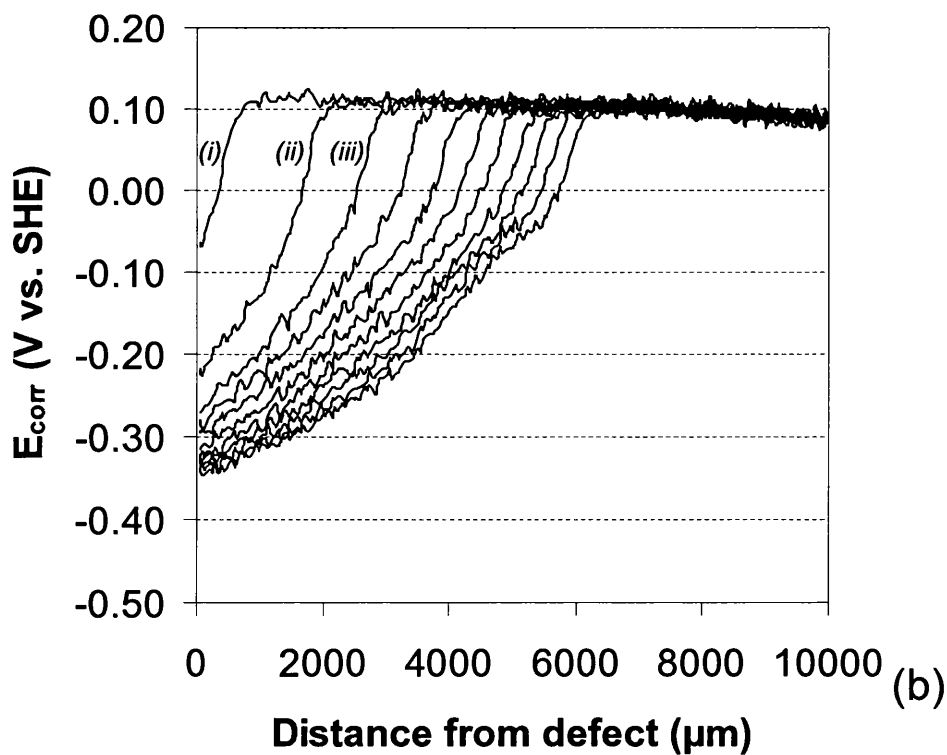
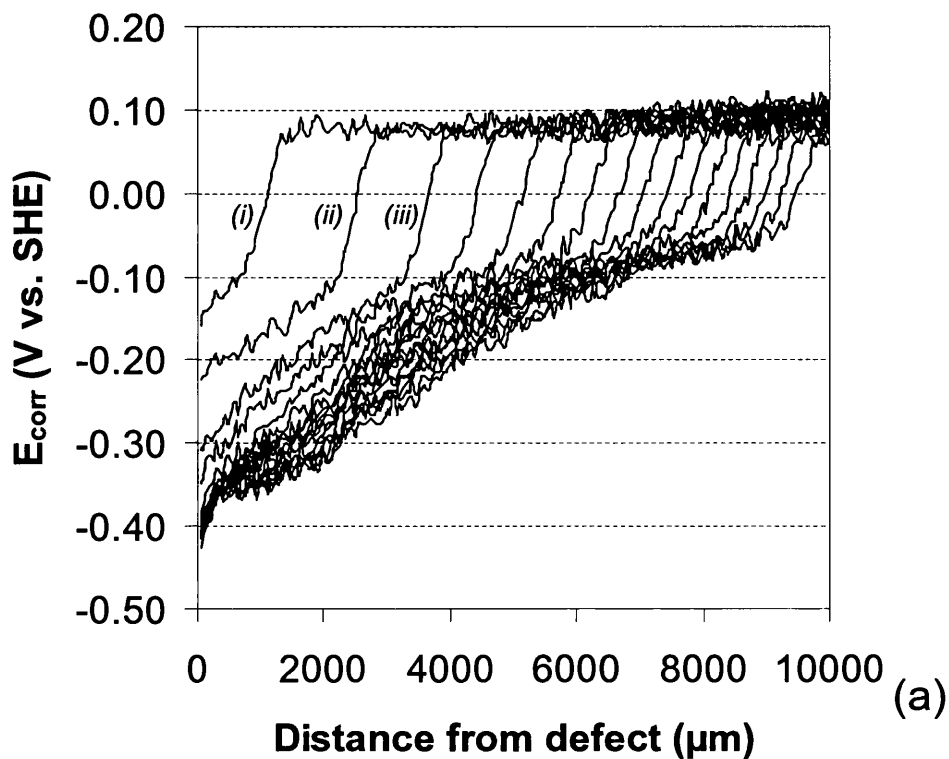


Figure 3.5. E_{corr} vs. distance from defect edge (x) profiles on Fe for (a) $30\mu\text{m}$ PVB coating on a prepared Fe surface. Key: $t_{del} =$ (i) 240 min, (ii) 300 min, (iii) 360 min and hourly intervals thereafter. (b) $0.25\mu\text{m}$ PAni-EB micro-film under $30\mu\text{m}$ PVB. Key: (i) 240 min, (ii) 360 min, (iii) 480 min and two hourly intervals thereafter.

3.3.4 Delamination of PANi-EB-PVB Bilayer Coatings

The non-conductive PANi-EB was coated directly as a micro-film onto a clean Fe substrate and over-coated with PVB, and the corresponding E_{corr} profile recorded by the SKP is shown in figure 3.5 (b). Here the PANi-EB has been shown to provide a degree of cathodic disbondment inhibition when compared to the PVB control coating, where the rate of cathodic disbondment has been slowed. Homogeneous films of PANi-EB micro-films applied directly to the Fe are non-conductive, as such electrochemical activity at the EB – substrate interface does not occur as highlighted by the E_{intact} studies. This would suggest that there is no interaction between the PANi-EB and the iron other than adhesion and indicates that any inhibition arising as a result of PANi-EB may not be electrochemical in origin.

Delamination kinetics resulting from the PANi-EB – PVB bilayer are parabolic in the same way as given by PVB coatings, signalling that in the same way as the PVB coatings, cation migration from the coating defect is the rate determining factor. Due to the parabolic delamination kinetics and the lack of E_{intact} potential rise, it is thought that PANi-EB – PVB bilayer coatings act as non-inhibiting barrier coatings. The initial delamination rate of the PANi-EB – PVB bilayer at $11\mu\text{m min}^{-1}$ is slower than the initial rate of the PVB coating, $19\mu\text{m min}^{-1}$, where such differences could possibly be due to adhesion strength between the coating and substrate.

3.3.5 Delamination of PANi-ES-PVB Bilayer Coatings

The application of a conductive PANi-ES micro-film directly to an Fe surface causes electrochemical reactions between the coating and substrate as previously mentioned. This has the effect of ennobling E_{intact} in comparison to the PVB control coating and the PANi-EB systems. The E_{corr} profile of figure 3.6 (a) shows an example of an SKP recorded delamination experiment of a $0.44\mu\text{m}$ thick PANi-CSA bilayer coating adherent to a pure Fe substrate. Comparing the SKP profile of the $0.44\mu\text{m}$ PANi-CSA coating in figure 3.6 (a) directly to a thicker $1.75\mu\text{m}$ PANi-CSA coating in figure 3.6 (b), a higher degree of substrate ennoblement is apparent as denoted previously in figure 3.4 and caused by the increase in PANi-ES coating thickness. Similarly, figures 3.7 (a) and 3.7 (b) show SKP profiles for a $0.33\mu\text{m}$ PANi-PP bilayer coating and a $1.35\mu\text{m}$ PANi-PP bilayer coating respectively. This also highlights the increase of E_{intact} caused by increased coating thickness albeit to a lesser extent than with the PANi-CSA systems. The corrosion driven delamination front is clearly recognisable within these E_{corr} profiles. The rate of corrosion driven coating delamination as a function of coating thickness is important to fully understanding the active mechanisms of cathodic disbondment taking place in the presence of these inhibitors. Accordingly the effects of altering the PANi-ES solid film thickness from $0\mu\text{m}$ (PVB only) to just under $6\mu\text{m}$ thick are investigated in the case of PANi-CSA, and in the case of PANi-PP thickness variations of up to $4.5\mu\text{m}$ have been recorded.

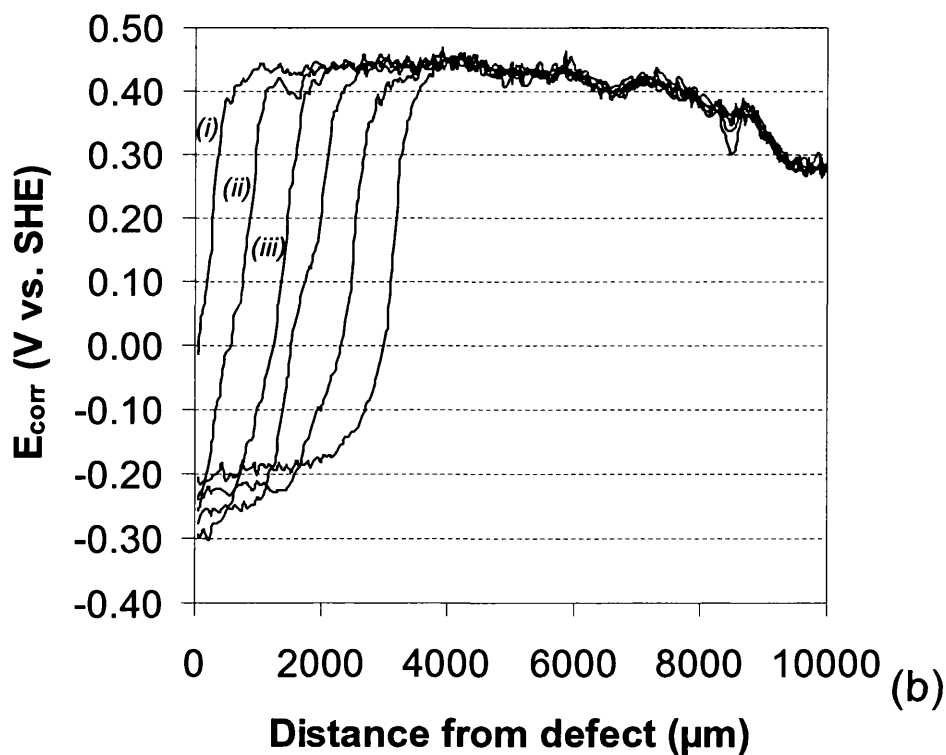
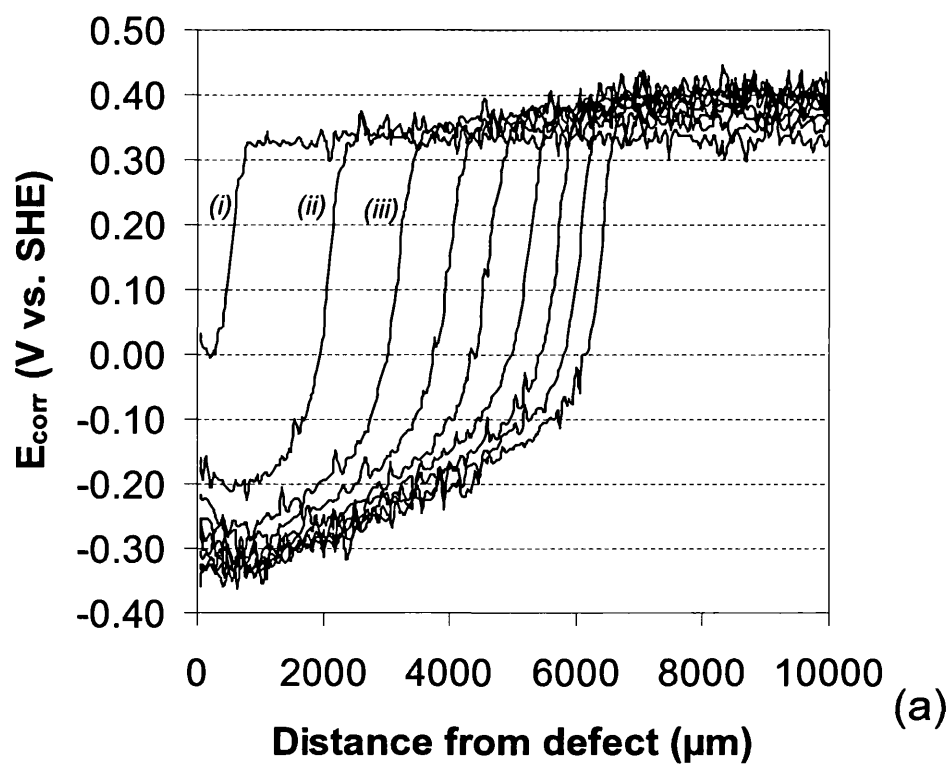


Figure 3.6. E_{corr} vs. distance from defect edge (x) profiles on Fe for (a) $0.44\mu\text{m}$ PANi-CSA micro-film under $30\mu\text{m}$ PVB. Key: (i) 360 min, (ii) 480 min, (iii) 600 min and two hourly intervals thereafter. (b) $1.75\mu\text{m}$ PANi-CSA micro-film under $30\mu\text{m}$ PVB. Key: (i) 300 min, (ii) 540 min, (iii) 780 min and four hourly intervals thereafter.

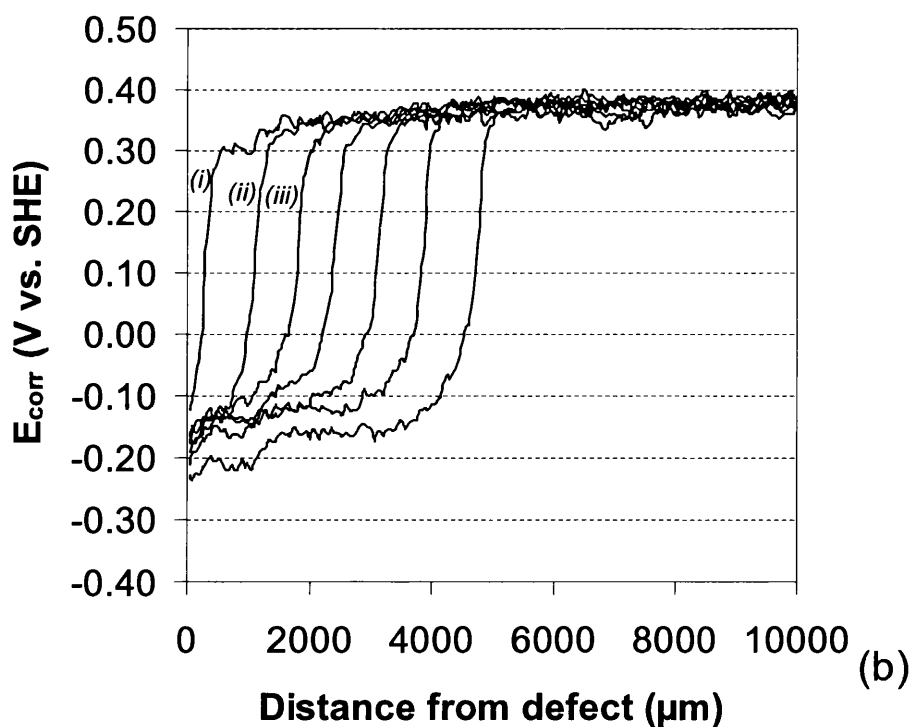
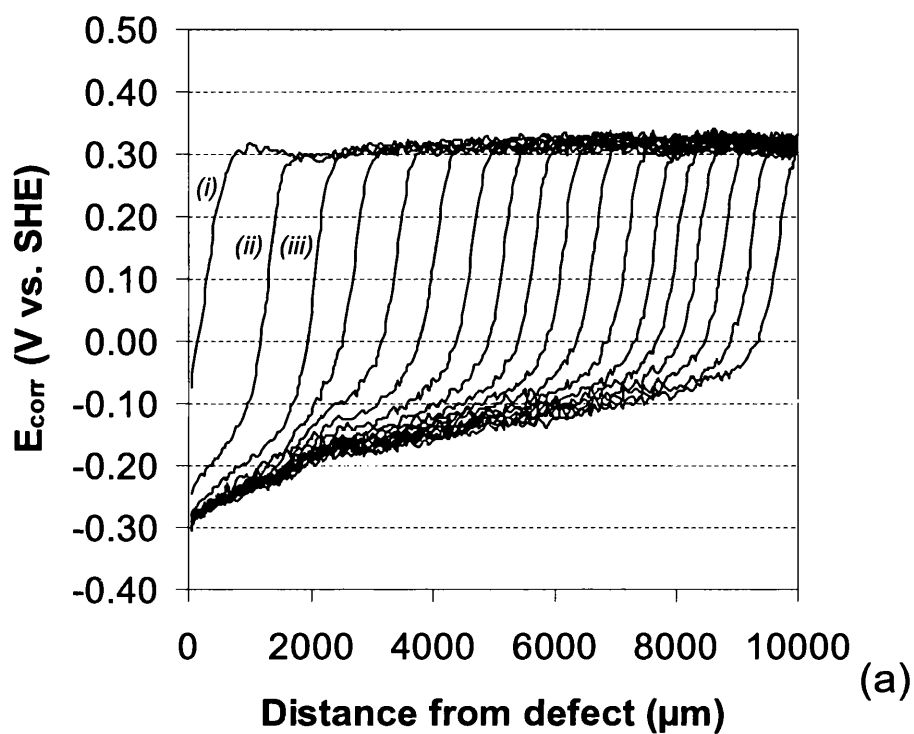


Figure 3.7. E_{corr} vs. distance from defect edge (x) profiles on Fe for (a) $0.33\mu\text{m}$ PANi-PP micro-film under $30\mu\text{m}$ PVB. Key: (i) 180 min, (ii) 240 min, (iii) 300 min and hourly intervals thereafter. (b) $1.35\mu\text{m}$ PANi-PP solid film under $30\mu\text{m}$ PVB. Key: (i) 360 min, (ii) 540 min, (iii) 720 min and three hourly intervals thereafter.

In common with potentiometric studies carried out using the SKP, PVB coatings are directly coated to the Fe substrate and it is the delamination rates recorded from these coatings that determine the level of experimental error and also provide the basic delamination rate of the non-inhibited coating system. Due to the nature of the PVB coating being non-inhibiting, delamination kinetics recorded from such coating are parabolic because cation migration from the coating defect to the delamination front is the rate determining process. Accordingly, under these circumstances the delamination rate is showed to slow as a result of propagation distance from the defect. Due to this phenomenon, the rate recorded for all experiments is the initial rate. The recorded delamination rate for PVB control coatings was measured as being $18.88 \pm 4.02 \mu\text{m min}^{-1}$.

Parabolic delamination kinetics as seen with PVB coatings are also present with thinner layers of PANi-CSA and PANi-PP. Values of x_{del} are plotted against $(t_{\text{del}}-t_i)$ for PANi-CSA micro-films in figure 3.8 (a) and for PANi-PP solid films in figure 3.8 (b). Curved lines are obtained for thinner PANi-ES coatings of both dopants, which imply that under-coating cation migration remains rate limiting for these.

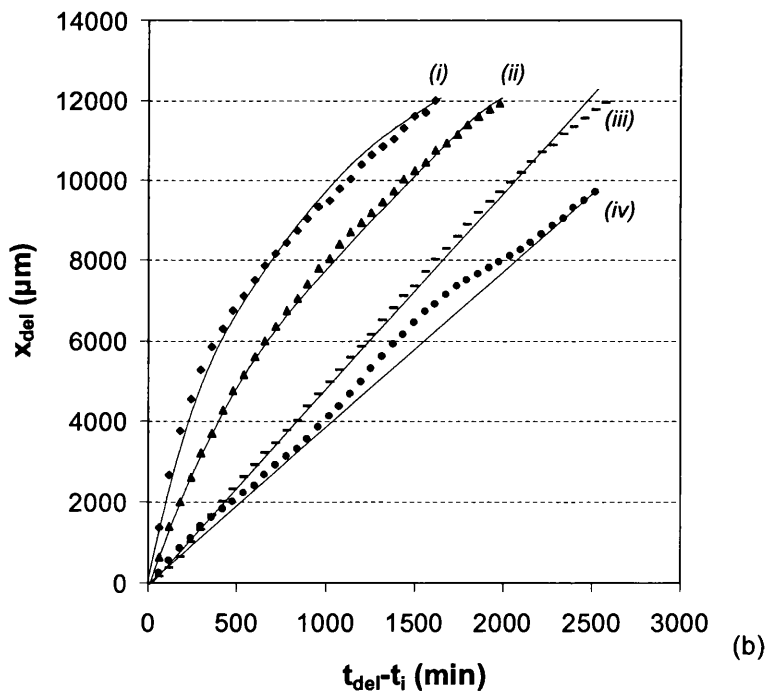
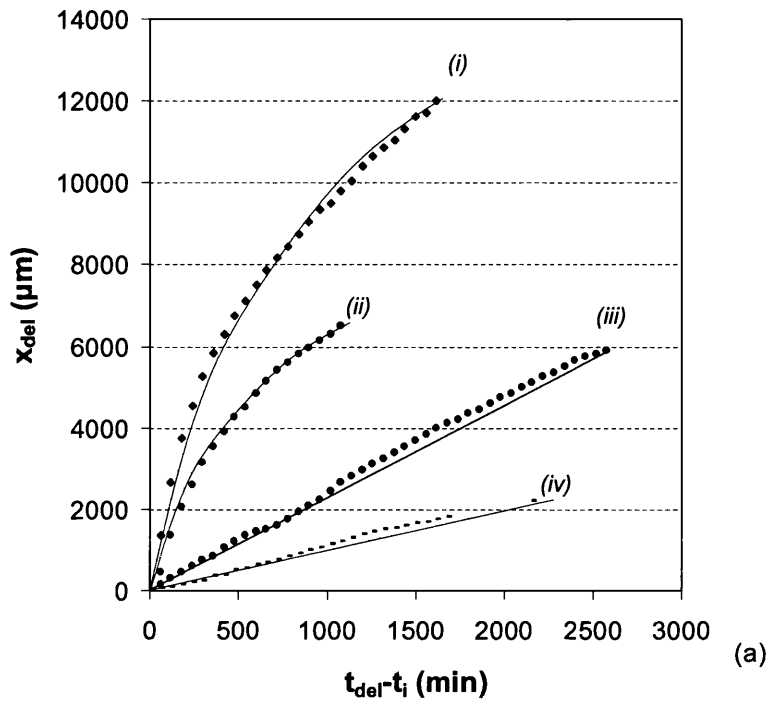


Figure 3.8. Plots of delamination distance (x_{del}) vs. $(t_{del}-t_i)^{1/2}$ for PANi-ES micro-films under $30\mu\text{m}$ PVB on Fe, in air at 96% RH and 20°C (a) PANi-CSA. Key: d (μm) = (i) 0, (ii) 0.18, (iii) 0.32, (iv) 0.44, (v) 0.80, (vi) 1.75 and (vii) 2.44. (b) PANi-PP. Key: d (μm) = (i) 0, (ii) 0.33, (iii) 0.49, (iv) 0.51, (v) 0.68, (vi) 1.35 and (vii) 2.46.

A comparison of the two summary plots shows that a common factor between PANi-CSA and PANi-PP micro-films is that at coating thickness ca. $0.80\mu\text{m}$ there is a sharp

change from parabolic to linear kinetics. This change from parabolic to linear delamination kinetic almost coincides with the thickness PANi-ES coating required to produce maximum E_{intact} values for PANi-ES of each dopant. Another micro-film thickness that both dopants have in common is the thickness of ca. $1\mu\text{m}$ where increasing this thickness any further produces very little further retardation of the delamination rate. This is highlighted in figure 3.9, where the difference in delamination rate as a function of PANi-ES micro-film thickness is clearly shown. In this summary plot PANi-PP is shown to be a less effective inhibitor of corrosion driven coating delamination than the PANi-CSA. Up to thicknesses of ca. $1\mu\text{m}$ both PANi-ES have an almost equal inhibitory effect. The limit of the effectiveness of PANi-PP is to slow the delamination rate down to ca. $4\mu\text{m min}^{-1}$, whereas PANi-CSA continues to slow up the rate of disbondment to ca. $1\mu\text{m min}^{-1}$. Figure 3.9 also highlights the low level of cathodic delamination inhibition provided by PANi-EB micro-films of varying thicknesses in direct comparison with the similar gauge PANi-ES coatings.

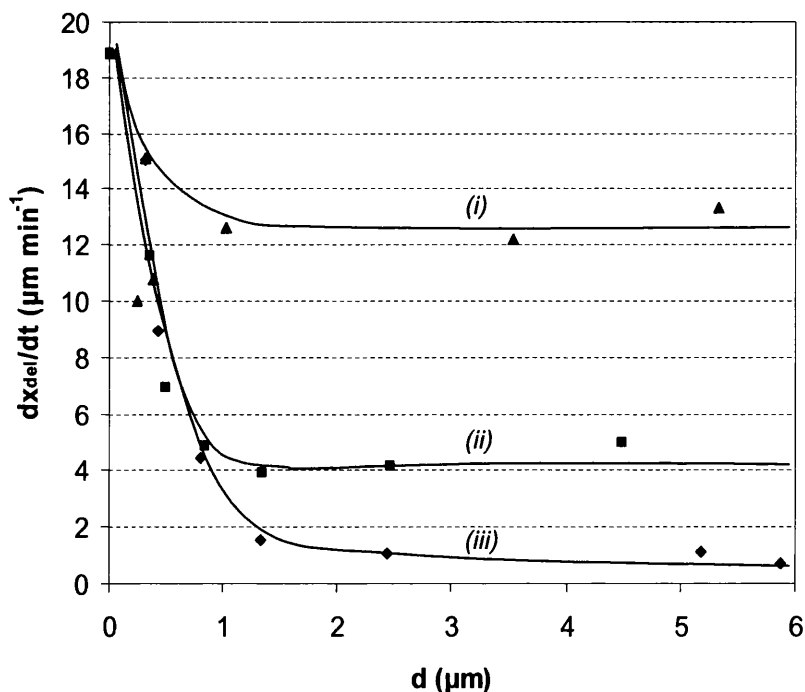


Figure 3.9. Delamination rate vs. coating thickness comparison for homogenous PANi-ES films over coated with $30\mu\text{m}$ PVB on Fe in air at 96% RH and 20°C . Key: (i) PANi-EB, (ii) PANi-PP and (iii) PANi-CSA.

Of significant importance is the point at which the delamination kinetics change from parabolic to linear as shown in figure 3.8. At and above this critical film thickness for PANi-CSA and PANi-PP coatings, the rate determining factor ceases being cation migration from the artificial defect to the delamination front. A suggested possibility is that at polymer micro-film thicknesses greater than this critical measure, the reduction of PANi-ES is taking the place of the O₂ reduction reaction.

For practical applications of homogeneous films of PANi-ES to inhibit cathodic delamination on Fe substrates, it does not appear to be worth while applying coating thicknesses of greater than 1 μm thickness, as highlighted in figure 3.9.

3.3.6 Optical Cathodic Disbondment Studies

Due to the opaque nature of the PANi-ES composite coatings used in previous SKP studies [7, 8], PANi-CSA has been solution cast directly as a micro-film onto an Fe substrate, and subsequently over coated with an optically transparent 30 ± 5 μm clear film of PVB by solution casting from ethanol to create a bilayer coating. This study provides evidence to support previous findings that were carried out on plain carbon steel [9], differing by using a high purity Fe substrate as well as a different optically transparent top coat. In the work of Gabriel et al [9] it has been shown that when an optically transparent layer of PANi-ES applied to a carbon steel substrate and is subject to cathodic delamination conditions, PANi state changes caused by the cathodic disbondment are visually recognisable. It has been shown that in the undelaminated regions (intact coating) under normal oxygenated environmental conditions the PANi-ES is green, where at the delamination front the green PANi-ES is reduced to clear PANi-LB, which subsequently undergoes re-oxidation to PANi-EB. This phenomena is illustrated within the optical photograph of figure 3.10, which clearly shows the differing PANi colours (associated to the different states) upon cathodic delamination.

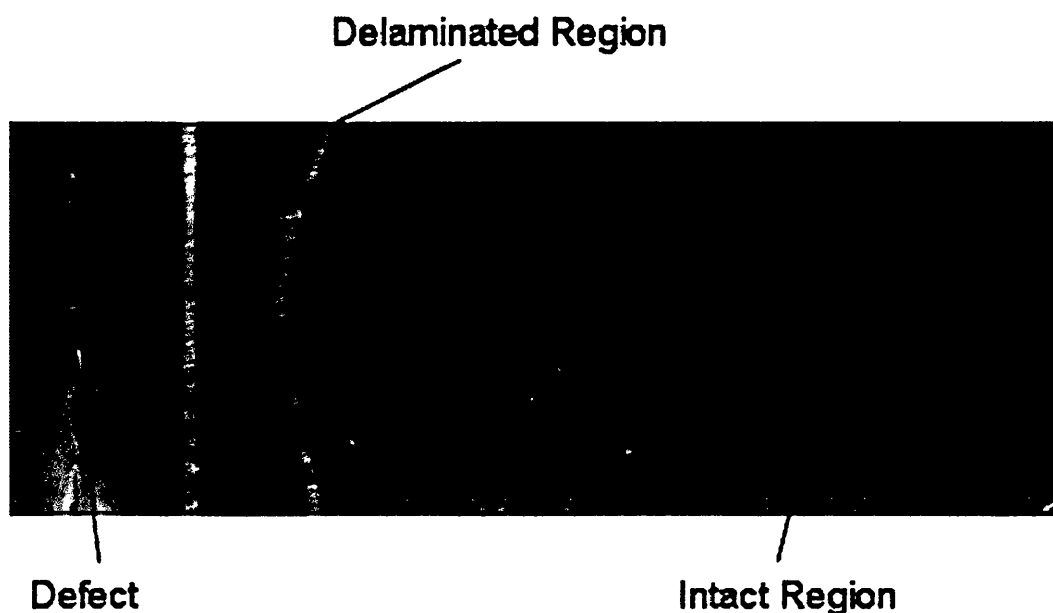


Figure 3.10. Digital photograph showing PANi state changes resulting from cathodic delamination originating from a penetrative coating defect.

By simulating these same environmental conditions with the material changes already mentioned, it was found that the PANi acid-base and redox changes were only visible in this way for micro-films of ca. $< 1\mu\text{m}$ thick. For film thicknesses ca. $> 1\mu\text{m}$, the PANi is too opaque for easy optical recognition of state changes, which is undoubtedly a property of the PANi-ES. Coating thicknesses ca. $< 1\mu\text{m}$ clearly show that under the experimental conditions employed the onset of cathodic disbondment causes PANi state changes to occur at the delamination front. These state changes are directly related to the electrochemical reactions taking place as a result of the cathodic delamination cell and substrate – coating interactions, and are consistent with the findings of Gabriel et al [9].

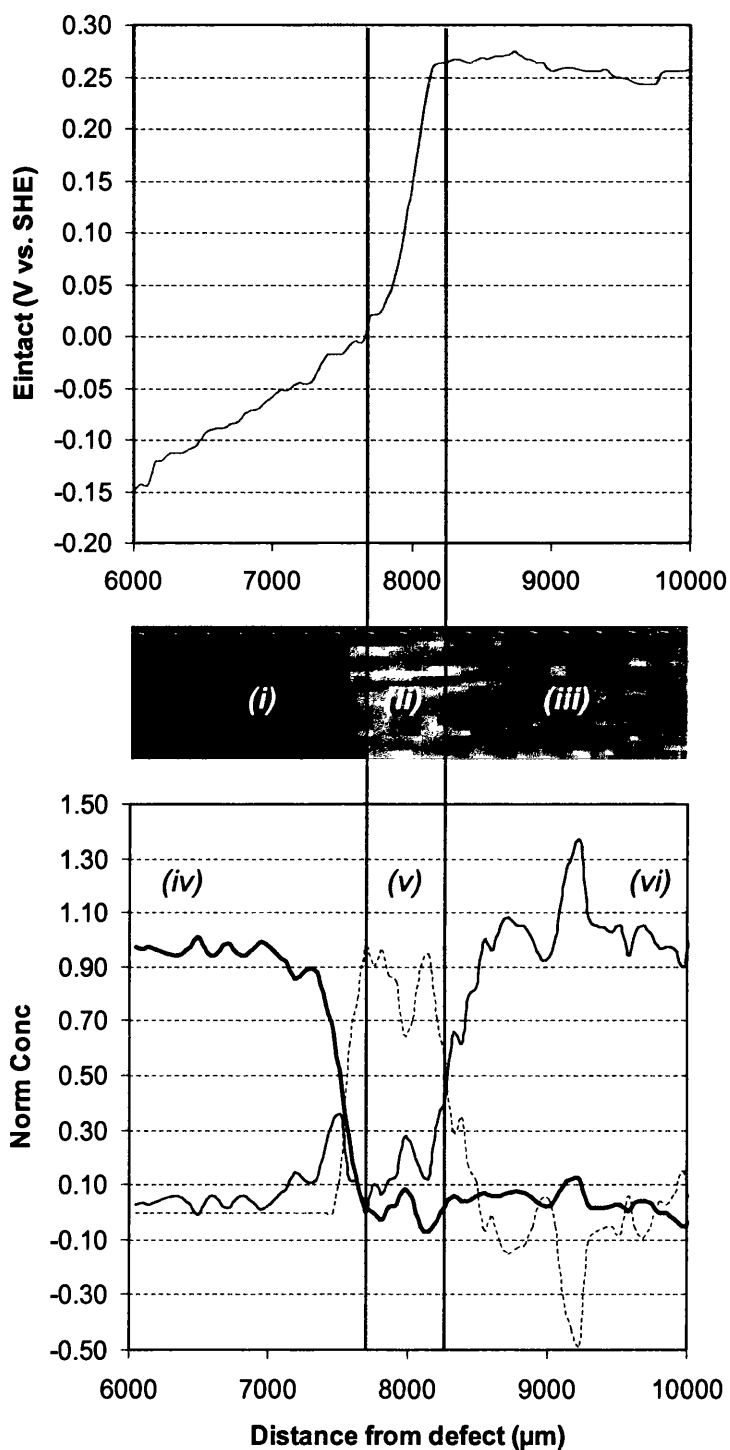


Figure 3.11. Spatially and temporally resolved digital image analysis of the cathodic delamination front of a PANi-CSA micro-film on pure Fe in relation to the corresponding E_{corr} profile as recorded by the SKP. Key: (i) PANi-EB (blue region), (ii) PANi-LB (clear region), (iii) PANi-ES (green region), (iv) normalised concentration of PANi-EB, (v) normalised concentration of PANi-LB and (vi) normalised concentration of PANi-ES.

Creating thin ($\leq 0.30\mu\text{m}$) PANi-CSA micro-film on iron and over coating it with clear PVB allows the optical delamination used by Gabriel et al [9] to be re-created. Combining this method of coating production and optical analysis with the SKP allows a great deal of information about the various mechanisms at the delamination front to be realised. Recording the cathodic delamination process using the SKP with a high level of spatial accuracy, in addition to simultaneous optical recording of the delamination front allows the exact position of the cathodic delamination front in relation to the corresponding E_{corr} profile to be pinpointed. The results of which are shown in figure 3.11, and as a break-down of this diagram, the top graph shown is the E_{corr} profile recorded by the SKP moments before the digital image shown in the centre was recorded. The bottom graph of figure 3.11 shows the normalised concentration of the species present analysed in terms of colour intensity of the individual pixels recorded by the digital camera. By spatially linking all three components together an accurate description of the delamination front can be theorised.

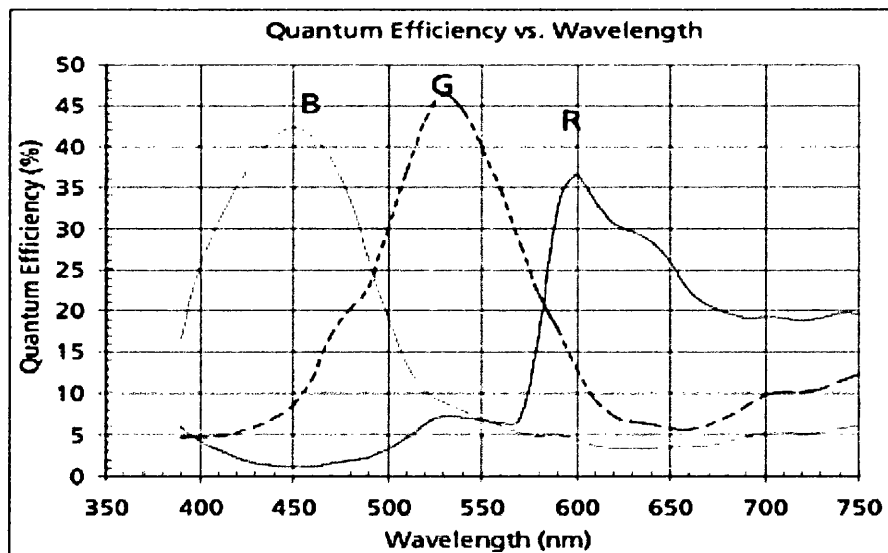


Figure 3.12. Example of Bayer transmission spectral profiles as used by digital cameras such as the Canon Powershot G6.

The Canon Powershot G6 digital camera used to acquire the image seen in figure 3.11 used a standard Bayer filter system to obtain red green and blue pixel values. The red green and blue filter pass bands were centred at 600nm, 525nm and 450nm

respectively as illustrated in figure 3.12. The filter pass band width does not permit a fully quantitative analysis of the spectral data in figure 3.11. Nevertheless a semi-quantitative analysis is possible and this analysis is presented here principally as a means of rendering graphically what is evident by eye in the coloured image. Colours in figure 3.11 arise from the absorbance of light passing through the PANi coating layer after reflection from the iron substrate. Optical absorbance values were calculated as follows:

$$A_{\text{Green}} = -\log_{10} \left[\frac{I_{\text{Green Pixel}}}{I_{\text{max Green Pixel}}} \right] \quad (\text{Equation 3.2})$$

$$A_{\text{Blue}} = -\log_{10} \left[\frac{I_{\text{Blue Pixel}}}{I_{\text{max Blue Pixel}}} \right] \quad (\text{Equation 3.3})$$

Where quantities of I denote the light intensity value associated with a particular green or blue pixel. Quantities I_{max} denote the maximum light intensity associated with green or blue pixels anywhere in the image. This includes portions of the image where PANi is in the non-absorbing leuco state so that I_{max} is a measure of light transmitted in the absence of PANi absorption (I_0 in standard Beer Lambert notation).

By reference to equation 3.2 the quantity A_{Green} corresponds reasonably well to absorbance by PANi-EB, such that we may write:

$$[\text{EB}] = \text{const} \times A_{\text{Green}} \quad (\text{Equation 3.4})$$

and
$$[\text{EB}]_{\text{N}} = [\text{EB}] / [\text{EB}]_{\text{max}} \quad (\text{Equation 3.5})$$

Where $[\text{EB}]$ is the concentration of emeraldine base in the PANi film, $[\text{EB}]_{\text{max}}$ is the maximum $[\text{EB}]$ value in the image and $[\text{EB}]_{\text{N}}$ is the normalised $[\text{EB}]$ value. Because

[EB] may derive from positions of the image which are known to contain only EB, the quantity $[EB]_N$ corresponds to the fraction of total PANi in the EB state. We could similarly write:

$$[ES] = \text{const} \times A_{\text{Blue}} \quad (\text{Equation 3.6})$$

and
$$[ES]_N = [ES] / [ES]_{\text{max}} \quad (\text{Equation 3.7})$$

Where [ES] is the concentration of emeraldine salt and $[ES]_N$ is the fraction of total PANi in the ES state. By an extension of this reasoning we can further write:

$$[LE]_N = 1 - ([ES]_N + [EB]_N) \quad (\text{Equation 3.8})$$

Where $[LE]_N$ is the fraction of total PANi in the leuco state.

It is shown that in the region of the intact coating (green region), the E_{corr} profiles remain ennobled and this is caused by interactions between the PANi-ES and the Fe substrate and have been explained fully elsewhere [7]. At the point in the image where the green PANi-ES coating changes colour to become transparent, it is clear that the PANi-ES begins to be reduced to the PANi-LB state. The intact coating potentials begin to fall through the area of PANi-LB shown in the image. Comparing this to the lower plot showing the normalised concentrations of the various PANi states present, it can be seen that near to the left hand edge of the PANi-LB region (denoted by the left hand vertical line) the normalised concentration of PANi-EB begins to increase to the point where the coating changes colour to blue PANi-EB, which indicates the delaminated region of coating. The exact point at which coating delamination occurs is therefore assumed to be where the normalised concentration of PANi-EB begins to rise from the minimum value, i.e. at approximately 7800 μm from the defect where the normalised concentration of PANi-EB is at its lowest, which is denoted by the left hand vertical line.

From knowing the exact point where coating delamination occurs, which corresponds to the exact point at which the PANi-LB coating begins to re-oxidise to PANi-EB, it is possible to calculate the period of time it takes for the coating to re-

oxidise. This has been achieved by accurately knowing the delamination kinetics of the particular experiment and linking these kinetics directly to delamination distance. From the delamination kinetics as calculated from the data gained in obtaining figure. 3.11, it can be shown that coating re-oxidation of a $0.30\mu\text{m}$ PANi-LB coating over coated with PVB and freshly delaminated from an iron substrate is approximately 40 minutes, which is shown in figure 3.13.

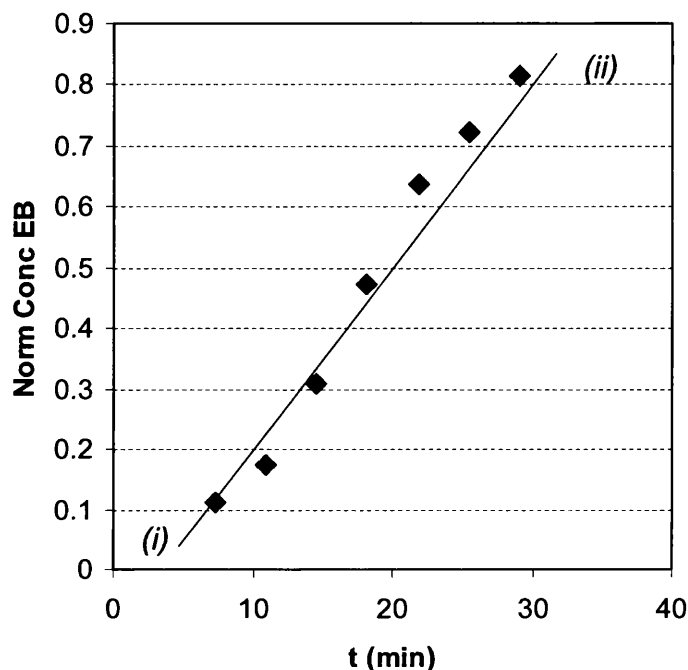


Figure 3.13. PANi-CSA re-oxidation kinetics showing the time taken for the colourless PANi-LB to fully change to the blue PANi-EB after delamination has occurred on Fe. Key: (i) colourless PANi-LB and (ii) blue PANi-EB.

A number of PANi-CSA micro-films were applied to the surface of ITO coated glass and subsequently reduced to PANi-LB in 100ml of 0.86 mol dm^{-3} (5% w/v) aqueous NaCl electrolyte and reduced to clear leuco base (PANi-LB) by applying a potential of -0.20V vs. SCE. Full deprotonation of the PANi-ES to PANi-LB was ensured by adding 1ml of aqueous 0.1M ammonium hydroxide to the electrolyte. Upon full reduction to PANi-LB the PANi coating was completely clear and removed from the electrolyte and mounted inside the UV-VIS spectrophotometer and the re-oxidation is shown according to absorbance vs. time within figure 3.14.

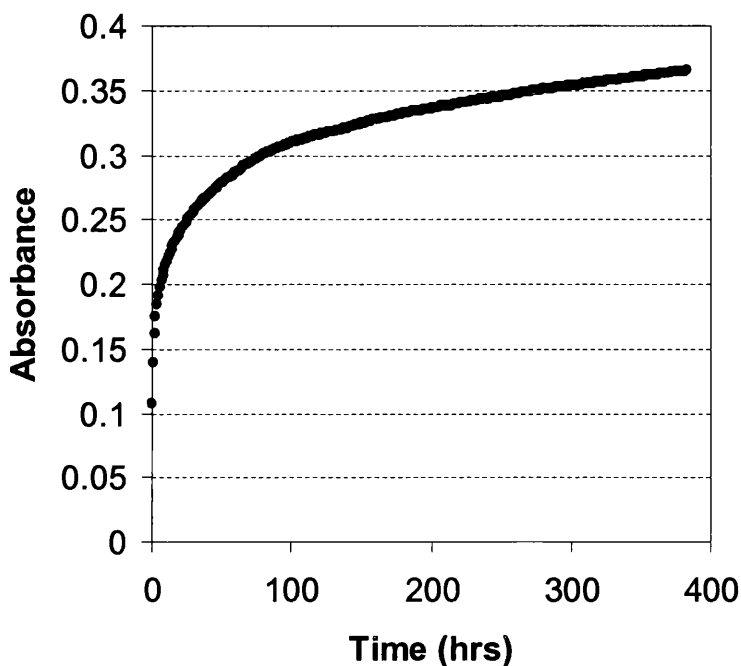


Figure 3.14. PANi re-oxidation showing the time taken for the colourless 0.20 μ m PANi-LB to re-oxidise to the blue PANi-EB under atmospheric conditions when adherent ITO coated glass.

The UV-VIS spectrophotometer was set to record the optical absorbance of the PANi film at 650nm, which has already been established as being the peak absorbance of the quinoid segment of the polymer (figure 3.1). The PANi micro-film undergoing re-oxidation in figure 3.14 is 0.20 μ m thick, and accordingly should re-oxidise to show an optical absorbance of approximately 0.4 (equation 3.1). After 400hrs of atmospheric exposure the PANi-ES micro-film still has not reached this value, signifying that re-oxidation is not yet complete. This shows a significantly large difference in re-oxidation kinetics, where rapid re-oxidation of the PANi micro-film occurs in close proximity to Fe, and prolonged re-oxidation occurs without the presence of Fe (and electrolyte). A study by Moon et al has shown that re-oxidation of PANi-EB to PANi-LB in a solution of NMP agrees with the findings presented here [13]. Moon found that in the presence of O₂ alone, re-oxidation of the PANi followed pseudo first order kinetics and took place over a number of hours. Moon also found that in the presence of FeCl₃, the speed of re-oxidation was reduced to minutes rather than hours. This agrees with the findings presented here, where it is

possible that the fast re-oxidation of the PANi micro-films in close proximity to Fe could cause the creation of ferrous species to catalyse the re-oxidation reaction.

3.3.7 Comparing Polyaniline Micro-films with Composite Coatings

To compare the effectiveness of PANi composite coatings with that of PANi micro-films, it is most practicable to first consider coatings such that the PANi component is the non-conducting PANi-EB. Previous SKP studies [7] of PANi-EB composite coatings have shown that by adding PANi-EB as a fine particulate dispersion within a PVB coating, no effect is observed with regards to either delamination kinetics or the ennoblement of E_{intact} regardless of coating pigment loading. E_{intact} measurements of PANi-EB micro-films on Fe substrates have also shown that no surface ennoblement occurs as a result of coating – surface interactions, which implies there are not any, (figure 3.4).

A greater insight into the mechanisms of cathodic disbondment inhibition by PANi-ES is provided by directly comparing bilayer micro-film coatings with pigmented PVB coatings. The data presented here for all PANi-ES pigmented PVB coatings originates from published works by Williams et al [7]. Plotting the reciprocal cathodic disbondment kinetics as a function of micro-film thickness for each coating thickness; PANi-CSA solid films, PANi-PP solid films, PANi-CSA dispersions and PANi-PP dispersions as in figure 3.15 reveals important information about the mechanisms of the cathodic disbondment process for each individual coating system.

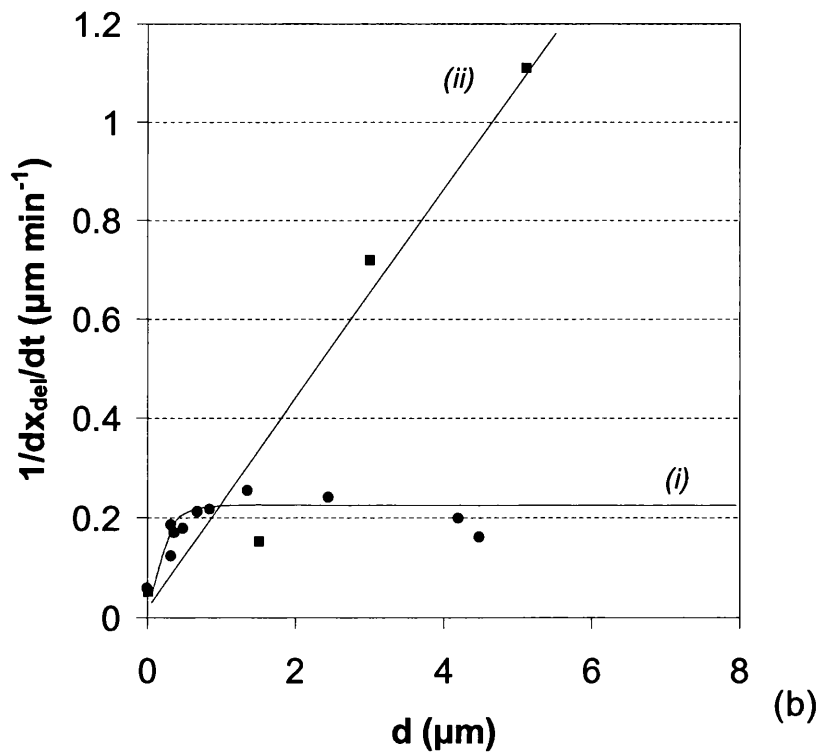
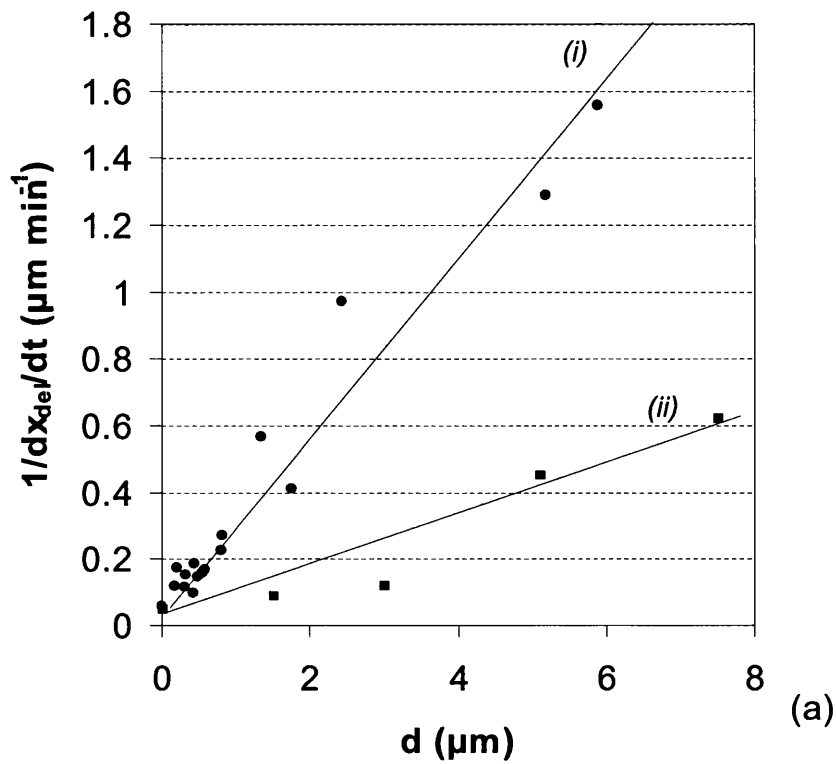


Figure 3.15. Reciprocal delamination kinetics comparing the effects of varying the quantity of in-coating PANi-ES on Fe. (a) PANi-CSA. Key: (i) Homogenous solid films) and (ii) Dispersion coatings. (b) PANi-PP. Key: (i) Homogeneous solid films and (ii) Dispersion coatings [7].

Comparing the four reciprocal plots in figure 3.15, it is apparent that all coating systems with the exception of the PANi-PP solid films follow a linear pattern. Linear reciprocal delamination kinetics show that the progress of the cathodic delamination front is wholly dependent upon the amount of active PANi present within the coating system. By doubling the coating thickness the rate of cathodic disbondment is halved. Within these coating systems, delamination proceeds when all PANi within that portion of the coating is fully reduced. Because the PANi-PP homogeneous solid film system does not exhibit linear reciprocal delamination kinetics as a function of coating thickness, and because inhibition of cathodic disbondment is poor, the mechanisms in action require explanation.

The difference between PANi-PP composite coatings and the PANi-PP solid films can be explained in terms of the levels of lateral conductivity of the coating. The lateral conductivity of PANi-ES micro-films have been measured to be $2.68 \pm 1.72 \text{ Sm}^{-1}$ by four point conductivity testing. This is in comparison to the negligible lateral conductivity measured for composite coatings, which were recorded by independently measuring a number of PANi-CSA coatings of varying pigment loadings.

Previous studies have found that an insulating phosphonate salt film is formed between substrate and coating [7], and it is proposed that this interfacial resistance in addition to the high levels of lateral conductivity are destructive in terms of inhibition performance. To explain this in more detail, the mechanistic proposals for each of the four coating systems under discussion are shown schematically in figure 3.16. Progression of the cathodic delamination front occurs upon reduction of the PANi-ES coating as a result of interfacial electron transfer between the substrate and the PANi coating at the delamination front. This explains the reason why doubling the coating thickness halve the rate of disbondment in the case of the three coating systems showing linear reciprocal kinetic plots. The interfacial electron transfer resulting from the cathodic delamination process is depicted at the delamination front within each of the four schematics.

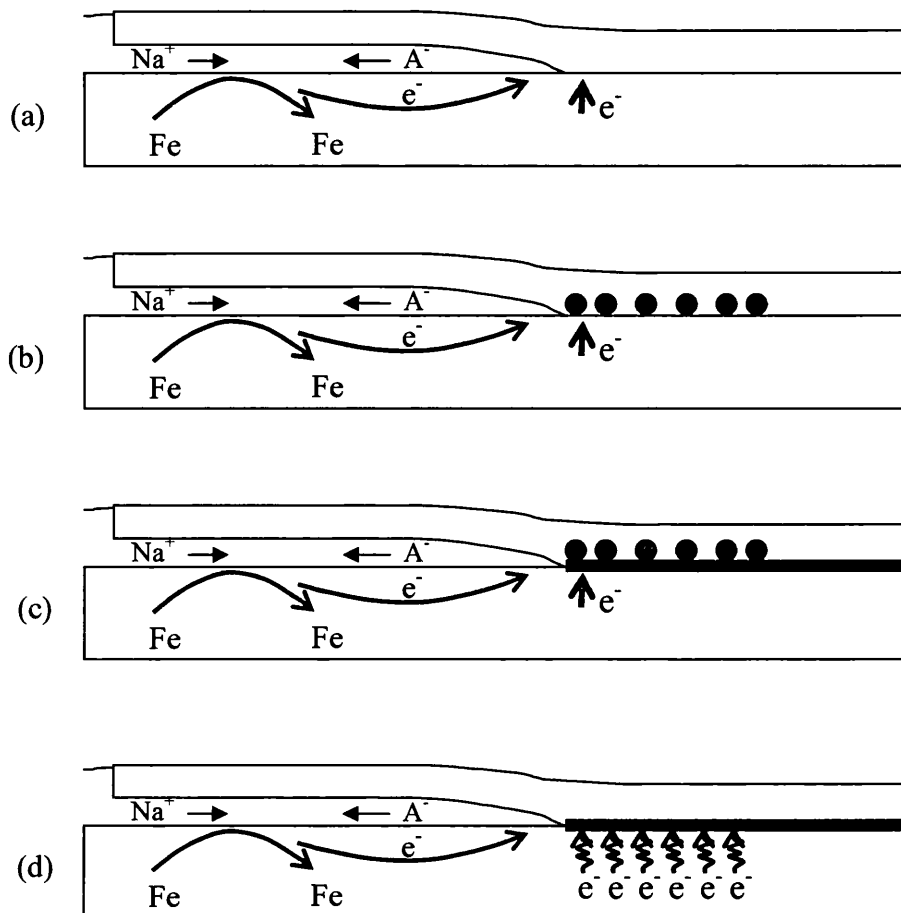


Figure 3.16. Proposed mechanism of interfacial electron transfer between the underlying Fe substrate and the in-coating PANi-ES. (a) PANi-CSA micro-films, (b) PANi-CSA dispersion coatings, (c) PANi-PP dispersion coatings and (d) PANi-PP micro-films.

Figures 3.16 (a) and (b) represent the mechanistic schematics of PANi-CSA micro-films and PANi-CSA composite coatings respectively. These two coating systems are identical in terms of the conductive nature of the interfacial oxide film lying at the coating substrate interface, differing only in terms of in-coating lateral conductivity levels. Due to the conductive nature of the interface between the PANi-CSA and the Fe substrate, interfacial electron transfer is able to readily take place at the very edge of the delamination front, which limits the spread of current density into the coating in both cases.

Figures 3.16 (c) and 3.16 (d) represent the mechanistic schematics of the PANi-PP composite coatings and the PANi-PP micro-films respectively. The resistive

interfacial phosphonate salt film produced from interactions between the PANi-PP and Fe substrate has a great effect upon the way electron transfer between the substrate and PANi occurs at the delamination front. Considering the PANi-PP composite coatings, which exhibit a linear plot of reciprocal delamination kinetics, it is known that PANi-ES at the delamination front must be completely reduced in order for the delamination front to proceed. It is the resistive phosphonate salt film that changes the ease of electron transfer at the delamination front due to the electron being forced to pass through a resistive boundary. The low levels of lateral conductivity of the composite coatings have the effect of only allowing this electron transfer to occur at PANi directly adjacent to the delamination front, meaning current density is not spread into the coating and reduction of the PANi-PP occurs in a very similar manner to the PANi-CSA systems.

Figure 3.16 (d) shows the proposed mechanism by which The PANi-PP system acts in terms of electron transfer at the delamination front. Considering the PANi-PP composite coatings, the interfacial electron transfer is forced to take place directly at the delamination front because the lateral conductivity of the coating is not high enough to allow the spread of current density way from the defect. This is not the case for PANi-PP homogeneous solid films, where the high lateral conductivity of the coating coupled with the resistivity of the coating substrate interface causes the current density of the interfacial electron transfer process originating at the delamination front to travel deeper into undelaminated regions of coating. This travel of current density causes PANi-PP reduction to occur over greater lengths and this explains why inhibition provided by the coatings is far inferior to the other three systems studied.

3.4 Conclusions

The SKP has been successfully employed alongside time lapse digital photography to fully record corrosion driven coating delamination of PANi coatings where PANi-ES is applied directly to an Fe substrate and subsequently over coated with PVB to create a bilayer coating. By being able to accurately measure the PANi-ES coating depth, microfilms of various thicknesses have been produced and the ensuing effects upon delamination kinetics and values of SKP recorded E_{intact} have been fully characterised. Following on from previously completed studies [7] involving PANi-ES dispersions, a camphorsulphonate dopant (PANi-CSA) was chosen alongside a phenylphosphonate dopant (PANi-PP). This study of PANi-ES bilayer coatings has provided further evidence to support the mechanistic proposals regarding delamination mechanisms and dopant specific substrate-PANi interactions [7-9]. Long term humidification of the intact PANi-ES micro-films under conditions of ca. 96% RH was found to cause a linear rise in E_{intact} in relation to film thickness until the PANi-ES potential is reached at a thickness of ca. $1\mu\text{m}$ in both cases, which is 0.40V vs. SHE for PANi-PP and 0.52V vs. SHE for PANi-CSA. Incidentally, PANi-EB was found not to have any effect upon E_{intact} . The effects of varying PANi-ES film thickness on the corrosion driven delamination kinetics have also highlighted $1\mu\text{m}$ coating thickness as being a significant PANi-ES thickness. This is true for both dopants, where coating delamination rates are slowed significantly up to this thickness and further coating thickness increase has very little extra effect, slowing the rate to ca. $4\mu\text{m min}^{-1}$ in the case of PANi-PP and $\leq 1\mu\text{m min}^{-1}$ in the case of PANi-CSA micro-films. Analysis of the reciprocal delamination kinetics for PANi-ES bilayer micro-film coatings and PANi-ES dispersion coatings on show a non-linear plot for PANi-PP solid films, whereas all other coating systems produce linear plots.

Time lapse digital photography has proven to be successful in visually identifying the delamination front, and proof the technique is valid has been provided by accurately linking the recorded images spatially and temporally with the SKP profile of the delamination front. Additionally, the PANi colour changes resulting from cathodic delamination first reported by Gabriel et al[9] have been reproduced, but analysed in a more complete manner to give the amount of time it takes for the

reduced and unstable PANi-LB in the delamination zone to be re-oxidised to PANi-EB.

The combination of all findings has lead to the conclusion that for the most effective inhibition of cathodic disbondment to occur, interfacial electron transfer as part of the cathodic disbondment process should be kept as near to the delamination front as possible, and according cathodic disbondment performance is highly dependent upon the physical make-up of the PANi coating systems and interfacial chemistry created.

3.5 References

- [1] H. Leidheiser, *Corrosion Control by Organic Coatings*, NACE, Houston, 1981.
- [2] A. Leng, H. Streckel, and M. Stratmann, *Corrosion Science* **41**:547 (1999).
- [3] A. Leng, H. Streckel, and M. Stratmann, *Corrosion Science* **41**:579 (1999).
- [4] M. Stratmann, R. Feser, and A. Leng, *Electrochimica Acta* **39**:1207 (1994).
- [5] D. E. Tallman, G. Spinks, A. Dominis, and G. G. Wallace, *Journal of Solid State Electrochemistry* **6**:73 (2002).
- [6] G. M. Spinks, A. J. Dominis, G. G. Wallace, and D. E. Tallman, *Journal of Solid State Electrochemistry* **6**:85 (2002).
- [7] G. Williams, A. Gabriel, A. Cook, and H. N. McMurray, *Journal of the Electrochemical Society* **153**:B425 (2006).
- [8] R. J. Holness, G. Williams, D. A. Worsley, and H. N. McMurray, *Journal of the Electrochemical Society* **152**:B73 (2005).
- [9] A. Gabriel, N. J. Laycock, H. N. McMurray, G. Williams, and A. Cook, *Electrochemical and Solid State Letters* **9**:B57 (2006).
- [10] B. Wessling, *Synthetic Metals* **85**:1313 (1997).
- [11] Y. Y. Wang and X. L. Jing, *Polymer Testing* **24**:153 (2005).
- [12] M. X. Wan, *Journal of Polymer Science Part a-Polymer Chemistry* **30**:543 (1992).
- [13] D. K. Moon, M. Ezuka, T. Maruyama, K. Osakada, and T. Yamamoto, *Macromolecules* **26**:364 (1993).
- [14] L. A. P. Kane-Maguire, A. G. MacDiarmid, I. D. Norris, G. G. Wallace, and W. G. Zheng, *Synthetic Metals* **106**:171 (1999).
- [15] F. Fitrilawati and M. O. Tjia, *Optical Materials* **16**:361 (2001).
- [16] M. Stratmann, *Corrosion* **61**:1115 (2005).
- [17] J. S. Hammond, J. W. Holubka, and R. A. Dickie, *Journal of Coatings Technology* **51**:45 (1979).
- [18] A. Leng, H. Streckel, K. Hofmann, and M. Stratmann, *Corrosion Science* **41**:599 (1999).

Chapter 4

Polyaniline as an Inhibitor on Zinc

4.1 Introduction

Increasing zinc prices and the long term desire to phase out the use of strontium chromate has led to the need for alternative inhibitors that will extend the service life of galvanised strip steel products. Inherently conducting polymers (ICP) have been the focus of much recent interest as a means of corrosion control due to their ability to provide inhibition of cathodic delamination of organic coatings, and the topic has been reviewed [1, 2]. Polyaniline emeraldine salt (PAni-ES) produced by doping emeraldine base (PAni-EB) with para-toluenesulfonic acid (PAni-pTS) has proven to be a successful inhibitor of cathodic disbondment of organic coatings adherent to Zn substrates [3]. Additionally PAni-ES has been shown to effectively inhibit cathodic disbondment when adherent to Fe substrates as a pigment within an organic binder material [4] and also as a homogeneous coating in its own right [5]. The research conducted on Fe has led to a full mechanistic understanding of the dopant dependant cathodic disbondment inhibition provided by polyaniline at penetrative coating defects under atmospheric conditions. Here it is intended to apply a similar approach to polyaniline coatings on Zn substrates and determine what role (if any) the dopant plays.

PAni-ES is produced by protonating or “doping” partially oxidised PAni using a Bronsted acid. PAni-pTS has been chosen in a number of previous studies because it is readily available commercially in experimental quantities [3, 6, 7]. A series of model coatings were formulated comprising systematic variations in pigment volume fraction (Φ_{pa}) of PAni-pTS to explore how the quantity of in-coating PAni-pTS effects the kinetics of corrosion driven cathodic disbondment. In-situ SKP measurements were used to monitor the inhibitory effects of PAni-pTS on both the coating delamination kinetics and the under-film potentials resulting from coating-substrate interaction [8-12]. Williams et al [3] proposed that the inhibition provided by PAni-pTS at penetrative coating defects under conditions of high relative humidity (RH) arises primarily due to the Zn oxide layer formed at the substrate interface blocking cathodic O_2 reduction in this region. Additionally it was proposed that this effect is magnified and prolonged by the residual in-coating PAni-pTS acting to absorb the OH^- ions produced by cathodic O_2 reduction and inhibiting

alkaline dissolution of the Zn oxide barrier layer, because of the ability of PANi-ES to act as a pH buffer and limit any local pH increase [13].

In the work to be described here, polyaniline emeraldine base (PANi-EB) is systematically compared with PANi-ES doped with camphorsulphonic (HCS), phenylphosphonic (H_2PP) and phosphoric (H_3PO_4) acids. The findings are considered together with the previous study using polyaniline doped with paratoluenesulfonic acid (PANi-pTS) [3]. The intention is to provide a mechanistic overview of the dopant dependant inhibition of corrosion driven coating disbondment of organic coatings adherent to Zn substrates by PANi-ES.

The SKP is used to record spatially and temporally resolved interfacial electrochemical potentials at regions of intact (E_{intact}) and delaminated coating (E_{del}) across the surface of the coated zinc substrate to obtain the cathodic delamination kinetics under atmospheric conditions[14]. Atomic force microscopy (AFM) calibrated depth profiling secondary ion mass spectrometry (SIMS) is used to characterise chemical composition and growth kinetics of interfacial oxide or salt films [14, 15] developing at the coating substrate interface as a result of the dopant dependent PANi-ES. Finally, the inhibitory performance of PANi-ES is directly compared to the inhibitory performance of conventional strontium chromate corrosion inhibitors.

4.2 Experimental

Doping of the PANi-EB by camphorsulphonic (HCS), phenylphosphonic (H_2PP) and phosphoric (H_3PO_4) acids was undertaken following the method described in section 2.2.2. Formulation of the composite PANi-ES – PVB organic coatings also followed the method described in section 2.2.2. Pigment loading (pigment volume fraction) was varied systematically following equation 2.1 for PANi-ES coatings of each dopant. Values of Φ_{pa} were calculated using densities of 0.8 and 1.36gcm^{-3} for PVB [16] and PANi-pTS [17] respectively. Pigments were fully dispersed within the PVB resin by high shear mixing for 10 minutes prior to bar casting to create a $30 \pm 5\mu\text{m}$ dry film thickness.

Stratmann-type delamination cells were prepared following the method described within section 2.2.4.1. The SKP was used to fully monitor the corrosion-driven cathodic disbondment originating from the organic coating defects as described within section 2.3. All delamination experiments using the SKP were carried out in static air at 20°C and approximately 96% relative humidity (RH) in isopiestic equilibrium with a 0.86 mol dm^{-3} (5% w/v) aqueous NaCl reference solution. For corrosion driven coating delamination experiments the sample was first allowed to equilibrate at 96% RH for a period of 6 hours before an aliquot of 0.86 mol dm^{-3} NaCl was applied to create a 1mm thick electrolyte layer at the coating defect (note, not over the coating surface) and initiate corrosion.

PAni-CSA micro-films were cast at $0.5\mu\text{m}$ thicknesses onto Zn substrates prepared by abrading with 1200 grit paper as described within section 2.2.4.2. The PANi-CSA was subsequently over-coated with a $30 \pm 5\mu\text{m}$ PVB layer by bar coating. Optical changes in the PANi micro-film resulting from contact with the Zn were recorded photographically using a Canon Powershot G6 digital camera following the method described in section 2.4.

The nature of the zinc surface resulting from contact with PANi-ES beneath regions of adherent (intact) composite coatings was determined by mechanically peeling the organic coating from the metal substrate prior to measuring the surface film thickness using secondary ion mass spectrometry (SIMS). SIMS depth profiling was

carried out on 0.4mm^2 sample areas with a mass resolution of ± 0.1 Da using a Millbrook Instruments MC300 (MkII) Chemical Microscope as described in section 2.5. Prior to coating with PVB/PAni organic coatings, zinc substrates were in a polished condition. SIMS depth profiling of any surface oxide films were undertaken by converting SIMS ion current-time profiles in to ion current-depth profiles by periodically conducting calibration measurements of SIMS sputtering craters using a Topometrix Explorer atomic force microscope. SIMS current-depth profiles are assumed to accurately reflect oxide thickness at the coating substrate interface. Following the method employed by Williams et al [3], the absence of any demarcation between oxide film and substrate reflects the areas averaging of the non-uniform depth profiles. The depth at which normalised O^{2-} ion-current fell to half its maximum value (D_{50}) has been used as an approximate measure of mean oxide thickness.

4.3 Results and Discussion

4.3.1 PAni-EB in PVB on Zinc

PVB coatings containing a particulate dispersion of non-conducting polyaniline emeraldine base (PAni-EB) were applied to the surface of pure Zn substrates. Systematic increases in pigment loading were applied to explore the inhibitory properties of PAni-EB towards corrosion-driven cathodic disbondment. In a previous study involving the application of identical PAni-EB pigmented coatings to iron substrates, it was discovered that they were not capable of passivating the iron or modifying the iron-coating interface [4]. Accordingly it was concluded that PAni-EB does not act to slow the delamination kinetics to any extent, leading to the assumption that PAni-EB is non-protective.

PVB coatings containing PAni-EB pigment volume fractions (Φ_{EB}) of 0, 0.05, 0.10, 0.15 and 0.20 were applied to the Zn substrates and maintained at 96% RH. The transient E_{corr} profiles from an active artificial defect are shown in figure 4.1 (a) and (b) for Φ_{EB} 0 and 0.20 respectively. The PVB control coating shown in figure 4.1 (a) is the same control experiment as used throughout this chapter and is presented to allow the effects of PAni-EB pigmentation to be observed. Because of the active corrosion-driven cathodic delamination shown in these profiles, the full effect of PAni-EB can be visualised. To firstly consider the E_{corr} values in the delaminated region, it is clear that no deviation is observed from the recorded values in the control coating, and this remains constant under increasing PAni-EB pigment loading.

The E_{intact} values recorded for each of the PAni-EB coatings are characteristic of figure 4.1 (b) (Φ_{EB} 0.20), remaining near -0.4V vs. SHE independently of pigment loading. This is slightly different to the E_{intact} values recorded for the non-pigmented PVB control coating, which shows a value of -0.3V vs. SHE. This observation indicates that although the PAni-EB is not expected to interact with the Zn substrate as a PAni-ES coating would [3], there is a degree of interaction that causes a slight increase in negativity of E_{intact} .

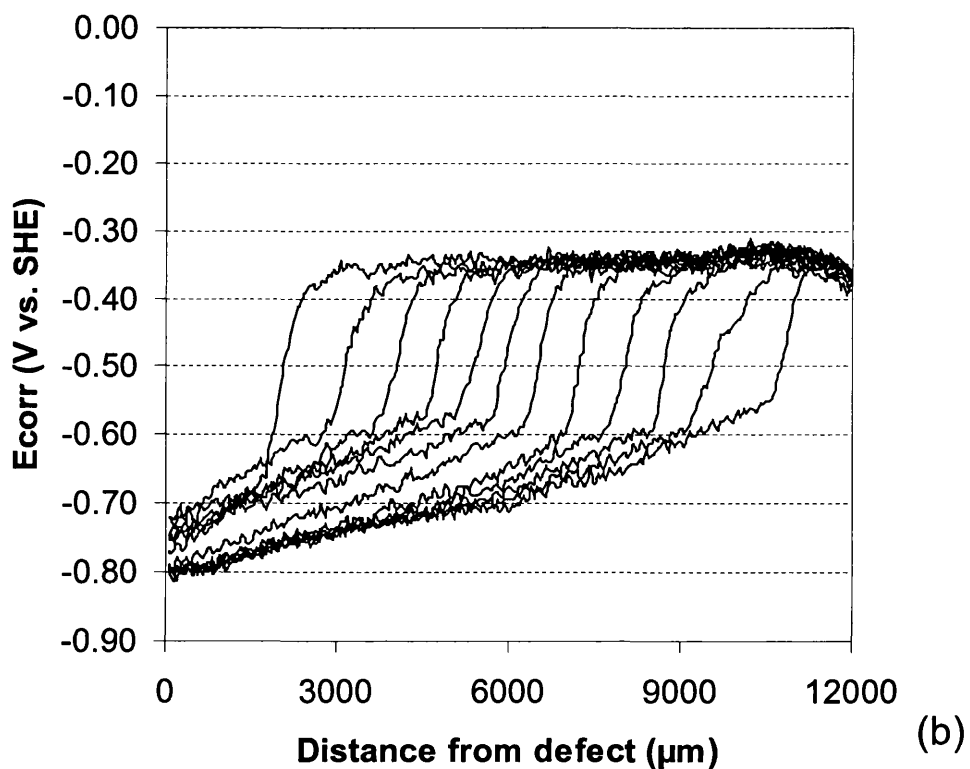
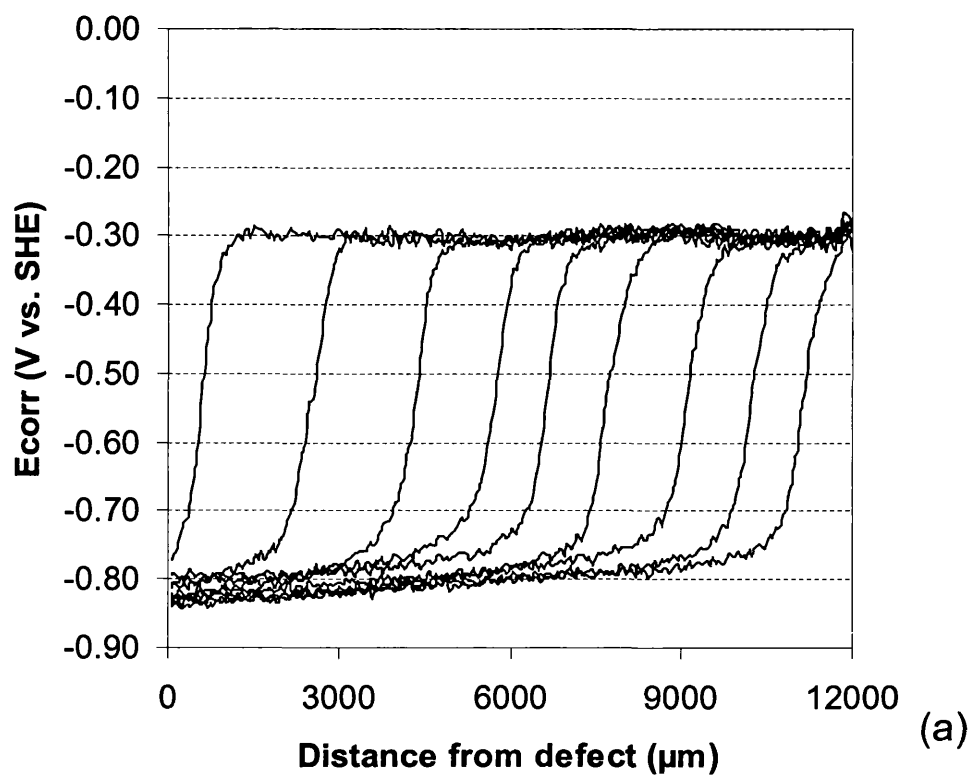


Figure 4.1. E_{corr} vs. distance from defect edge (x) profiles on Zn from 60 min and hourly intervals thereafter (a) for a $30\mu\text{m}$ PVB coating, (b) 0.20Φ PANi-EB-PVB.

The delamination kinetic summary plot of figure 4.2 shows the initial delamination rates for each of the Φ_{EB} tested. Also plotted on this summary plot is the PAni-pTS delamination kinetics measured by Williams et al using an identical experimental method [3]. This highlights the effectiveness of PAni-ES as an inhibitor of cathodic disbondment on zinc in direct comparison to the PAni-EB. The uninhibited control coating has an initial delamination rate of $22\mu\text{m min}^{-1}$ and the addition of PAni-EB to the organic layer is shown to slow this rate to approximately $15\mu\text{m min}^{-1}$ independently of pigment loading. In comparison to the PAni-pTS, the level of inhibition provided by the PAni-EB is poor.

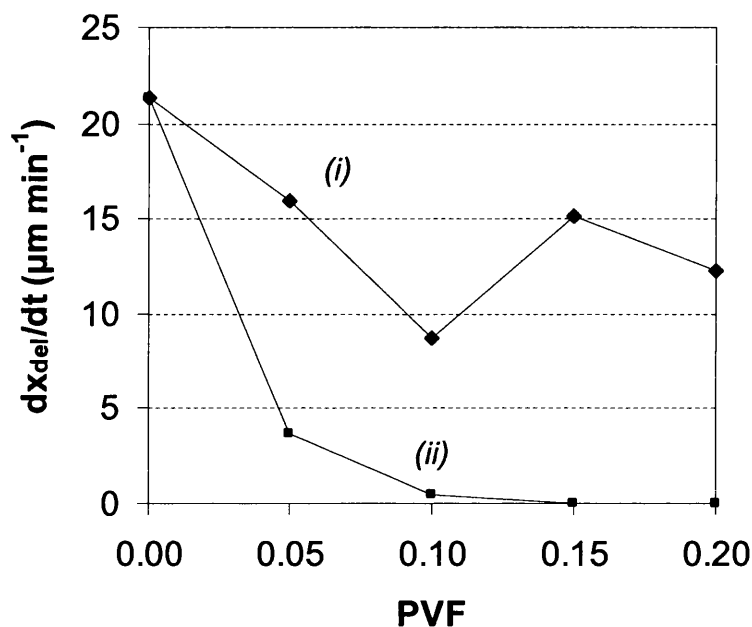


Figure 4.2. Summary plots of delamination rate (dx_{del}/dt) vs. PVF for (i) PAni-EB and (ii) PAni-pTS pigmented $30\mu\text{m}$ PVB coatings on Zn.

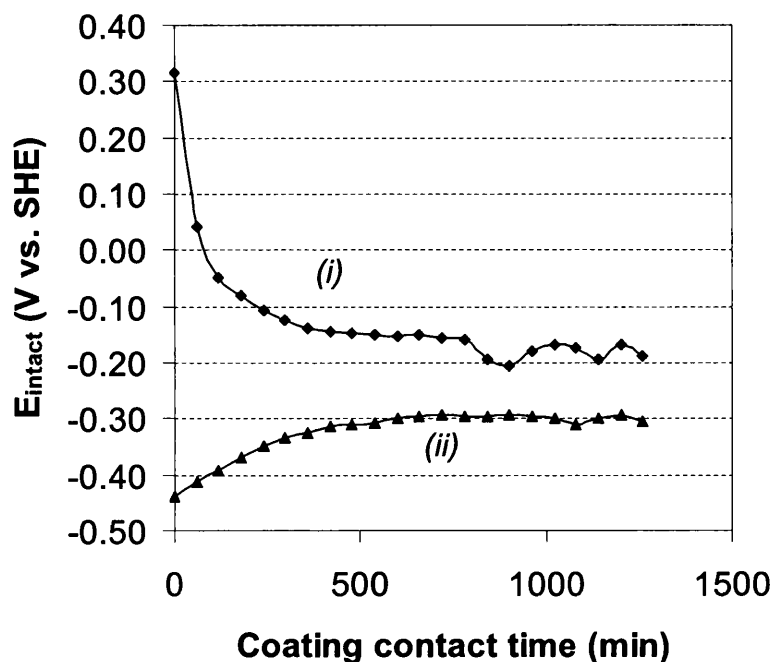


Figure 4.3. E_{intact} vs. contact time comparison between (i) 0.25Φ PANi-pTS and (ii) 0.20Φ PANi-EB composite coatings adherent to Zn.

In terms of interfacial activity between the PANi-EB containing coatings and the zinc substrate, the PANi-EB has little effect to E_{corr} as a function of contact time in comparison to the findings of Williams et al [3] as shown within figure 4.3. The average E_{corr} values as a function of time for the PANi-pTS pigmented coatings adherent to pure zinc shows that the potential of the coating-substrate interface becomes more negative as the polyaniline is electronically isolated from the zinc surface. It was proposed by Williams et al that this occurs due to the reduction of PANi-pTS when adherent to the Zn surface [3]. Of interest within figure 4.3 is that the PANi-EB shown in profile (ii) does not follow this trend. E_{intact} of PANi-EB coated Zn remain close to the expected value for un-inhibited PVB throughout. This suggests that PANi-EB is inert, and indicates that any inhibition arising as a result of PANi-EB may not be electrochemical in origin.

4.3.2 Visualisation of Interfacial Electrochemistry

The work to be described within this section is designed to provide support for the propositions made by Williams et al regarding the way in-coating particulate PANi-pTS interacts with Zn [3]. An important discovery within the published work was the development of a Zn oxide layer at the substrate-coating interface. Williams et al found that this growth occurred within 6hrs of coating application and the thickness attained was proportional to the amount of in-coating PANi-pTS. Over a similar period of time the potential (E_{intact}) measured over the intact (un-delaminated) coated surface was seen to fall from a value approaching E^0 PANi-pTS (ca. 0.4V vs. SHE) to a value characteristic of PVB coated zinc (-0.2V vs. SHE). This led to the proposition that oxide growth resulting from the PANi-pTS-Zn interaction stops when the portion of PANi-pTS electrically connected with the zinc surface through charge percolation becomes electrochemically reduced to non-conducting leucoemeraldine, and is therefore electrically insulated from the zinc surface.

To investigate and provide further evidence to support this theory, 0.50 μm films of PANi-CSA were solution cast onto Zn following the method outlined in section 2.2.4 and the micro-film thickness was verified using depth calibrated AFM. Each state that PANi can exist in has its own representative colour and the technique of solution casting PANi-ES micro-films directly to the metal surface allows any PANi state changes to be visualised through successive optical colour changes. The main states of interest here are the green PANi-ES, the blue PANi-EB and the clear leucoemeraldine.

If the PANi – Zn interactions proposed by Williams et al at regions of intact coating are correct, then the PANi-ES layer will be reduced to leucoemeraldine. This state change will include a representative colour change from green to clear, indicating the reduction. This colour change could not be seen by Williams et al when using polyaniline pigmented PVB coatings due to the opaqueness of the particulate dispersion. The results of applying a thin ($\sim 50\mu\text{m}$) homogeneous PANi-ES film to the zinc substrate is shown in figure 4.4.

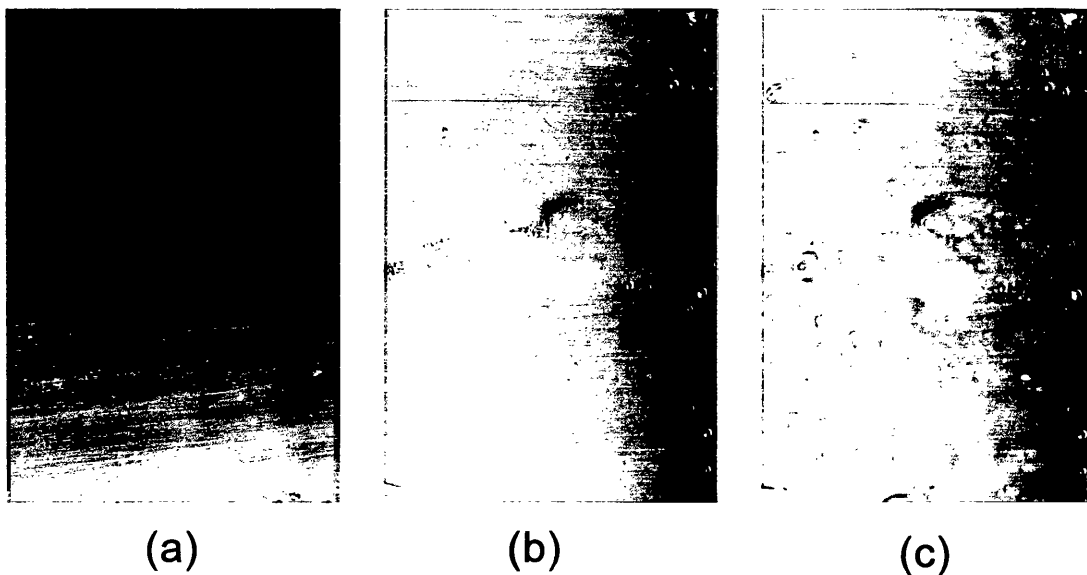
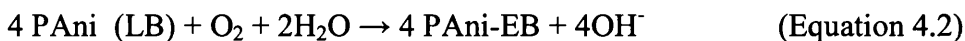
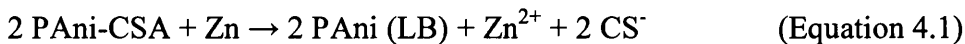


Figure 4.4. Time dependent images of 0.50 μm PANi-CSA - 30 μm PVB bilayer organic coatings adherent to (a) Fe 0hrs, (b) Zn 0hrs and (c) Zn 72hrs.

Upon initial application of the PANi-CSA coating via solution casting from M-Cresol, the PANi is green in colour. Directly upon contact with the zinc surface, the solution of PANi-ES rapidly changes clear within a few seconds, signifying an immediate state change to leucoemeraldine. The polyaniline coating remains this colour for considerable time, even after over-coating with PVB layer as used as the experimental top-coat. Figure 4.4 (a) shows an example photograph of an identically prepared 0.50 μm PANi-CSA-PVB duplex coating system adherent to an Fe substrate. This has been used as an example within the figure because of the difficulty of obtaining an optical image of PANi-CSA on Zn due to the speed of reduction. The intact coating stability of PANi-CSA adherent to Fe has been proven elsewhere, and accordingly it can be considered an accurate representation of the true colour of a PANi-CSA micro-film [5].

Upon initial application of the PANi-CSA solution to the prepared Zn substrate, the green PANi-ES is immediately reduced to the clear leucoemeraldine following reaction (4.1) written below. This change is depicted within figure 4.4 (b), which shows a 0.50 μm homogeneous PANi-CSA film adherent to the zinc substrate directly after the application of the PVB top-coat. Comparison between figure 4.4 (a) and (b)

highlights the extent of the polyaniline colour change resulting from the PANi-ES reduction to leucoemeraldine.



Once the PANi coating is adherent to the Zn substrate, and fully reduced to leucoemeraldine via reaction (4.1), the leuco state is then re-oxidised to the blue PANi-EB via reaction (4.2). However, in contact with the Zn substrate, PANi-EB is unlikely to become fully re-oxidised because of reaction (4.3). Consequently the blue colour of PANi-EB is not fully developed, depicted by figure 4.4 (b) by the slight blue tint exhibited by the PANi film. Nevertheless, the Zn(OH)₂ layer produced by reaction (4.3) will thicken over time and the facility of reaction (4.3) will eventually decrease, allowing the blue colour of the coating to intensify gradually over time. This signifies the gradual PANi state change of the intact coating to increase the amount of PANi-EB present.

4.3.3 PANi-ES – PVB Composite Coatings

4.3.3.1 SKP Potentiometry

Williams et al discovered that directly upon application of the PANi-pTS composite coating, E_{intact} recorded by the SKP showed a value of 0.4V vs. SHE [3]. This positive potential value is within the range reported for PANi-ES [3], and was seen to rapidly fall within ~6hrs to -0.25V vs. SHE, which is in the range previously reported for non-inhibited PVB coated Zn [18, 19]. This data is reproduced within figure 4.8 (a), and the proposed reason for this decay in E_{intact} is attributed to the rapid oxidation of Zn and the corresponding reduction of PANi-ES to PANi-LB via reaction (1) in section 4.3.2.

Following these published findings of PANi-pTS it was thought prudent to obtain equivalent potentiometric data for PANi-CSA, PANi-PP and PANi-H₃PO₄. Accordingly the methodology used previously [3], was repeated for each individual

PAni-ES, and 0.25 Φ of each PAni-ES was coated onto prepared Zn substrates. Each sample was scanned using the SKP over intact regions of coating immediately after the ethanolic component of the organic coating had fully dissipated in air (five minutes after casting), and the organic coating could be deemed solid. It is unlikely that the relative humidity within SKP chamber would have reached its equilibrium conditions of 96 %RH during the initial scan.

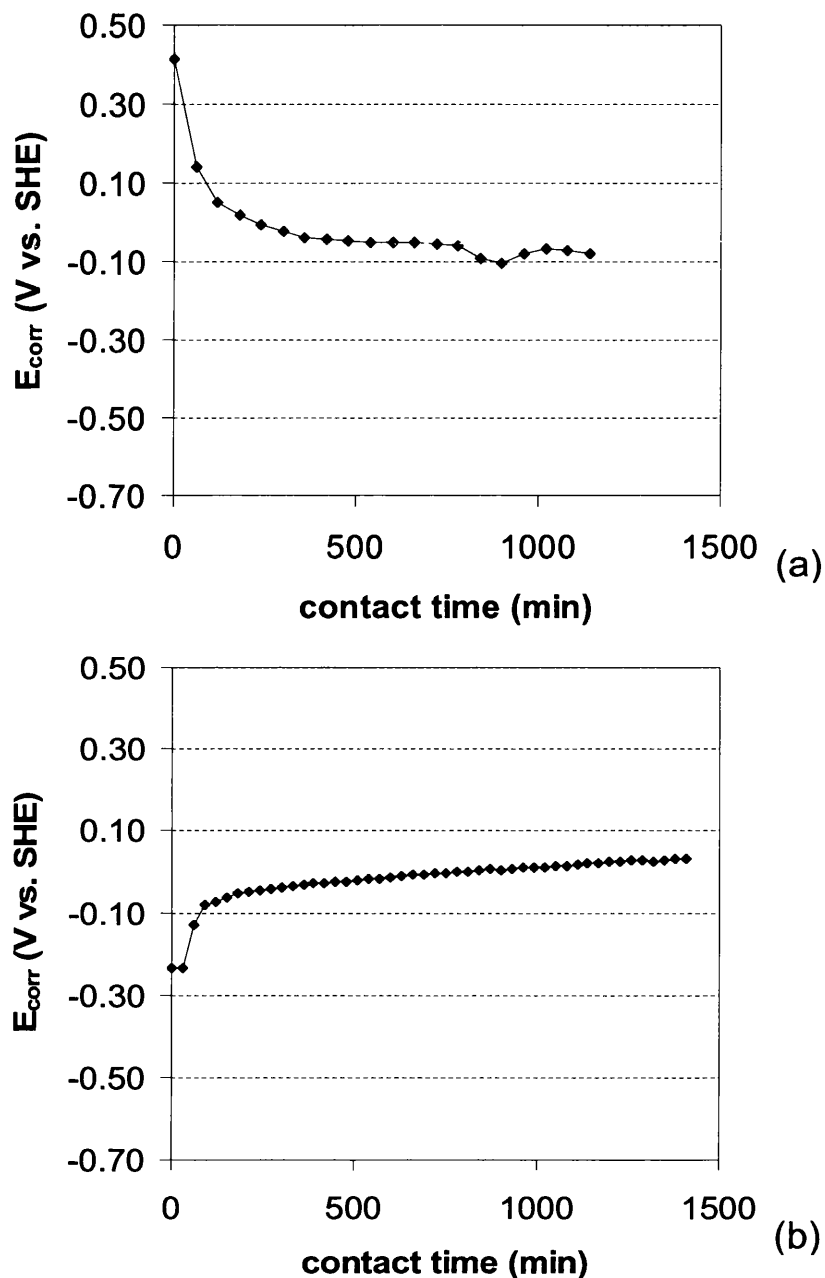


Figure 4.5. Plots of E_{intact} vs. contact time for 0.25 Φ PAni-ES PVB composite coatings adherent to Zn substrates key:- (a) PAni-pTS [3], (b) PAni-CSA.

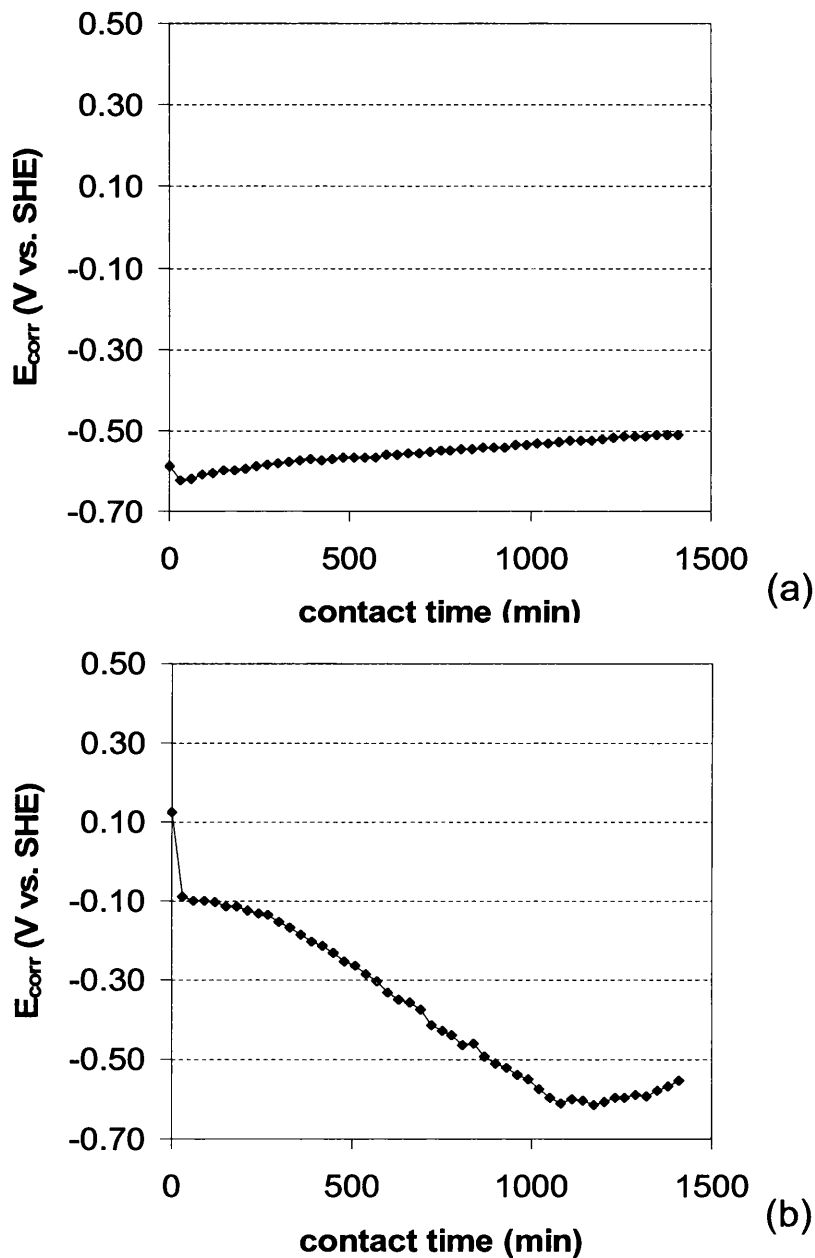


Figure 4.6. Plots of E_{intact} vs. contact time for 0.25Φ PANi-ES PVB composite coatings adherent to Zn substrates key:- (a) PANi-PP, (b) PANi-H₃PO₄.

E_{intact} as function of contact time for PANi-pTS, PANi-CSA, PANi-PP and PANi-H₃PO₄ are plotted within figures 4.5 (a), (b) and 4.6 (a), (b) respectively. Comparing the effect of contact time for each of the four differently doped PANi-ES coatings it is clear that the only coating that shows a potential close to that expected for polyaniline (0.40 - 0.50V vs. SHE) is the PANi-pTS, although PANi-H₃PO₄ does

clearly show a decreasing E_{intact} as a function of contact time over the first 17hrs. The highest potential recorded in this case is positive and approaching the PANi-ES potential at ca. 0.10V vs. SHE, and thirty minutes later E_{intact} is shown to have dropped a further 0.2V vs. SHE. This sharp drop of E_{intact} over such a short space of time suggests that in the case of PANi- H_3PO_4 , it is possible that the majority of proposed reduction of the polyaniline to PANi-LB has taken place within the fifteen minutes or so taken to coat the substrate and set up the SKP to record the first scan. The sharp drop in E_{intact} within the first recorded thirty minutes of contact time makes it possible to believe that it is probable the PANi- H_3PO_4 PVB composite coating – Zn interface may have been initially close to the PANi-ES potential of $\sim 0.5\text{V}$ vs. SHE.

In the case of the PANi-CSA and the PANi-PP composite coatings, very little change of E_{intact} has been captured. In both cases the recorded value of E_{intact} directly after coating application (15 minutes time lag due to setting up time) is nowhere near the PANi potential. One possible explanation for this is that any interfacial electrochemistry between the PANi-ES and the coating is sufficiently fast to render the PANi-ES fully reduced and non-conducting within the time taken to mount the sample within the SKP chamber.

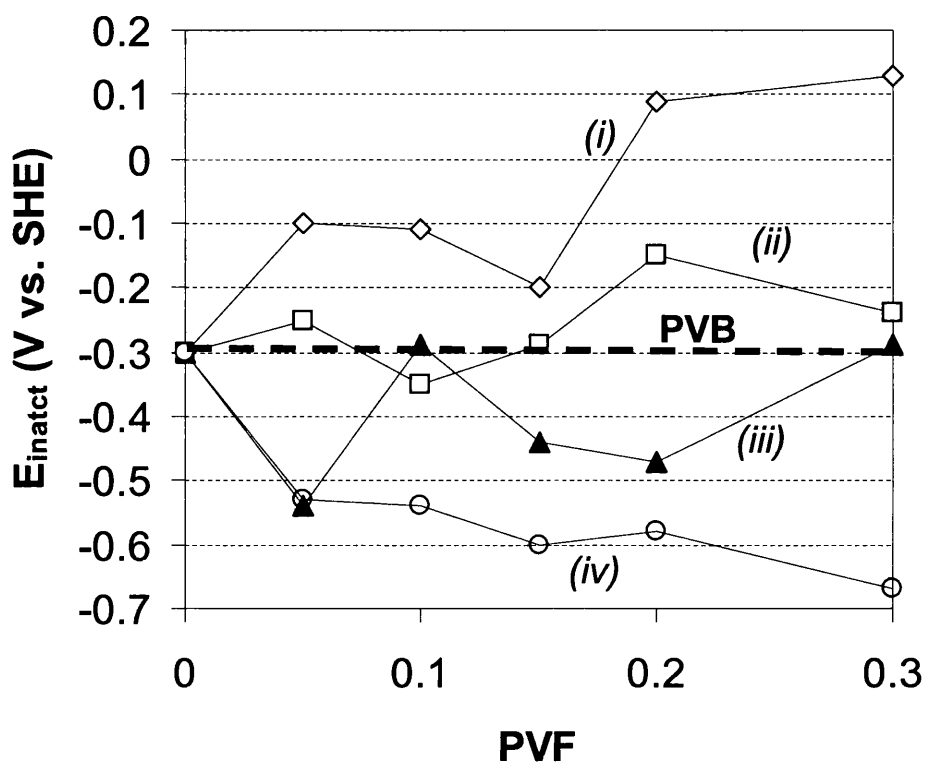


Figure 4.7. Summary plot of time independent E_{intact} as a function of pigment volume fraction after 48hrs exposure to 96% RH, key:- (i) PANi-CSA, (ii) PANi-pTS [3], (iii) PANi-PP and (iv) PANi-H₃PO₄.

Figure 4.7 shows a comparison of summary plots of time independent E_{intact} as a function of pigment volume fraction (Φ) for PANi-ES of all dopants. Each summary plot is representative of E_{intact} recorded under equilibrium conditions, i.e. after 48hrs under the experimental humidity. Figure 4.7 (ii) shows the E_{intact} of PANi-pTS to remain consistently at ca. -0.30V vs. SHE regardless of PVF, indicating it has been reduced to a non-conducting form at the coating substrate interface. The non-conducting nature of this interface will create a situation where further interfacial electron transfer between any remaining in-coating PANi-pTS and the Zn substrate can not occur.

From PANi-PP data within figure 4.7 it can also be said that PANi-PP follows a similar rule to the PANi-pTS, although potentials are pushed to a slightly lower level, although are generally near identical to non-inhibited PVB coated Zn independently of PVF. The two PANi-ES that do not follow this trend so obviously are the PANi-

CSA coatings and the PANi-H₃PO₄ coatings. In both of these cases there is a marked difference in the effect towards E_{intact} . PANi-CSA causes a consistent rise in E_{intact} as a function of increasing PVF, whereas PANi-H₃PO₄ causes a marked decrease in E_{intact} also as a function of increasing PVF. The PANi-CSA seems to be providing a small level of passivity at the Zn-coating interface. The rise of E_{intact} is too small to be considered ennoblement, and the PANi-ES potential is not being reached. Therefore the degree of passivation may not be providing a high level of corrosion protection in itself. Conversely to this, the PANi-H₃PO₄ system does not cause ennoblement, instead it could be considered aggressive towards the Zn substrate upon moisture uptake by the organic coating reaching the coating-substrate interface.

It is unlikely that the PANi-H₃PO₄ is capable of forming a Zn phosphate layer on the surface at such a low pH as would be expected at the coating substrate interface. The regions of intact coating will be of a low pH because of the dopant containing polymer (pH 5) rather than the higher alkaline conditions required to form the Zn phosphate layer (pH 11). In the case of PANi-H₃PO₄ it has already been shown in figure 4.6 (b) that it takes approximately seventeen hours for E_{intact} to fall and equilibrate to these low potentials of -0.5V vs. SHE. Figure 4.7 confirms that within ~0.10V vs. SHE, these low values of E_{intact} are consistent independently of pigment loading. Figure 4.6 (a) and figure 4.7 (iv) can be summarised simply by the slow reactivity of PANi-H₃PO₄ with the underlying substrate, highlighted because of low reliance of pigment loading effecting E_{intact} .

4.3.3.2 Oxide Growth Studies

PAni-ES coatings of varying pigment volume fractions were mechanically stripped (peeled) from polished Zn substrates after holding for periods of 24hrs under 96% RH. Upon removal of the PANi-ES containing organic coatings from their Zn substrates it was discovered that both PANi-PP and PANi-H₃PO₄ composite coatings do not produce a visibly noticeable oxide film on the Zn surface. Conversely to this, the PANi-CSA composite coatings do produce a visible white oxide film, as does the PANi-pTS containing organic coatings described by Williams et al [3].

Figures 4.8 – 4.11 show a series of normalised O^{2-} ion-current vs. depth profiles obtained from depth calibrated SIMS sputtering of the oxide covered Zn surface resulting from particulate PANi-pTS [3], PANi-CSA, PANi-PP and PANi- H_3PO_4 contact respectively. The depth at which normalised O^{2-} ion-current fell to half its maximum value (D_{50}) has been used as an approximate measure of mean oxide thickness. Following the method employed by Williams et al [3], the absence of any demarcation between oxide film and substrate reflects the area averaging of the non-uniform depth profiles. The depth at which normalised O^{2-} ion-current fell to half its maximum value (D_{50}) has been used as an approximate measure of mean oxide thickness in each case.

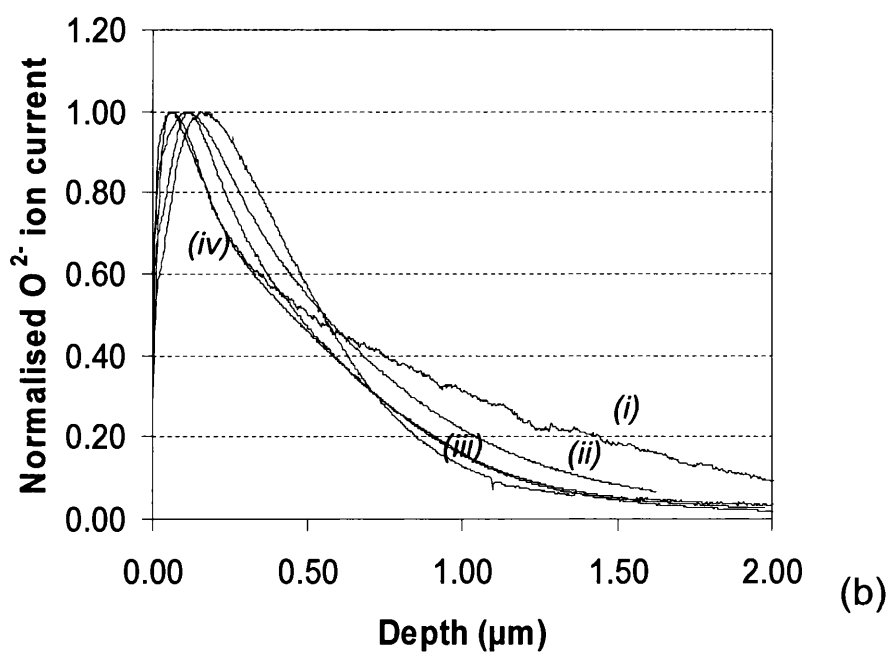
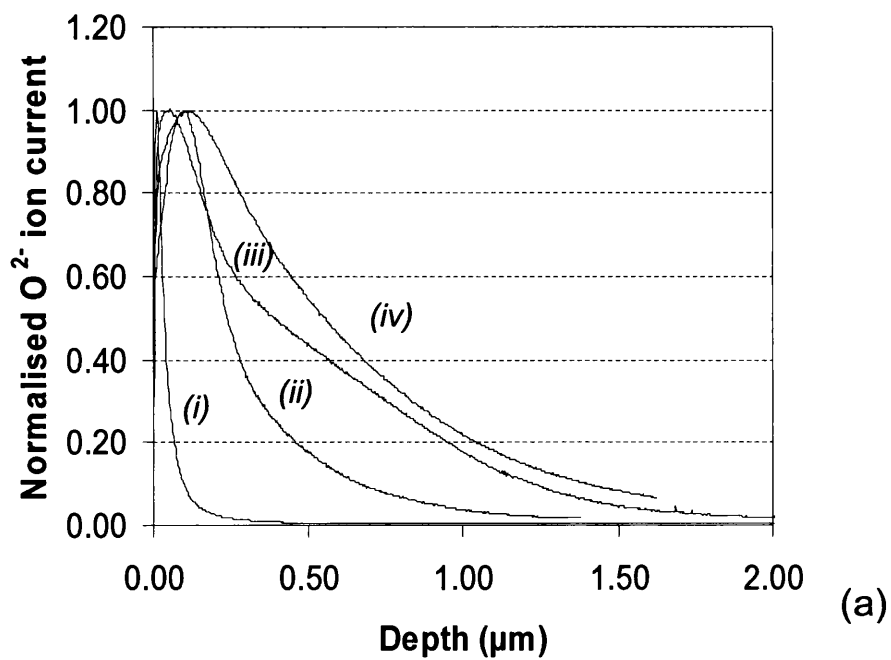


Figure 4.8. Normalised SIMS O^{2-} ion current vs. depth profiles for Zn oxide layers generated by holding PANi-pTS coated Zn at 96% RH and 20°C. (a) holding time 24hrs coating key Φ_{pa} : (i) 0, (ii) 0.10, (iii) 0.25 and (iv) 0.30. (b) Coating Φ_{pa} 0.30 holding time key (i) 24, (ii) 48, (iii) 90 and (iv) 164 h.

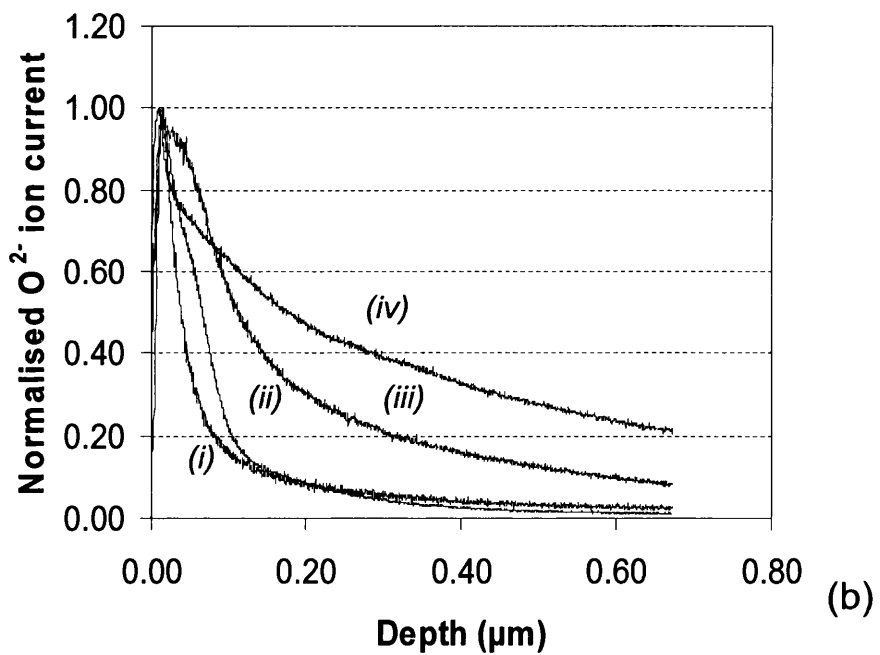
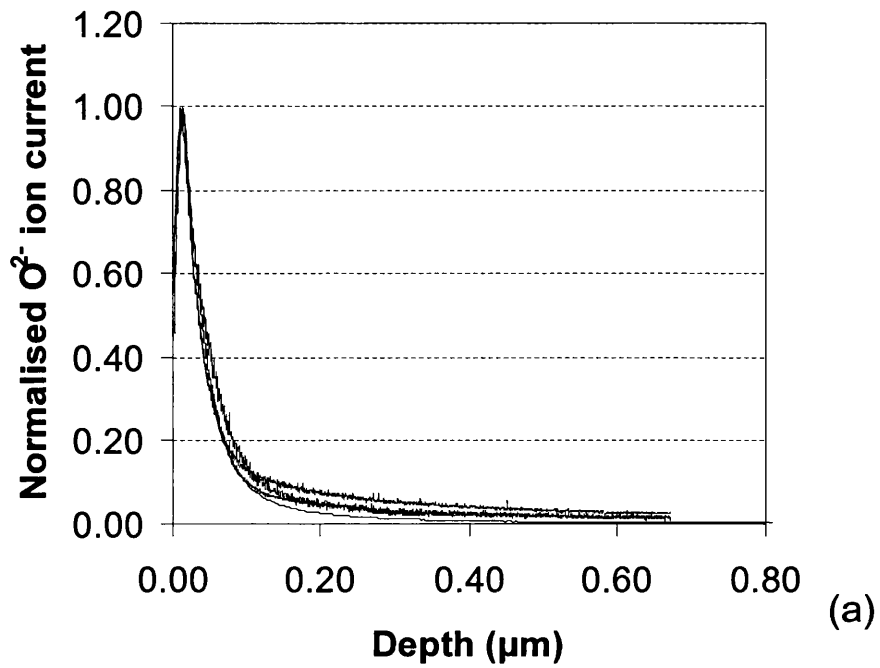


Figure 4.9. Normalised SIMS O^{2-} ion current vs. depth profiles for Zn oxide layers generated by holding PANi-CSA coated Zn at 96% RH and 20°C. (a) holding time 24hrs coatings Φ_{pa} : 0, 0.10, 0.20 and 0.30. (b) Coating Φ_{pa} 0.30 holding time key (i) 24, (ii) 72, (iii) 170 and (iv) 236 h.

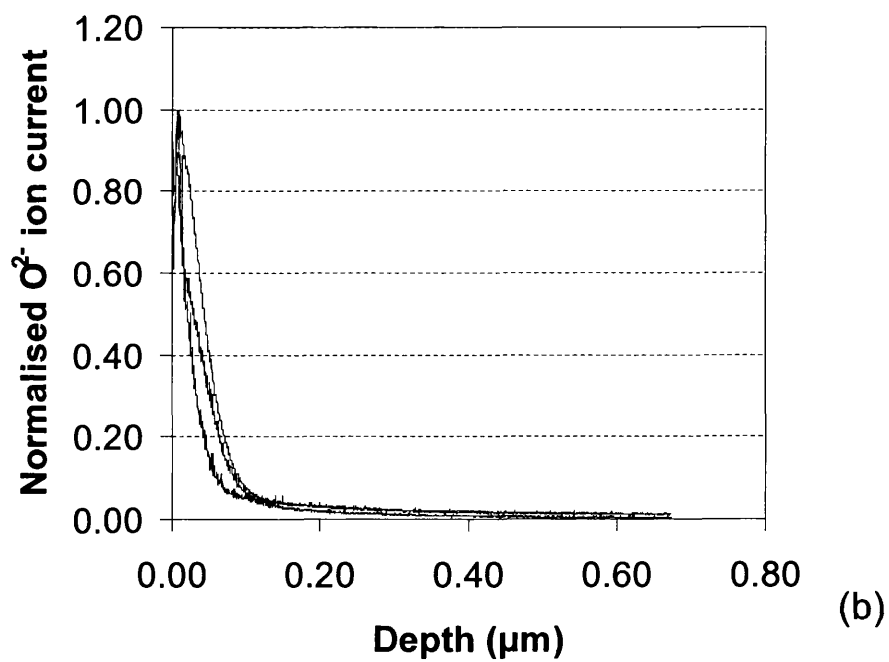
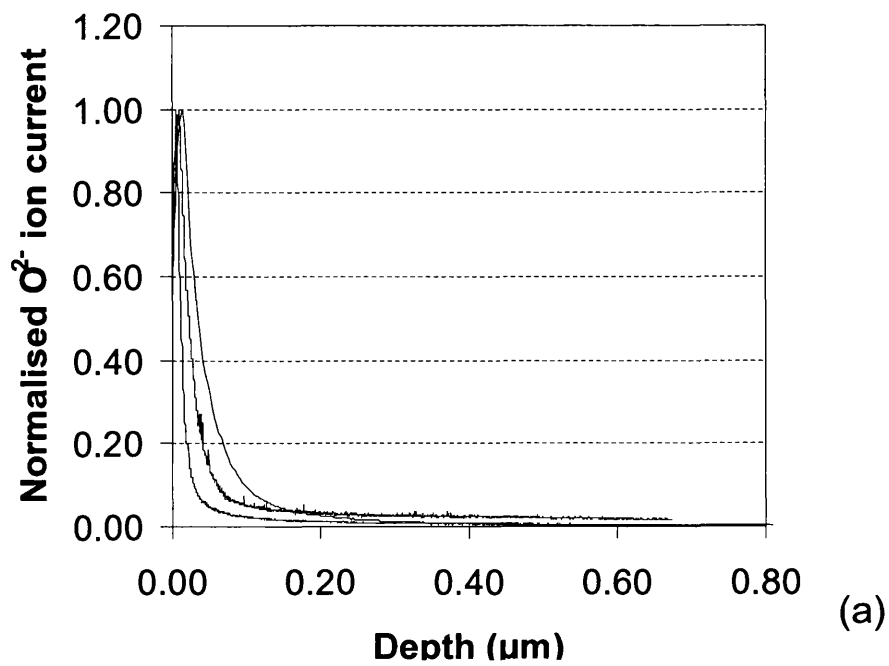


Figure 4.10. Normalised SIMS O^{2-} ion current vs. depth profiles for Zn oxide layers generated by holding PANi-PP coated Zn at 96% RH and 20°C. (a) holding time 24hrs coatings Φ_{pa} : 0, 0.10 and 0.30. (b) Coating Φ_{pa} 0.30 holding times 48, 96 and 240 h.

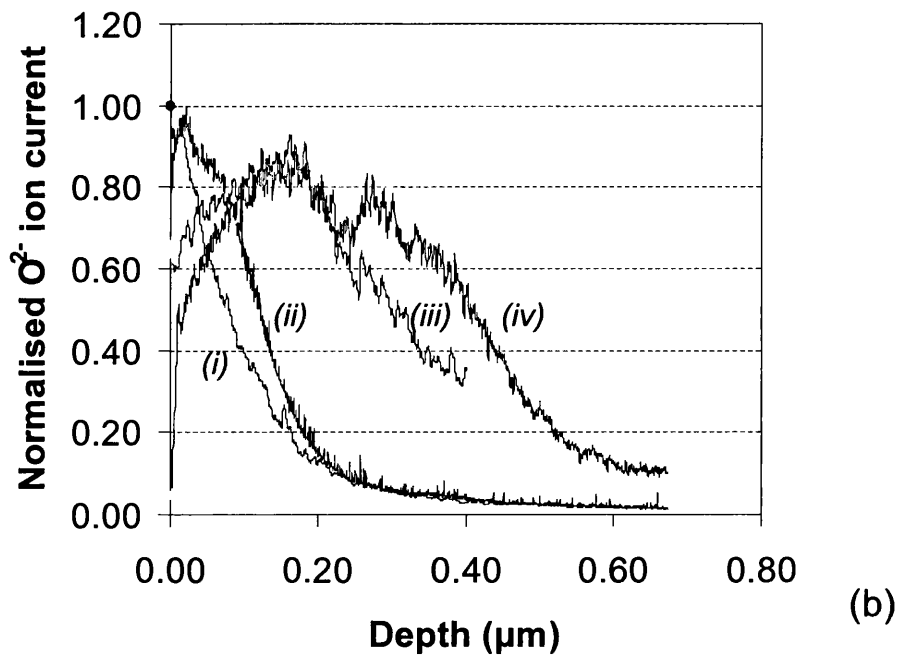
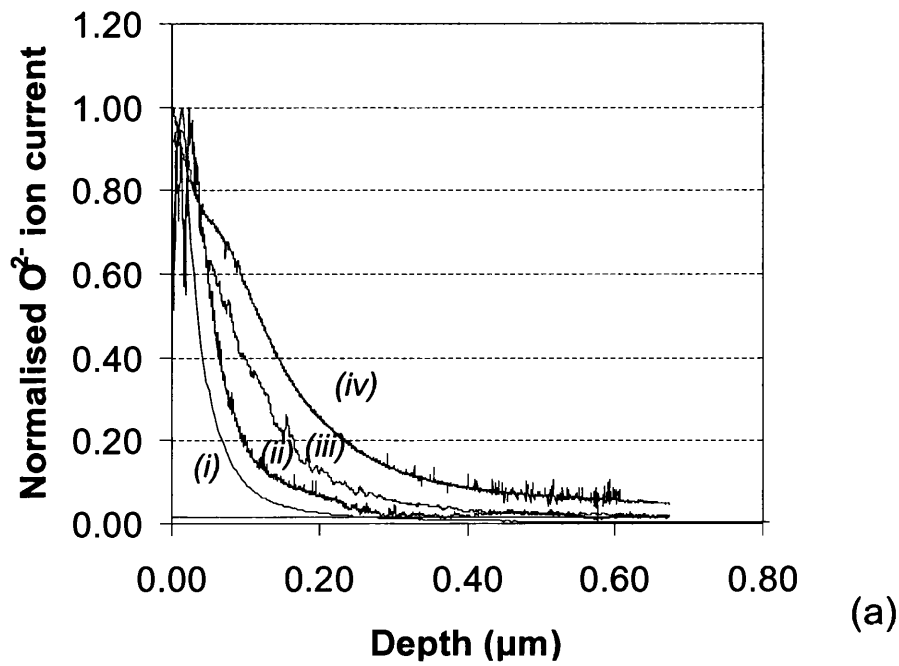


Figure 4.11. Normalised SIMS O^{2-} ion current vs. depth profiles for Zn oxide layers generated by holding PANi- H_3PO_4 coated Zn at 96% RH and $20^\circ C$. (a) holding time 24hrs coating key Φ_{pa} : (i) 0, (ii) 0.20, (iii) 0.25 and (iv) 0.30. (b) Coating Φ_{pa} 0.30 holding time key (i) 24, (ii) 96, (iii) 216 and (iv) 240 h.

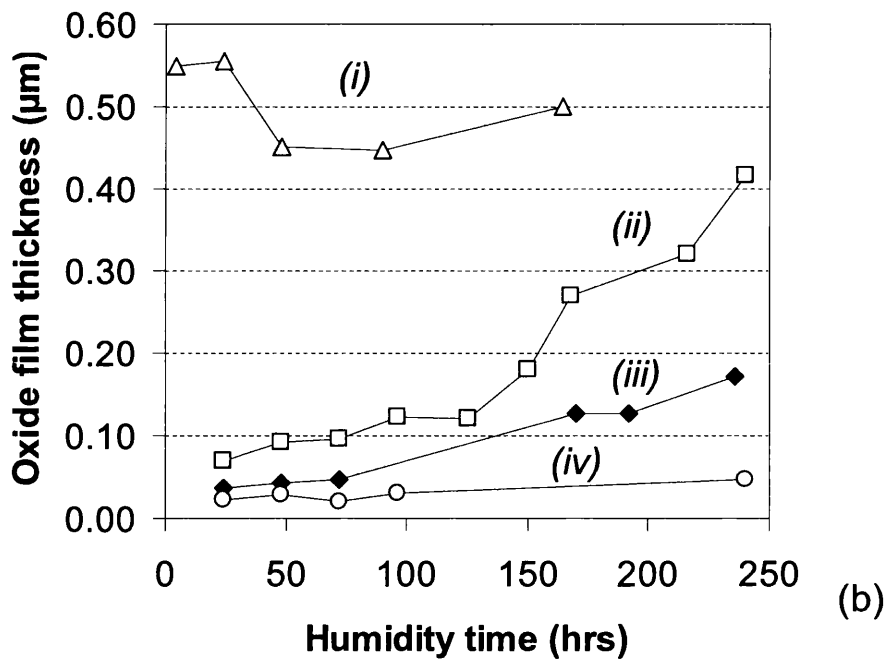
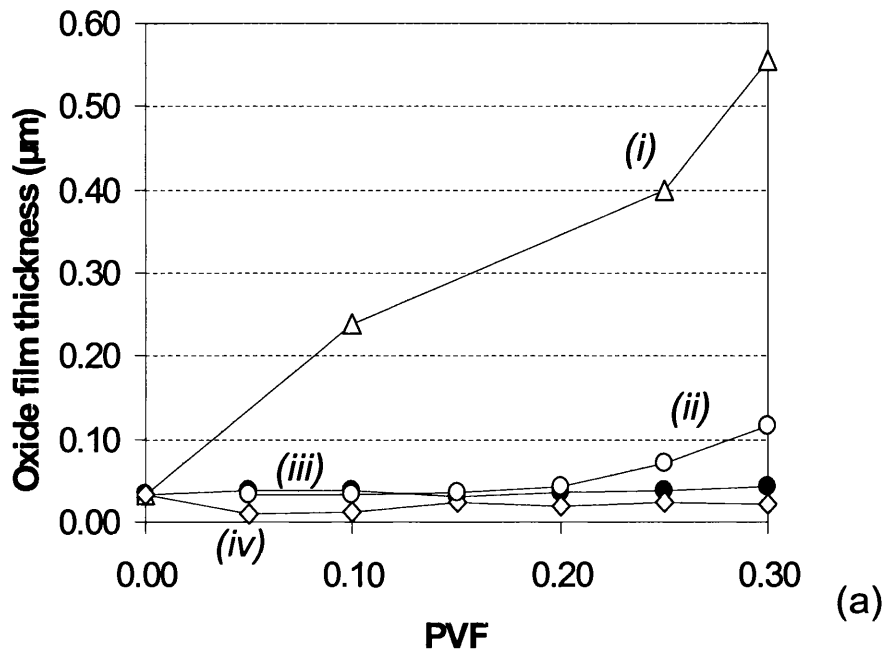


Figure 4.12. Summary plot of oxide layer thickness (D_{50}) induced on Zn substrates (a) as a function of Φ_{ES} after 24hrs exposure and (b) as a function of contact time (Φ_{PA} 0.30). Key: (i) PANi-pTS [3], (ii) PANi-H₃PO₄, (iii) PANi-CSA and (iv) PANi-PP.

A summary plot highlighting the differences between the PANi-ES induced interfacial oxide thicknesses is shown in figures 4.12. The effect of 24hrs exposure to 96% RH towards oxide growth as a function of PVF is summarised in Figure 4.12

(a). It is clear from this summary the only PANi-ES to increase the thickness of the interfacial oxide is the PANi-pTS, which causes a linear increase in oxide thickness with increasing pigment loading. The other three polyaniline salts, PANi-CSA, PANi-PP and PANi-H₃PO₄ all show a near identical trend. The increasing Φ in these cases does not cause a marked increase in oxide thickness from that recorded for the control PVB coating system.

The summary plot of figure 4.12 (b) shows the effect of coating contact time on the induced oxide thickness. High PVF (Φ_{PA} 0.30) coatings were applied to the Zn substrates and subsequently held at 96% RH. This plot reveals that in the case of the PANi-pTS system, contact time does not cause an increase in the oxide thickness [3]. The other three PANi-ES with perhaps the exception of PANi-PP show an increase in oxide growth that rapidly increases only after the contact time is in excess of 100hrs. This would be significant if the cathodic delamination experiments employed were of that time scale, but only that first 48hrs of oxide growth shown within figure 4.12 (b) is significant in determining the inhibition mechanisms taking place.

To summarise the results of SIMS oxide growth studies of pre-oxidised zinc surfaces, it is clear that the only PANi-ES capable of creating a substantially thick interfacial oxide layer is PANi-pTS. All other polyaniline salts investigated here are shown only to be capable of producing a relatively thin surface oxide layer within the time-scale employed for cathodic delamination studies.

4.3.3.3 Delamination of PANi-ES - PVB Composite Coatings

The kinetics and mechanisms by which uninhibited organic coatings become cathodically delaminated from Zn substrates have been extensively discussed within section 1.3.3.1 and elsewhere [8, 12, 18]. The cathodic delamination of non-pigmented (control) PVB coating from a Zn substrate, rapidly initiates following electrolyte contact to the artificial defect in a period of less than 60 min. Corrosion-driven cathodic disbondment of all coatings within this section were recorded using the SKP. The E_{corr} profile recorded for the PVB control coating is shown in figure 4.13 (a) and it shows that E_{intact} remains constant at -0.30V vs. SHE as discussed previously in this section. This E_{corr} profile also shows that in the delaminated region

the potential falls to approximately -0.8V vs. SHE, i.e. the potential for freely corroding Zn.

An example of a cathodically disbonded 0.05Φ PANi-ES coating from a Zn substrate is shown photographically in figure 4.13. This photograph is typical of the extent of cathodic disbondment occurring on Zn substrates for low PVF composite coatings after 48hrs of electrolyte contact. It is clear from this photograph that a considerable amount of cathodic delamination has occurred, and this is confirmed with the E_{corr} profiles within figures 4.14 and 4.15.

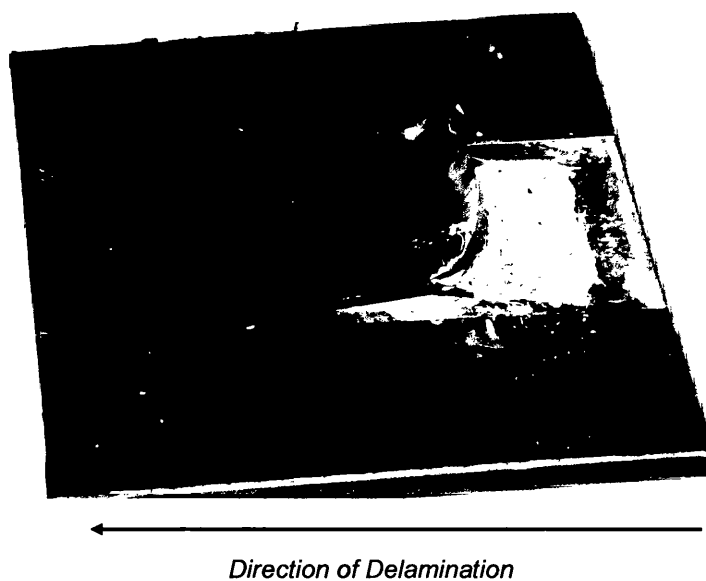


Figure 4.13. Photograph of a delaminated 0.05Φ PANi-ES composite coating on a Zn substrate after 48hrs cathodic delamination testing in the SKP.

Figure 4.14 and figures 4.15 (a) and (b) show the corresponding E_{corr} profiles for 0.05Φ PANi-CSA, PANi-PP and PANi- H_3PO_4 respectively, and in each case there is a clear demarcation between the non-delaminated (intact) region of coating and the delaminated region at ca. -0.8V vs. SHE in the case of PANi-PP and PANi- H_3PO_4 composite coatings, and -0.6V vs. SHE in the case of the PANi-CSA composite coating, which were typical in all case independently of Φ .

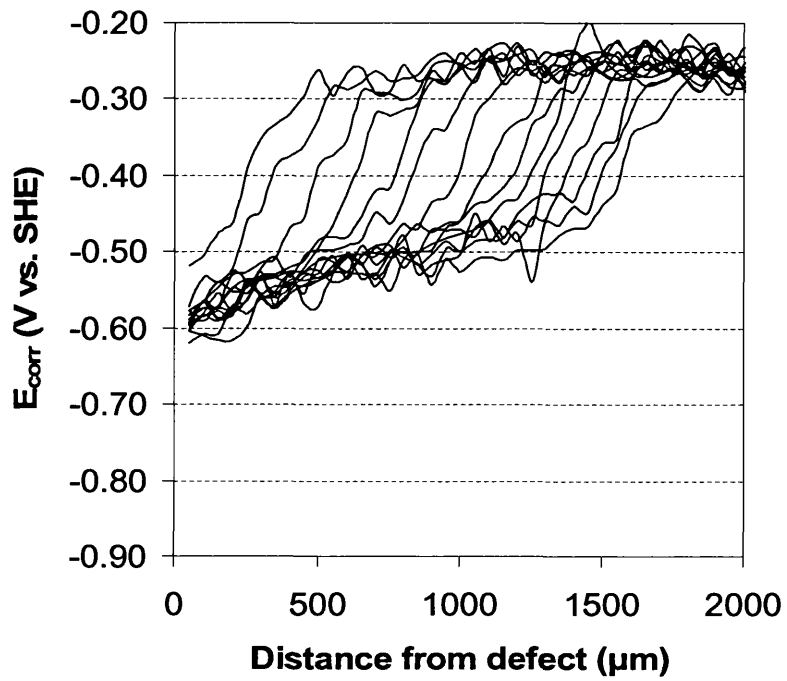


Figure 4.14. E_{corr} vs. distance for defect edge (x) profiles on Zn for a 0.05Φ PANi-CSA coating.

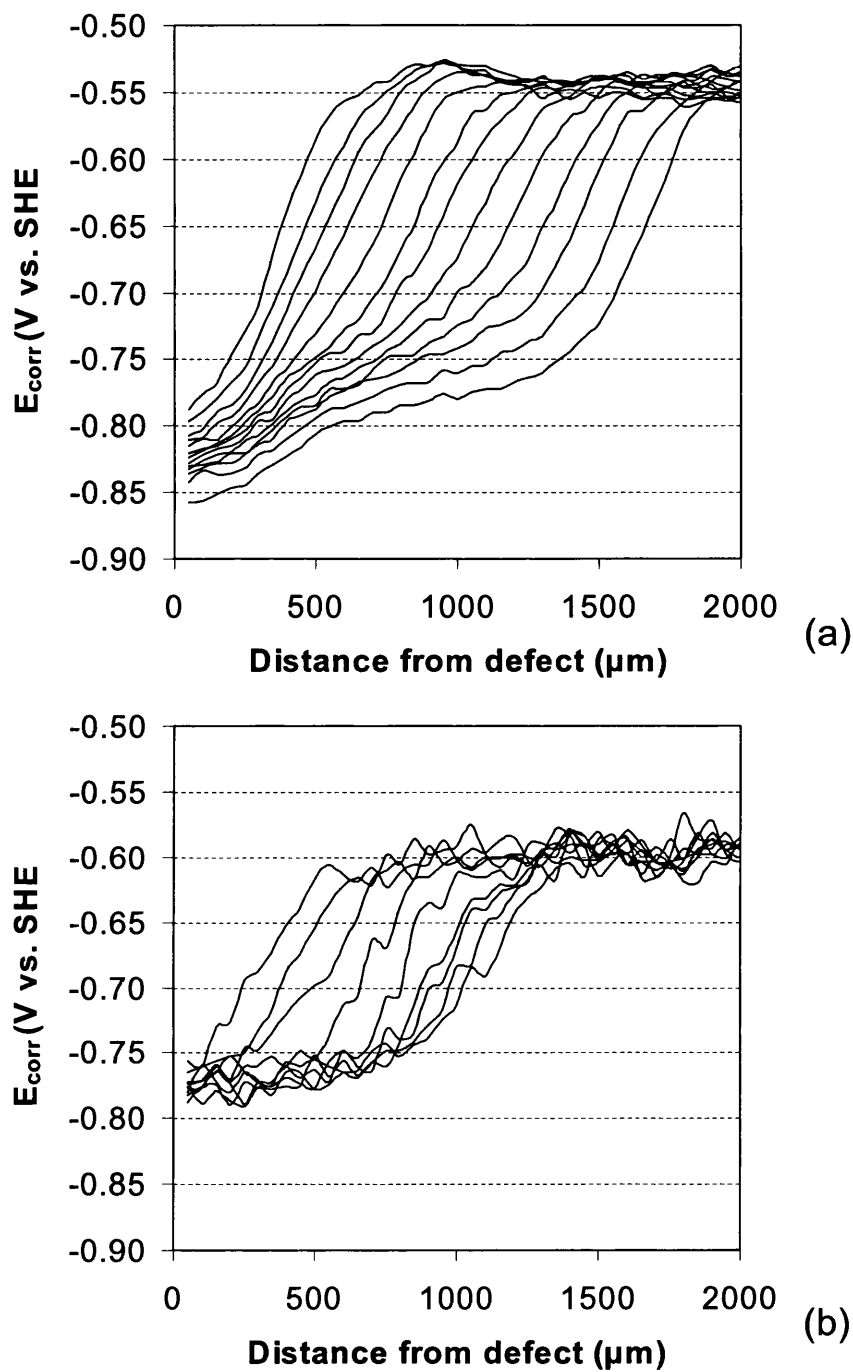


Figure 4.15. E_{corr} vs. distance for defect edge (x) profiles on Zn (a) for a 0.05Φ PANi-PP coating and (b) for a 0.05Φ PANi- H_3PO_4 coating.

The E_{corr} potential profiles shown in figures 4.14 and 4.15 highlight the dopant dependence towards the recorded intact coating potentials at relatively low pigment volume fraction additions to the organic PVB coating. Considering the E_{corr} profile of the PVB control coating, 0.05Φ PANi-CSA additions do not significantly alter the

recorded value of E_{intact} from ca. -0.3V vs. SHE. The E_{corr} potential profiles of figures 4.15 (a) and (b) showing the phosphonate and phosphate dopants respectively, indicate a marked drop in E_{intact} to ca. -0.6V vs. SHE, which emphasises the dopant dependency of the PANi-ES - substrate interaction, confirming the potentiometric findings outline previously in this section.

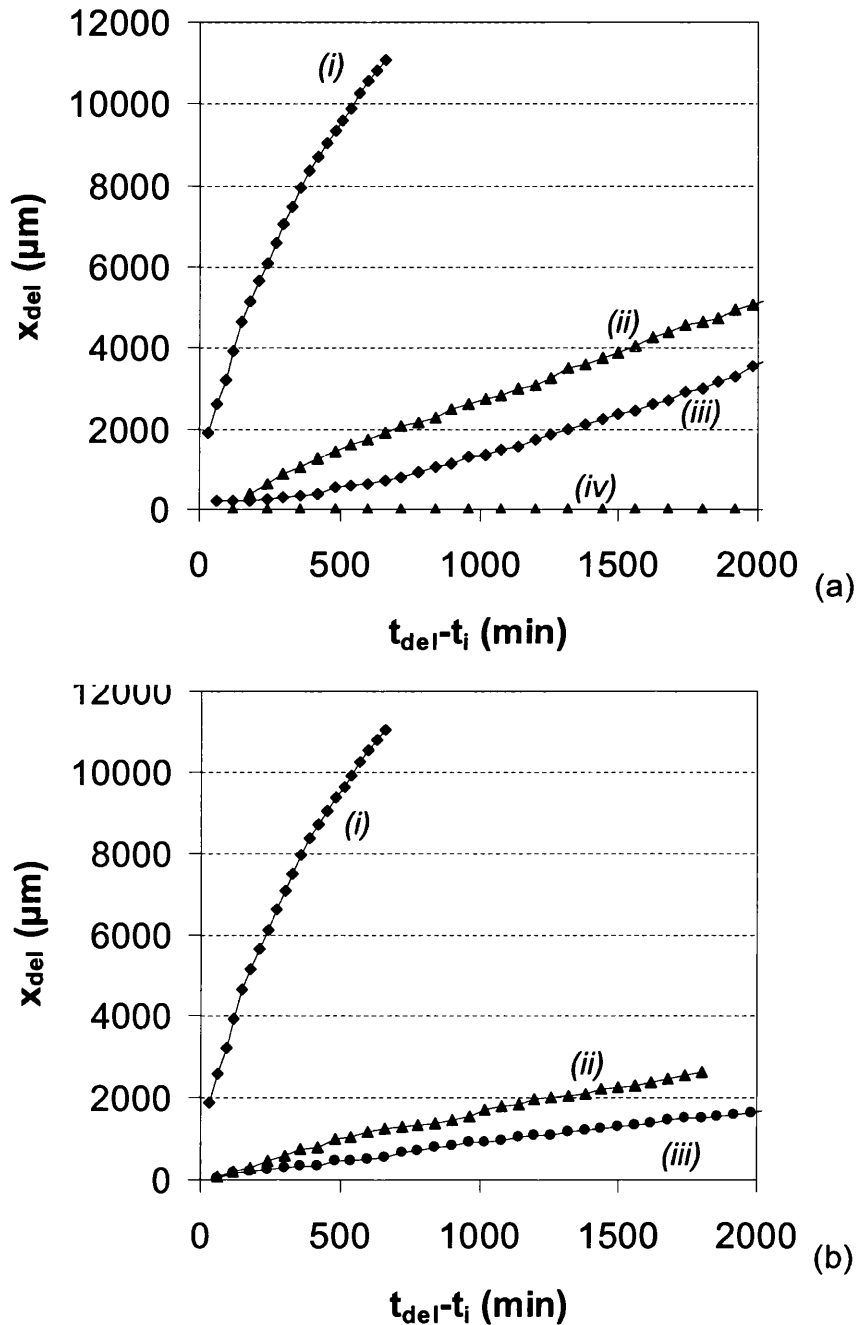


Figure 4.16. Plots of x_{del} vs. $(t_{\text{del}} - t_i)$ for 30 μm PVB/PAni-ES composite coatings adherent to Zn. (a) PANi-pTS [3] key: $\Phi_{\text{ES}} = (i) 0, (ii) 0.05, (iii) 0.10$ and $(iv) 0.20$. (b) PANi-CSA key: $\Phi_{\text{ES}} = (i) 0, (ii) 0.05$ and $(iii) 0.30$.

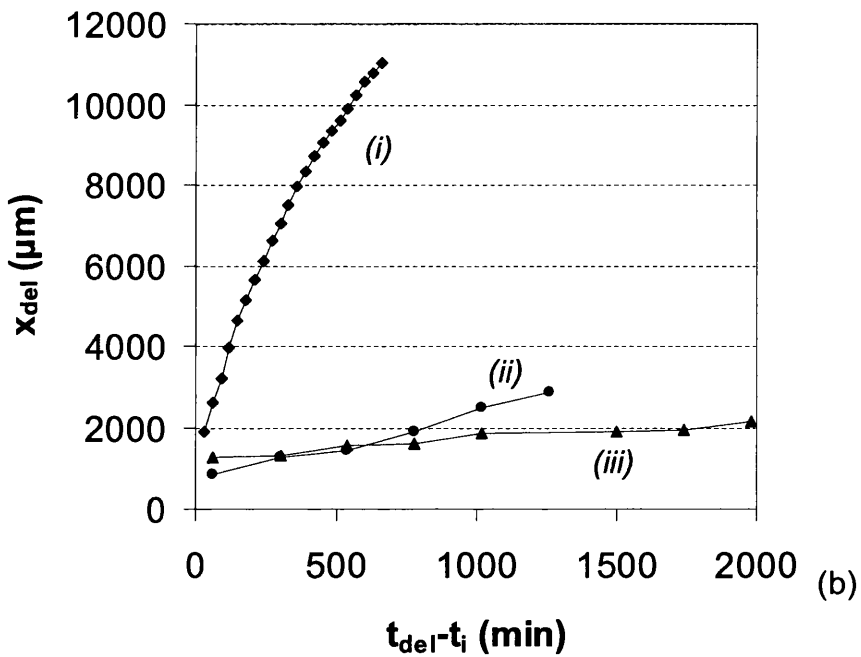
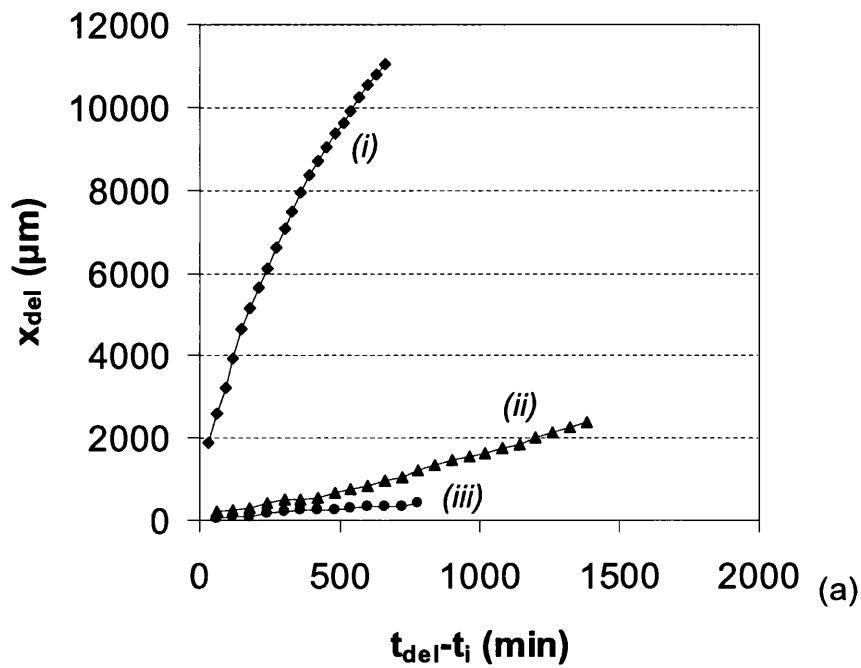


Figure 4.17. Plots of x_{del} vs. $(t_{del}-t_i)$ for $30\mu\text{m}$ PVB/PAni-ES composite coatings adherent to Zn. (a) PAni-PP key: $\Phi_{ES} = (i) 0, (ii) 0.05$ and $(iii) 0.30$. (b) PAni- H_3PO_4 key: $\Phi_{ES} = (i) 0, (ii) 0.30$ and $(iii) 0.20$.

The dopant dependency of delamination inhibition resulting from systematic increases in pigment volume fraction is shown for each different PAni-ES in figures 4.16 and 4.17, where figure 4.16 (a) and (b) show the delamination kinetics of PAni-

pTS, PANi-CSA, and figure 4.17 (a) and (b) show PANi-PP and PANi-H₃PO₄ respectively. As a reference, the delamination kinetics of the control PVB only coating is shown also, highlighting the increased delamination performance gained due to in-coating PANi-ES addition. Comparing the shape of the delamination curves after the addition of PANi-ES to the organic coating for each of the four dopants examined makes clear the transition from parabolic to linear delamination kinetics resulting from the pigment addition. It is clear that only small quantities of pigment addition is required to transform the parabolic cation migration controlled delamination kinetics to linear kinetics, which signifies that cation migration from the artificial defect is no longer the rate determining factor of cathodic delamination.

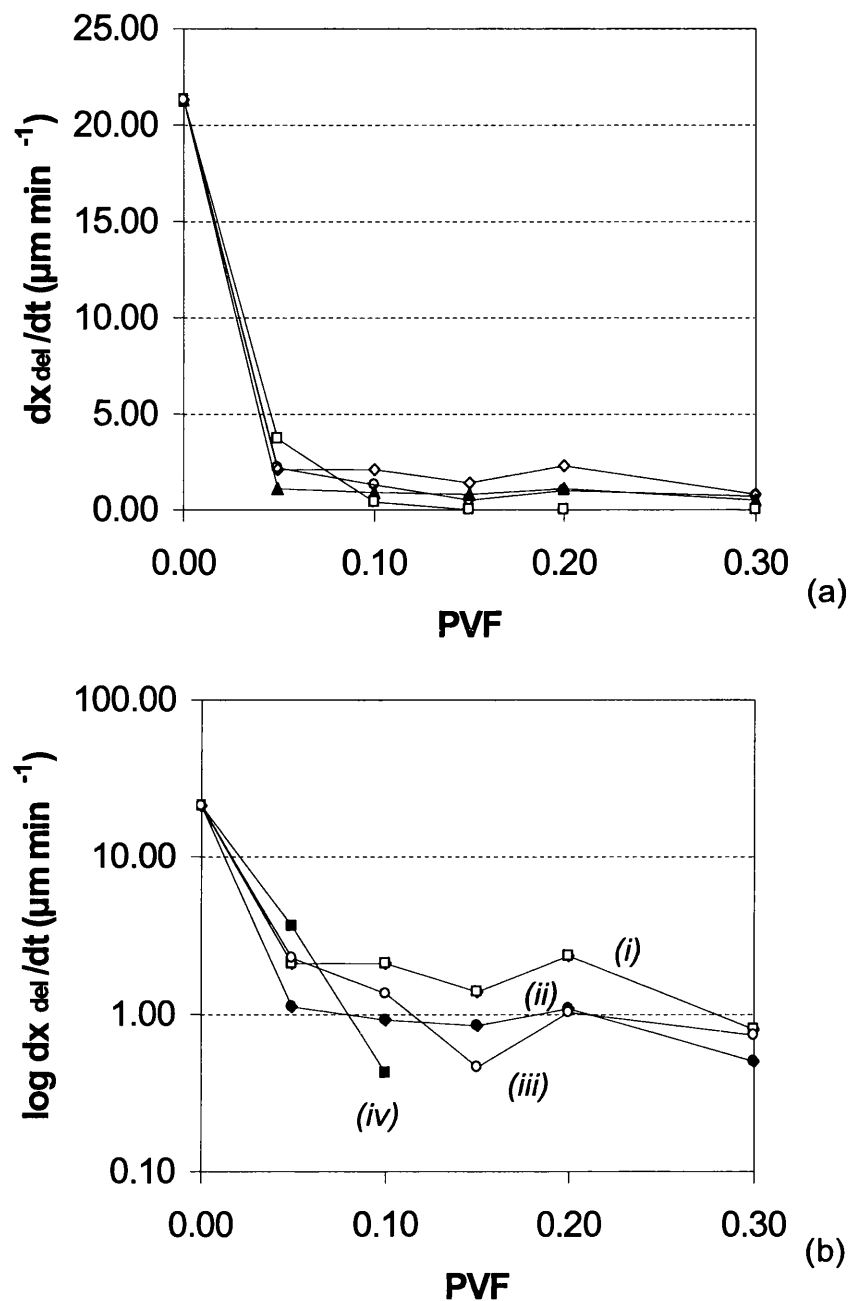


Figure 4.18. Summary plots of delamination rate (dx_{del}/dt) vs. Φ_{ES} for $30\mu\text{m}$ PVB/PAni coatings on Zn. (a) Summary highlighting extent of inhibition. (b) Log dx_{del}/dt key: (i) PAni-CSA, (ii) PAni-PP, (iii) PAni- H_3PO_4 and (iv) PAni-pTS [3].

The comparison of dopant dependent delamination kinetics shown within figure 4.18 (a) shows that there is a large similarity between the inhibition properties of all dopants with the exception of PAni-pTS, which is capable of completely inhibiting cathodic disbondment at higher ($\Phi_{ES} \geq 0.15$) over the 48hr time period employed

experimentally. The other three PANi-ES investigated differ from the PANi-pTS in that they are only capable of slowing the rate of disbondment over the 48hr time period, not stopping it completely.

Due to the strong similarities of cathodic disbondment inhibition capabilities of the differently doped PANi-ES tested, differences in performance are best viewed in figure 4.18 (b) on a logarithmic scale, which better capable of highlighting the differences. It is clear that the best delamination inhibition is provided by PANi-pTS due to the fact delamination is totally inhibited. PANi-PP and PANi-H₃PO₄ are shown to provide a near identical degree of inhibition, which is possibly due to them being able to produce a thin insulating salt film on the Zn surface. Of all four dopants examined, it is the PANi-CSA that is shown to be consistently poorer at inhibiting cathodic delamination in comparison to the other dopants, although this is only by a small amount.

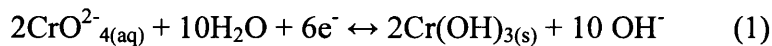
4.3.4 Strontium Chromate Pigmented PVB on Zinc

Many studies to explore the active mechanism of strontium chromate have been undertaken, and similarly many comparative studies have been made to try and identify alternative inhibitors [20, 21]. This set of unpublished experimentation was completed by Dr Williams of Swansea University as a counterpart study to support the findings on HDG [18]. Here strontium chromate (SrCrO₄) has been added as a pigment dispersion within an ethanolic polyvinyl butyral (PVB) resin in order to explore its ability to inhibit corrosion-driven cathodic disbondment of the organic coating. The main purpose of this chapter is to investigate the effectiveness of polyaniline – PVB composite coatings at inhibiting corrosion-driven cathodic disbondment. The inhibitory properties of SrCrO₄ – PVB composite coatings are described for comparison, due to their current commercial utilisation.

In the study conducted by Williams et al [18], two main approaches were made to discover the mechanisms by which SrCrO₄ acts to provide inhibition of cathodic disbondment. Firstly, CrO₄²⁻ anions were added directly to the experimental electrolyte and secondly, powdered SrCrO₄ was systematically added to the organic PVB coating in varying pigment volume fractions (Φ_{SC}) to create composite

coatings. The effect of adding CrO_4^{2-} anions directly to the applied experimental electrolyte was found to cause passivation of the exposed HDG substrate (Zn). And from this it was found that delamination rates of the uninhibited PVB organic coating was only slowed by ~25%. The simplest explanation attributed to this inhibition from the in-electrolyte CrO_4^{2-} anions is that due to the delamination cell electric field, inhibitor anions are unable to enter the under-film electrolyte, where inhibition is required.

In contrast, the inhibition of corrosion-driven coating disbondment by systematically increasing the amount of in-coating SrCrO_4 , was found to be substantial due to the cessation of cathodic disbondment at low pigment loadings ($\Phi_{\text{SC}} 0.064$). Although capable of completely inhibiting cathodic disbondment, in-coating SrCrO_4 was seen to be unable to provide inhibition of the bare zinc in the defect area. Observed also was that E_{corr} values in the delaminated region were seen to increase over time as cathodic delamination continued, for pigment loadings $\Phi_{\text{SC}} < 0.064$. E_{corr} values in the delaminated region were seen to increase over time from -0.60V vs. SHE to -0.35V vs. SHE. This was explained by the diffusion of CrO_4^{2-} anions into the under-film electrolyte layer. It was subsequently proposed that the most important factor in reducing the corrosion-driven delamination rates is the replacement of O_2 reduction by a self-limiting under-film CrO_4^{2-} reduction, where the reduction reaction follows equation 1:



It was proposed that the reason why this process is self-limiting is because of the build-up of solid $\text{Cr}(\text{OH})_3$ eventually blocking further interfacial electron transfer and CrO_4^{2-} reduction. Under these circumstances, all under-film cathodic activity is effectively stifled and delamination cell currents and subsequent delamination rates fall to minimum values.

Here the results of adding SrCrO_4 to PVB resin to create composite coatings of varying Φ_{SC} , and subsequently applied to 99.99% pure Zn substrates are described. In the absence of inhibitor species, the delamination characteristics of PVB coatings adherent to pure Zn substrates are represented by the transient E_{corr} profiles shown

within figure 4.1 (a). This is the same control coating used previously, and is included to compare the effect of SrCrO₄ inhibitor addition.

Upon application of SrCrO₄ pigmented PVB coating to the Zn substrate, differences between the inhibited and non-inhibited coatings in terms of both the shape of the E_{corr} profile and the delamination kinetics are obvious. This is shown in figure 4.19 (b), and in common with the previous work undertaken using HDG steel [18], the delamination rate is significantly slowed as a function of increasing Φ_{SC}. It is apparent from figure 4.19 (b), showing the effect towards E_{corr} of 0.08Φ_{SC}, addition of the in-coating SrCrO₄ does not cause E_{intact} to change from -0.3V vs. SHE, in agreement with the findings on HDG.

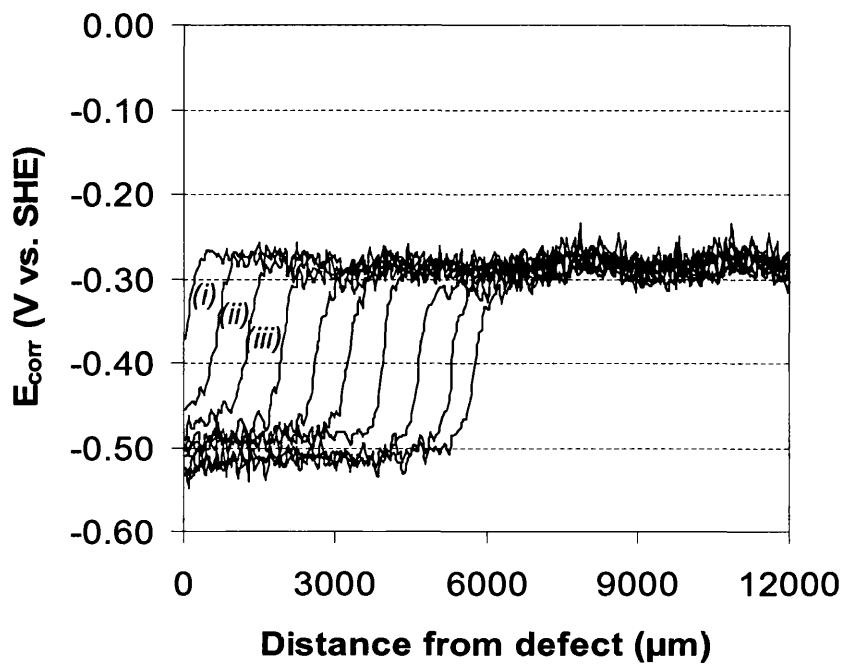


Figure 4.19. E_{corr} vs. distance from defect edge (x) profiles on Zn for $30\mu\text{m}$ 0.08Φ SrCr-PVB, key:- (i) 360 min, (ii) 480 min, (iii) 600 min and 2 hourly intervals thereafter.

Considering the under-film potential obtained within the delaminated area shown within the E_{corr} profiles of figure 4.19, it is apparent that compared to the PVB control coating there is a slight ennoblement. This ennoblement has caused a 0.3V increase in E_{corr} under the delaminated coating, which is consistent with the notion previously proposed by Williams that CrO_4^{2-} anions are able to diffuse into the under-film electrolyte layer to provide a degree of passivation to the Zn surface.

The initial delamination rates as a function of systematic increases in Φ_{SC} are shown in figure 4.20. It is clear from this that only a very small SrCrO_4 addition to the coating is able to slow the rate of corrosion-driven cathodic disbondment considerably. Further increase in pigment seems to have very little further effect until Φ_{SC} 0.15 whereby disbondment is prevented altogether within the 48hrs experimental time. During the study on HDG published by Williams et al [18], cessation of cathodic disbondment was found to occur at Φ_{SC} 0.064.

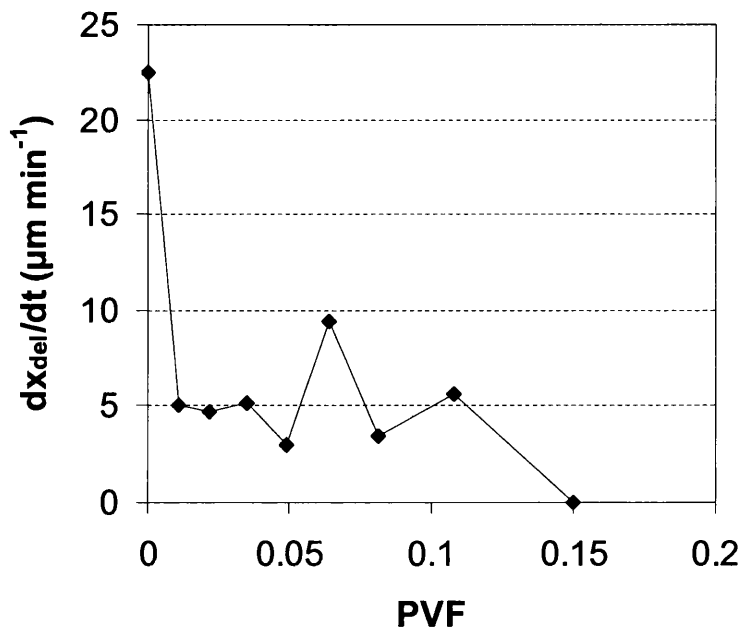


Figure 4.20 Summary plots of delamination rate (dx_{del}/dt) vs. Φ for SrCr pigmented $30\mu\text{m}$ PVB coatings on Zn.

The delamination kinetics are presented in terms of X_{del} vs. $(t_{del} - t_i)^{1/2}$ within figure 4.21 for varying levels of Φ_{SC} , showing the $t^{1/2}$ kinetics to be of a similar trend to the published data by Williams [18].

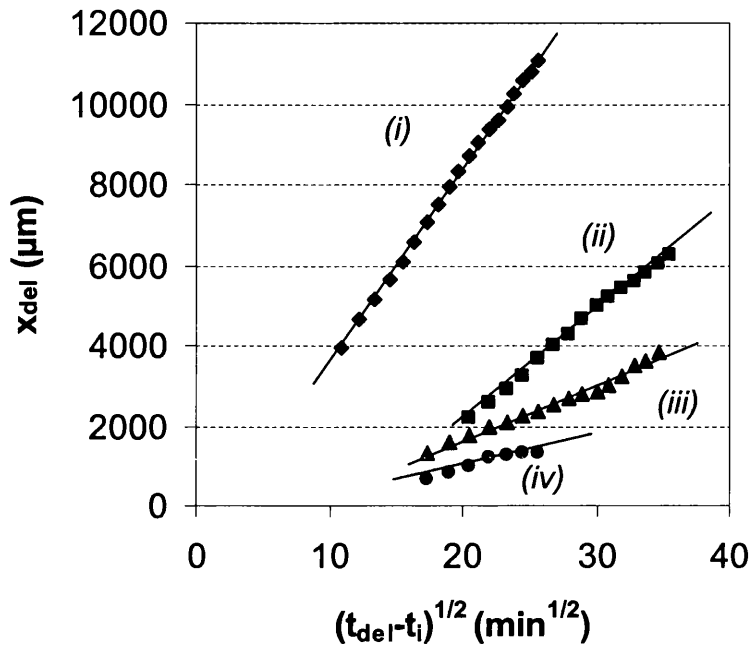


Figure 4.21 Plots of delamination distance (X_{del}) vs. $(t_{del} - t_i)^{1/2}$ for $SrCrO_4$ pigmented $30\mu m$ PVB on Zn. Key: $\Phi_{SC} = (i) 0, (ii) 0.02, (iii) 0.035$ and $(iv) 0.08$.

The findings presented throughout figures 4.19 – 4.21 are supportive of the previous findings by Williams et al on HDG [18]. It is likely that the inhibitory effect of in-coating $SrCrO_4$ when adherent to pure Zn is likely to follow the same proposed mechanism.

4.4 Conclusions

The studies presented within this chapter follow the work of Williams et al who conducted a study into the inhibitory performance of PANi-ES doped with paratoluenesulfonate (PANi-pTS) [3]. PANi-pTS was added used as pigment within an organic coating and was found to provide a significant degree of cathodic disbondment inhibition, to similar extent as found when using similar strontium chromate containing coatings on HDG substrates [18]. To prove the validity of the findings on HDG, the results of a repeat test on pure Zn has been included here, and it is concluded that the Zn coating and the pure Zn substrates interact in a similar manner.

Here, differently doped PANi-ES powders have been incorporated into the organic coating following the same method as Williams et al to discover if dopant choice significantly affects the level of inhibition provided by the PANi-ES. Additionally, PANi-ES micro-films have been coated directly to the Zn surface, providing support for the theories of Williams et al [3] by providing reactive PANi colour changes. Comparisons have also been made between the performance of in-coating PANi-ES and non-conducting PANi-EB. It was discovered that PANi is not capable of providing cathodic disbondment inhibition in the non-conductive state.

The results clearly show that PANi-ES acts to provide a significant degree of cathodic disbondment inhibition, although the performance is dopant dependant. The PANi-ES of the other dopants are not capable of providing such a high level of inhibition, although in each case the extent of cathodic disbondment is inhibited significantly.

Potentiometric findings within this study show that E_{intact} is pushed lower in the case of all PANi-ES containing coatings, indicating the reduction of each PANi-ES as a result of PANi-ES – Zn interfacial contact. In terms of the SIMS oxide growth studies conducted for each PANi-ES, it was discovered that for all except PANi-pTS, only a thin interfacial film is formed during the experimental time period. The total inhibition of cathodic delamination is only found in the case of PANi-pTS, most likely due to the thicker interfacial oxide formation. The inhibitory performance of the other PANi-ES investigated is considerably poorer than PANi-pTS, and the

recorded interfacial film thicknesses for each are also thinner. This supports the theory that the interfacial film thickness is important to inhibit corrosion-driven cathodic disbondment.

Direct comparison of the work presented here with the findings in the following chapter (chapter 5) describing the inhibitory properties of acid etch primers provides an interesting fact. The etch primers containing the same organic acids used to protonate the polyaniline pigments here are shown to provide a similar level of inhibition. This opens the possibility that the PAni-ES pigments simply act to deliver exchangeable Zn^{2+} from the coating following equation 4.1, maintaining the interfacial film by equation 4.3 and preventing cathodic disbondment.

Following the work of Williams et al [3], the interfacial film formation between the polymer coating and the Zn substrate acts to block the cathodic O_2 reduction reaction. This subsequently acts to block cathodic disbondment and accordingly inhibition performance increases with increasing film thickness. This work shows that PAni-ES is a viable environmentally friendly alternative to strontium chromate for the prevention of cathodic disbondment under atmospheric conditions.

4.5 References

- [1] G. M. Spinks, A. J. Dominis, G. G. Wallace, and D. E. Tallman, *Journal of Solid State Electrochemistry* **6**:85 (2002).
- [2] D. E. Tallman, G. Spinks, A. Dominis, and G. G. Wallace, *Journal of Solid State Electrochemistry* **6**:73 (2002).
- [3] G. Williams, R. J. Holness, D. A. Worsley, and H. N. McMurray, *Electrochemistry Communications* **6**:549 (2004).
- [4] G. Williams, A. Gabriel, A. Cook, and H. N. McMurray, *Journal of the Electrochemical Society* **153**:B425 (2006).
- [5] A. R. Bennett, H. N. McMurray, and G. Williams, *ECS Trans. Volume* **11**:71 (2008).
- [6] W. K. Lu, R. L. Elsenbaumer, and B. Wessling, *Synthetic Metals* **71**:2163 (1995).
- [7] B. Wessling, *Synthetic Metals* **102**:1396 (1999).
- [8] W. Furbeth and M. Stratmann, *Corrosion Science* **43**:207 (2001).
- [9] W. Furbeth and M. Stratmann, *Progress in Organic Coatings* **39**:23 (2000).
- [10] A. Leng, H. Streckel, and M. Stratmann, *Corrosion Science* **41**:547 (1999).
- [11] A. Leng, H. Streckel, and M. Stratmann, *Corrosion Science* **41**:579 (1999).
- [12] W. Furbeth and M. Stratmann, *Fresenius Journal of Analytical Chemistry* **353**:337 (1995).
- [13] C. Menardo, M. Nechtschein, A. Rousseau, J. P. Travers, and P. Hany, *Synthetic Metals* **25**:311 (1988).
- [14] R. J. Holness, G. Williams, D. A. Worsley, and H. N. McMurray, *Journal of the Electrochemical Society* **152**:B73 (2005).
- [15] G. Williams and H. N. McMurray, *Electrochemical and Solid State Letters* **8**:B42 (2005).
- [16] H. Dominighaus, *Plastics for Engineers*, Hanser Publications, Munich, 1988.
- [17] J. Stejskal and R. G. Gilbert, *Pure and Applied Chemistry* **74**:857 (2002).
- [18] G. Williams and H. N. McMurray, *Journal of the Electrochemical Society* **148**:B377 (2001).
- [19] G. Williams, H. N. McMurray, and D. A. Worsley, *Journal of the Electrochemical Society* **149**:B154 (2002).

- [20] R. L. Howard, I. M. Zin, J. D. Scantlebury, and S. B. Lyon, *Progress in Organic Coatings* **37**:83 (1999).
- [21] I. M. Zin, R. L. Howard, S. J. Badger, J. D. Scantlebury, and S. B. Lyon, *Progress in Organic Coatings* **33**:203 (1998).

Chapter 5

Organic

Acid Etch Primers

5.1 Introduction

This chapter describes an alternative low cost coating system that holds the possibility to replace conventional strontium chromate inhibitors used in pre-painted steels. The application of organic coatings containing acids (acid etch primers) directly to steel or Zn galvanised steel is investigated. The acids included within the organic coatings tested here are the same acids used to protonate polyaniline within a published study on pure iron [1] and on pure Zn as described within chapter 4. The scientific driving force for this research is to explore the possibility of using the dopant acid as a means of inhibiting corrosion driven cathodic disbondment. Acid etch primers have been investigated elsewhere, it was found that a phosphoric acid etch primer was able to provide substantial resistance to cathodic disbondment under polarised immersion conditions [2]. It is also intended as an evaluation of the importance of polyaniline as a delivery method for any observed inhibition. The industrial incentive originates from concerns regarding the current elevated raw material costs associated with the procurement of polyaniline.

This alternative method of organic coating formulation has previously been investigated by Coleman et al and was shown to be capable of inhibiting anodic coating disbondment [3]. The study involved investigation of filiform corrosion (FFC) that occurs under organic polyvinyl butyral (PVB) coatings adherent to AA6111-T4 substrates. Within the study only one organic acid was investigated, namely phenylphosphonic (H_2PP), by systematically increasing the weight percentage additions of acid contained within the coating. Organic coatings were formulated by fully dissolving H_2PP within ethanolic PVB prior to bar coating directly onto the Al alloy surface to give a total dry film thickness of $\sim 30\mu m$.

Following the coating formulation method of Coleman et al [3], acids known to effectively protonate polyaniline are included within a PVB binder. The acid content of these coatings are systematically varied and applied to both pure Fe and pure Zn and cathodic disbondment cells are initiated [4]. The inhibitory effects provided these acid etch primers are documented and mechanistic proposals are made.

5.2 Experimental

Formulation of acid – PVB organic coatings also followed the method described in section 2.2.1. Organic acids were fully dispersed within the PVB resin by high shear mixing for 10 minutes prior to bar casting to create a $30 \pm 5\mu\text{m}$ dry film thickness as confirmed using a micrometer screw gauge. Stratmann-type delamination cells were prepared following the method described within section 2.2.4.1 on a mixture of both pure Zn and pure Fe substrates of 50 x 50 mm dimensions. The model PVB organic coatings were then partially peeled back to create a defect comprising 10 x 10 mm of area of bare metal. The SKP was used to fully monitor the corrosion-driven cathodic disbondment originating from the organic coating defects as described within section 2.3. All delamination experiments using the SKP were carried out in static air at 20°C and approximately 96% relative humidity (RH) in isopiestic equilibrium with a 0.86 mol dm^{-3} (5% w/v) aqueous NaCl reference solution. For corrosion driven coating delamination experiments the sample was first allowed to equilibrate at 96% RH for a period of 6 hours before an aliquot of 0.86 mol dm^{-3} NaCl was applied to create a 1mm thick electrolyte layer at the coating defect (note, not over the coating surface) and initiate corrosion. Scans were conducted immediately after the addition of the experimental electrolyte to the coating defect and successive scans were taken at 1 hour intervals for 48 hrs thereafter, recording under film potentials at $50\mu\text{m}$ intervals over the 12mm scan length.

5.3 Results and Discussion

5.3.1 Inhibition of Cathodic Disbondment on Iron

Organic coating (cathodic) disbondment of organic coatings adherent to Fe substrates is most efficiently monitored using the SKP, the theory of which has been fully explained previously in chapters 1 and 2. The mechanism by which cathodic disbondment occurs under non-inhibited polyvinyl butyral (PVB) coatings is fully understood (section 1.3.3.1). To explore and elucidate the inhibitory effects provided by the addition of organic acids directly into the ethanolic PVB coating, the effects of varying acid content is explored. Figure 5.1 shows how increasing the acid addition effects the intact coating potentials (E_{intact}) of the coated Fe system. Figure 5.1 (i) shows the effect of adding camphorsulphonic acid (HCS) and figure 5.1 (ii) shows the effect of adding phenylphosphonic acid (H_2PP).

Non-inhibited PVB is used as a control coating and this shows a recorded E_{intact} of ca. 0.11 V vs. SHE, which is consistent with published findings [1, 5]. Even very small acid additions (3.1 wt%) in the case of HCS and H_2PP are seen to increase E_{intact} significantly by 0.20 V vs. SHE. Further acid additions to the PVB coating produce no further increase of intact coating potential for HCS additions, but increasing the acid loading to 19.5 wt% in the case of H_2PP causes a further rise in under-film potential to just over 0.4 V vs. SHE. The increase of E_{intact} due to the acid additions suggests the coatings are creating an interfacial surface layer which renders the surface more passive than when coated with un-inhibited PVB. Upon mechanically peeling the intact coating from the substrate surface, a uniform dark brown oxide layer was found, confirming this theory.

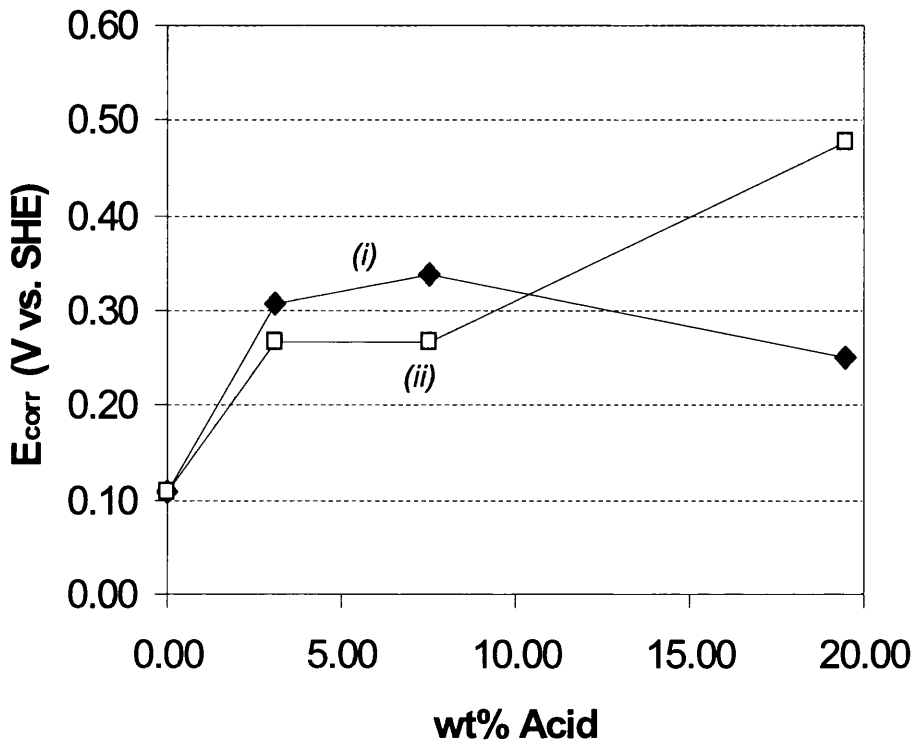


Figure 5.1 Summary plot showing time independent E_{intact} as a function of in-coating acid after 48 hrs humidification at 96% RH on Fe. Key: (i) HCS and (ii) H₂PP.

Time-dependant E_{corr} profile plots as recorded by the SKP of delaminating organic coatings on Fe are shown in figures 5.2 and 5.3, where each profile is recorded at hourly time intervals. The E_{corr} profile recorded for 3.1wt% HCS-PVB is shown in figure 5.2 compared directly to the E_{corr} profile representative of the uninhibited PVB control coating. The obtained E_{corr} potential plot of PVB shows the potential of the delaminated area, marked by the sudden potential drop, to be consistently -0.4V vs. SHE. This is consistent for both the HCS and H₂PP containing systems containing 3.1 wt% acid loadings. This suggests that the Fe in this region is freely corroding. Additionally, the E_{corr} profiles in figure 5.2 confirm the rise of E_{intact} due to the passivation caused by the in-coating acids.

Increases in acid loading from 3.1 wt% have already been shown not to have any significant effect on the potential of the intact coating (E_{intact}). Figure 5.3 shows that in the delaminated region there is a slight ennoblement to -0.15V vs. SHE caused by the 19.5 wt% loading of HCS. This phenomenon is equally matched in the case of

19.5 wt% H₂PP containing coatings. Additionally in both cases the high acid loadings are shown to significantly inhibit the observed rate of cathodic disbondment, although it is not totally inhibited. The ennoblement of the delaminated region caused by the higher acid loadings is most likely due to the in-coating acid anions being available to migrate towards the anodic defect region, providing a certain degree of anodic inhibition.

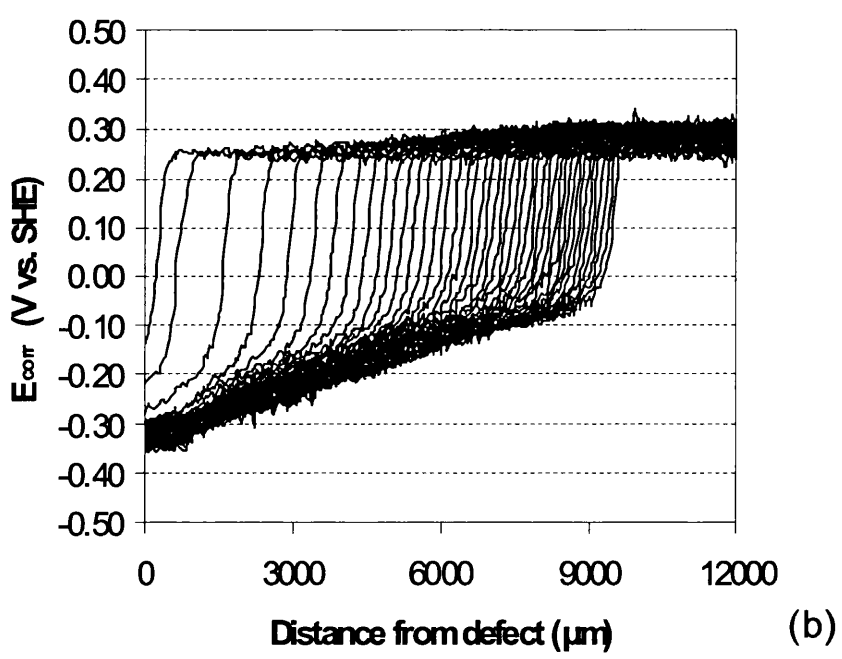
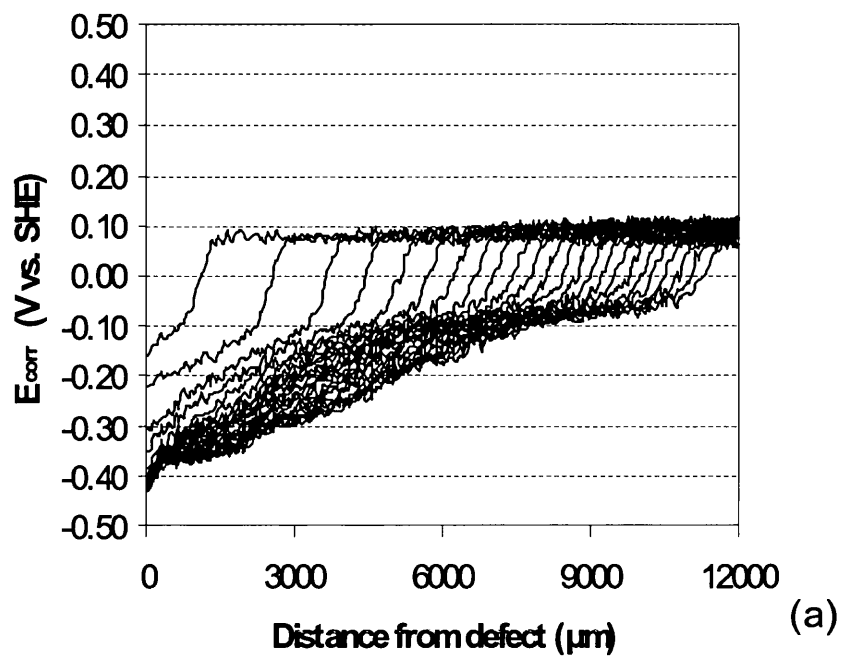


Figure 5.2 E_{corr} vs. distance from defect edge (x) profiles for (a) $30\mu\text{m}$ PVB coating from 200min and hourly intervals thereafter and (b) $30\mu\text{m}$ 3.1% wt:wt HCS PVB coating from 200min and hourly intervals thereafter; on pure Fe substrates.

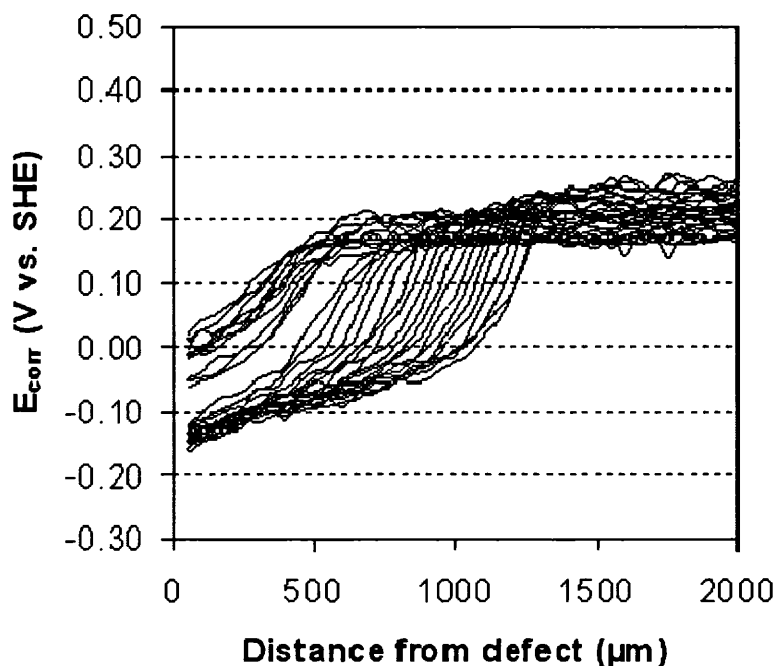


Figure 5.3 E_{corr} vs. distance from defect edge (x) profiles for a 30 μm 19.5% wt:wt HCS PVB coating from 1020min and hourly intervals thereafter on pure Fe substrates.

The delamination kinetics are summarised within figure 5.4 for both the H₂PP and HCS systems, and a high level of cathodic disbondment inhibition is observed. It is suggested that the primary mechanism of inhibition arises from the fact there is a reservoir of H⁺ in the coating that can neutralise the alkalinity from the cathodic disbondment reaction.

Evidence to support this is contained within figure 5.4 where it is clearly shown that small 3.1 wt% acid loadings slow the rate of cathodic delamination significantly in the case of both the acids tested. However, at the smallest acid addition of 3.1 wt% the H₂PP is significantly more efficient at slowing the cathodic disbondment compared to the HCS, and this is true of acid additions up to 7.5 wt%. At the 19.5 wt% acid loading both the HCS and H₂PP slow the rate of cathodic disbondment to a very similar level. This is consistent with the notion that pH buffering is the primary inhibition mechanism, because the H₂PP has twice the buffering capacity of the HCS.

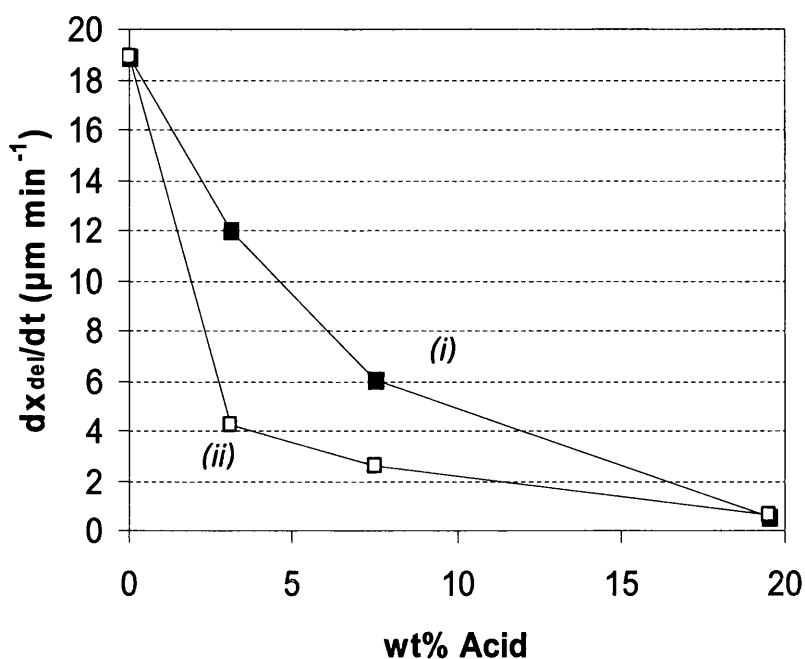


Figure 5.4. Delamination rate vs. quantity of in-coating acid comparison for (i) HCS and (ii) H₂PP, adherent to Fe substrates.

An alternative suggestion to the proposition that inhibition is provided solely by pH buffering alone is as follows. For H₂PP it may be the case that the interaction between the in-coating acid and the iron substrate will result in the formation of an insoluble and non-conducting Fe-PP salt film. The reason why this may be expected follows on from a full mechanistic study involving PANi-ES protonated with PP⁻, as well as the findings of chapter 3. The presence and release of the PP⁻ anion was found to interact with the Fe substrate causing the formation of the thin non-conductive and insoluble Fe-PP salt [1, 6]. This interfacial salt film is capable of restricting the amount of electrons available at the salt-polymer interface, hence stifling the cathodic reaction within the cathodic disbondment cell and significantly slowing the rate of cathodic disbondment.

It is highly possible that the thin insoluble and non-conductive salt film caused by the H₂PP is capable of reaching its maximum thickness even at very low levels of acid loading within the organic coating. Only a small loading of acid within the PVB coating is required to form the salt film uniformly across the substrate surface. This

is because the interfacial salt film reaches a maximum thickness when conductivity between the substrate and acid is lost due to the insulating nature of the salt film at very thin thicknesses.

A possible explanation as to the reason why HCS containing organic coatings are less efficient at slowing cathodic disbondment at lower acid loading levels is as follows. In coatings with lower acid loading levels such as 3.1 wt%, there is a possibly not enough H^+ is free within the system to adequately buffer the under film pH and stop the degradation of the sulphonate oxide layer. It is this oxide layer that develops on the iron surface and is effectively what the organic coating is adherent to. This is not an issue for lower acid loadings of H_2PP because the insulating salt film blocking the cathodic reaction acts as a primary mechanism of inhibition, and it is proposed that the pH buffering effect of the in-coating H^+ acts as a secondary means of disbondment inhibition. In the case of HCS the pH buffering action of the in-coating H^+ is the primary mechanism of cathodic disbondment inhibition that is only capable of matching the performance of H_2PP containing coatings at higher acid loadings.

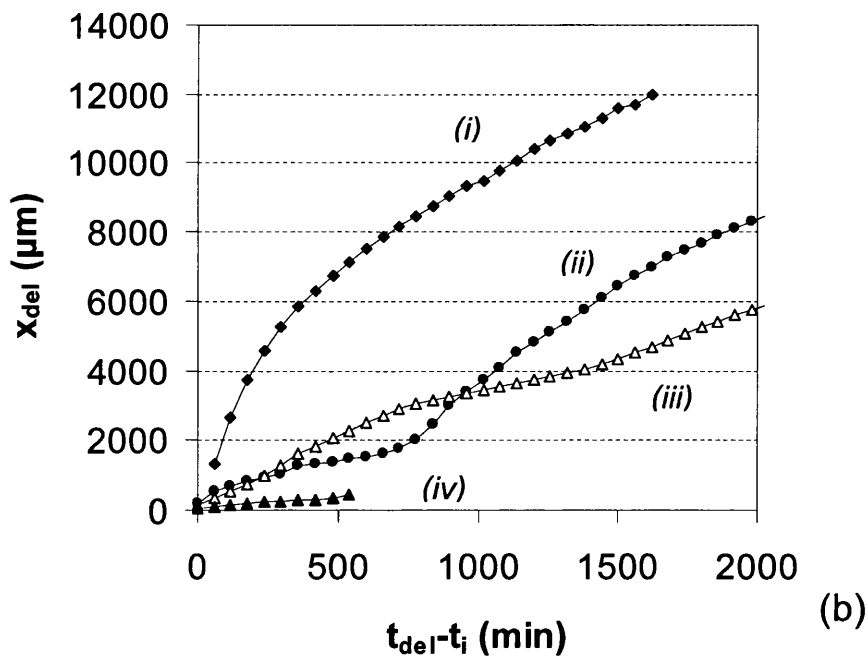
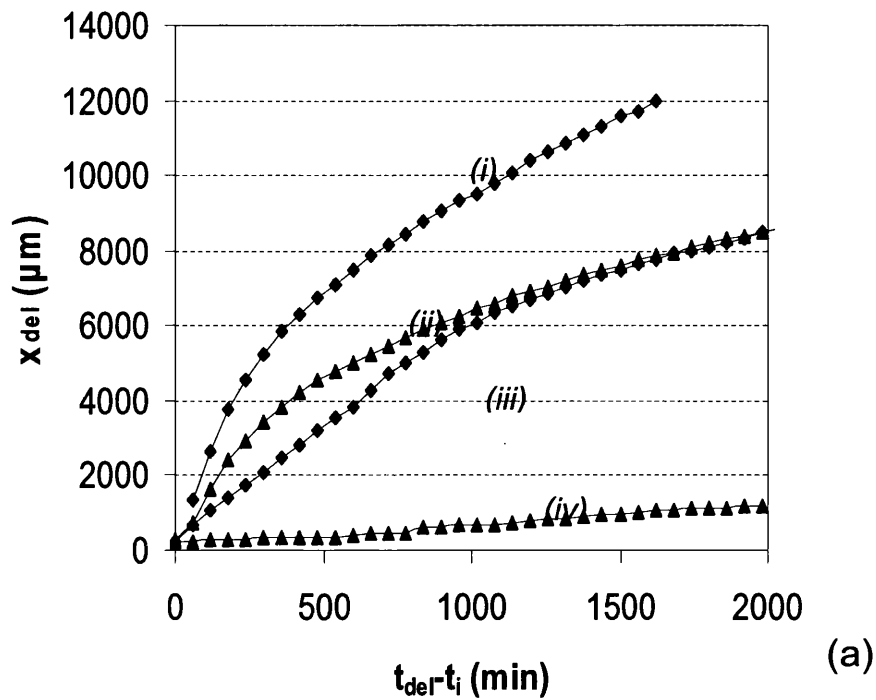


Figure 5.5 Plots of (x_{del}) vs. ($t_{del}-t_i$) for $30\mu\text{m}$ PVB containing systematic variations of in-coating acid additions on Fe substrates. Key: (a) HCS (i) 0, (ii) 3.1, (iii) 7.5 and (iv) 19.5 %wt:wt. (b) H_2PP (i) 0, (ii) 3.1, (iii) 7.5 and (iv) 19.5 % wt:wt.

Another observation when considering the cathodic delamination kinetics of acidic primers adherent to Fe is the shapes of the resulting delamination distance vs. time

plots. The delamination kinetics of non-inhibited PVB are parabolic, which indicates that the process determining the rate of cathodic delamination is cation migration from the artificial defect to the cathodic delamination front. The further away from the artificial defect the delamination front becomes, the slower it will advance.

The delamination vs. time curves of HCS and H₂PP are shown within figure 5.5 (a) and (b) respectively, and included in each is the parabolic delamination vs. time curves for non-inhibited PVB control coatings. In the case of HCS, the 3.1 wt% and 7.5 wt% loadings both show parabolic delamination kinetics, whereas the higher 19.5 wt% loading shows linear kinetics. This suggests a transition from the delamination rate limiting step being cation migration to something else. In the case of the H₂PP system shown in figure 5.5 (b) there is a contrast in the shape of the delamination vs. time curves from parabolic to near linear even at the smaller 3.1 wt% acid loading.

This change from the parabolic delamination kinetics of non-inhibited PVB to linear kinetics due to the addition of H₂PP to the coating system is consistent with the notion of an interfacial salt film stifling the O₂ reduction reaction. In the case of the HCS system, the mild transition from parabolic kinetics to linear kinetics supports the theory that a sufficient reservoir of H⁺ capable of neutralising the alkalinity generated from the cathodic reaction is only reached at the highest acid loading.

5.3.2 Inhibition of Cathodic Disbondment on Zinc

The possibility of using acid containing organic coatings to provide cathodic delamination inhibition on Zn substrates is also proven to be feasible. As with the previous study on Fe, systematic increases in acid loadings are presented, which show significant inhibition of organic coating failure. The two organic acids investigated within this study dissolved within the ethanolic PVB are para-toluenesulfonic acid (HpTS) and phenylphosphonic acid (H₂PP). Cathodic delamination rates and under-film potentiometry has been obtained using the SKP in the same manner as before using identical coating formulation methods and sample geometries. Once again the cathodic delamination of a non-inhibited PVB control coating adherent to a Zn substrate is presented alongside PVB containing organic acids.

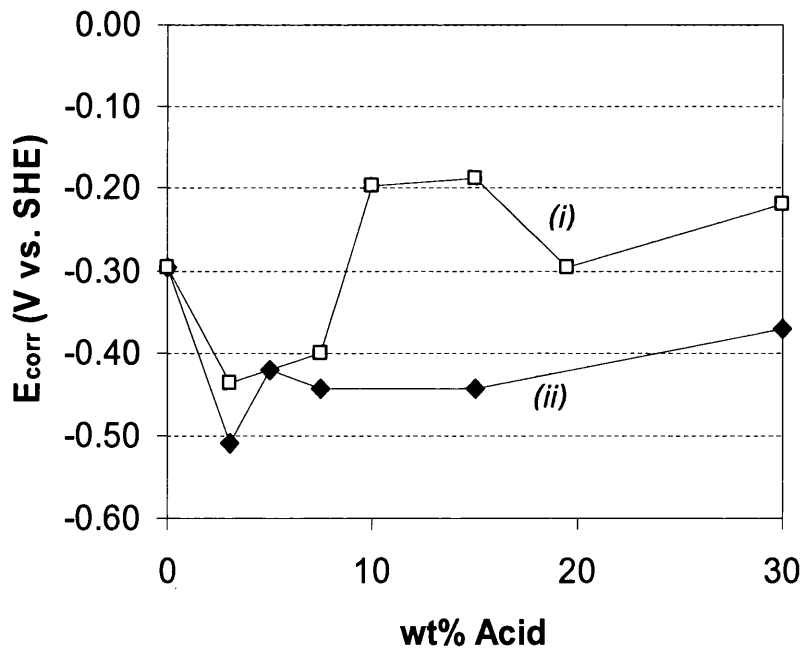


Figure 5.6 Summary plot showing time independent E_{intact} as a function of coating acid additions after 48 hrs humidification at 96% RH for organic coatings adherent to Zn. Key: (i) H₂PP, (ii) HpTS.

Figure 5.6 shows the comparison of time independent E_{intact} for each individual systematic increase in acid loading for both the phosphonate and sulphonate acids

tested. E_{intact} for a non-inhibited PVB coating adherent to a Zn substrate has been consistently shown to be ca. -0.3 V vs. SHE via measurement within an SKP at 96% RH. The addition of H₂PP acid to the PVB and systematically increasing the loading levels does not have any significant overall effect upon E_{intact} . Conversely to this the addition 3.1 wt% HpTS to the PVB coating has the effect of depressing E_{intact} , and any further systematic increase in acid loading maintains the more negative potential of ca. -0.4 V vs. SHE. This depression of E_{intact} suggests the HpTS loaded coating is causing a degree of anodic activity at the substrate polymer interface due to the high atmospheric humidity employed experimentally.

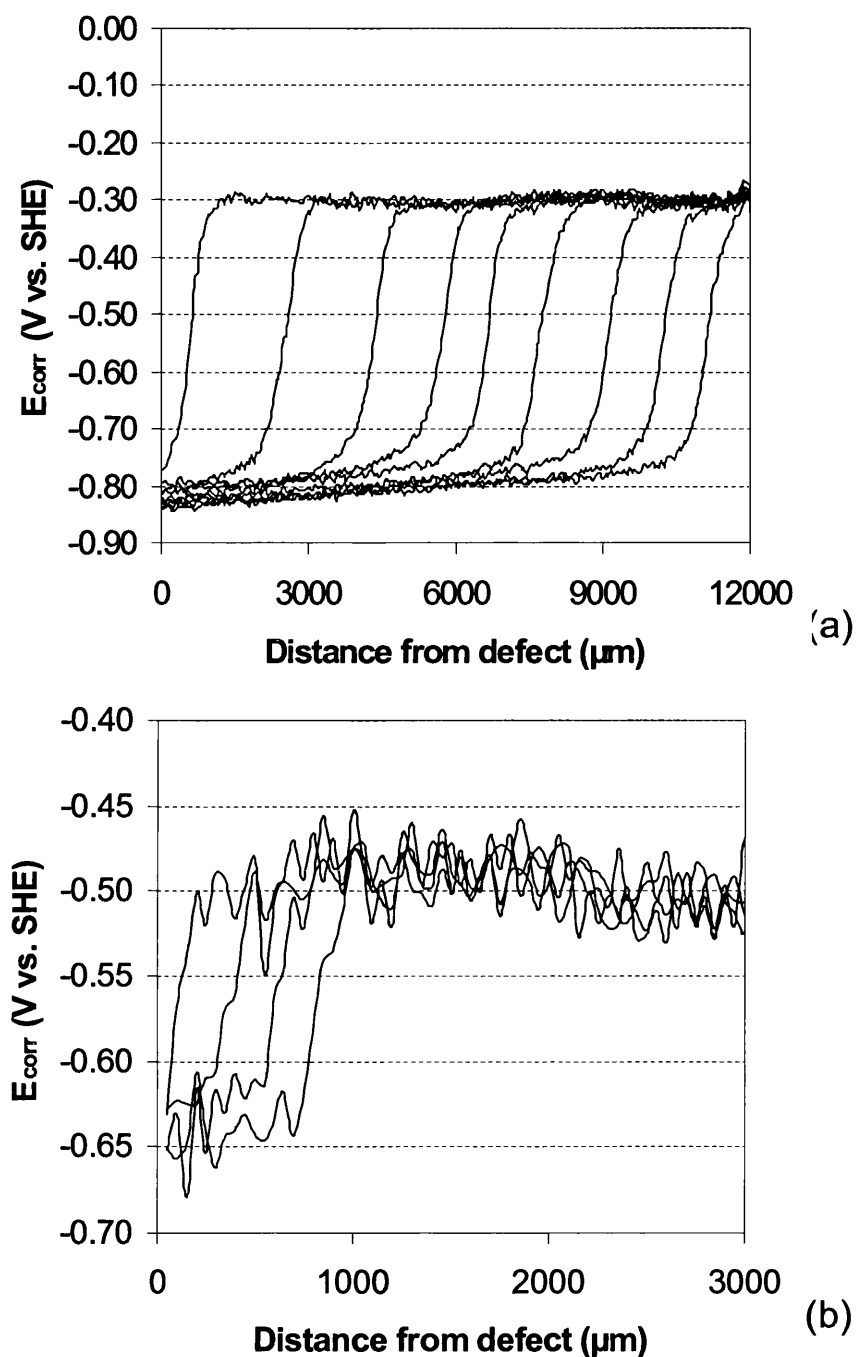


Figure 5.7 E_{corr} vs. distance from defect edge (x) profiles for (a) $30\mu\text{m}$ PVB coating, (b) $30\mu\text{m}$ 3.1% wt:wt HpTS PVB coating adherent to pure Zn.

The corresponding E_{corr} profiles as recorded directly by the SKP of the PVB control coating and 3.1 wt% HpTS-PVB 5.7 (a) and (b) respectively. In the case of the non-inhibited PVB control coating, the free corrosion potential for Zn in the region where cathodic delamination has already taken place is ca. -0.8V vs. SHE. In the case of the

two acid containing systems, E_{corr} is shown to be slightly higher in both cases, which could be ascribed to the large presence of acid entering the defect electrolyte.

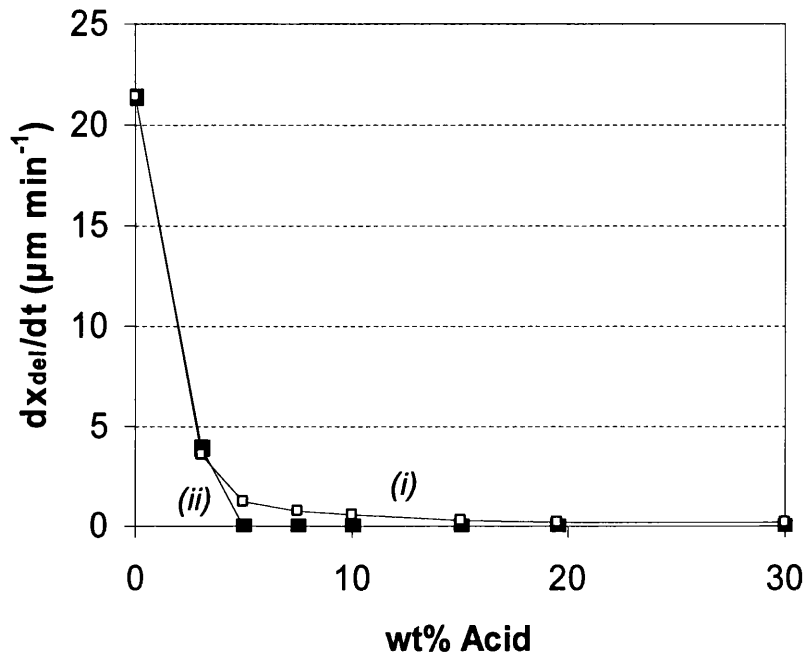


Figure 5.8 Delamination rate vs. quantity of in-coating acid, comparison for organic coatings adherent to Zn (i) H₂PP and (ii) HpTS.

A summary of how the systematic increase in coating acid loading slows the rate of cathodic delamination is shown within figure 5.8 for (i) H₂PP and (ii) HpTS. At 5 wt% HpTS loading, cathodic disbondment is halted and does not occur within the 48hr time period used experimentally, although the H₂PP coatings are only able to significantly slow the delamination but not stop it outright.

The findings of this work show that the HpTS coating provides a higher level of cathodic disbondment inhibition than the H₂PP containing coating. The proposed explanation for this extra degree of inhibition is that the HpTS containing coatings have a dual action inhibition mechanism, whereas the H₂PP coatings do not. The inhibition mechanism that both organic acids share is the ability to create a pH buffering effect. The in-coating acid (H^+) acts as a pH buffer, neutralising the damaging OH^- created as a result of the cathodic O_2 reduction, which allows the coating to remain free of cathodic disbondment.

The additional inhibition mechanism provided by the HpTS acid additions is the reason why the E_{intact} values of organic coated Zn are pushed down uniformly by ca. 0.1 V vs. SHE. When HpTS containing organic coatings are adherent to Zn substrates a thick conductive oxide film is generated in addition to Zn^{2+} . The Zn^{2+} will migrate into the coating near to the coating-substrate interface. If any increased alkalinity occurs as a result of cathodic disbondment driving the cathodic O_2 reduction, the Zn^{2+} can react directly with any OH^- anions released. The Zn^{2+} combining with the damaging OH^- results in the formation of insoluble metal oxide/hydroxides. This has the effect of repairing/healing any protective oxide that has been dissolved by the cathodic products.

The H_2PP containing coatings also interact with the Zn surface but act to create a surface salt rather than a surface oxide layer. This Zn-PP salt is created at the substrate-polymer interface and it is thought that it does not provide total inhibition of the cathodic disbondment. It is proposed that the Zn-PP salt film is actually detrimental to the performance of the inhibition provided because the film is insulating. The insulating nature of the salt film actually hinders the generation of the in-coating Zn^{2+} reservoir.

In order to prove that Zn-PP is an insoluble species, 10^{-2}M phenylphosphonic acid was dissolved in distilled water and buffered to pH 5, hence allowing a sufficient amount of PP^{2-} free in solution. Aqueous 10^{-2}M Zn^{2+} was created by dissolving ZnCl_2 in distilled water. Upon mixing Zn-PP was found to rapidly precipitate out of solution to give a white powder. Gradual pH buffering up to pH 12 proved the stability of the salt under the highly alkaline conditions expected at the head of a cathodic delamination front.

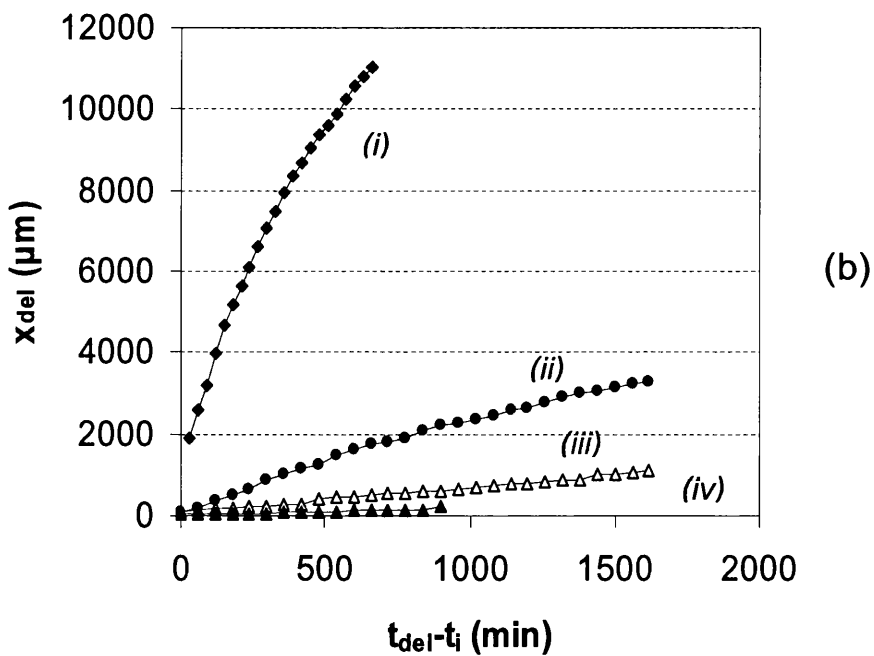
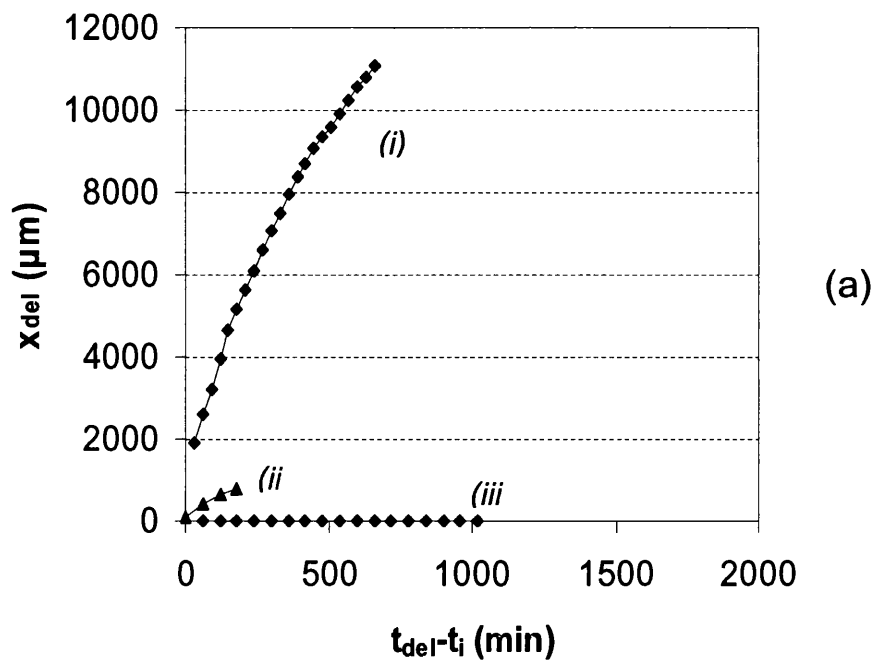


Figure 5.9 Plots of (x_{del}) vs. $(t_{del}-t_i)$ for $30\mu\text{m}$ PVB containing systematic variations of in-coating acid additions adherent on Zn substrates. Key: (a) H_pTS (i) 0, (ii) 3.1 and (iii) 5 %wt:wt. (b) H_2PP (i) 0, (ii) 3.1, (iii) 10 and (iv) 30 % wt:wt.

It is proposed that the interfacial salt film formed by the H_2PP etch primers does contribute to the degree of inhibition provided. The delamination kinetics of the PVB control coating shown in figure 5.9 are parabolic due to cation migration being the

rate determining step. In the case of the H₂PP delamination kinetics of figure 5.9 (b) there is an obvious transition to linear kinetics resulting from the in-coating addition of the H₂PP acid. This is the case for small additions and supports the notion that an interfacial salt film is produced that hinders interfacial electron transfer, stifling cathodic O₂ reduction, making this the rate determining step.

5.4 Conclusions

Considering acid etch primers adherent to pure Fe substrates, both in-coating HCS and H₂PP have been shown to provide a significant degree of inhibition of corrosion driven cathodic disbondment. The general finding is that up until higher acid loadings the H₂PP coatings provide a slightly higher level of inhibition. Removal of the organic coating from intact regions of substrate show that in the case of HCS an interfacial oxide film has formed on the metal surface. This is consistent with the findings that additions of both acids to the PVB cause a marked increase in E_{intact} from 0.1V vs. SHE to approximately 0.3V vs. SHE in both cases, independently of acid content. Further analysis of the E_{corr} profiles showed that the potential within the delaminated regions was also ennobled as a result of the organic acids. This ennoblement was seen to be significant at higher acid loadings, increasing the potential to -0.15V vs. SHE.

Comparison of the delamination rates for each acid as a function of loading shows that the H₂PP systems are more efficient at inhibiting the rate of cathodic disbondment at lower loadings. The proposed reason for this is that H₂PP containing coatings provide inhibition in two ways. The first way is through the formation of an insulating salt film that acts to block O₂ reduction. Evidence to support this comes from the knowledge that at small acid loadings the delamination rate no longer appears to be parabolic in nature, signifying that cation migration from the defect is no longer the rate determining step. The second way inhibition is provided is through a pH buffering action whereby the excess acid acts to neutralise the alkalinity of the cathodic reaction, hence maintaining the polymer-substrate adhesion. It is further proposed that the reason why H₂PP shows a higher degree of inhibition for primers of lower acid loading is because of its increased buffering effect compared to the HCS.

For organic acid etch primers adherent to pure Zn substrates it is concluded that these coating systems hold the possibility to replace strontium chromate inhibitor technology. The degree of inhibition has been found to be dependent upon the nature of the organic acid included within the polymer binder material. It was found that H₂PP additions to PVB are capable of significantly slowing the rate of disbondment

but not preventing it, whereas HpTS additions were able to completely prevent the onset of corrosion-driven cathodic disbondment at relatively low acid additions to the polymer matrix.

This inhibition was attributed to two mechanisms acting in unison, firstly a pH buffering effect acting to preserve the interfacial layer, and secondly through reinforcement of the interfacial zinc hydroxide film through the generation of an in-coating Zn^{2+} reservoir. In the case of the HpTS etch primers, this inhibition was enough to prevent disbondment, but the H₂PP etch primers were unable to achieve this. The proposed reason for this is that the insulating nature of the H₂PP induced surface film hinders the generation of the in-coating Zn^{2+} reservoir. The proposed mechanism by which this inhibition occurs in the case of PAni-pTS is through the migration of Zn^{2+} into the coating near to the coating-substrate interface. If any increase in alkalinity occurs resulting from O₂ reduction, the Zn^{2+} can react directly with the released OH⁻. This can result in the formation of insoluble metal oxides/hydroxides, repairing any protective oxide that has been dissolved by the cathodic products.

5.5 References

- [1] G. Williams, A. Gabriel, A. Cook, and H. N. McMurray, *Journal of the Electrochemical Society* **153**:B425 (2006).
- [2] J. Marsh, J. D. Scantlebury, and S. B. Lyon, *Corrosion Science* **43**:829 (2001).
- [3] A. J. Coleman, H. N. McMurray, G. Williams, A. A. Afseth, and G. M. Scamans, *Electrochemical and Solid State Letters* **10**:C35 (2007).
- [4] A. Leng, H. Streckel, and M. Stratmann, *Corrosion Science* **41**:547 (1999).
- [5] R. J. Holness, G. Williams, D. A. Worsley, and H. N. McMurray, *Journal of the Electrochemical Society* **152**:B73 (2005).
- [6] A. R. Bennett, H. N. McMurray, and G. Williams, *ECS Trans. Volume* **11**:71 (2008).

Chapter 6

Corrosion Studies of Mg-Al-Zn Galvanised Steels

6.1 Introduction

A strong desire currently exists within the pre-painted steel industry to decrease the gauge of Zn and Zn-alloy metallic coatings used for strip steel products, and this is driven primarily by the current high price of Zn. One such possibility of decreasing the raw material cost whilst maintaining high corrosion protection lies with the use of Zn-Mg alloy coatings, which have led to the trial production of Zn-Al-Mg alloy galvanised steels (Magizinc). Such metallic coating systems have been highlighted as being the next generation of galvanised steels for automotive and construction applications in particular. Zn-Mg alloy coatings have been proven to offer superior corrosion protection performance compared to conventional zinc galvanised steels in both the painted and unpainted states.

Morishita et al investigated the effect of applying a vapour deposited layer of Mg to the surface of electrodeposited Zn layers on steel in a manner that ensured the diffusion of Mg into the Zn surface layer to produce a Zn-Mg alloy [1]. Salt spray testing of these metallic coatings was carried out in a comparative manner in the unpainted state. It was discovered by salt spray testing using 5wt% NaCl solution that the Mg addition produced a 10-fold increase in time to red rust formation compared to the conventional electrodeposited Zn coated steel. The study indicated that this was due to reduced anodic dissolution and enhanced cathodic protection of the steel caused by the Mg addition to the surface layer.

Industrial corrosion tests have indicated that the levels of protection offered by Zn coatings can be improved by alloying the Zn with a number of different elements such as Mg or Ti, when used in conjunction with an organic coating layer. This scenario has only been given limited attention in the past and studies [2, 3] indicate the success of these metallic layers, leading to the possibility of omitting the application of corrosion preventative pre-treatments.

Studies investigating the specific inhibitory performance of the cathodic disbondment of organic coatings from a model Zn-Mg alloy system have been investigated by Hausbrand et al. The particular Zn-Mg alloy system under investigation was the Zn -Mg intermetallic $MgZn_2$, and is relevant to the work

presented here because $MgZn_2$ is present as the eutectic region in Magizinc alloy coatings [4].

This inhibition of cathodic disbondment has been proposed as a significant cause of why Mg containing Zn alloys exhibit superior performance to conventional galvanising in organic coated (paint) systems [2]. The cathodic delamination test samples and the methodologies used by Hausbrand et al are similar to those described within section 2.2.4.1 and section 2.3.3 respectively. Cathodic delamination is generally caused by cathodic O_2 reduction at the metal-coating interface, initiating near an organic coating defect and propagating beneath the intact coating. Disbondment is produced by the aggressive products of the O_2 reduction reaction that cause the degradation of the oxide-polymer bond, as explained fully in chapter 1.

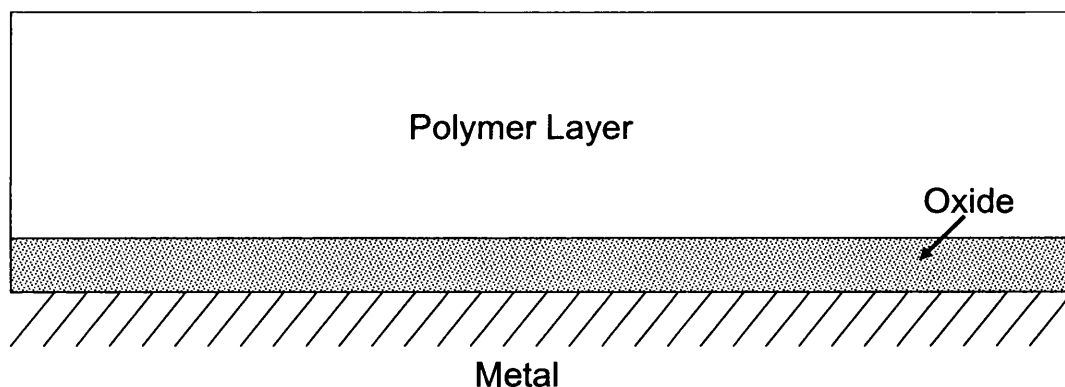


Figure 6.1. Schematic cross-sectional diagram of a typical organic coated metal.

To slow down the rate of cathodic disbondment, polymer-substrate interfaces must be developed that have the ability to inhibit O_2 reduction. The metal-oxide-polymer interface is illustrated in figure 6.1. One way of achieving inhibition of O_2 reduction is to reduce rates of interfacial electron transfer at the oxide-polymer interface, so as to stifle O_2 reduction. The availability of electrons at the oxide surface depends greatly upon the trans-oxide conductivity and oxides with large band gaps have very low surface electron concentrations, even at very cathodic potentials [5]. In addition to the preference for large band gap oxides, the oxide should ideally exhibit a high alkaline stability [5]. Amphoteric and acidic oxides which are alkali soluble will tend to dissolve in the highly alkaline electrolytes produced by cathodic O_2 reduction.

From the perspective of inhibiting cathodic disbondment of organic coatings from galvanised steels, magnesium is an ideal alloying element because it acts to create a large band gap oxide (MgO) which has a large band gap of between 7.3eV and 8.7eV [6] and accordingly has excellent alkaline resistance. Another alloying element that creates a large band gap oxide in addition to Mg is Al, where the band gap of Al₂O₃ is stated as being 6.3eV [7].

A study by Hausbrand et al [2] investigated the effect of MgZn₂ intermetallic on the cathodic delamination of non-inhibited organic coatings. It was thus shown that cathodic disbondment could not be produced on MgZn₂. The MgZn₂ intermetallic was chosen for study because it is the most stable of the three known Zn-rich Mg-Zn₂ crystalline intermetallics [8] and therefore most likely to form within Zn-Mg alloys. Other findings were that in the organic coating defect (where MgZn₂ is exposed to the experimental NaCl electrolyte), the corrosion potential within the artificial defect on the MgZn₂ intermetallic alloy is similar to Zn. The potential is similar to Zn due to rapid loss of Mg from MgZn₂ exposed to aqueous NaCl. Conversely the effect of magnesium was significant at areas of intact organic coating, where the potential of the intact interface is ca. 0.7V more negative than in the defect region. This reverses the normal polarity of the cathodic delamination cell and causes there to be no driving force for cathodic delamination. If the substrate was zinc, the driving force for delamination would exist because the defect area is of a lower potential than the intact coating [9, 10]. The more negative under-film potential (E_{intact}) in the case of MgZn₂ is attributed to the oxide layer formed at the MgZn₂-polymer interface. The potential is low because this oxide layer has a large band gap, i.e. the electronic properties of the oxide at the surface are more like MgO than ZnO. Thus the increased resistance to cathodic disbondment on MgZn₂ derives from the electronic properties of the MgO. However it was also found that anodic dissolution of the Zn-Mg does occur at regions of cut edges where sacrificial protection of steel takes place in the usual way.

This novel galvanising alloy, known as Magizinc consists of Zn-1.5%Al-1.5%Zn and has been produced commercially as a prototype line trial material for full analysis. Magizinc is described fully with section 1.4.4 and was developed with the intention of utilising the wide band gap metal oxides (MgO and Al₂O₃) occurring naturally on

its surface to provide enhanced corrosion protection as previously describe. Here this alloy coating is investigated for the inhibition of cathodic disbondment of adherent organic coatings, and other coating failure mechanisms are fully documented.

6.2 Experimental

Hot dip Zn-1.5%Al-1.5%Mg coated steel panels (Magizinc) were obtained directly from a pilot line trial with a metallic coating thickness of approximately 10 μ m [11]. Samples were cut into 50 x 50 mm foils using metallographic shear cutters. Polyvinyl butyral-co-vinyl alcohol-co-vinyl acetate (PVB), molecular weight 70,000 – 100,000 was obtained from the Aldrich chemical company. All other chemicals were obtained from the Aldrich chemical company in analytical grade purity. Metal samples were de-scaled and cleaned using aqueous slurries of alumina made from 6 μ m alumina powder obtained from Buehler UK followed by cleaning with distilled water and degreasing using analytical grade ethanol.

Organic coatings were created by bar coating PVB solutions (15.5 wt:wt) in ethanol over prepared metal substrates as described with section 2.2.4.1. Scanning Kelvin probe (SKP) potentiometry is fully explained in chapter 2.3, together with details of the Stratmann type delamination cell. In order to fully study corrosion phenomena on the Zn-Al-Mg alloys, a mixture of Secondary Ion Mass Spectrometry (section 2.5) and atomic force microscopy (section 2.6) were utilised, details of which are fully described within chapter 2. Optical microscopy was undertaken using a Meiji light microscope and corresponding image recording using an adapted Nikon Coolpix digital camera.

Corrosion samples were subject to initiation and equilibrium under high relative humidity (96%) and static air at 20°C (room temperature). The standard method used to induce filiform corrosion (FFC) is used as documented in chapter 2.

6.3 Results and Discussion

6.3.1 The Microstructure of Hot Dip Mg 1.5/Al 1.5/Zn Coatings

The microstructure of Magizinc was revealed by metallographic polishing prior to etching with Nital as described within section 2.9. The revealed microstructure is shown in the optical micrograph of figure 6.2 and is taken at approximately 50% of the alloy coating thickness. The microstructure consists of primary Zn dendrites of containing trace amounts of Al and Mg, surrounded by $MgZn_2$ eutectic containing Al in solid solution [4].

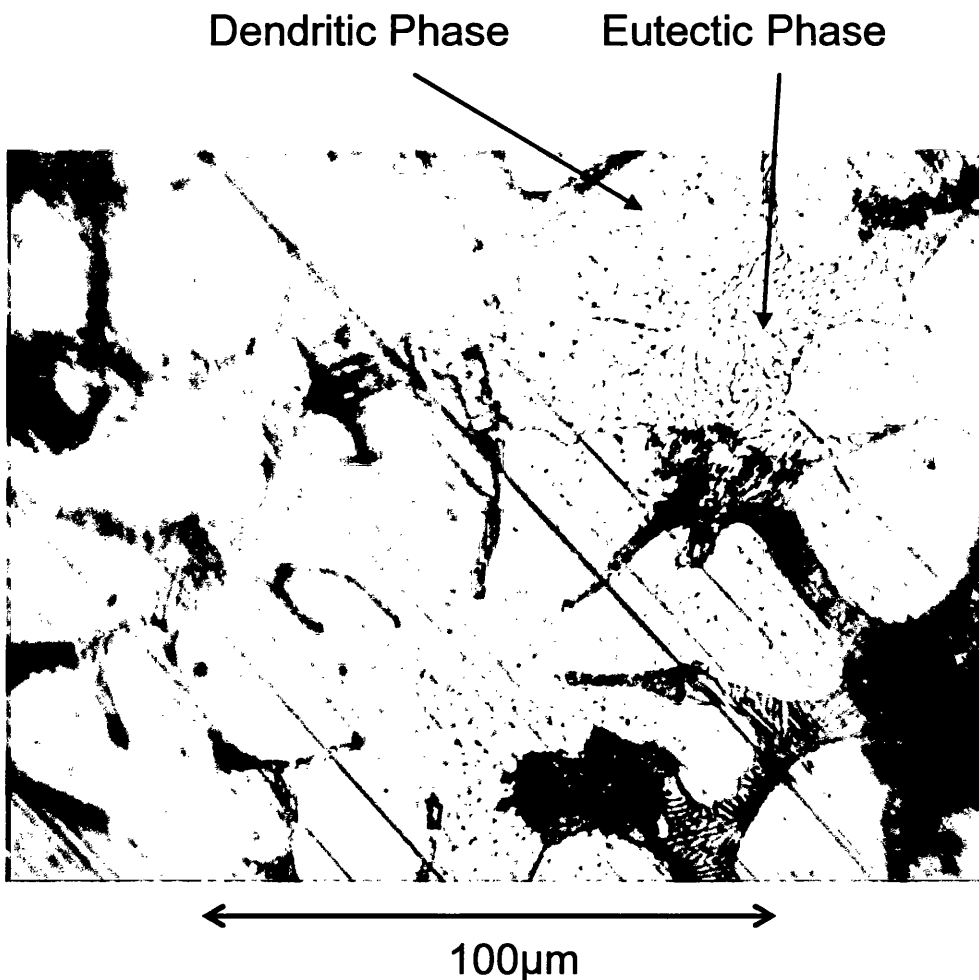


Figure 6.2. Optical microscopy of Magizinc at high magnification, showing primary zinc dendrites surrounded by Zn-Mg-Al eutectic 50% depth through coating.

The Magizinc coating was removed via metallographic polishing to reveal microstructure changes as a function of distance from the steel surface. This was achieved by metallographic polishing at a slight angle to the alloy coating surface as described in section 2.9. Figure 6.3 contains optical micrographs of the Magizinc microstructure in a sequence (a) to (h). These images show the changing microstructure from the steel surface up to the surface of the Magizinc and are taken at a lower magnification than the micrograph of figure 6.2.

Close examination of the image sequence of figure 6.3 shows that as the distance from the steel surface increases, so does the amount of dark areas amongst the zinc dendrites. This dark region is the eutectic phase as labelled at higher magnification within figure 6.2. It is clear from these micrographs that the eutectic is continuous and the individual dendrites are separated from one another. The surface topography of the Magizinc alloy surface is undulating and this observation is highlighted in figure 6.3 (c) onwards, where the eutectic region is seen to become part of the surface. Following the series of images in sequence to figure 6.3 (h) would suggest that a large portion of the Magizinc alloy surface is Mg-rich eutectic (possibly > 75%).

To explore the constituents of the Magizinc alloy surface in more detail, secondary ion mass spectrometry (SIMS) has been undertaken to record the ionic species present on the alloy surface. SIMS analysis of the Magizinc alloy surface was undertaken using the equipment described with section 2.5, whereby a broad mass spectrograph of the sample surface was recorded. To remove contaminants from the alloy surface, samples were cleaned using 5µm alumina slurry following the method described within section 2.2.4.1. The major finding of the SIMS analysis was that the surface layer of the Magizinc alloy contains a large amount of MgO.

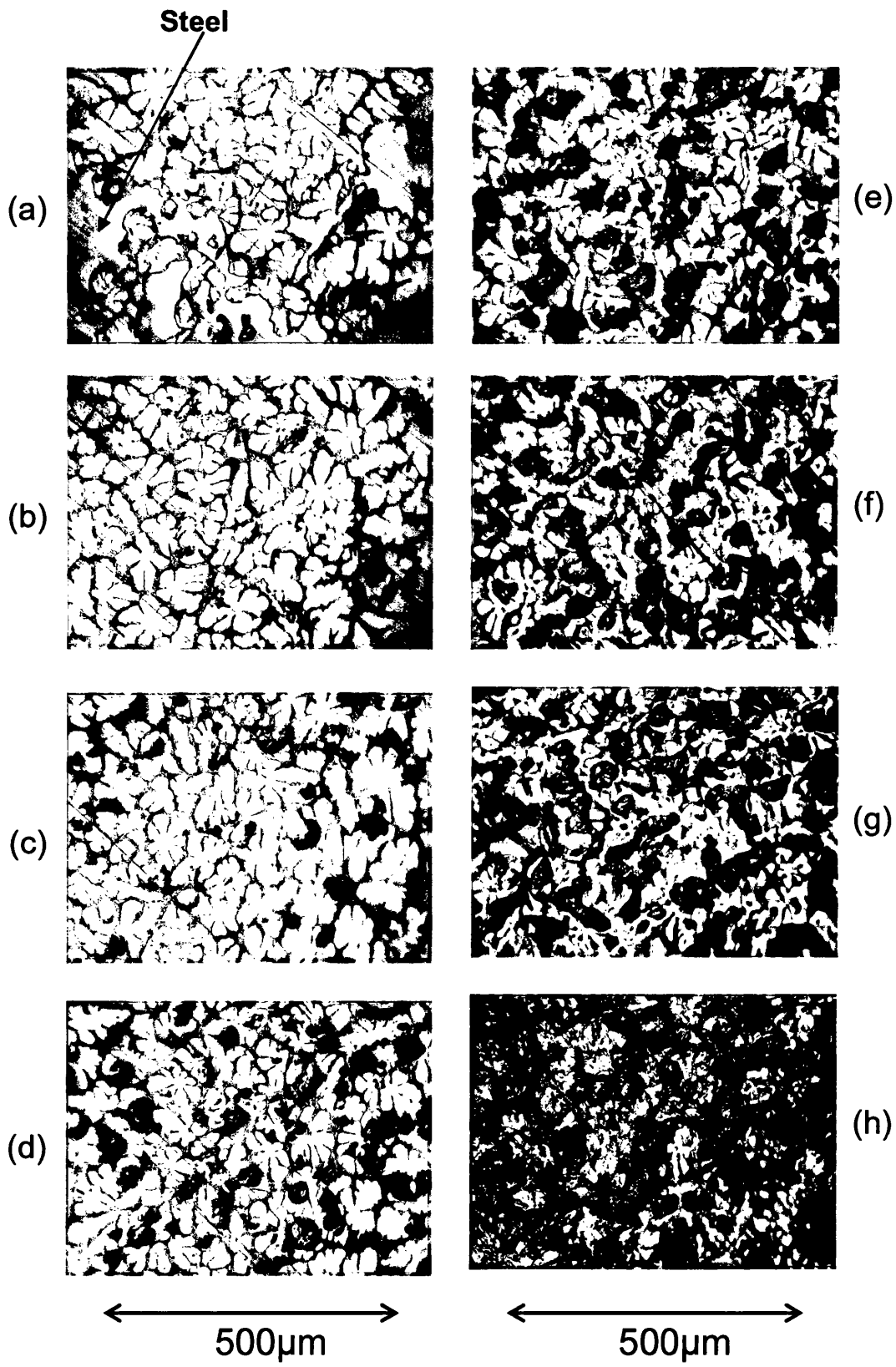


Figure 6.3. Optical microscopy of Magizinc microstructure through the metallic coating from (a) the steel surface systematically through the coating to the Magizinc surface (h) at $\sim 10\mu\text{m}$ intervals.

6.3.2 Cathodic Delamination Testing

Cathodic delamination samples containing artificial coating defects were created following the method of Stratmann et al as described within section 2.2.4.1. Non-inhibited PVB was used as the organic coating over the Magizinc alloy layer. Aliquots of 5% aqueous NaCl electrolyte were added to the artificial defects in an attempt to initiate cathodic disbondment of the organic coating. At no region within this artificial defect was any underlying steel exposed to the corrosive environment, and the entire defect region comprised only intact Magizinc. The scanning Kelvin probe (SKP) was used to monitor under-film electrode potentials following exactly the same cathodic delamination testing procedure described in section 2.3.3, and the environmental conditions were kept constant throughout at 96% RH and 20°C. Figures 6.4 (a) and 6.4 (b) show photographs of the cathodic delamination sample before initiation with 5% NaCl and after 300hrs corrosion respectively. Comparison of 6.4 (a) and 6.4 (b) reveals no visual sign of organic coating disbondment, only generalised corrosion within the defect and this is the case for other alloy galvanised steels [12].

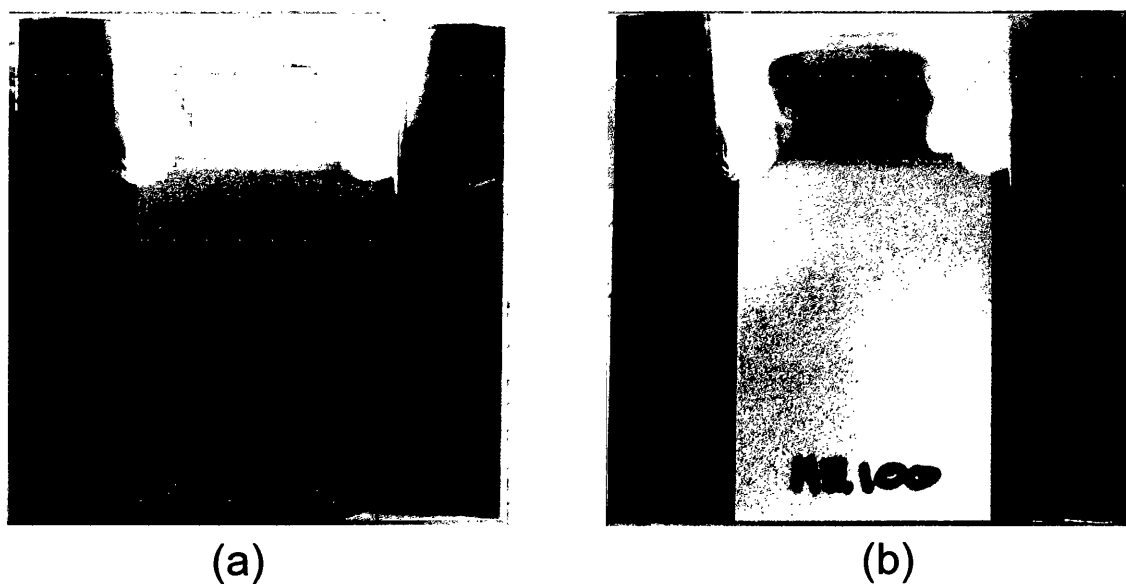


Figure 6.4. Cathodic delamination testing of organic coatings on Magizinc after (a) 0hrs and (b) 300hrs testing.

The SKP profile obtained from the cathodic delamination test sample after 300hrs is shown in figure 6.5, where in this profile no deviation from the intact coating

potential of ca. -0.45V vs. SHE is observed. This absence of change in potential distribution confirms that no cathodic delamination is taking place on the Magizinc substrate. The E_{intact} value of -0.45V vs. SHE is 0.15V vs. SHE more negative than recorded with identical coating systems adherent to pure zinc substrates (chapter 4). The simplest explanation of this depreciation of recorded E_{intact} is the low work function of the Mg (3.68eV) compared to the work function of Zn (4.3eV) [13]. Hausbrand et al [2] have published an E_{intact} of ca. -1.05V vs. SHE for the MgZn₂ intermetallic system, which is considerably lower than observed in the case of organic coated Magizinc. The differences between their value of E_{intact} and these findings may be explained by the much lower amounts of Mg present within the Magizinc system, which could render the system incapable of creating such low electrode potentials. It is suspected that the lack of cathodic delamination after such extended time periods is due to the mechanism proposed by Hausbrand et al [2].

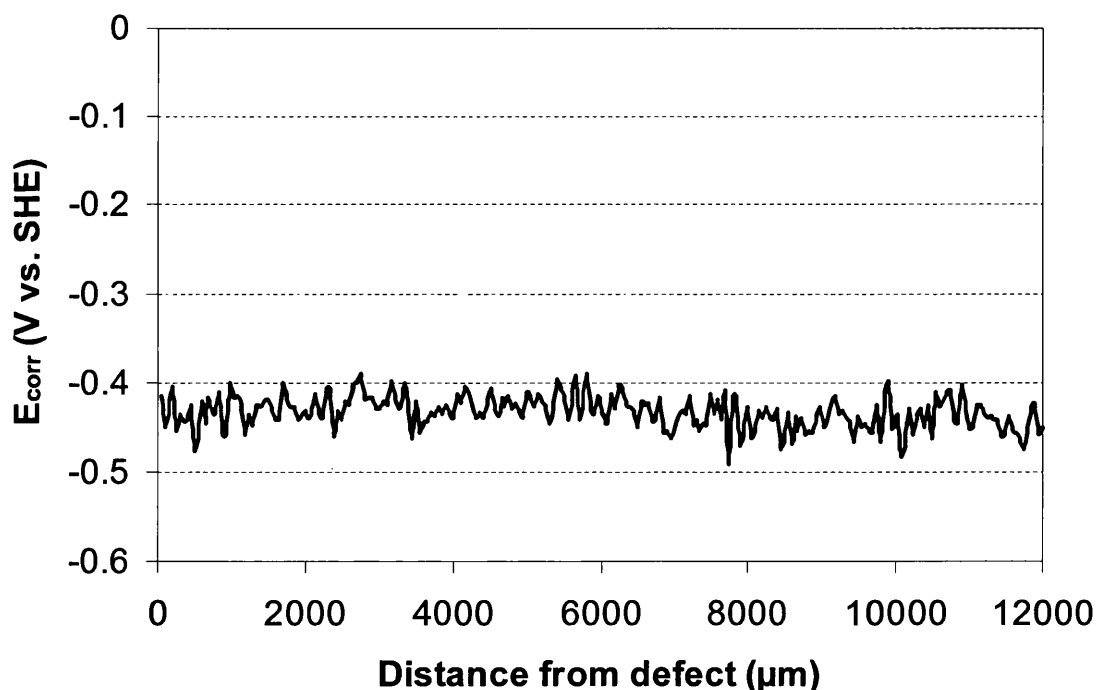


Figure 6.5. SKP profile of under-film electrode potentials after 300hrs corrosion, showing no cathodic delamination.

6.3.3 Exposing the Steel at the Defect Edge

The high cathodic delamination resistance imparted by the Magizinc alloy coating is proven in section 6.3.2. Accordingly it was thought prudent to explore other possible organic coating failure mechanisms that could occur in such a system. Using the design of the Stratmann type delamination cell described within section 2.2.4.1, the Magizinc alloy coating was totally dissolved from the defect region using concentrated HCl to expose the underlying steel substrate. Throughout preparation of the test samples it was ensured that the exposed steel substrate was solely located within the defect region as shown in the schematic of figure 6.6.

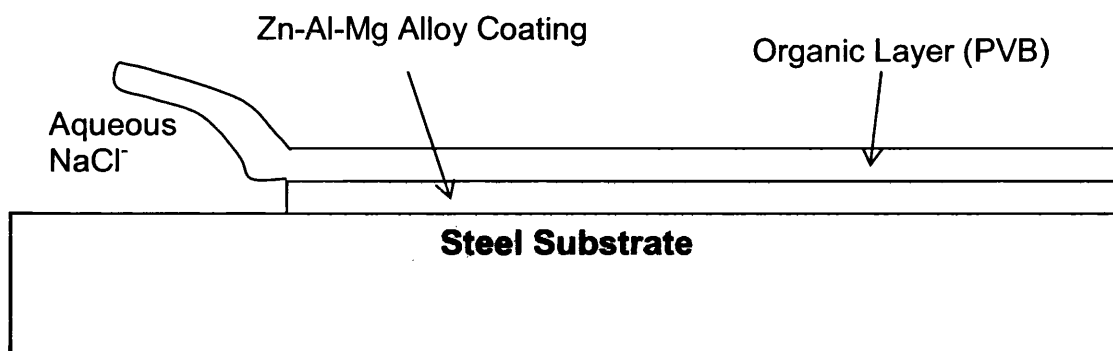


Figure 6.6. Cross sectional schematic diagram of Magizinc corrosion samples with an exposed steel organic coating defect.

Application of 0.86 mol dm^{-3} (5% w/v) aqueous NaCl to the sample defect under conditions of high (96%) RH caused visibly recognisable red rust formation within the defect region within an hour of electrolyte contact. Cathodic delamination would not be expected in such a system because the free corrosion potential of the steel is higher than the zinc-based metallic coating. The expected result is that the metallic coating will dissolve sacrificially in an attempt to provide a degree of protection to the exposed steel in the artificial defect.

Samples were subject to the accelerated corrosion conditions for over 6 months, and organic coatings remained un-delaminated (free from cathodic delamination) throughout this time consistently on all individual samples tested. As expected the anodic dissolution of the Zn-Al-Mg alloy coating became apparent after

approximately 3 months of testing although proceeded into regions of intact coating at a very slow rate (<1mm penetration).

A major discovery made using this method of corrosion testing of the Magizinc alloy coatings is the initiation and propagation of filiform corrosion (FFC) from the artificial defect – intact organic coating boundary into the intact regions of coating. Visible threads of FFC became apparent four weeks after application of the experimental electrolyte to the artificial defect. Once initiated the FFC was seen to propagate robustly into the intact coating in an apparently random manner. Figure 6.7 shows photographs of one of the test samples, highlighting the extent of the FFC attack in relation to the relatively low levels of anodic dissolution of the metallic coating.

Over time the FFC was observed to initiate randomly at cut edges (figure 6.8) and also remotely at areas of seemingly intact coating in the centre of the sample (figure 6.9) where exposed steel is not expected.

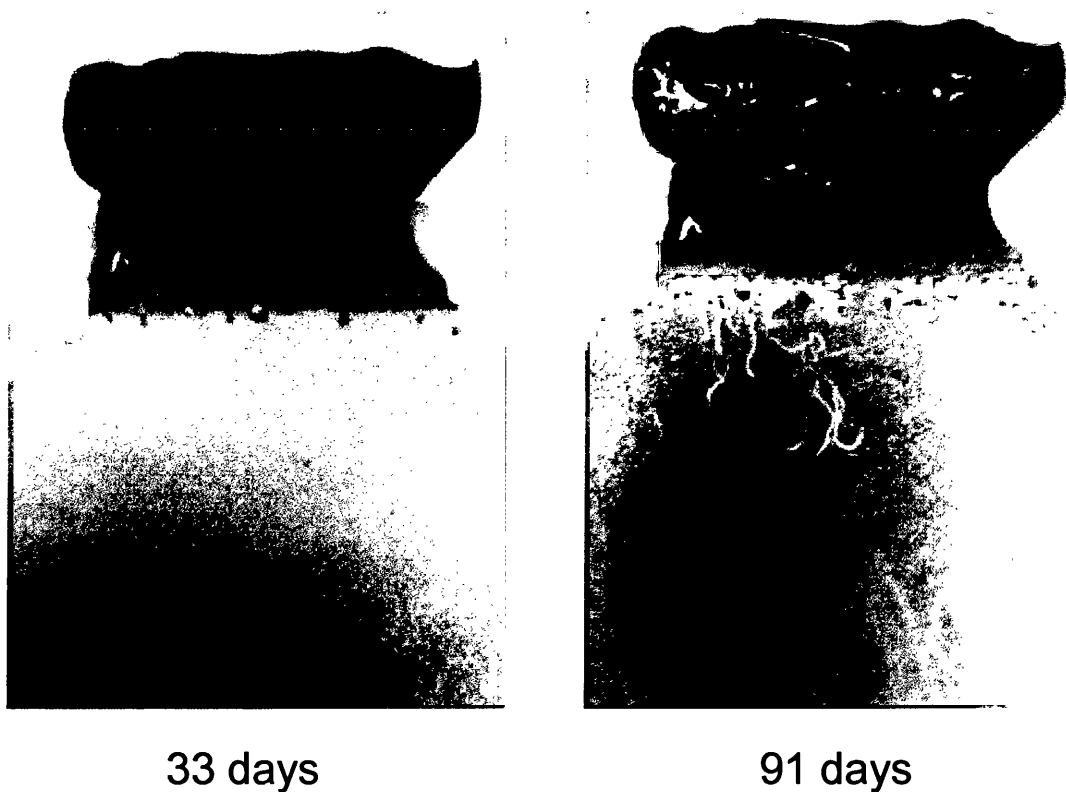


Figure 6.7. The discovery of Filiform corrosion on Zn-Al-Mg coating upon exposure of steel in the artificial defect.

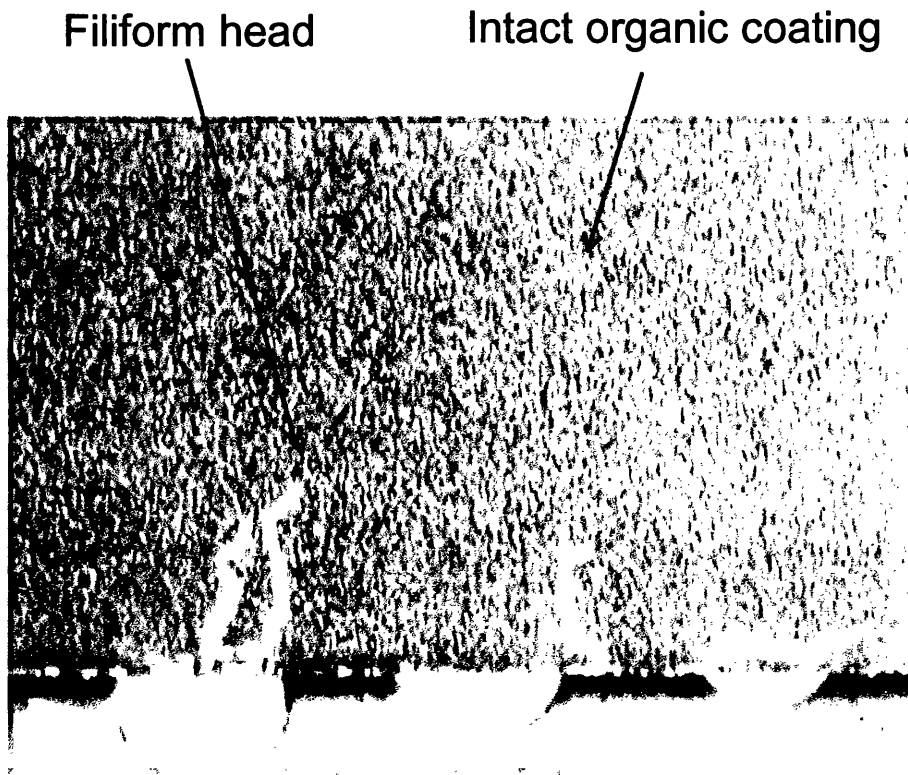


Figure 6.8. Filiform corrosion occurring at cut edges, propagating into region of intact coating after 3 months exposure to 96% RH.

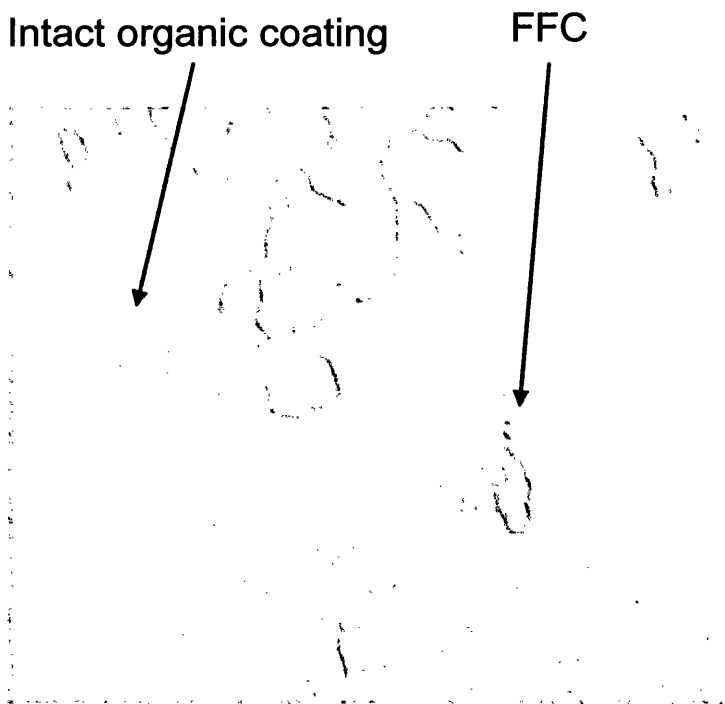


Figure 6.9. FFC occurring under regions of intact organic coating.

FFC was observed to grow significantly over a period of 6 months causing widespread attack across the sample surface. Bulk anodic dissolution of the Magizinc alloy coating is significantly less than the extent of the FFC attack, which is illustrated photographically in figure 6.10.

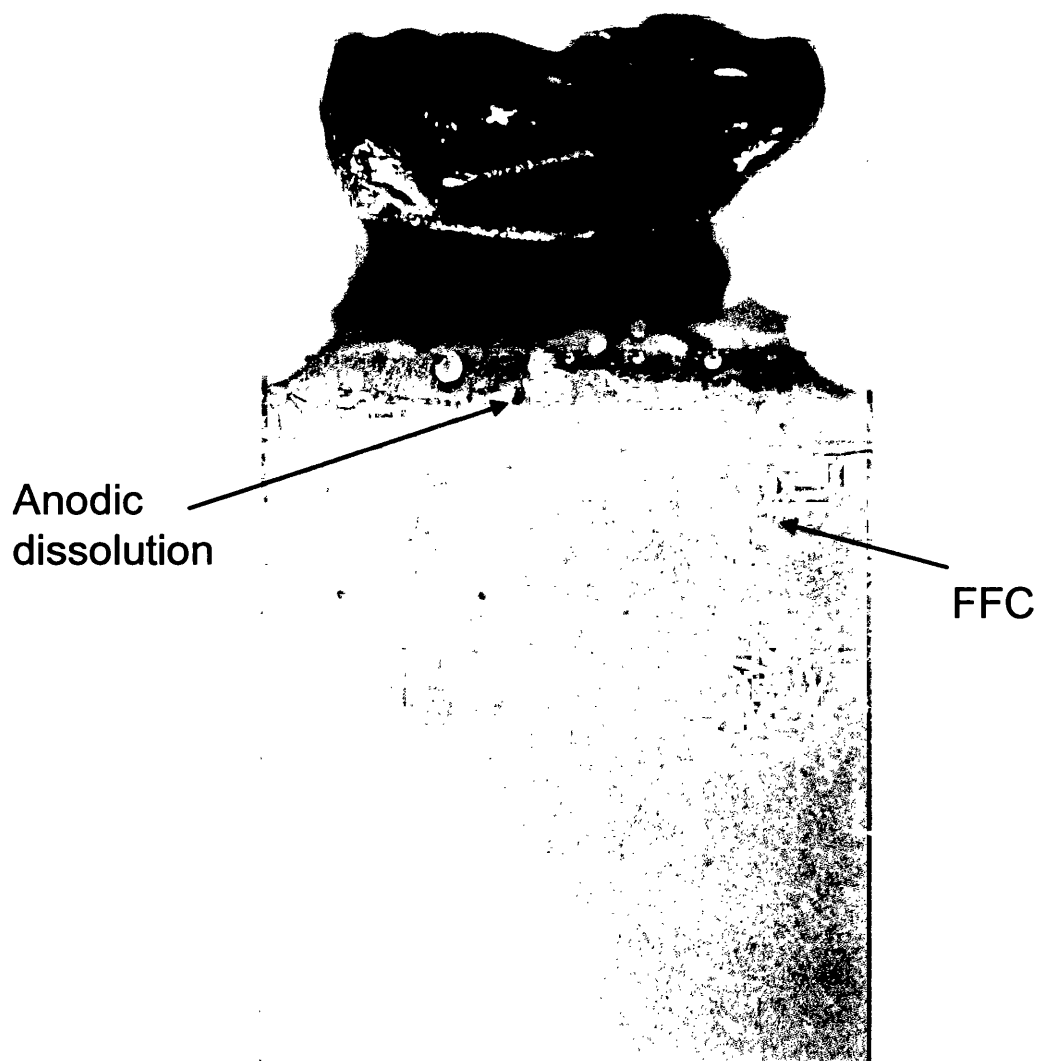


Figure 6.10. The extent of FFC after 6 months exposure to experimental conditions.

6.3.4 Mechanism of Conventional FFC

Filiform corrosion (FFC) was first described within the literature by Sharman in 1944 [14], who witnessed the corrosion phenomena to occur under lacquer coated steel. FFC is known to principally affect organic-coated iron (steel) or aluminium surfaces, where it initiates at penetrative coating defects to produce characteristic thread-like under-film deposits of corrosion product. FFC has also been reported to occur under organic-coated magnesium, but is not reported to occur under organic coated Zn or Zn-alloys, whereas in the work described here it has been found to do so.

The mechanism of FFC corrosion found to occur at the metal – polymer interface of organic-coated aluminium is shown in figure 6.11. In this schematic, (a) represents the mechanism of corrosion initiation and (b) represents the mechanism by which the FFC propagates. Corrosion filaments consist of a mobile electrolyte filled head, which contains metal cations and aggressive anions such as chloride, the forefront of which houses the anodic reaction. The FFC tail is dry, and is made up of porous corrosion product that provides a path for oxygen to reach the rear of the filament head where the cathodic O₂ reduction reaction occurs. The way in which FFC occurs is primarily due to differential aeration, where upon the introduction of a penetrative organic coating defect and incursion of corrosive electrolyte begins the anodic attack of the exposed metal surface near to and under the adjacent organic layer. Cathodic O₂ reduction occurs preferentially at sites that have greatest oxygen availability, and this initially occurs at the location of the organic coating defect. It is the localised condition of differential aeration that is thought to be the primary driving force for filament advance.

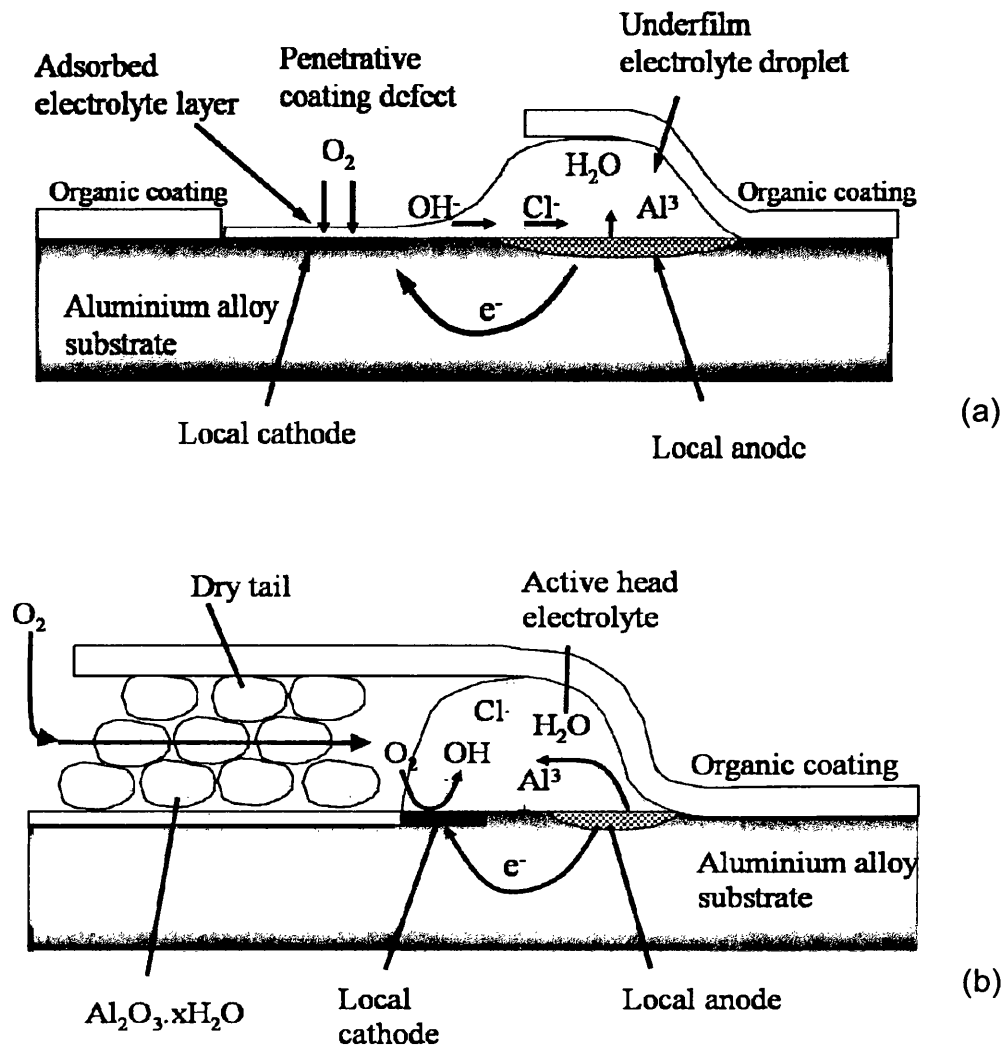


Figure 6.11. Conventional FFC mechanism as occurs on organic-coated aluminium;
 (a) initiation of FFC and (b) propagation of FFC.

Once the FFC corrosion cell has become established the mechanism of filiform advancement illustrated in figure 6.11 (b) takes effect. The anodic metal dissolution reaction takes place at the front of the filiform head, generating metal cations that migrate towards the cathodic region. The FFC head regions are known to typically exhibit a low pH towards their leading edge (as low as pH 1). The oxygen reduction reaction takes place at the rear of that head, and is fuelled by oxygen travelling through the filiform tail (the path of least resistance). Hydroxyl formed by the cathodic reaction migrates towards the anode (front of the head), where halfway they meet the metal cations to form metal oxide/hydroxides, which are subsequently insoluble and precipitate out of solution. This causes the electrolyte at the front of the

filiform head to become concentrated in ions, whereas the electrolyte at the rear of the filiform head becomes relatively pure water due to the precipitation of the corrosion product. This concentration differential causes an osmotic effect where the electrolyte at the rear of the head is drawn forwards to dilute the ionic concentration at the front of the head, causing the tail region to become dry.

6.3.5 SKP Analysis of FFC Attack of Magizinc

The SKP was used to scan the regions of the organic coated Magizinc subject to FFC attack, creating surface potential maps such as shown in figure 6.12 (b). FFC threads are easily recognisable within this potential map and are confirmed within the optical image of figure 6.12 (a). The FFC tail regions are highlighted as areas of light colour and the anodic regions (FFC heads) are shown as low anodic potential. As mentioned previously in section 6.3.2, the areas of the potential map corresponding to approximately -0.45V vs. SHE represent regions of intact organic coating.

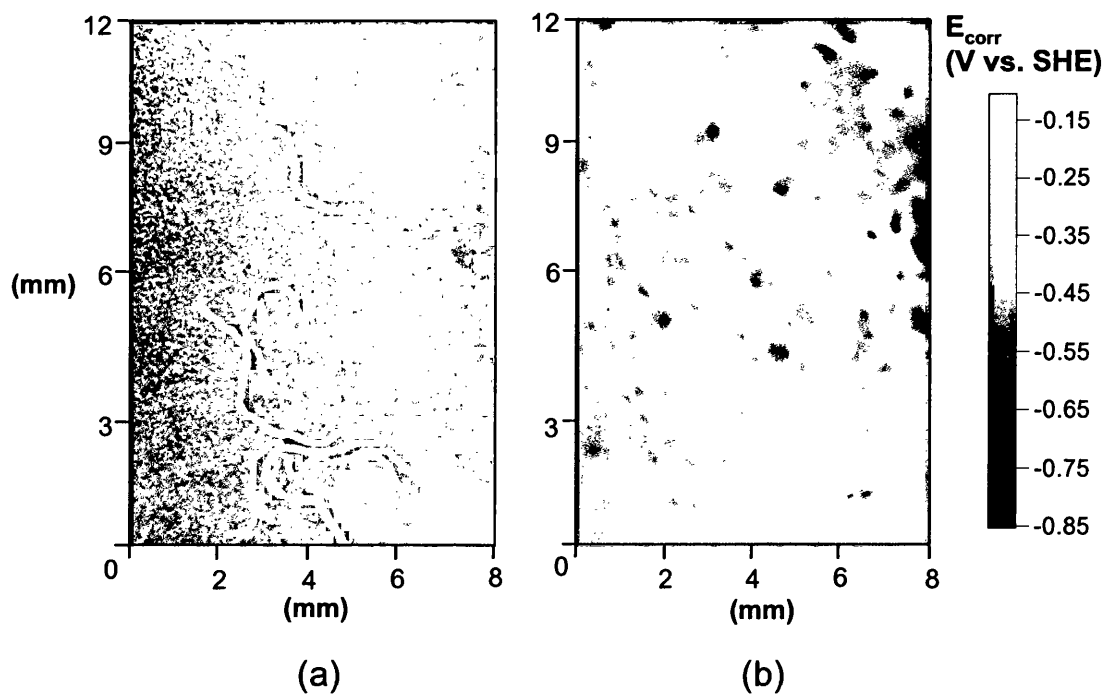


Figure 6.12. (a) Optical image of FFC under organic layer, (b) corresponding SKP potential map over same surface.

From figure 6.12 (b) it is clear that over the 8mm x 12mm sample area shown, many low potential regions (dots) are present, characteristic of anodic areas that could represent a filiform head. These regions do not have any following tail regions (white areas of high potential). This suggests the low potential regions are representative of random anodic sites of independent localised corrosion. This localised corrosion is believed to be caused by the diffusion of moisture through the organic layer, and it is reasonable to assume these anodic sites do not interfere with the FFC corrosion in any way.

To aid elucidation of the precise corrosion mechanism occurring within this system, an E_{corr} profile was taken through the centre of a filament head, and this is presented in figure 6.13. The E_{corr} values were taken directly from the potentiometric data shown in figure 6.12 (b). Three distinct regions are clear within this E_{corr} profile and were verified by optical photography (figure 6.12 (a)); the intact coating surface, filiform head and the filiform tail.

The potential of the intact region (E_{intact}) is ca -0.4V vs. SHE - which is slightly lower than the value of ca. -0.3V characteristic of pure PVB coated zinc and is consistent with the findings of section 6.3.2. Filament heads appear at potential minima of ca -0.7V vs. SHE – characteristic of zinc freely corroding in a chloride containing electrolyte [10]. Filament tails appear as regions of increased potential at ca -0.3V vs. SHE – a value typical for organic coated zinc [10]. The correspondence of these potentials to the localised FFC corrosion cell is shown schematically in Figure 13 (b). It is proposed that anodic acidification due to release of Al^{3+} aquocations and cathodic activation (in the tail region) due to surface Mg depletion are the principal factors sustaining the FFC mechanism.

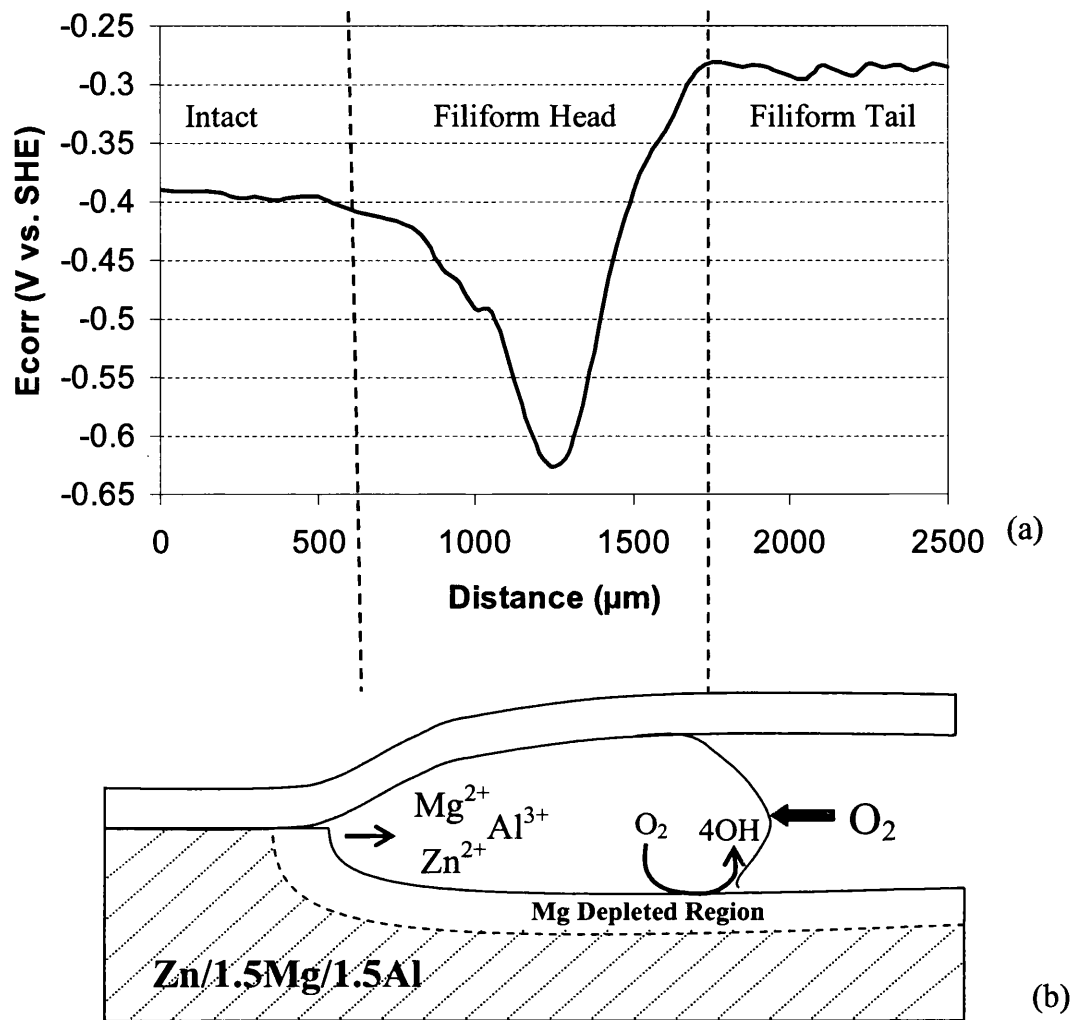


Figure 6.13. SKP derived potential variations through a FFC head on Zn-Al-Mg alloy coated steel.

6.3.6 Exploring the Significance of Exposed Steel

An observation of this particular FFC is that it primarily initiates at areas of exposed steel at locations such as cut edges and the artificially created defect (figure 6.6). Because FFC is not widely known to occur on Zn or Zn-alloys, a possibility exists that this alloy is not capable of maintaining a cathode at all. A possible situation is that the O_2 reduction reaction takes place on the steel substrate, whilst anodic dissolution of the Magizinc alloy takes place as conventionally described at the forefront of the filament head.

Following the conventional FFC mechanism outlined within section 6.3.4, for a steel cathode to be continuously located at the rear of a filament head, the anodic dissolution would have to be sufficiently severe to expose the underlying steel as the filament advances. This would create what is effectively a dynamic steel cathode trailing at the rear of the filament head. Both secondary ion mass spectrometry (SIMS) and atomic force microscopy (AFM) have been used here to discover if the level of anodic dissolution is severe enough to expose the underlying steel substrate as the filament advances. SIMS mass imaging has been utilised to detect any exposed steel, and the depth calibrated AFM has been applied to physically measure the depth of metal dissolution. Before each of these techniques could be employed, both the organic coating and the corrosion product were removed from the metal surface as described in section 2.5. This involved mechanically peeling away the organic layer followed by removal of the corrosion product by sonication in distilled water prior to ethanolic solvent drying.

The SIMS Fe^+ mass image is shown in figure 6.14, and does not highlight any characteristic FFC tracks. This indicates that the anodic attack is not sufficiently deep enough to expose the underlying steel. However, this mass image does indicate scattered Fe^+ across the substrate surface. This could have been caused by the hot-dip galvanising process, where trace amounts of steel may have become intermixed with the Magizinc alloy. An alternative explanation is that the trace Fe^+ could simply be meaningless background noise from the mass imaging technique itself. Either way the SIMS analysis of the Magizinc surface has not shown any traces of the underlying steel being exposed as a direct result of the anodic FFC attack.



Figure 6.14. SIMS derived mass image detecting Fe^+ on a FFC attacked Zn-Al-Mg (Magizinc) alloy after the organic layer and all corrosion products had been removed from the FFC tails. Not able to show FFC tracks.

FFC tail depth was measured using depth calibrated AFM on a number of different filaments after removal of the organic layer and corrosion products following the method described in section 2.5. The average depth of anodic metal dissolution was calculated to be $\sim 1.04\mu\text{m}$, and a recorded AFM image of a filament tail is shown in figure 6.15. This image clearly shows the filament tail in relation to the non-corroded (intact) Magizinc alloy surface. Within the filament tail track there are two distinct regions that have been subject to differing levels of anodic dissolution. With reference to the optical micrograph of figure 6.2, it is a possibility that the shallowest metal dissolution has occurred on the zinc dendrites. It is therefore proposed that the deeper anodic attack has taken place over the MgZn_2 eutectic, where preferential dissolution of the Mg has taken place. The average FFC depth of $1.04\mu\text{m}$ is consistent with the results of Fe^+ mass imaging because the corrosion has only attacked the surface 10% of the $10\mu\text{m}$ thick alloy. This is highlighted by optical microscopy within figure 6.16 that clearly shows the underlying surface topography is largely intact after removal of the corrosion products.

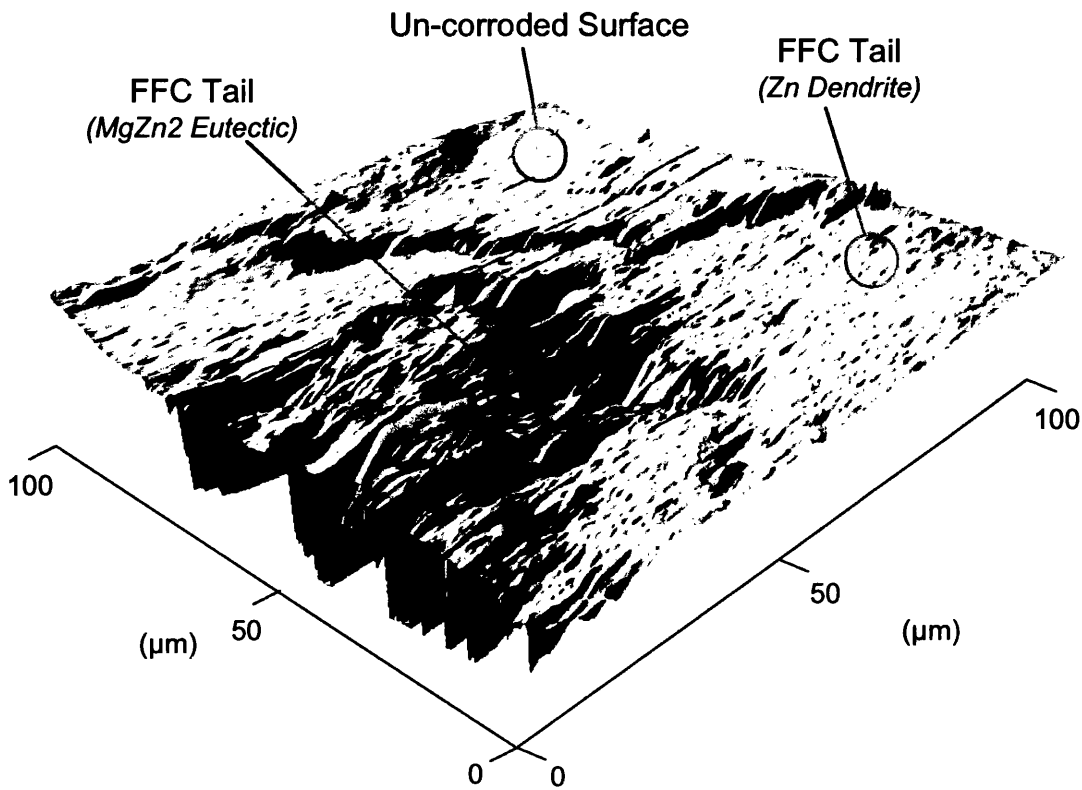


Figure 6.15. Depth calibrated AFM imaging of FFC attacked Zn-Al-Mg alloy following removal of corrosion products.

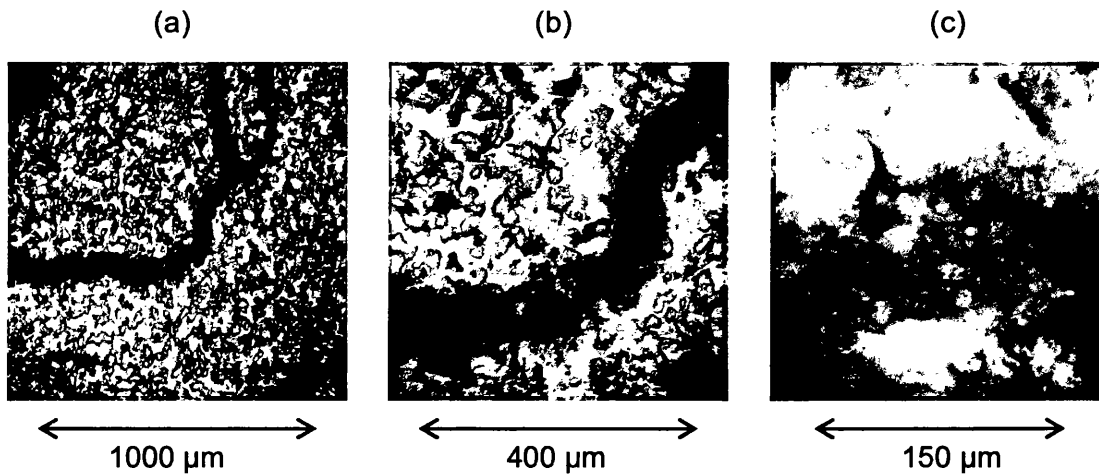


Figure 6.16. Optical imaging of FFC attacked Zn-Al-Mg alloy following removal of corrosion products, at varying magnifications.

This confirmation that FFC induced anodic metal dissolution does not penetrate deep enough to expose a mobile cathode provides further support to the notion outlined schematically in figure 6.13.

6.3.7 Indications of Unconventional FFC

The mechanism outlined within figure 6.13 is a plausible theory of how the FFC propagates. Further investigation of FFC occurring on organic coated Magnesium alloys has shown that the filament heads are capable of crossing the filament tails. If the corrosion propagation mechanism occurs as outlined in figure 6.13 it would be impossible for this to happen, signifying the true mechanism is unconventional. The incursion of a filament head into a filament tail under the conventional mechanism would expose the filament head to relatively large amounts of O_2 . The differential aeration cell would be altered, causing the filament head to alter course away from the tail it was about to cross. For a filament head to be able to cross a filament tail in this manner, the tail must be void of O_2 .

Three dimensional time-lapse potentiometry has been employed to record E_{corr} surface maps over live FFC and are presented in figure 6.17 at 30 hr intervals. A number of filament heads are first seen approaching filament tails and in the later maps are seen to make contact and cross through them. This has been repeated for a number of samples and the findings were found to be fully reproducible.

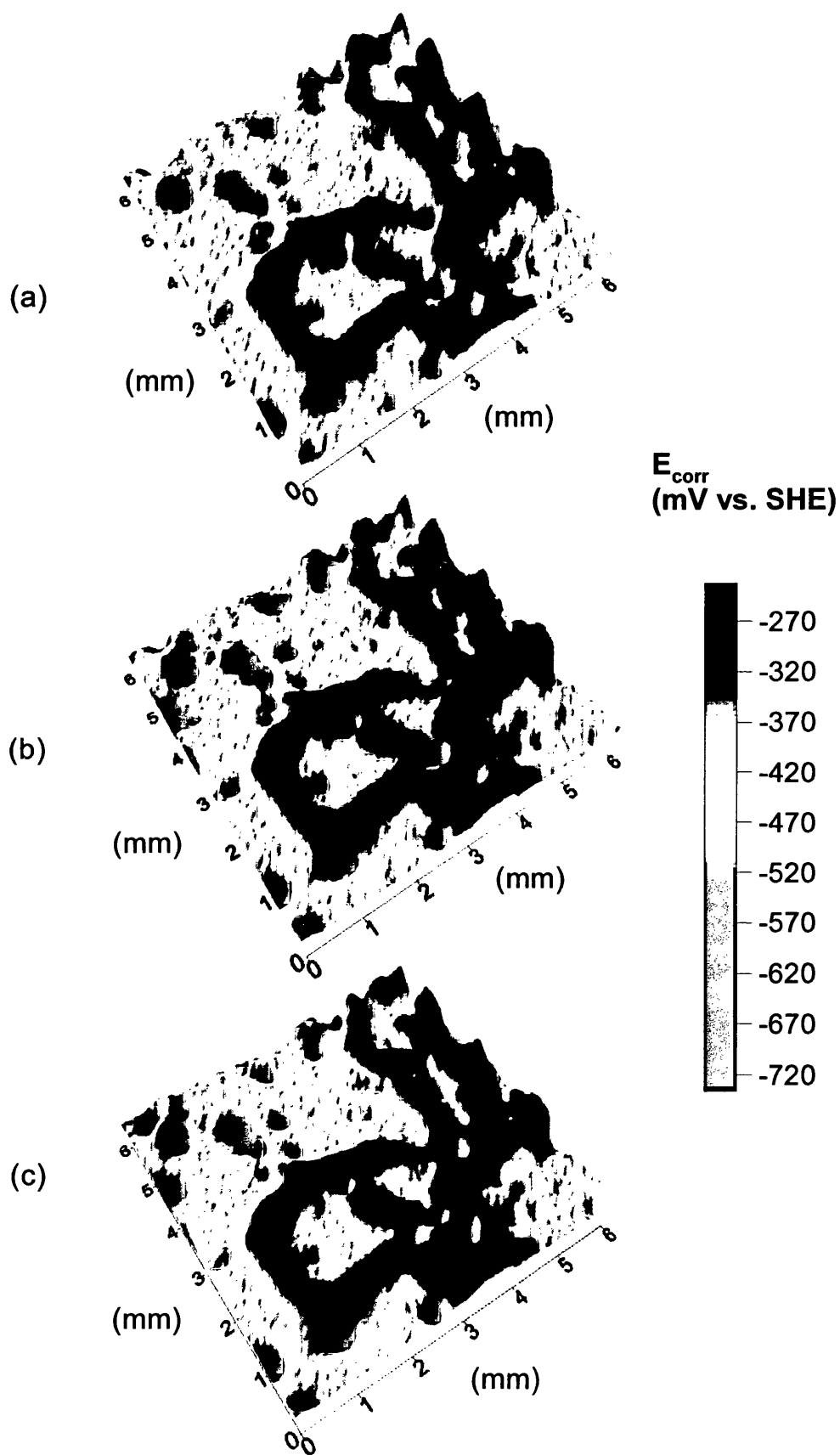


Figure 6.17. 30hr interval E_{corr} potential maps showing FFC heads crossing filament tails. Image maps (a) approaching tail, (b) touching tail and (c) dissecting tail.

6.3.8 Further Investigations into the Active FFC Mechanism

The findings so far shed doubt towards a corrosion mechanism whereby O_2 reduction occurs at the rear of the FFC head. Additionally it is unlikely that diffusion of O_2 through the organic coating would be able to sustain the FFC corrosion cell because this would cause the differential aeration cell to break down. To elucidate the active corrosion mechanism taking place, it is important to determine the reason why filament tails do not contain O_2 . It is possible that the corresponding O_2 reduction reaction takes place at a stationary location remote from the filament head such as at the exposed steel where the FFC originates. For this to occur, an electrochemical connection between the cathode and anode would be essential. The most plausible explanation for this would be to suggest that the filament tail contains electrolyte and is not dry.

If active filament tails contain electrolyte, then it is expected that they will contain a significant amount of Cl^- ions originating primarily from the experimental electrolyte within the artificial defect. The Cl^- ions will naturally migrate towards the anodic region of the corrosion cell through the filament tail. To deduce whether the active filament tails contained electrolyte, SIMS Cl^- mass imaging of the FFC in-situ corrosion product was undertaken. The organic coating was mechanically stripped (peeled) from the surface of the alloy coating to reveal undisturbed corrosion product lying within the filament tail tracks.

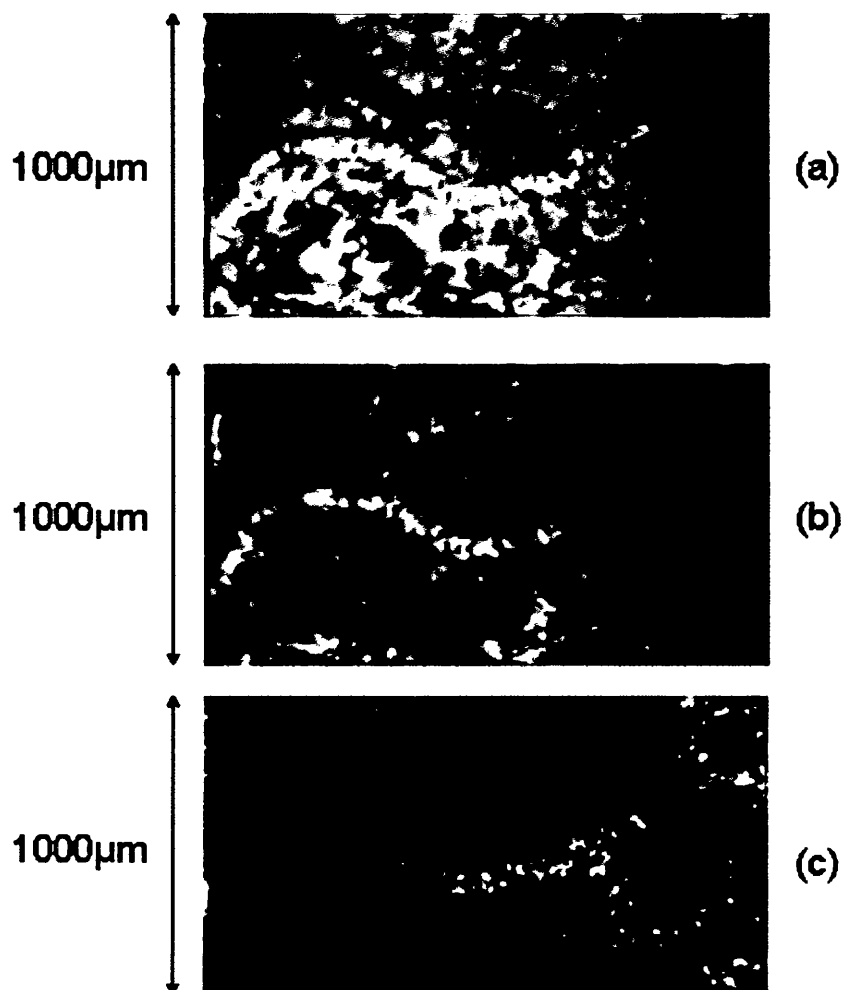


Figure 6.18. SIMS derived mass images of an FFC filament with in-situ corrosion product, (a) SED image, (b) Cl⁻ image and (c) Na⁺ image.

The location of the filament tail within this sample was verified by obtaining a secondary electron discharge image (SED), which is shown within figure 6.18 (a) highlighting the position of the FFC filament as a light line roughly in the centre of the shown image. The location of Cl⁻ across the sample surface is shown in the Cl⁻ mass image of figure 6.18 (b). It is clear that a high concentration of Cl⁻ exists with the FFC corrosion product, although there are trace amounts located generically over the sample surface. This provides evidence to support the theory that the active filament tails do contain electrolyte. The Na⁺ SIMS derived mass image of figure 6.18 (c) also supports the notion that the corrosion tails are electrolyte filled, possibly allowing remote contact to a stationary steel cathode site.

This test was repeated to ensure experimental accuracy using an identical but totally separate sample, and the results have been magnified and shown in figure 6.19. In this figure, (a) shows an optical image and (b) shows the corresponding Cl^- mass image. This strengthens the argument that there is a possible electrochemical connection between a stationary steel cathode and a remote dynamic anode.

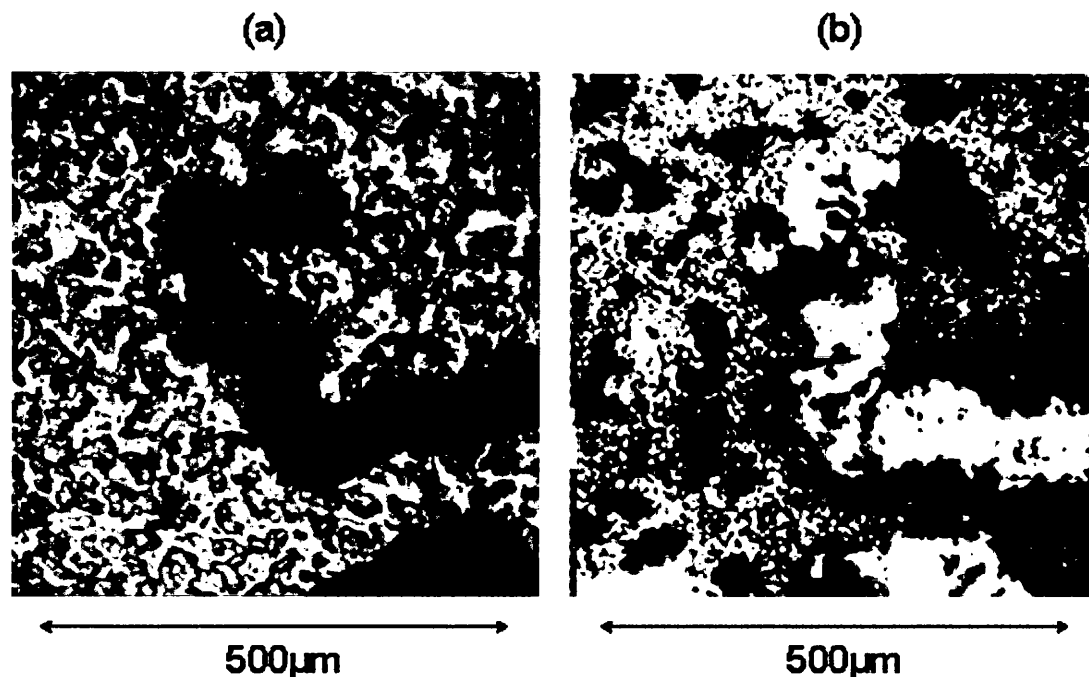


Figure 6.19. (a) Optical image and (b) SIMS derived mass image of an FFC filament with in-situ corrosion product after stripping of the organic layer.

6.3.9 Proposition of the Active FFC Mechanism

The knowledge that FFC is unreported to occur at the metal – organic coating interface of conventional zinc or zinc-aluminium alloys lead to the possible theory outlined schematically within figure 6.13. Using under-film SKP potentiometry it was theorised that due to the potentiometric variations between intact regions of organic coating surface and the corroded tail regions, a magnesium depleted surface resulted. This indicated that the principal anodic activity involved magnesium dissolution to leave a magnesium depleted region that is better capable to support O_2 reduction.

The discovery that filament heads are capable of propagating through the tails of other filaments lead to the discovery that it is unlikely for the tails to contain O₂ as previously thought. This discovery lead to the assumption that filament tails do not act as an oxygen conduit to the rear of the filament head to sustain O₂ reduction at this location. It is unlikely that O₂ will be able to diffuse through the organic layer to reach the rear of the filament head, leading to the assumption that the FFC propagation discovered here does not follow a conventional FFC mechanism.

The observation that FFC primarily initiates at areas of exposed steel upon electrolyte contact suggested that these regions of exposed steel could sustain O₂ reduction in preference to the magnesium depleted region as thought initially. The depth of anodic metal dissolution was measured using calibrated atomic force microscopy to be ~1µm deep, i.e. 10% of the Magizinc alloy coating thickness, which is too shallow to dynamically expose the steel substrate as the corrosion propagates. The inability of the FFC attack to expose the underlying steel substrate was also confirmed using SIMS mass imaging.

A final proposition is made whereby it is suggested that the FFC occurring on organic coated Magizinc alloys is sustained via a stationary remote cathode acting directly on the steel substrate. Evidence supporting the theory that filament tails are filled with electrolyte comes from the discovery of Cl⁻ within the corrosion product. It is theorised that the ionic conductivity of the electrolyte links the dynamic anode at the filament head to the stationary steel cathode located in the artificial defect and allows the FFC to propagate within this particular system.

One more piece of evidence supporting the theory of a stationary remote steel cathode is the visual observation of parabolic propagation kinetics. Propagation of the FFC upon initiation was observed to be relatively fast in comparison to the rate of propagation after a number of weeks. This supports the notion of a stationary remote cathode, and suggests the rate determining step in FFC propagation is anion transportation from the site of initiation to the position of the filament head.

The conventional FFC mechanism as occurs on organically coated aluminium alloys involves only a small amount of electrolyte located directly within the filament head.

This electrolyte is drawn forwards via a process of osmosis upon precipitation of the corrosion products (metal oxide/hydroxides).

In the case of organic coated Magizinc, where it is thought the filament tails are electrolyte filled, there are two possibilities as to how electrolyte could remain within the tail. The first possibility applies only in the case of FFC that has initiated from artificial defects containing a reservoir of aqueous NaCl electrolyte. That is the sheer amount of electrolyte present within the system forces its way through the filament tail via capillary action, maintaining the electrochemical cell.

The second possibility applies under conditions of limited electrolyte availability, where it is proposed that metal dissolution occurs within the filament head, resulting in the creation of metal cations (zinc and aluminium). Metal cations then combine with OH^- to form metal oxide/hydroxides to precipitate out of solution to create a solid corrosion product within the filament tails as corrosion proceeds. Under these circumstances alone it would be expected that upon precipitation of the corrosion product, the osmotic process would occur as in conventional dry tail FFC to draw the electrolyte forwards. Within the organic coated Magizinc system being described here, it is suggested that this osmotic process does not occur to the full extent because of the Mg content of the Magizinc alloy.

In the FFC mechanism being described there will be in existence a decreasing pH gradient from the site of cathodic oxygen reduction at the exposed steel defect to the low pH (acidic) environment of the filament head. A study of the magnesium oxide/hydroxide solubility has shown that under alkaline conditions the Mg^{2+} is able to exist in solution, i.e. the corrosion product due to magnesium dissolution is soluble [15]. Therefore cation migration from the filament head into the tail region towards more alkaline conditions could allow Mg^{2+} to remain in solution within the tail. This could possibly have the ability to significantly reduce the osmotic process upon precipitation of the zinc and aluminium oxide/hydroxides. This may allow electrolyte to remain within the filament tail, maintaining electrochemical contact to the remote stationary cathode. This process is illustrated within the schematic diagram shown in figure 6.20.

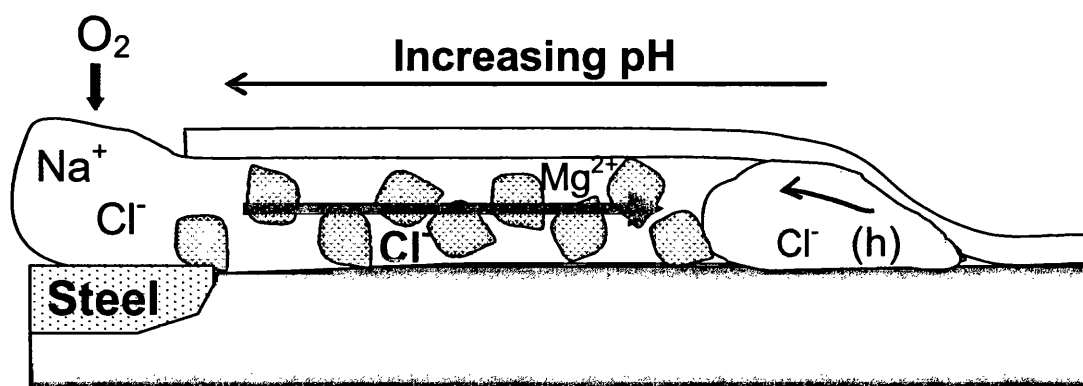


Figure 6.20. Schematic diagram illustrating the proposed mechanism of FFC on organic coated Magizinc alloys from an exposed steel defect.

6.3.10 Exploring the Factors of FFC Initiation

The primary form of corrosion driven disbondment of organic coatings adherent to the Magizinc alloy has been identified as being FFC and the active corrosion mechanism has been elucidated. Attempts to discover the required factors of FFC initiation began before the importance of the exposed steel cathode was realised. The observation that FFC occurred most fruitfully from the bulk aqueous NaCl electrolyte filled artificial defect indicated a possibility that the presence of Cl^- may be the cause.

To explore the importance of Cl^- for the initiation of FFC at areas of no exposed steel, standard filiform corrosion test samples were created following the method described in section 2.3.4. Organic coating defects 10mm in length were introduced by scribing with a scalpel using minimum force. Into these defects $2\mu\text{l}$ of varying concentrations of aqueous HCl acid were introduced. Five different aqueous HCl acid concentrations were applied on five separate but identical Magizinc samples and left at conditions of ambient room temperature (20°C) and 96% RH. The test samples were left for 2 months and the results are shown in the optical photographs of figure 6.21.

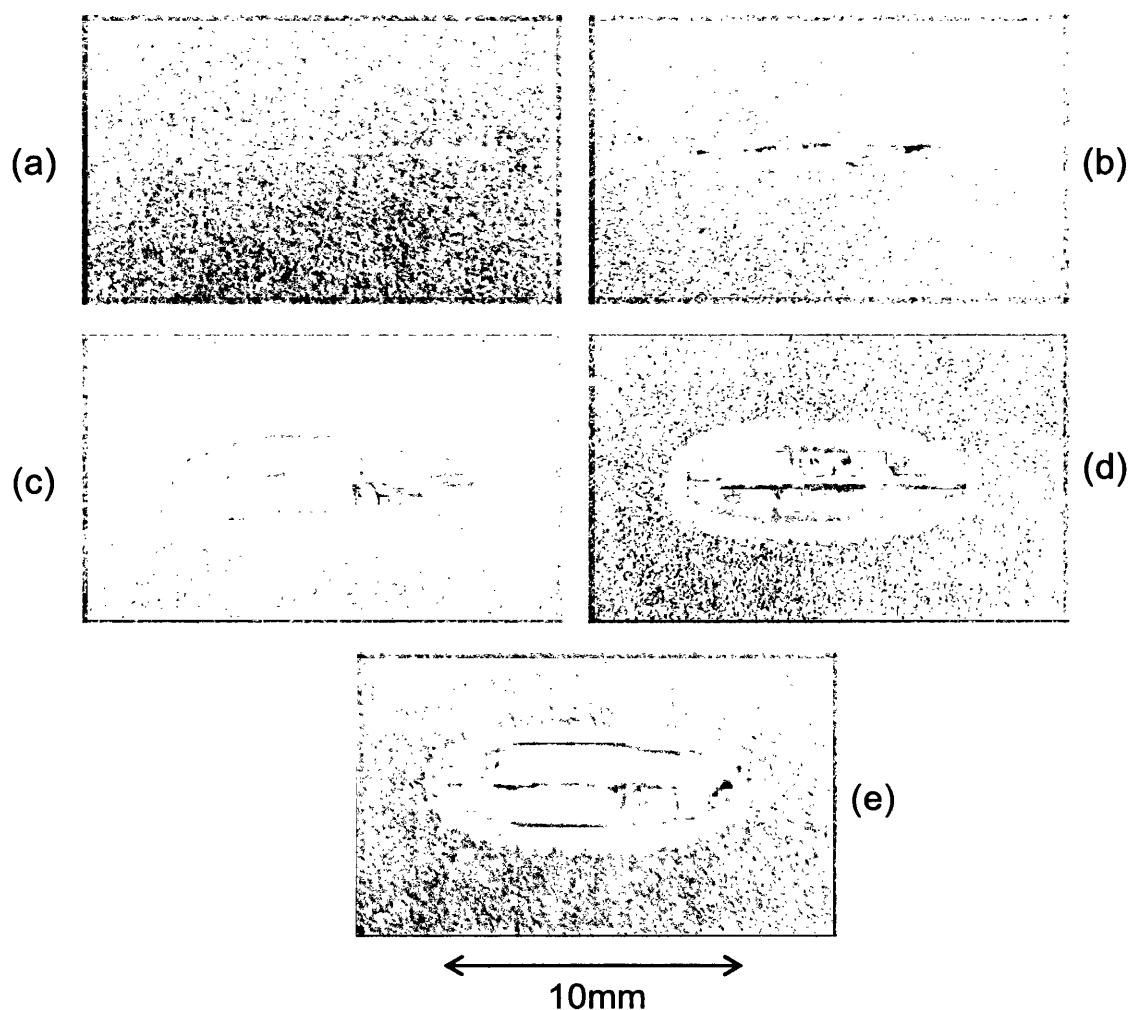


Figure 6.21. Inoculation of organic coating defects with aqueous HCl acid on PVB-coated Magzinc alloy test samples after 2 months. Key; (a) 0.1M HCl, (b) 1M HCl, (c) 2M HCl, (d) 3M HCl and (e) 4M HCl.

As apparent from figure 6.21, only minor coating failure non-representative of FFC is observed. The weaker aqueous HCl acid solutions below 2M concentration have had almost no detrimental effect to the integrity of the organic layer in any way. Accordingly it was acknowledged that aqueous HCl acid was ineffective at initiating FFC.

The same experimental procedure was then applied using aqueous NaCl, where 2 μ l of varying concentrations were applied to 10mm organic coating scribe defects. Concentrations ranging from 1M to 4M were explored and the results of 2 months exposure to corrosion conditions is shown in figure 6.22. It is clear that aqueous

NaCl is not capable of initiating FFC on its own, although slight corrosive attack is apparent but not representative of the FFC observed previously.

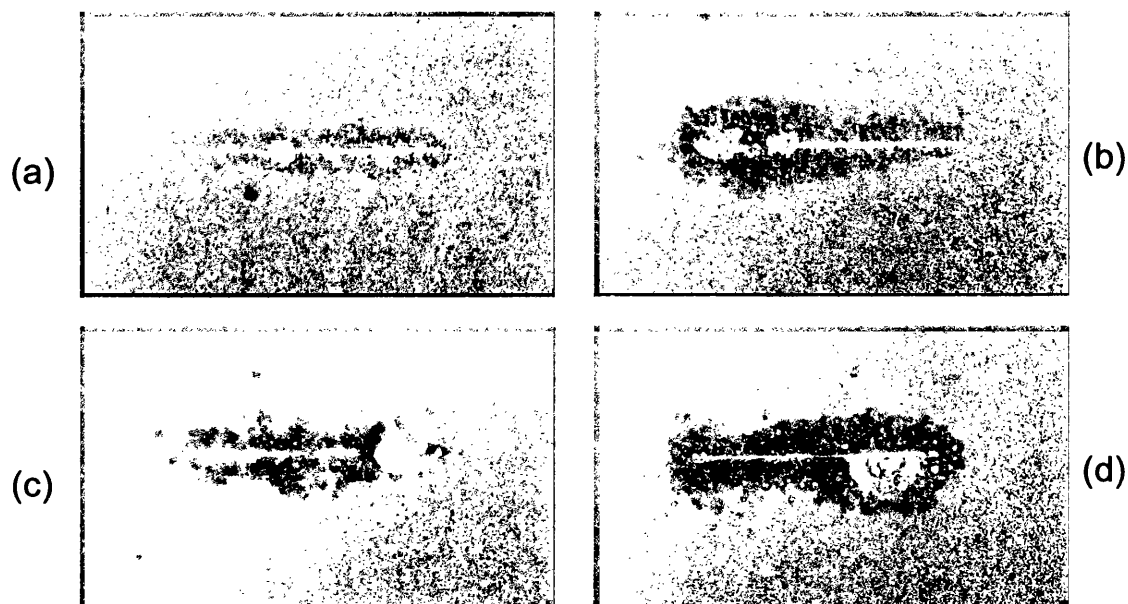


Figure 6.22. Artificial organic coating defects on Magizinc containing aqueous NaCl after 56 days of corrosion key; (a) 1M, (b) 2M, (c) 3M and (d) 4M concentrations.

Following the failure to initiate FFC aqueous HCl acid or aqueous NaCl, note was taken of the fact the FFC primarily originates from areas of exposed steel. It was hypothesised that an important factor in the FFC of the organic coated alloy could be ferrous chloride (FeCl_2). This would exist naturally within the corrosion cell as part of the iron dissolution reaction and is denoted by the brown colour within the Stratmann-type artificial defects (figure 6.7). To explore the importance of FeCl_2 to initiate FFC, further scribed test samples were created and the same experimental procedure used as before. Aliquots of FeCl_2 were added to the artificial organic coating defects and samples were once again stored under 96% relative humidity. Figure 6.23 shows the effect of FeCl_2 on the initiation of the FFC, and no visual signs of FFC is apparent 2 months after initiation.

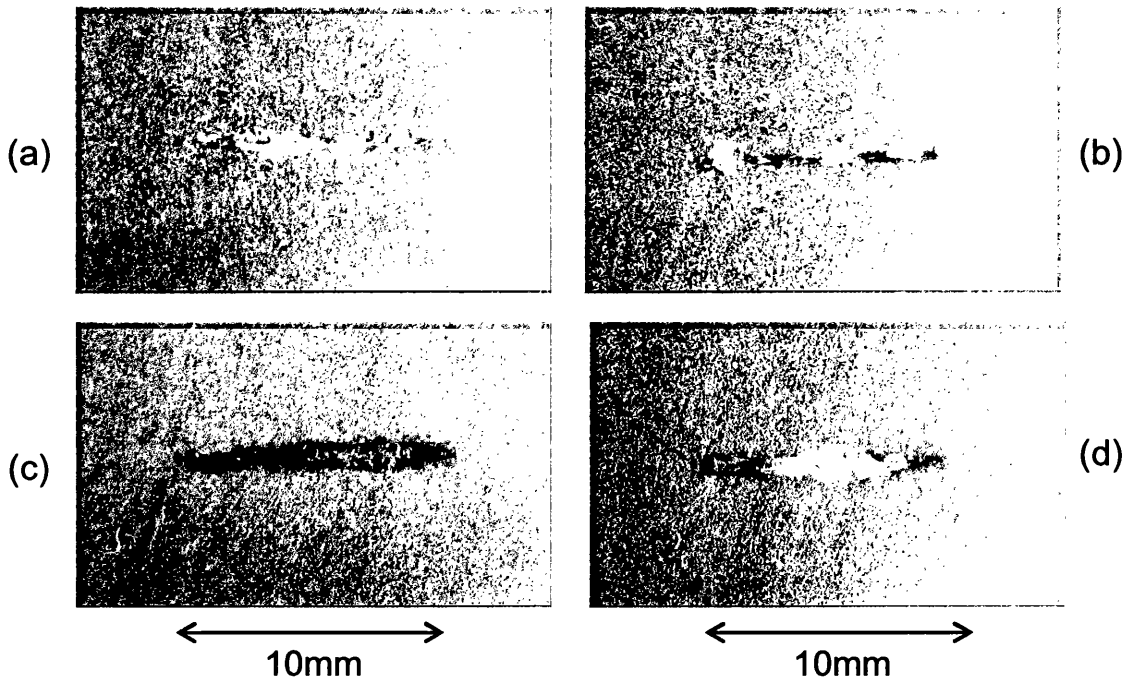


Figure 6.23. Artificial organic coating defects on Magizinc containing aqueous FeCl_2 after 2 months corrosion key; (a) 0.5M, (b) 1M, (c) 1.5M and (d) 2M concentrations.

The inability to re-create FFC on organic coated Magizinc alloy using separate additions of NaCl or FeCl_2 led to the idea of inoculating organic coating defect scribes with a mixed aqueous NaCl - FeCl_2 electrolyte. This was deemed logical considering that at regions of cut edges and exposed steel both NaCl and FeCl_2 will exist in unison. $2\mu\text{l}$ of mixed solutions were added to penetrative organic coating defects, and numerous variations of defect electrolyte mixtures were tested, formulated as a 50:50 mix of the individual solutions.

The findings of mixing aqueous NaCl with FeCl_2 are shown in the optical photographs of figure 6.24, and this is shown to be unsuccessful at reproducing FFC after 2 months of exposure. Due to the lack of success initiating FFC using chloride containing solutions, it was realised that a different approach may be required to successfully determine the critical initiation factors within this particular system.

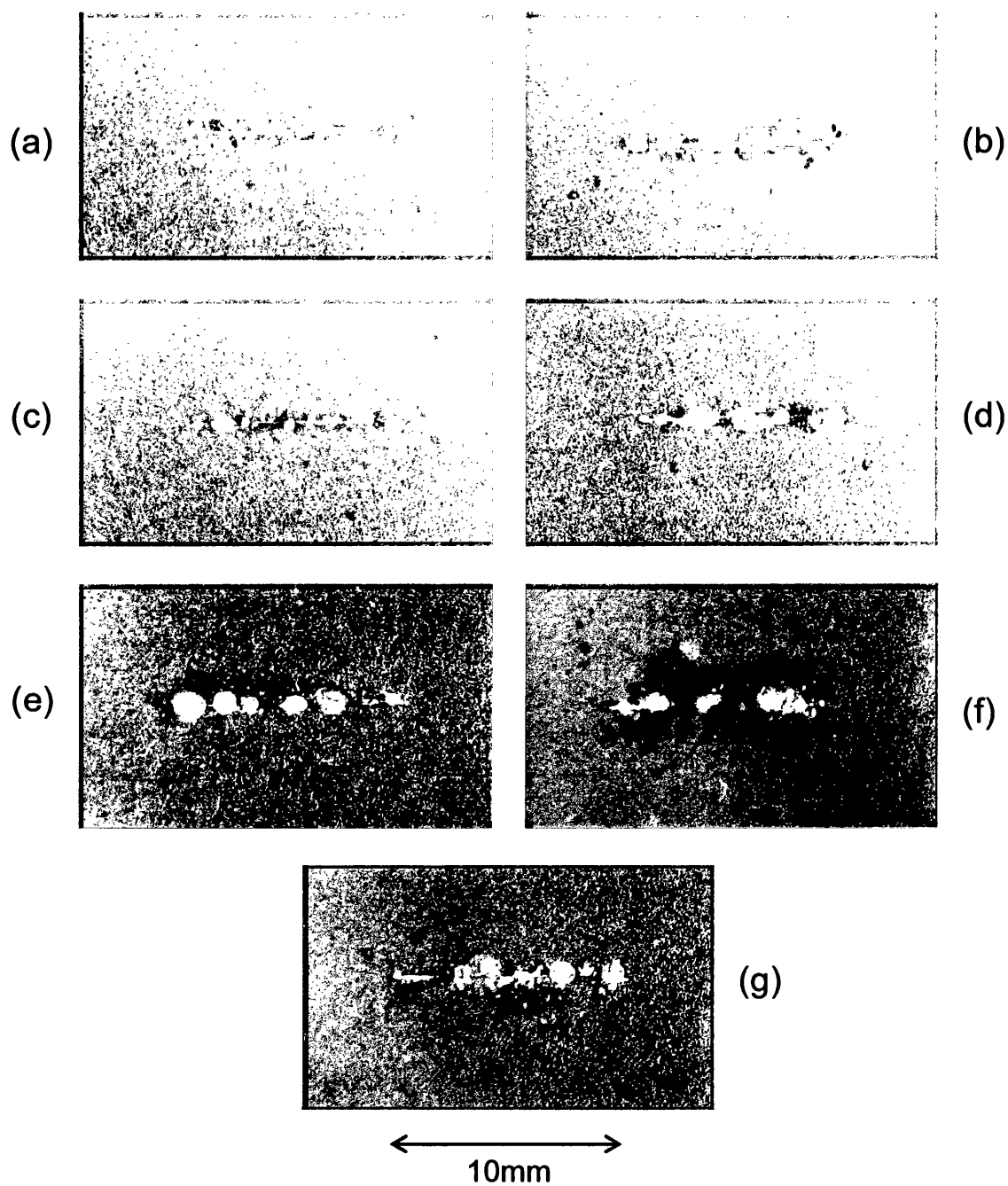


Figure 6.24. Artificial organic coating defects on Magizinc containing mixed solutions of aqueous NaCl and FeCl₂ after 2 months of corrosion key; (a) 1M NaCl & 0.5M FeCl₂, (b) 1M NaCl & 1M FeCl₂, (c) 1M NaCl & 1.5M FeCl₂, (d) 1M NaCl & 2M FeCl₂, (e) 1M FeCl₂ & 2M NaCl, (f) 1M FeCl₂ & 3M NaCl and (g) 1M FeCl₂ & 4M NaCl.

6.3.11 Acetate Release from the Organic Layer

In the original experimental test samples described schematically in figure 6.6, there is a possibility that acetate may be present at the PVB – Magizinc alloy interface. If this hypothesis is correct, acetate will be released through the environmental degradation of the Poly (vinyl butyral-co-vinyl alcohol-co-vinyl acetate) (PVB) organic layer. The proposed mechanisms of PVB degradation leading to the release acetic acid and acetate to the organic coating-substrate interface are outlined in figure 6.25.

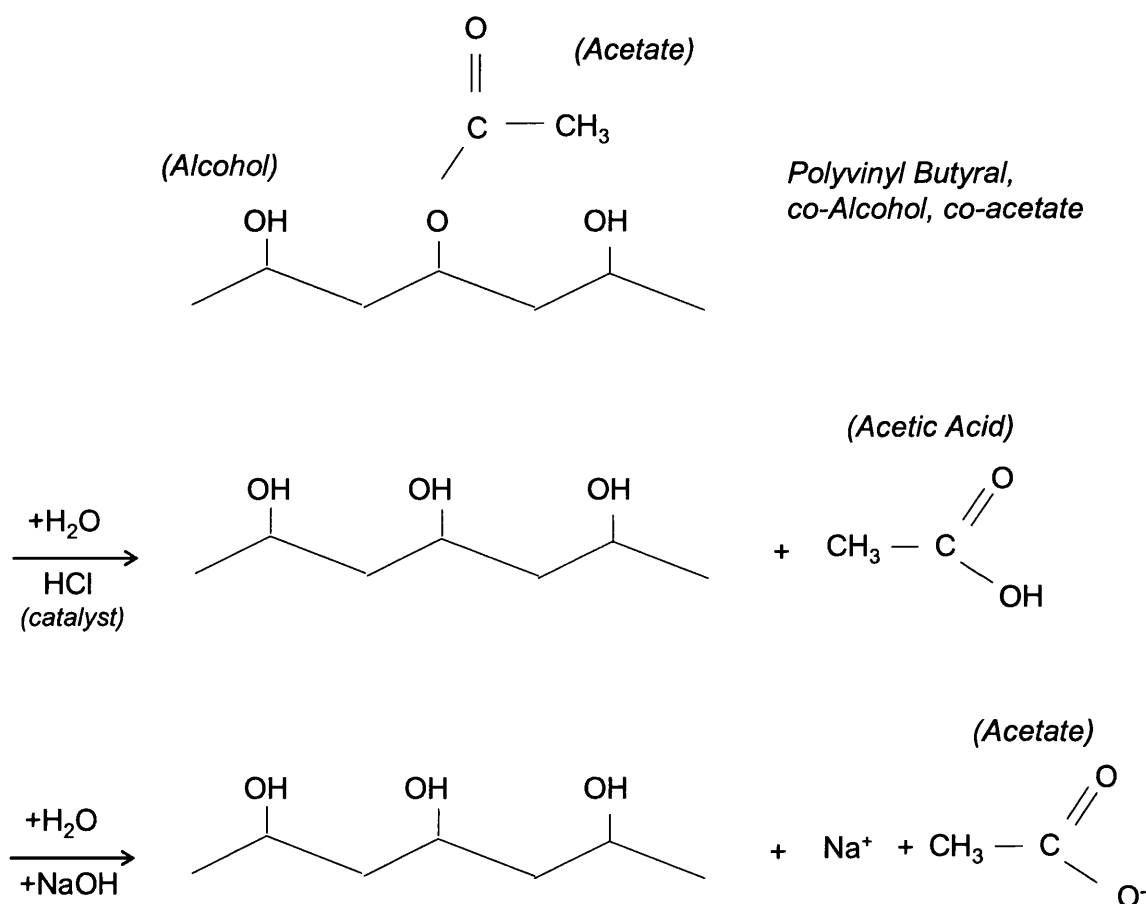


Figure 6.25. Proposed mechanism of acetate release from polyvinyl butyral co-alcohol, co-acetate.

In order to investigate the proposition that the acetic group is a critical factor in the initiation of FFC attack an organic (PVB) coated galvanised sample was created following the method outlined in section 2.3.4. This sample contained two 10mm

scribes and is shown in the optical photograph of figure 6.26 (a). The top scribe penetrates both the organic layer and the alloy coating to reveal the underlying steel substrate. The lower scribe is very light and only penetrates the organic layer to expose the galvanised layer. Each of the two defects were identically inoculated with 2µl of aqueous 10% acetic acid prior to being stored under 96% RH. This test was repeated five times for reproducibility, and identical results were obtained.

The results shown in the time-dependant optical photographs indicate that acetic acid is capable of initiating FFC in a short period of time after inoculation (14 days). It is clear from these results that FFC is able to propagate from both defects. The defect penetrating to the underlying steel shows the strongest filament growth, where filaments shape and direction of travel remains constant one month after inoculation.

The finding that FFC is able to propagate from the artificial defect where exposed steel is not present complicates the mechanism of FFC previously proposed. Figure 6.9 showing FFC occurring from Stratmann type artificial defects has a corrosion filament that does not appear to have originated from a region of exposed steel, which is consistent with the findings highlighted with figure 6.26 and may simply originate from trace amounts of steel.

Generally this FFC attack shown in figure 6.26 from both the upper and lower defects resemble the corrosion seen to occur from large artificial defects on the Magizinc substrates as originally tested. It is therefore believed that acetate release from the organic layer is a key initiation factor of the FFC.

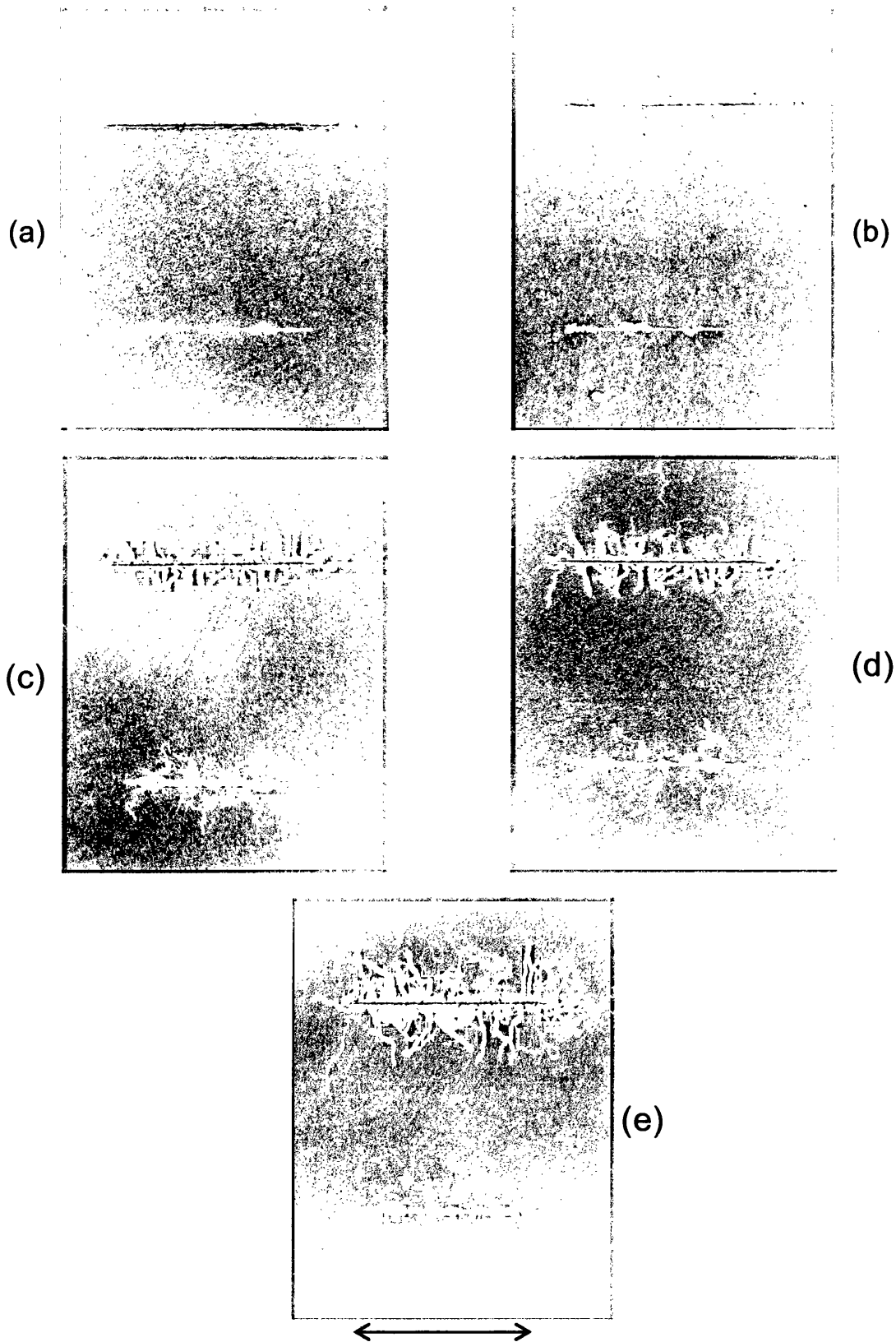


Figure 6.26. Artificial organic coating defects on Magzinc containing $2\mu\text{l}$ of aqueous 10% acetic acid key: (a) upon initiation, (b) 340hrs, (c) 720hrs, (d) 960hrs and (e) 1700hrs. Where the top defect is scribed through to steel and lower scribe only penetrates to Magzinc.

6.4 Conclusions

The ability of filament heads to cross the tails of other filaments indicate that this form of FFC does not follow the conventional FFC mechanism described within section 6.3.4. The detection of Cl^- within the filament tail corrosion product suggests that active FFC tails contain electrolyte, providing evidence that the FFC observed within this chapter follow an unconventional mechanism. Under these circumstances it is unlikely that the cathodic O_2 reduction reaction takes place at the rear of the filament head. Consequently the notion of a remote steel cathode is suggested, linked to the anodic site at the forefront of the filament head via ionic conductivity through the tail. To support this proposition, the high solubility of Mg^{2+} under the alkaline condition within the tail allows moisture to remain there; under these conditions there will be a much lower osmotic pressure pulling moisture solely into the filament head.

The ability of aqueous acetic acid to initiate FFC at organic coating defects without a defined region of exposed steel could be seen to provide evidence to support a more conventional FFC mechanism. In particular the theory that dynamic cathodic O_2 reduction takes place on the Mg depleted surface directly behind the filament head. This is unlikely, close inspection of the corrosion filament that initiated without an artificial defect within figure 6.9 shows the filament head has been able to cross its own tail. This indicates the tail is free from O_2 and supports the notion of a remote cathode, possibly located on steel washed into the alloy surface to support the cathodic reaction.

The increased strength of filament growth originating from the acetic acid inoculated at the site of exposed steel in figure 6.26 when initiated with aqueous acetic acid suggests that the availability of exposed steel is a significant factor. The relatively small size of the filaments originating from the non-steel defect could be explained as being proportional to the size of the available cathode. Figure 6.14 shows the presence of trace Fe^+ on the metallic surface, and it is a possibility that this could support a cathodic reaction. In summary, it is proposed that the FFC under organic coatings adherent to of hot dip Mg 1.5/Al 1.5/Zn (Magizinc) alloy coatings will

initiate and propagate most readily in the presence of acetate at regions of steel exposure.

6.5 References

- [1] M. Morishita, K. Koyama, M. Murase, and Y. Mori, *ISIJ International* **36**:714 (1996).
- [2] R. Hausbrand, M. Stratmann, and M. Rohwerder, *Steel research international* **74** (7):453 (2003).
- [3] B. Schuhmacher and D. Wolfhard, in *Galvatech 2001*, Verlag Stahleisen, 2001, p. 3.
- [4] M. Zuijderwijk and M. Vlot, *Corusgroup*, 2006, p. 1
- [5] M. Rohwerder, R. Hausbrand, and M. Stratmann, in *Gavatech 2004*, 2004, p. 971
- [6] Henderson and Hughes, *sov. phys JETP Letter* **22**:36 (1975).
- [7] F. DiQuarto, M. C. Romano, and M. Santamaria, *Russian Journal of Electrochemistry* **36**:1358 (2000).
- [8] Gmelins, *Gmelins Handbuch der anorganischen Chemie*, Weinheim/Bergstrasse, 1952.
- [9] W. Furbeth and M. Stratmann, *Corrosion Science* **43**:207 (2001).
- [10] W. Furbeth and M. Stratmann, *Progress in Organic Coatings* **39**:23 (2000).
- [11] T. Maalman, *Corusgroup*, 2006, p. 1
- [12] R. M. Souto and D. J. Scantlebury, *Progress in Organic Coatings* **53**:63 (2005).
- [13] P. Tipler and R. Llewellyn, *Modern Physics*, W. H. Freeman, 1999.
- [14] C. Sharman, *Nature*:621 (1944).
- [15] G. Williams and H. N. McMurray, *Electrochemical and Solid State Letters* **8**:B42 (2005).

Chapter 7

Photovoltaic Applications of Polyaniline

7.1 Introduction

Polyaniline emeraldine salt (PAni-ES) has already been proven to be an active material with the ability to considerably inhibit cathodic disbondment of organic layers adherent to both iron or zinc substrates. The purpose of this chapter is to expand upon the usefulness of PAni and to investigate the possibility of adapting its properties to create pre-painted steel systems of higher commercial value. A particular application of PAni that could in future be incorporated into pre-painted steel coating systems is its ability to act as an organic photovoltaic material.

Micro-films of PAni have reportedly been successfully incorporated as an active layer within a Schottky solar cell by Chung et al. The sulfonic acid doped PAni-ES micro-film layer was sandwiched between thin layers of ITO and Al [1]. A similar study into Schottky diodes utilising polyanilines was made by Narasimhan et al [2]. Other studies investigating the use of polyaniline for photovoltaic applications has concentrated upon including them as part of dye sensitised solar cell systems. In these dye sensitised solar cell systems the polymer has been utilised as the hole transporting layer within cells containing TiO_2 [3, 4].

A study of the rectifying effect of a heterojunction between porous silicon and a water soluble copolymer of PAni is also published [5]. This reports the creation of diode characteristics by creating a heterojunction between n-type amorphous silicon and polyaniline. This indicates that PAni - n-type silicon junctions may have the ability to act as organic-inorganic (hybrid) bilayer heterojunction photovoltaic cells.

PAni-ES of different dopants including sulfonates and phosphonates are applied as micro-layers to n-type single crystal silicon wafers. Variations in cell performance are measured according to PAni-ES dopant choice and photo-induced degradation. Photocells incorporating the more conventional conducting polymer polystyrenesulfonate-doped polyethylene dioxythiophene (PEDOT:PSS) are also examined as a comparison to the performance of PAni-ES.

7.2 Experimental Details

Single organic layer hybrid bilayer photovoltaic cells were created following the method outlined in section 2.12, creating cells as shown photographically in figure 7.1. Single organic layer photocells fabricated with micro-layers of PANi-ES protonated with camphorsulfonate (PANi-CSA), phenylphosphonate (PANi-PP), paratoluenesulfonate (PANi-pTS) or dodecylbenzenesulfonate (PANi-DBSA) were solution cast onto the Si substrates from M-Cresol following the method described in section 2.2.4.2. Similarly, single organic layer photocells were also fabricated using polyaniline emeraldine base (PANi-EB) and polystyrenesulfonate doped polyethylenedioxythiophene (PEDOT:PSS) micro-films as the organic layer.

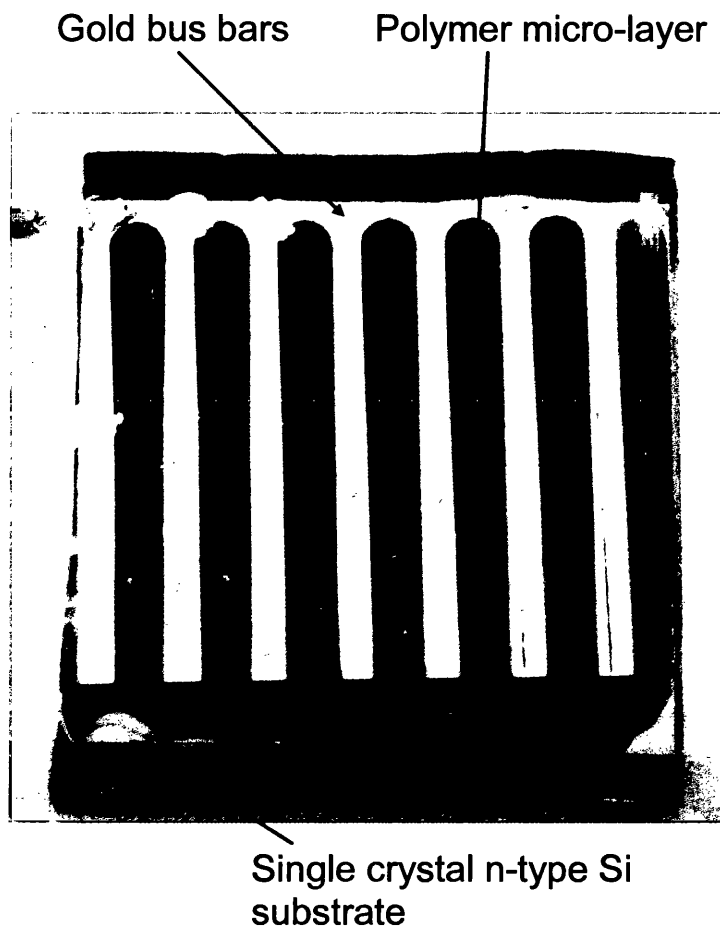


Figure 7.1 Active surface (face) of a hybrid polyaniline-single crystal n-type photovoltaic cell.

Completed hybrid photovoltaic solar cells follow the structure depicted schematically within figure 7.2, representative of cells containing a single organic layer. More complex double organic bilayer hybrid heterojunction photovoltaic cells fabricated within this work are shown schematically within figure 7.3. Double organic layer devices were fabricated by solution casting the surface polymer micro-layer over the lower after the solvent had evaporated from the lower micro-film to become dry.

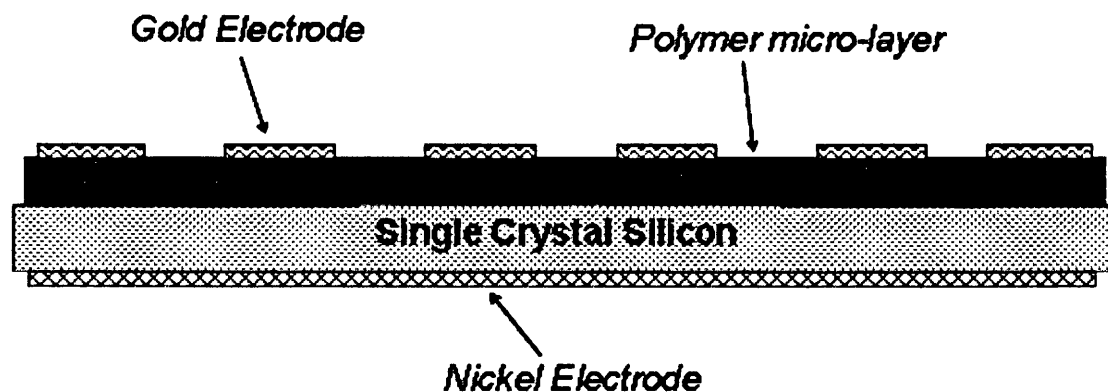


Figure 7.2. Schematic representation of the single organic layer hybrid photovoltaic devices fabricated for this work.

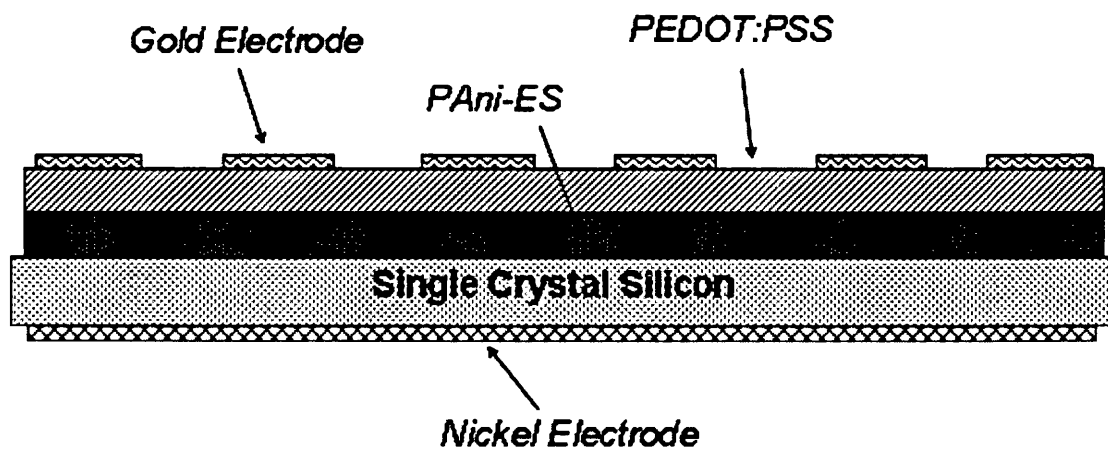


Figure 7.3. Schematic representation of the double organic layer hybrid heterojunction photovoltaic devices fabricated for this work, PAni-ES – PEDOT:PSS.

Light soaking of the photocells to investigate the effect of prolonged light exposure towards their performance took place within a calibrated Dyesol light soaker at one sun light intensity. Photovoltaic cells remained exposed to the calibrated light source constantly for a period of 21 days. After light soaking, cells characterisation was undertaken within the Dyesol solar simulator following the method outline previously.

7.3 Results and Discussion

7.3.1 Single Organic Layer Hybrid Photocells

A total of two identical single organic layer photocells (figure 7.2) containing a 1 μ m layer of PAni-EB were produced and characterised at one sun light intensity. The performances recorded of the non-conducting PAni-EB – Si bilayer photocells is shown in table 7.1. It can be seen that hybrid solar cells based upon this material selection do produce a slight photocurrent when exposed to a light intensity of one sun. The open circuit voltage (V_{oc}) of one PAni-EB 0.19V and indicative of diode characteristics, and the short circuit current (I_{sc}) is negligible at just over one tenth of a mA. This incapability to produce a significant photocurrent is consistent with the notion that PAni-EB is not capable of acting as a photovoltaic material. A possible reason why the PAni-EB is shown to be incapable of producing a photocurrent is that its non-conducting nature insulates the top electrical contacts from the Si semiconductor.

In contrast to the photocells utilising PAni-EB, single organic layer hybrid photovoltaic cells containing conductive PAni-ES have been fabricated, once again following the cell design of figure 7.2. Due to literature reports of functional PAni-ES – amorphous Si photocells [5], it was expected that successful photocell production using single crystal Si could be achieved. Here the dopant dependency of the PAni-ES is explored in terms of photocell performance. Cells were fabricated using PAni-ES doped with camphorsulfonate (PAni-CSA), paratoluenesulfonate (PAni-pTS), dodecylbenzenesulfonate (PAni-DBSA) and phenylphosphonate (PAni-PP).

The I-V curve of PAni-pTS recorded at one sun light intensity is shown within figure 7.5 (b) and the full cell performance is listed in table 7.1 along with the performance of the other PAni-ES. Close inspection of table 7.1 shows that apart from a few exceptions PAni-ES photocells produce a photocurrent and have strong open circuit voltages (V_{oc}). The ability to create a strong V_{oc} and a photocurrent in this manner

when adherent to n-type Si suggests that PAni-ES may be considered comparable to a p-type semi-conductor.

In addition to the PAni cells described previously, Polystyrenesulfonate doped polyethylenedioxythiophene (PEDOT:PSS) was used as the organic layer on two separate cells. The characterisation of these cells are listed in table 7.1 and a representative I-V curve is shown in figure 7.3 (b). PEDOT:PSS is widely known to act as a p-type organic semi-conductor and is incorporated into this study as a benchmark material to compare the PAni-ES. For this reason the organic layer thickness and cell design used for the fabrication of the PEDOT:PSS photocells is consistent with the PAni-ES cell design. The I-V characteristics of this PEDOT:PSS cell shows it to exhibit a respectably large V_{oc} of 0.33V and an I_{sc} of 15mA, indicating a comparable, if not slightly better performance than the PAni-ES photocells.

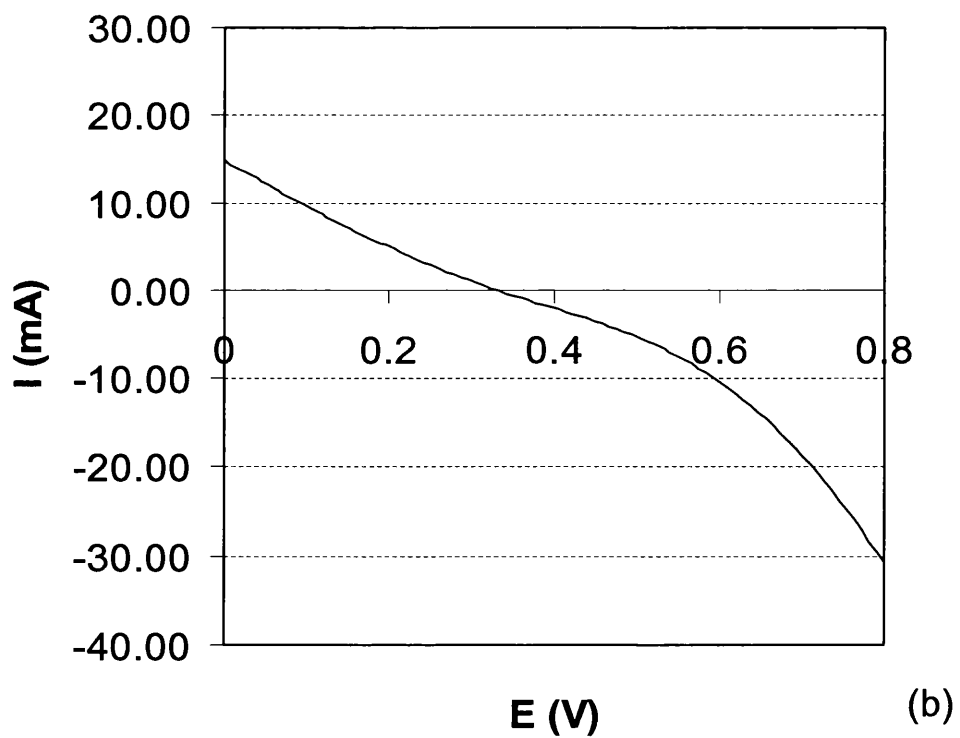
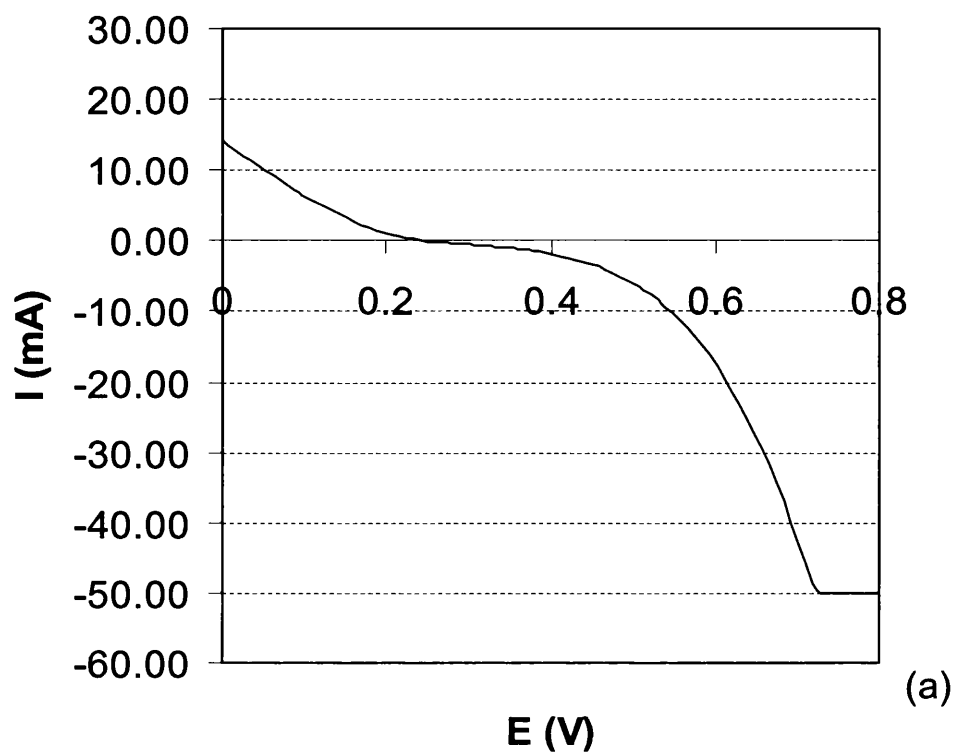


Figure 7.5. Example I-V curves recorded using the Dyesol solar simulator at one sun light intensity for (a) PANi-pTS and (b) PEDOT:PSS micro-films adherent to Si.

The linear shape of both I-V curves shown in figure 7.5 between 0 and $\sim 0.30\text{V}$ is representative of all the other organic layers investigated here irrespective of the organic component. This is indicative of a low fill factor (FF), which is confirmed by the values calculated for each photocell and presented in table 7.1. The fact that photovoltaic devices consisting of PANi-EB, PANi-ES and PEDOT:PSS all show I-V curves of a non-ideal nature (low FF) indicate a shortfall within either the cell design or the compatibility of the materials being investigated.

Figure 7.6 illustrates schematically the difference between the linear I-V curves obtained for each photocell, and a near ideal I-V curve ($\text{FF} > 0.9$). The maximum possible fill factor for a photovoltaic cell under illumination is 1, and the shape of the I-V curve required for this is a rectangle with no curvature at all. In reality ideal I-V curves are unobtainable, and an acceptable FF is considered to be 0.6 and above [6].

Two identical photocells of each organic polymer variation have been fabricated in order to explore the cell reproducibility and the cell characteristics of each. Cell characterisation includes cell efficiency ($\eta\%$), FF, maximum power output (P_{mp}), open circuit voltage (V_{oc}) and short circuit current (I_{sc}) are shown within table 7.1 for comparison. Before the reproducibility of the solar cells is discussed it should be noted that the FF values obtained for all cells lie in the region of ~ 0.25 , with the maximum obtained being ~ 0.35 recorded for one of the PANi-PP cells, i.e. they are all well below that considered to be acceptable.

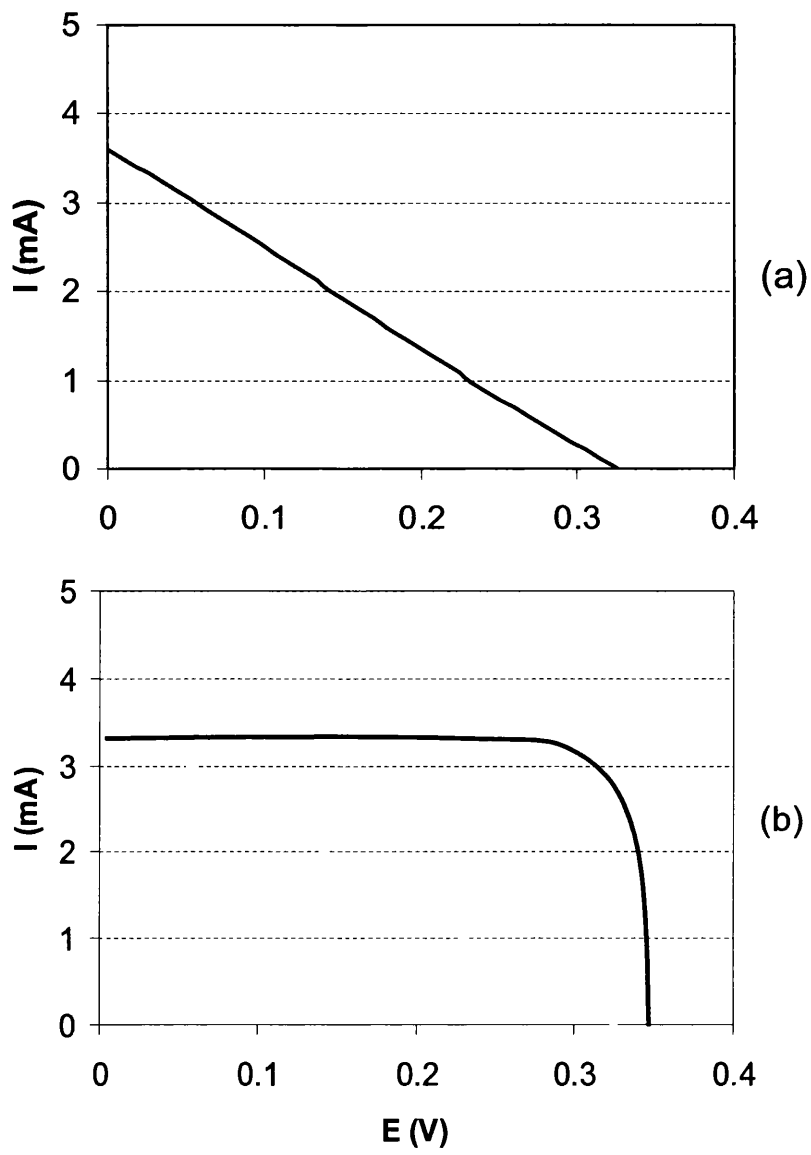


Figure 7.6. Schematic diagram highlighting the difference in I-V curve shape of (a) single organic layer hybrid photovoltaic cells tested here and (b) theoretically ideal photovoltaic I-V curve.

	η (%)	FF	P_{mn} (mW)	V_{oc} (V)	I_{sc} (mA)
PAni-EB (cell 1)	0.001	0.19	0.004	0.19	0.11
PAni-EB (cell 2)	0.000	0.23	0.001	0.04	0.07

	η (%)	FF	P_{mp} (mW)	V_{oc} (V)	I_{sc} (mA)
PAni-pTS (cell 1)	0.24	0.18	0.64	0.25	14.13
PAni-pTS (cell 2)	0.13	0.30	0.36	0.30	4.04

	η (%)	FF	P_{mp} (mW)	V_{oc} (V)	I_{sc} (mA)
PAni-CSA (cell 1)	0.19	0.33	0.51	0.29	5.39
PAni-CSA (cell 2)	0.002	0.30	0.005	0.01	2.11

	η (%)	FF	P_{mp} (mW)	V_{oc} (V)	I_{sc} (mA)
PAni-DBSA (cell 1)	0.003	0.14	0.004	0.23	0.23
PAni-DBSA (cell 2)	0.07	0.24	0.20	0.28	2.99

	η (%)	FF	P_{mp} (mW)	V_{oc} (V)	I_{sc} (mA)
PAni-PP (cell 1)	0.06	0.35	0.16	0.28	1.59
PAni-PP (cell 2)	0.07	0.24	0.20	0.28	2.99

	η (%)	FF	P_{mp} (mW)	V_{oc} (V)	I_{sc} (mA)
PEDOT (cell 1)	0.40	0.22	1.08	0.33	14.85
PEDOT (cell 2)	0.12	0.27	0.32	0.29	4.13

Table 7.1. Efficiencies, fill factors, power outputs, open circuit voltage values and short circuit current values recorded for all single organic layer photocells tested.

Single organic layer photocell reproducibility between each two identical cells is shown in figure 7.7. This highlights the experimental deviation of measured characteristics in terms of η , V_{oc} and I_{sc} , and variation between cells is apparent. The PAni-EB photocells have not been included within figure 7.7 because it has already been confirmed not to act as a photovoltaic material in hybrid photocells of this configuration.

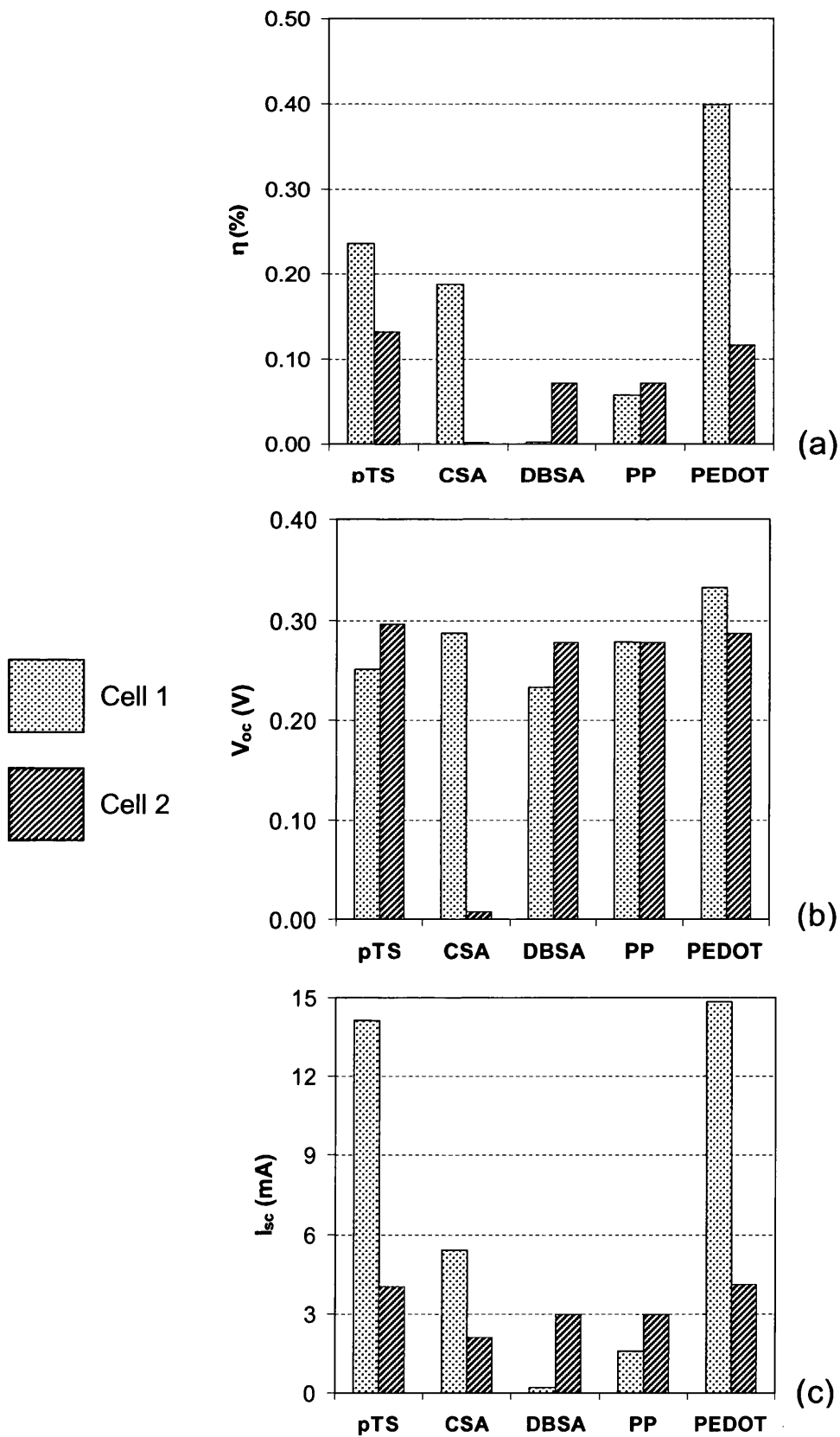


Figure 7.7. Influence of organic layer choice upon cell performance in terms of (a) efficiency, (b) V_{oc} and (c) I_{sc} . Two identical cells of each to explore reproducibility.

A key observation from the tabulated data shown in table 7.1 and graphically within figure 7.7 is that two photocells, namely PAni-CSA cell 2 and PAni-DBSA cell 1, show extremely poor energy conversion characteristics and do not fit with the results obtained from the photocells. Accordingly these two cells are not included in any subsequent analysis.

It is proposed that the reason for these two anomalous cells is the poor quality of the organic microfilm layers in each case. To highlight the poor film quality associated with these cells a number of SEM images were produced at varying magnifications of PAni-DBSA cell 1 and are shown in figure 7.8. As a comparison to this, SEM images were also taken of PAni-CSA cell 1 to provide an example of the film quality needed to produce more acceptable photovoltaic characteristics.

Close examination of the PAni-CSA surface (figure 7.8 (d), (e) and (f) at increasing magnifications from 128x magnification to 500x magnification and finally 2000x magnification shows a relatively uniform smooth surface. In contrast to this the surface of the poor PAni-DBSA photocell is noticeably rough and particulate in nature, even down to very high magnifications (2000x). This supports the argument that poor/anomalous photocell performance is primarily due to poor polymer film quality.

There are number of possible causes of poor quality microfilm layers, although it is difficult to pin-point the exact cause. One suggestion is that the particulate nature of the film could be caused by precipitation of PAni-ES in solution. Another possible cause could be that the casting temperature was too high.

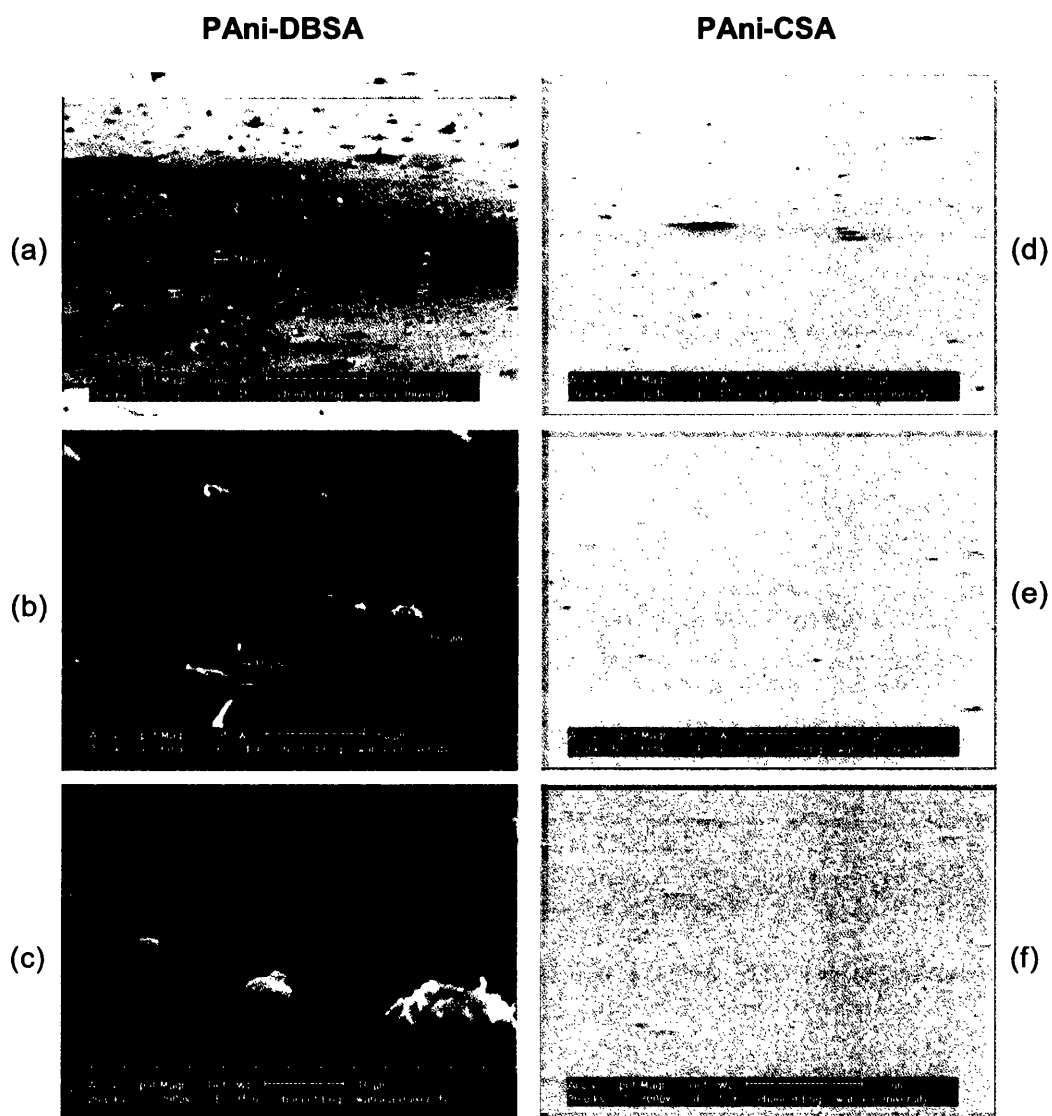


Figure 7.8. SEM images of PANi-DBSA (a) to (c), and PANi-CSA (d) to (f).

As highlighted graphically in figure 7.7 (a), there are marked differences between the efficiencies of the identical repeated cells. In the case of single organic layer cells consisting of PANi-pTS, PANi-CSA and PEDOT:PSS the first cell produced (cell 1) is considerably more efficient than the second cell produced. The only cells that show good reproducibility in terms of efficiency values and V_{oc} values utilise PANi-PP as the conducting layer.

Ignoring slight variations in performance, the single organic bilayer photovoltaic cells being investigated here can be summarised in general terms as exhibiting efficiency values of between 0.05% and 0.40%. This low performance can be

explained by the FF values being consistently low at ~ 0.25 , indicating that the shape of obtained I-V curves are reproducibly non-ideal and certainly less than the 0.6 FF generally considered acceptable.

The V_{oc} values obtained for all these single organic bilayer hybrid photovoltaic cells at one sun light intensity are shown in figure 7.7 (b). As a general overview of the cell performances in terms of V_{oc} , it is obvious that cell potentials the zero current output level are relatively uniform for each cell at ~ 0.28 with the exception of PEDOT:PSS, of which the first cell produced was capable of producing a photocurrent of $\sim 0.32V$. All identical cells do show very slight variations, although these variations are small and could be considered to lie within experimental error.

The I_{sc} performance recorded for each of the photocells at one sun light intensity show considerable variation between cells, highlighting the difficulties of cell reproducibility. This is highlighted most dramatically with the photocells using PANi-pTS and PEDOT:PSS as the organic layer. For each of these two systems the first cell produced in each case (cell 1) has an I_{sc} approaching 15mA, but upon production of the second cell, this I_{sc} value is reduced to $\sim 5mA$ in both cases even though fabrication methods were kept as consistent as possible and polymer layers solution cast from exactly the same solutions.

7.3.2 Cell Performance at Varying Light Intensity

The light source within the Dyesol solar simulator was re-calibrated to provide light intensities of 1/3 sun and 1/10 sun. This is achieved by passing the light through a fine mesh, which reduces the light intensity passing through it to reach the sample. Single organic layer photocells were tested under these conditions of lower light intensity.

The effects of varying the intensity of light incident on the cell surfaces in terms of cell efficiencies and FF values are summarised within the charts of figure 7.9 (a) and (b) respectively. To consider the effect towards cell efficiency, figure 7.9 (a) clearly shows that with the exception of the cell using PAni-PP as the organic layer, photocell efficiency increases considerably as a function of decreasing light intensity. The cell utilising the organic layer of PAni-DBSA already proven to be of a very poor standard has been included within the summary because the efficiency has also been increased as a result of decreasing the light intensity. The efficiency of the cells containing PAni-CSA, PAni-pTS and PEDOT:PSS have all more than doubled as a result of decreasing the light intensity to 1/10 sun. The cell containing PEDOT:PSS has reached an efficiency of well over 1% at 1/10 sun, compared to the value of just 0.4% at 1 sun.

The FF values calculated for each solar cell shown within figure 7.9 (b) indicate that along with increasing efficiency, the decrease in light intensity causes a slight improvement in FF. This improvement is not as drastic as the improvement seen towards efficiencies, although is still noteworthy, and is consistently the case for all cells shown. The PAni-PP FF value at 1/3 sun light intensity is anomalous in that it is nearly double the other recorded values for the same cell at ~0.70, which is considered a desirable quantity [6].

The tabulated values of V_{oc} shown within table 7.2 also indicate a trend with decreasing light intensity. Decreasing the light intensity actually causes very slight decreases in V_{oc} for all cells. The I_{sc} also becomes smaller with decreasing light intensity, which is expected because the cell input energies are considerably smaller.

The same principle applies in the case of maximum power outputs, which also decrease as expected with decreasing input energy/light intensity.

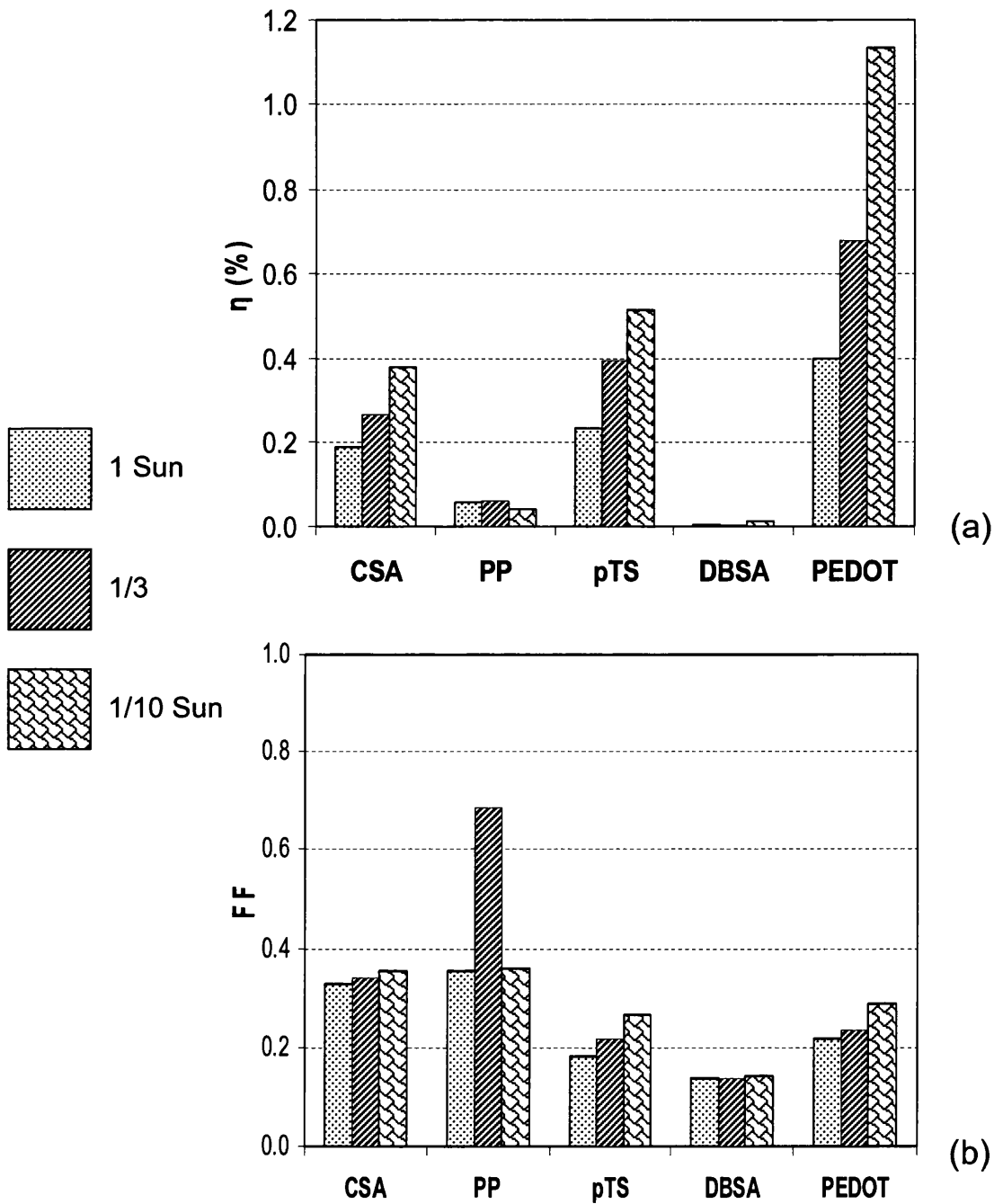


Figure 7.9. Illumination intensity effects towards (a) cell efficiency and (b) cell FF, recorded for single organic bilayer photovoltaic cells.

	η (%)	FF	P_{mp}	V_{oc} (V)	I_{sc}
PAni-pTS (1 Sun)	0.24	0.18	0.64	0.25	14.13
PAni-pTS (1/3 Sun)	0.40	0.22	0.36	0.25	6.59
PAni-pTS (1/10 Sun)	0.52	0.26	0.14	0.22	2.36

	η (%)	FF	P_{mp}	V_{oc} (V)	I_{sc}
PAni-CSA (1 Sun)	0.20	0.33	0.50	0.29	5.39
PAni-CSA (1/3 Sun)	0.27	0.34	0.24	0.30	2.41
PAni-CSA (1/10 Sun)	0.38	0.36	0.10	0.29	1

	η (%)	FF	P_{mp}	V_{oc} (V)	I_{sc}
PAni-DBSA (1 Sun)	0.003	0.14	0.01	0.23	0.23
PAni-DBSA (1/3)	0.004	0.14	0.004	0.22	0.15
PAni-DBSA (1/10)	0.01	0.14	0.003	0.21	0.10

	η (%)	FF	P_{mp}	V_{oc} (V)	I_{sc}
PAni-PP (1 Sun)	0.06	0.35	0.16	0.28	1.59
PAni-PP (1/3 Sun)	0.06	0.69	0.05	0.26	0.30
PAni-PP (1/10 Sun)	0.04	0.36	0.01	0.24	0.13

	η (%)	FF	P_{mp}	V_{oc} (V)	I_{sc}
PEDOT:PSS (1 Sun)	0.40	0.22	1.08	0.33	14.85
PEDOT:PSS (1/3)	0.68	0.23	0.61	0.31	8.57
PEDOT:PSS (1/10)	1.13	0.29	0.31	0.28	3.84

Table 7.2. Tabulated efficiency values, FF values, max cell output power, open circuit voltage and short circuit currents for all cells subject to light intensity studies.

7.3.3 PANi-ES Cell Performance after Light Soaking

To explore the longevity of the hybrid photocells of single organic layers, cells were subjected to a period of twenty one days light soaking at one sun light intensity in the Dyesol light soaking cabinet. The only cells subjected to light soaking in this manner were the first photocells made for each hybrid system (cell 1) with the exception of PANi-EB, which has already been shown not to be capable of generating a photocurrent.

The light source used to produce the 1 sun light intensity was found to produce a lot of heat. The temperature photocells were subjected to over the 21 days was measured to be constant at 46°C. The results of this study are shown in terms of efficiency ($\eta\%$) and FF within figures 7.11 (a) and (b), and V_{oc} and I_{sc} in figure 7.12 (a) and (b) respectively.

The major finding of this study is that this exposure has not caused a dramatic change in performance, although there are slight variations. The cell efficiencies appear to be slightly reduced, particularly in the case of the PEDOT:PSS cell. On the contrary to this observation, the PANi-pTS cell shows an increase in performance as a reaction to the prolonged light exposure, also confirmed by the increased FF associated with this photocell. The values of FF for the other PANi-ES photocells does actually worsen, although only slightly.

For each of the four PANi-ES photocells V_{oc} has increased as a result of the light soaking by ca. 0.03V for each, conversely to this, the V_{oc} of the PEDOT:PSS cell has decreased by a similar amount. The PANi-DBSA cell 1 has been included for comparison within these results because even though this photocell has shown poor photovoltaic characteristics, it is worth mentioning that the cell V_{oc} has increased to the same extent as the other PANi-ES cells. The I_{sc} of each photocell was altered by the light soaking, only instead of an increase, the I_{sc} was seen to be uniformly reduced by ca. 0.3mA for all PANi-ES cells, which is also the case for the PEDOT:PSS cell, that showed an opposite trend to PANi-ES in terms of V_{oc} .

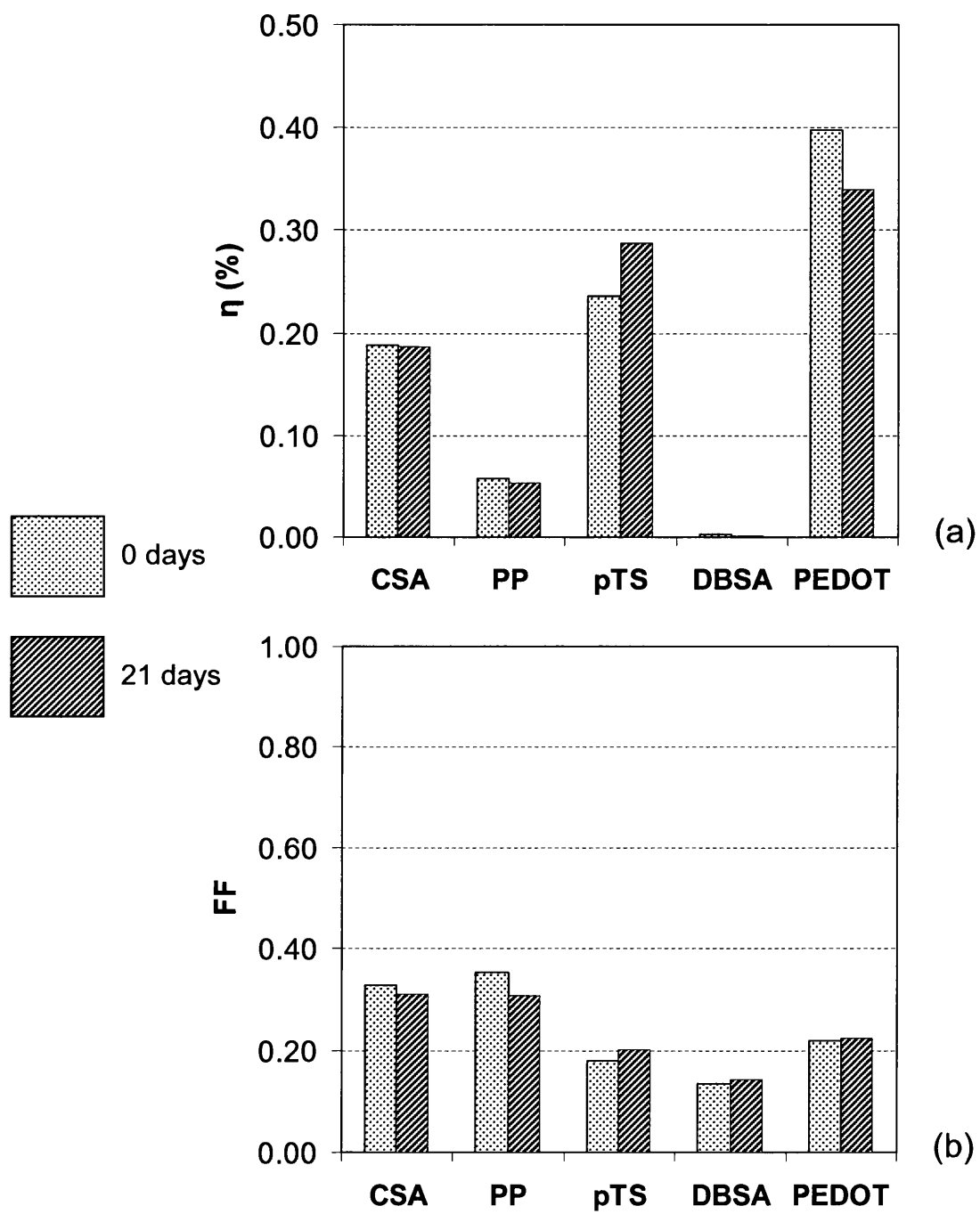


Figure 7.10 Effect of light soaking on PANi-ES solar cell performance key: (a) η % and (b) FF.

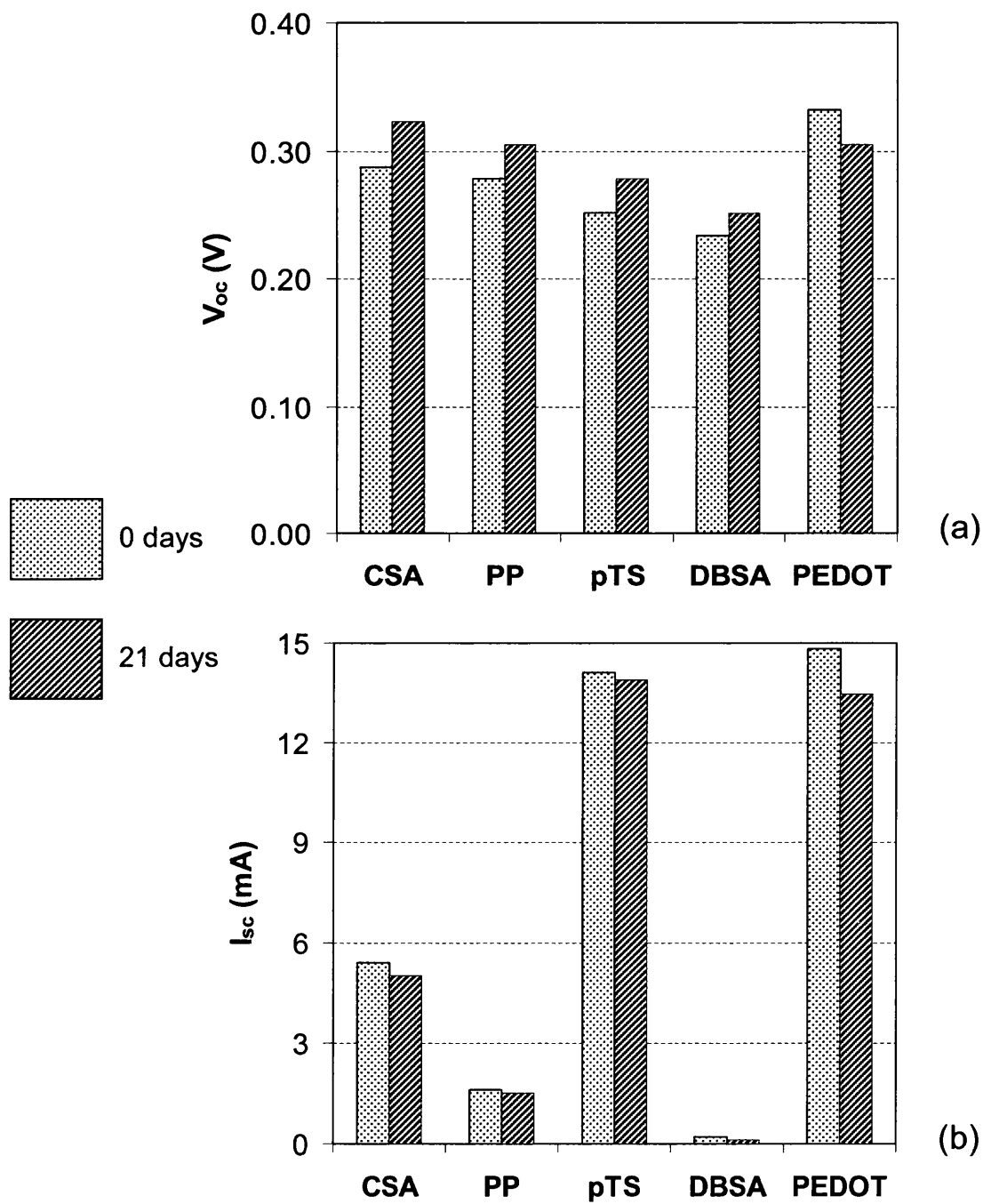


Figure 7.11 Effect of light soaking on PANI-ES solar cell performance key: (a) V_{oc} and (b) I_{sc} .

As a generalised summary of the effect of light soaking these single organic layer hybrid photocells, it is correct to state that these cells, or more correctly the organic component within these cells are relatively stable under high intensity light exposure. That is to say the PAni-ES organic layer would appear to be more stable under these conditions than the equivalent PEDOT:PSS organic layer. This is a positive result that provides grounds for PAni-ES to be considered alongside, if not preferentially to PEDOT:PSS in terms of photocell longevity.

7.3.4 Addition of a PEDOT:PSS Surface Electrode

Here an attempt has been made to provide a possible explanation as to the cause of the reproducibly low FF values obtained for all single organic layer hybrid cells, signifying the less than ideal shape of the corresponding I-V curves. It was hypothesised that the cause of the low FF values could be poor top electrical contact to the top (conducting polymer) surface of the photocells. This is logical considering the design of the top electrical contact used experimentally and the relatively poor lateral conductivity of the PAni-ES. The lateral conductivity of PAni-CSA microfilms has been measured as $2.68 \pm 1.72 \text{ Sm}^{-1}$ by four point conductivity measurement as described experimentally in section 2.8.

As shown in figure 7.12, the distance between gold bus bars of the top electrical contact is 3mm, i.e. considerably large relative to the polymer layer thickness. The design of the solar cells requires the produced photocurrent as recorded by the solar simulator to be conducted laterally through the PAni-ES into the gold electrical contacts. In this situation the upper area of the $1\mu\text{m}$ thick PAni-ES film is effectively acting as part of the top electrical contact in its own right.

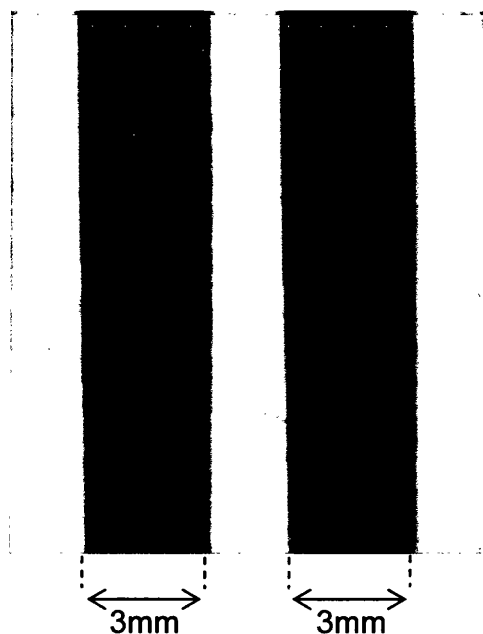


Figure 7.12. 3mm gap between gold buss bars (green PAni-ES).

As an attempt to increase the lateral conductivity of the surface electrode (gold bus bars), a secondary microfilm of PEDOT:PSS was applied to the surface of the PANi-ES layer as illustrated in figure 7.3. This was attempted because PEDOT:PSS is widely used commercially as a transparent organic electrode material. It was hypothesised that this could possibly improve photocell performance (increase FF) by easing the passage of electrons at the mid point between the gold buss bars by acting exclusively as a homogenous transparent electrode material.

Water soluble PEDOT:PSS was applied as transparent homogeneous layers of PANi-ES of all dopants tested previously. Successful multilayer cells were created of PANi-CSA, PANi-PP and PANi-pTS but not PANi-DBSA. The PANi-DBSA coating was found to wash off the Si surface upon application of aqueous PEDOT:PSS solution. This prevented the successful application of this second organic layer, possibly due to the nano-particulate nature of the PANi-DBSA microfilm as previously described (figure 7.8).

The consistent finding of applying the PEDOT:PSS as a top electrode contact on the surface of PANi-ES was that the shape of the I-V curves remain poor, and poor FF values are recorded as a result (figure 7.13). To ensure reproducibility two identical cells of each (PANi-CSA - PEDOT:PSS, PANi-PP – PEDOT:PSS and PANi-pTS – PEDOT:PSS) have been fabricated and all show similar results. Figure 7.14 shows an example I-V curve obtained from the PANi-CSA – PEDOT:PSS photocell configuration. This I-V curve shows that after the application of a conductive PEDOT:PSS top electrode, the curve shape remains characteristic of the single organic layer hybrid cells. The addition of a PEDOT:PSS layer to the photocell surface to act as an electrode material generally worsens photocell performance, and all efficiencies remain very small at less than 0.2%.

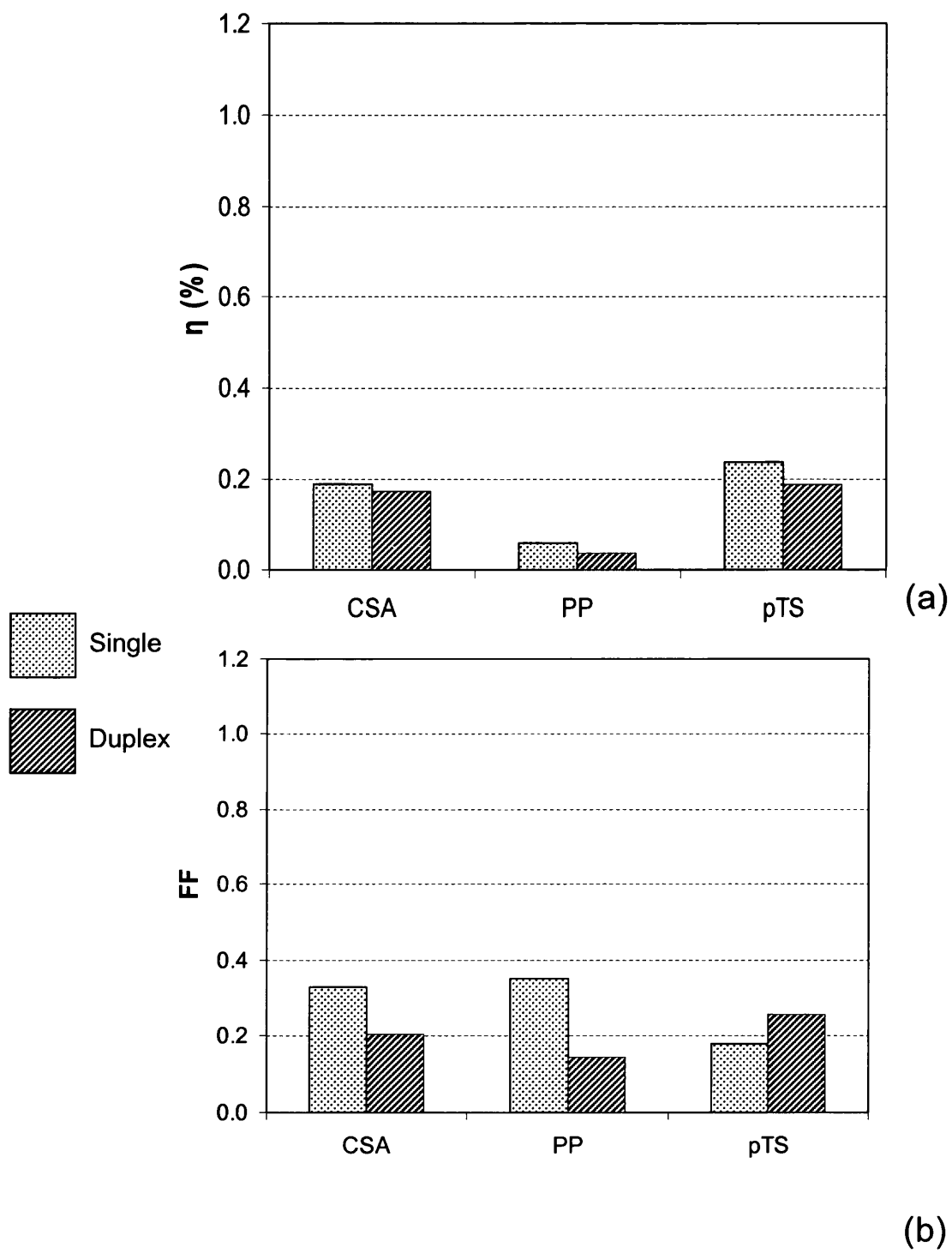


Figure 7.13. Comparison of photocell efficiency and FF between single PANi-ES layer and PANi-ES – PEDOT:PSS duplex photocells at one sun light intensity.

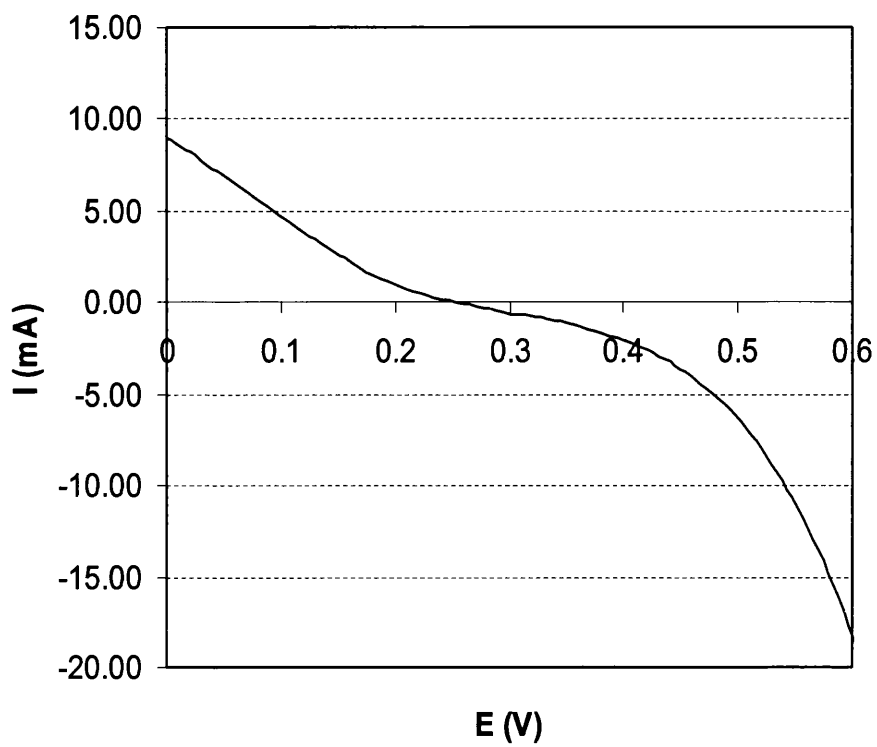


Figure 7.14. PANi-CSA – PEDOT:PSS I-V curve recorded using the Dysol solar simulator at one sun light intensity.

7.4 Conclusions

Polyaniline emeraldine base (PAni-EB) is shown to be ineffective when used as an organic layer within an organic hybrid photocell. Polyaniline emeraldine salt (PAni-ES) differs in that it has been proven to act as a p-type semiconductor when applied as the organic layer within a hybrid bilayer photocell in conjunction with an n-type Si. Additionally, PAni-ES has previously been proven to offer inhibition of corrosion driven cathodic disbondment on both iron [7-9] and zinc [10]. This multitude of abilities makes PAni-ES a valuable material for the future pre-painted steel industry.

In this study a number of differently protonated PAni-ES have been incorporated as the organic layer within the hybrid photocells, and all are seen to function as a p-type material. It was found that photocell performance depends greatly upon the quality of the organic layer, where poor quality PAni-ES layers cause very low efficiency. As a generalisation the performance of photocells where the organic layer is PAni-ES compare favourably with those using the more conventional organic p-type material (PEDOT:PSS). This indicates the viability of PAni-ES as an alternative material to PEDOT:PSS for organic photovoltaic applications.

Performances of the hybrid solar cells investigated here are generally very low (<0.4% efficiency), and FF values are calculated to be well below the value of 0.6 (60% energy conversion) [6]. Hybrid PAni-ES photocells are shown to produce V_{oc} 's in the range of 0.25V at 1 sun light intensity, comparing to 0.30V for PEDOT:PSS photocells. A noticeable result was that decreasing the light intensity from 1 sun to 1/10 sun causes the efficiency of the photocells to double, which is the case for both PAni-ES cells and PEDOT:PSS cells. This decrease in light intensity caused the efficiency of the PEDOT:PSS photocell to reach over 1%.

Light soaking the photocells for a period of 21 days at 1 sun light intensity at an elevated temperature (46°C) caused an increase in performance of the PAni-ES in terms of the V_{oc} . In the case of PEDOT:PSS a negative effect was seen, indicating that perhaps PAni-ES is a more stable material under prolonged light exposure at elevated temperatures. The I_{sc} and FF of all PAni-ES photocells were seen to fall

slightly due to this exposure, and accordingly the overall cell efficiencies remained practically unchanged.

Adding a thin film of PEDOT:PSS as an additional electrode material to the surface of the PAni-ES in an attempt to improve electrode efficiency was unsuccessful. There was a slight decrease in cell performance caused by this additional layer, indicating that the PAni-ES is sufficiently conductive in itself. The decrease in performance is most likely due to less light being able to reach the active layers of the photocell.

7.5 References

- [1] S. F. Chung, T. C. Wen, and A. Gopalan, *Materials Science and Engineering B-Solid State Materials for Advanced Technology* **116**:125 (2005).
- [2] M. Narasimhan, M. Hagler, V. Cammarata, and M. Thakur, *Applied Physics Letters* **72**:1063 (1998).
- [3] Z. R. Liu, J. R. Zhou, H. L. Xue, L. Shen, H. D. Zang, and W. Y. Chen, *Synthetic Metals* **156**:721 (2006).
- [4] S. X. Tan, J. Zhai, M. X. Wan, L. Jiang, and D. B. Zhu, *Synthetic Metals* **137**:1511 (2003).
- [5] J. H. Fan, M. X. Wan, and D. B. Zhu, *Synthetic Metals* **95**:119 (1998).
- [6] A. Luque and S. hegedus, *Handbook of Photovoltaic Science and Engineering*, Wiley, 2003.
- [7] A. R. Bennett, H. N. McMurray, and G. Williams, *ECS Trans.* **11**:71 (2008).
- [8] R. J. Holness, G. Williams, D. A. Worsley, and H. N. McMurray, *Journal of the Electrochemical Society* **152**:B73 (2005).
- [9] G. Williams, A. Gabriel, A. Cook, and H. N. McMurray, *Journal of the Electrochemical Society* **153**:B425 (2006).
- [10] G. Williams, R. J. Holness, D. A. Worsley, and H. N. McMurray, *Electrochemistry Communications* **6**:549 (2004).

Chapter 8

Conclusions and Future Work

8.1 Conclusions

The primary aim of this thesis was to provide fundamental understandings of alternative corrosion inhibitors intended as replacements for strontium chromate for use within pre-painted steel coating systems for construction and domestic applications. Looking towards conducting polymers to provide this corrosion inhibition, much effort has been made to expand upon published research. Polyaniline emeraldine salt (PAni-ES) has been applied as optically transparent micro-films of varying thickness to the surface of iron, allowing the visualisation of corrosion-driven interfacial polymer state changes. Using this technique, a comparison was made between coatings containing PAni-ES as a pigmented dispersion and PAni-ES micro-films in terms of the degree of cathodic disbondment inhibition. Additionally the dopant dependent nature of the PAni-ES as an inhibitor was investigated by comparatively exploring the inhibition properties of sulfonate and phosphonate dopants. It is believed that this study has succeeded in providing further knowledge towards the way in which PAni-ES provides inhibition of cathodic disbondment.

A mechanistic study of how PAni-ES inhibits cathodic disbondment of organic coatings adherent to zinc has also been conducted. This study evaluated the dopant dependent performance of the PAni-ES when applied as a pigmented dispersion within an organic coating. It was found that only small variations in performance were seen between the dopant choices investigated. The ability to cast optically transparent PAni-ES micro-films from solution directly onto metallic substrates was employed during this study to provide mechanistic information. The summary of the findings agreed with published work that proposed the inhibition primarily arose from the interfacial film formation between the coating and the substrate acting to block cathodic O_2 reduction. It was concluded that PAni-ES offers comparable performance to strontium chromate in terms of providing inhibition of cathodic disbondment of organic coatings adherent to zinc.

Due to the current elevated raw material costs associated with PAni-ES inhibitors, alternative cathodic disbondment inhibitor technologies were investigated. The organic acids used to protonate (dope) PAni-ES were incorporated directly model

organic coatings and applied directly to the surface of both iron and zinc substrates. The findings of this research were that for organic acid etch primers adherent to iron, the rate of cathodic disbondment is significantly reduced. In the case of the organic acid etch primers adherent to zinc, para-toluenesulfonic acid was observed to completely prevent cathodic disbondment at very small acid loadings. This suggests that organic acid etch primers could provide a cost effective replacement for strontium chromate.

Recent increasing zinc prices have lead to the commercial development of more effective metallic coatings that are able to be applied in thinner coating weights. These 1.5Mg/1.5Al/Zn alloy coatings have been found to resist cathodic disbondment of non-inhibited organic coatings, but were discovered to be susceptible to filiform corrosion (FFC). Published findings of FFC occurring on zinc or zinc alloys was unobtainable and accordingly much effort was employed to discover the active FFC mechanism and important factors of initiation. It was concluded within this thesis that the observed mechanism of FFC attack is unconventional and that an important factor in the initiation is acetate released due to breakdown of the organic coating.

The semiconductor properties of PANi-ES have been utilised and proven to act as an organic photovoltaic material. When applied as a micro-film adherent to a single crystal silicon substrate, diode characteristics were apparent. The exposure of the silicon-PAni-ES sandwich structure to light was found to produce a photocurrent comparable to photocells produced with the more recognised organic photovoltaic material; polyethylenedioxythiophene (PEDOT). This investigation of the photovoltaic characteristics of PANi-ES have proven it to be a more robust photovoltaic material than PEDOT. These findings offer further opportunity for PANi-ES to become a viable material for use within the pre-painted steel industry, for more novel and diverse applications than corrosion inhibition alone.

8.2 Future Work

- Apply the mechanistic understanding of the way in which PANi-ES inhibits cathodic disbondment of organic coatings adherent to steel to the pre-painted steel industry.
- Systematically coat PANi-ES micro-films to zinc, to explore what effect coating thickness has on the degree of cathodic disbondment inhibition.
- Explore the compatibility of organic acid etch primers with commercial organic coating systems currently used in pre-painted steels.
- Investigate long-term ways of inhibiting filiform corrosion of organic coating adherent to Magizinc alloys.
- Utilise the photovoltaic research presented within this thesis as an incentive to develop novel high-value coating systems to be used industrially for cladding applications.